# Surface science and chemical studies of NiO/single crystal $TiO_2$ heterostructure photocatalysts

**Dissertation submitted by Shun Kashiwaya to obtain the academic degree**
**Doctor-in-Engineering (Dr.-Ing.)**
**Date of submission: 15th October 2018**

**Supervisor: Prof. Dr. Wolfram Jaegermann**
**Co-supervisor: Prof. Dr. Thierry Toupance (University of Bordeaux)**

TECHNISCHE
UNIVERSITÄT
DARMSTADT

## Acknowledgements

First of all, I would like to thank my supervisors, Prof. Thierry Toupance, Prof. Andreas Klein, and Prof. Wolfram Jaegermann. Thierry and Wolfram accepted me as a PhD candidate. I moved between two institutes of Bordeaux and Darmstadt often. During the periods in Bordeaux, Thierry not only helped me conduct chemical parts of our research as I did not have much prior experience in chemistry, but also supported my life there. Andreas got me interested in fundamental works concerning on metal oxides, which turned out to be one of my research topics and subsequently one of the best results in our works. Wolfram gave me various opportunities, encouraged me, and showed me generous patience to focus on my research work. I sincerely appreciate my supervisors who are sincere to science and criticize and stimulate me constructively. Their attitude toward science has been and will be impressing me.

Performing experiments safely and productively was not possible without help of my colleagues. I like to thank Andreas Hubmann, Christian Lohaus, Phillip Wendel, and Hans Wardenga for helping me conducting experiments at DAISY-MAT, Andreas Hujdak for LEED measurements at DAISY-FUN, and Szu-Hsuan Lee and Yannick Hermans at chemical laboratories. I also appreciate Prof. Etienne Duguet and Dr. Cyril Aymonier who welcomed me at CNRS ICMCB in France. The help of Marie-Anne Dourges and Odile Babot for nitrogen sorption and Uli Castanet and Jerome Majimel for TEM and EDX also has been indispensable.

I am thankful to the Institutes of Material Science at TUD and Molecular Sciences at UB for allowing me to pursue a PhD degree there, and the Erasmus Mundus International Doctoral School IDS-FunMat for the funding.

Finally, I would like to express my gratitude to my parents, sisters, Tiffany and wife for always supporting me.

Shun Kashiwaya:
Surface science and chemical studies of NiO/single crystal $TiO_2$ heterostructure photocatalysts
Darmstadt, Technische Universität Darmstadt,
Published in TUprints in 2020
Date of the viva voce: 27th November 2018

## Statement regarding the thesis

I hereby confirm that I have written the present thesis independently and without illicit aid from third parties, using solely the aids mentioned. All passages from other sources are marked as such. This work has not been presented to an examination office before in this or a similar form.

## Erklärung zur Dissertation

Hiermit versichere ich, die vorliegende Dissertation ohne Hilfe Dritter nur mit den angegebenen Quellen und Hilfsmitteln angefertigt zu haben. Alle Stellen, die aus Quellen entnommen wurden, sind als solche kenntlich gemacht. Diese Arbeit hat in gleicher oder ähnlicher Form noch keiner Prüfungsbehörde vorgelegen.

Darmstadt, 15th October 2018

(Shun Kashiwaya)

# ABSTRACT

Photocatalysis on semiconductor metal oxide surfaces has attracted considerable attention as a sustainable environmentally friendly method for water/air purification and hydrogen production by water splitting. Among semiconducting metal oxides $TiO_2$ has been intensively investigated as a promising photocatalyst candidate. However, despite many efforts, its photocatalytic activity is far from a practical level mainly due to inefficient charge carrier separation and resulting charge carrier recombination. An advantageous strategy to address this issue is the development of heterostructures by coupling to a metal to form a Schottky junction or to metal oxides to create a p-n junction at their interface in order to prevent the recombination by vectorial charge carrier separation at these energy junctions. On the other hand it was revealed over the past decade that crystal facets play a decisive role in trapping of charge carriers and thus photocatalytic redox reactions. Thus, selective deposition of metal or metal oxides onto specific facets would enhance the photocatalytic activity by improving charge separation. To achieve higher activities, two methods, the supercritical fluid chemical deposition route and the photodeposition method, were investigated to deposit selectively p-type NiO onto specific facets of n-type $TiO_2$ single crystalline nanoparticles to establish a p-n junction. The resulting $NiO/TiO_2$ nanocrystals were characterized by X-ray diffraction (XRD), transmission electron microscopy (TEM), energy-dispersive X-ray spectroscopy (EDX), $N_2$ sorption measurements, UV-visible diffuse reflectance spectroscopy (DRS), X-ray photoelectron spectroscopy (XPS) and ultraviolet photoelectron spectroscopy (UPS). The heterojunction photocatalysts showed higher photocatalytic efficiency than pure $TiO_2$ for the decomposition of organic dyes. Particularly, 0.1-0.25 wt % of NiO was the optimal loading amount, showing the highest activity. To elucidate the role of crystal facets of $TiO_2$ and the effect of selective deposition of NiO, rutile (001), rutile (110), anatase (001), and anatase (101) surfaces with different surface states were prepared and their electronic properties were systematically compared by XPS and UPS measurements. Furthermore, water adsorption onto the different surfaces were also investigated. Regardless of surface stoichiometry, the Fermi level position of the anatase (001) surface is situated higher than that of the anatase (101) surface in energy while that of the rutile (001) surface is located lower than that of the rutile (110) surface. This can explain why photo-generated electrons and holes preferentially migrate to the (101) and (001) facets on $TiO_2$ anatase crystals, respectively. Work function values of these oriented surfaces vary depending upon the surface states related to distribution and amount of oxygen vacancies as well as adsorbed oxygen peroxo species on the surface. In order to experimentally determine energy band alignments, interface experiments were performed by stepwisely depositing NiO onto above well-defined oriented $TiO_2$ surfaces. The enhanced photocatalytic activity of $NiO/TiO_2$ heterostructure nanoparticles were rationalized on the basis of the obtained band alignments. The information of electronic properties of different oriented $TiO_2$ under various surface states would provide a new insight to construct the optimal energy band alignment of the heterostructure system with $TiO_2$. In addition, the concept of heterojuction nanocrystals where co-catalysts are selectively deposited should find practical application to purify the environment and to sustainably produce renewable hydrogen.

# Contents

# 1 Introduction

Our modern society faces enormous energy issues demanding innovative solutions: phasing down the nuclear power, substituting fossil fuels, and reducing emissions of potent climate-damaging and greenhouse gases such as carbon dioxide. According to energy forecasts of international energy agency[1], global energy needs would rise more slowly than in the past decades but still expand by 30 % by 2040. It is obvious that in order to meet this growing energy consumption in the long term a fundamental renewal of the energy sector is necessary, away from conventional strategy using limited resources and towards use of renewable energy sources. Among various energy resources, hydrogen is of particular interest as it can be consumed in a fuel cell to produce efficiently electrical energy with water as a byproduct instead of emitting greenhouse gasses. Compressed hydrogen and fuel cells can provide electricity with weights which are 8-14 times less than batteries[2]. The likely costs are expected that an electric vehicle using an advanced battery would cost more than a fuel cell vehicle in 2030[3]. Thus, a hydrogen economy has a clear advantage in reducing the emission of greenhouse gasses and in applying for industry owing to its economic rationality. Another environmental challenge is to secure clean abundant water without contamination to meet increasing demand for limited supply of freshwater. In this context photocatalysis, which usually involve a catalytic process taking place at the surface of semiconductors under the light illumination, is considered as a promising technology in the field of renewable energy and environment. It is a chemical process that underpins the development of critical renewable energy and environmental technology such as hydrogen production from water splitting and photocatalytic water/air purification. However, practical applications of photocatalysis are limited due to recombination of the photo-induced electron-hole pairs in the semiconductor photocatalysts.

Among the available metal oxide semiconductors, anatase titanium dioxide ($TiO_2$) is one of the best understood photocatalyst prototype. Recent advances revealed that photo-generated electrons and holes get trapped at and migrate toward specific facets of single crystalline $TiO_2$ nanocrystals[4]. Electrons are preferentially transferred to the anatase (101) surface while holes move to the (001) surface. As a result, the (101) and (001) surfaces act as reduction and oxidation redox reaction sites, respectively. Simultaneous consumption of both electrons and holes is necessary to effectively promote the reactions as accumulated electrons or holes, which are not consumed, lead to a higher possibility of the recombination. By selecting an optimal aspect ratio of these facets, the highest catalytic activity would be achieved. On the other hand conventional manipulation of charge carrier by Schottky or p-n junction created by coupling metal or semiconductor co-catalysts to semiconductor photocatalyst has been believed to be an attractive strategy to promote electron-hole pair separation[5]. In this context, currently emerging topic in the field of photocatalysts is to combine facet-engineering with loading co-catalysts. Selective deposition of appropriate co-catalysts onto specific facets of photocatalysts can lead to further less possibility of the recombination, resulting in superior photocatalytic activity. However, the mechanism of preferential migration of charge carrier toward different facets of $TiO_2$ still remains unclear and information on selective deposition of co-catalysts onto specific faces of $TiO_2$ is sparse.

The aim of the present work is to elucidate the mechanism of intrinsic charge carrier transfer in single crystalline $TiO_2$ and further improve the charge carrier separation by establishing p-n junction via depositing p-type NiO selectively onto specific facets of $TiO_2$ nanocrystals. The main objectives are:

1. To prepare differently oriented anatase and rutile substrates under various surface states and compare their electronic properties by XPS and UPS in order to elucidate the mechanism of charge trapping and separation between different facets. As electronic properties Fermi level positions dictate the charge transfer between the facets, variation of work function is also a crucial factor when one considers band alignments of $TiO_2$ and co-catalysts.
2. To experimentally determine the band alignments of $NiO/TiO_2$ by so-called interface experiments in order to rationalize the enhanced photocatalytic activities of $NiO/TiO_2$ heterostructure photocatalysts. Herein, NiO is deposited onto different oriented anatase and rutile substrates with different surface stoichiometry.
3. To prepare heterostructure photocatalysts of $NiO/TiO_2$ where NiO is selectively deposited onto the specific facet of $TiO_2$ nanocrystals via the supercritical fluid chemical deposition route and a photo-deposition method.
4. To characterize the prepared photocatalysts by XRD, TEM, EDX, DRS, XPS, and nitrogen sorption analysis and examine their photocatalytic activities in dye decomposition.

1. World Energy Outlook 2017. https://www.iea.org/weo2017/.
2. Fuel Cell and Battery Electric Vehicles Compared.
3. Kromer, M. A. Electric powertrains: opportunities and challenges in the US light-duty vehicle fleet. Massachusetts Institute of Technology, 2007.
4. Ohno, T.; Sarukawa, K.; Matsumura, M. Crystal faces of rutile and anatase TiO2 particles and their roles in photocatalytic reactions. *New Journal of Chemistry* **2002,** *26* (9), 1167-1170.
5. Kamat, P. V. Manipulation of Charge Transfer Across Semiconductor Interface. A Criterion That Cannot Be Ignored in Photocatalyst Design. *J Phys Chem Lett* **2012,** *3* (5), 663-72.

# 2 Fundamentals and state of the art

## 2.1 The surface science of single crystal

The relationship between surface structure and physical and chemical properties is an essential topic in surface science. Especially the surface structure of metal oxides such as $TiO_2$, which have a mixed ionic and covalent bonding, is expected to influence local surface chemistry stronger than expected for metals or elemental semiconductors[1]. The surface science of $TiO_2$ was reported in depth by Diebold in 2003[2]. In this section, surface structures of single crystalline rutile and anatase are briefly described and recent development of their preparation and surface physical and chemical properties are summarized.

### 2.1.1 Geometric and electronic structure

$TiO_2$ crystallizes in different structures; brookite (orthorhombic), rutile (tetragonal), and anatase (tetragonal). Among these polymorphs, rutile and anatase have been commonly used in applications such as photocatalysis. Although crystal structures of rutile and anatase are tetragonal and similar to each other, these two structures differ by the distortion of each $TiO_6$ octahedron and by the configuration of the octahedral chains. The unit cell of rutile and anatase are shown in figure 2.1. The octahedron of rutile is irregular and shows a orthrombic distortion while that of anatase is considerably distorted and shows a lower symmetry than orthorhombic. In addition, each octahedron of rutile has contacts with 10 neighbouring octahedrons whereas that of anatase is in contact with eight neighbouring octahedrons. These structural differences result in different electronic structures between rutile and anatase.

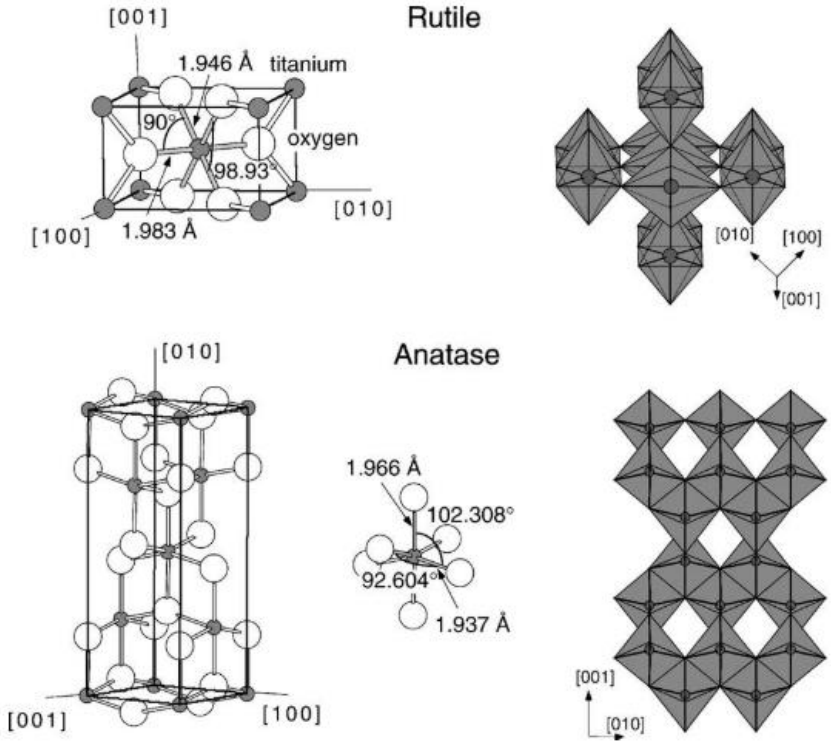


Figure 2.1. Structures of rutile (top) and anatase (bottom). The bulk unit cell of rutile has the dimensions, $a = b = 4.587$ Å, $c = 2.953$ Å, and that of anatase has $a = b = 3.782$ Å, $c = 9.502$ Å. Reproduced from ref[2].

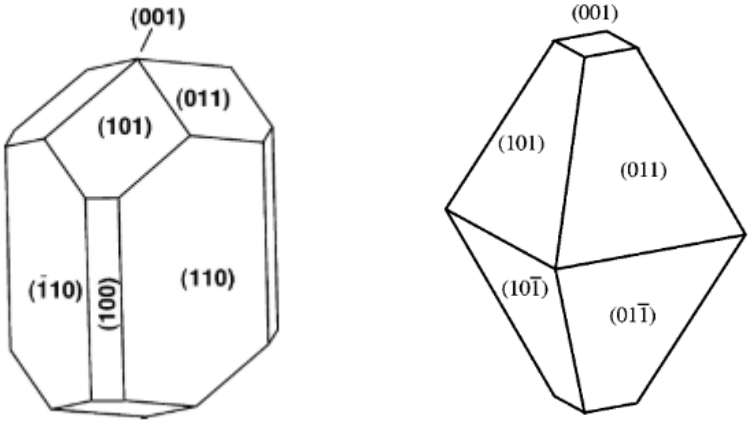


Figure 2.2. Equilibrium shapes of rutile (left) and anatase (right) according to the Wulff construction and the calculated surface energies. Reproduced from ref[3-4].

The equilibrium shapes of rutile and anatase were constructed according to Wulff construction and the surface energies were calculated[3-4] (figure 2.2). The rutile (110) and (001) surface have the lowest and highest energy, respectively[4]. Of different rutile orientations, the rutile (110) surface is the most stable and thus has been studied intensively as a model surface of metal oxides for investigations of various chemical phenomena on the surface. The anatase (101) and (001) surfaces have the lowest and highest surface energies, respectively[3].

## 2.1.2. Preparation of the anatase (001) and (101) surfaces

Despite the technical importance of anatase, experimental investigations of single crystalline $TiO_2$ surfaces have been mostly performed for rutile. This is mainly due to the difficulty in preparing pristine oriented anatase surfaces. Rutile surfaces are readily available and their preparation methods were summarized in a literature review[2]. In this section, recently developed preparation methods of oriented anatase surfaces in form of thin films and natural crystal substrates are discussed.

Oriented anatase surfaces can be epitaxially grown as thin films. The (001) surface has been grown on $SrTiO_3$ (001) and $LaAlO_3$ (001) by chemical vapor deposition (CVD)[5-6] and molecular beam epitaxy (MBE)[7-8]. The (101) surfaces can be grown on vicinal $LaAl_3$ (110) by MBE[9]. However, these techniques have not been widely employed due to rather complicated procedures. To avoid such difficulties, employing natural stones as $TiO_2$ single crystal substrates was investigated[10]. Thus Dulub *et al.*[10] proposed a new strategy to obtain a pristine anatase surfaces by cleaving. Anatase natural stones from Russia and Pakistan are readily available from mineral dealers as shown in figure 2.3. These crystals often contain impurities of alkali and alkaline earth elements. Cleaning cycles of Ar ion sputtering and annealing at elevated temperature in vacuum are the typical procedures to prepare clean surfaces of $TiO_2$. However, the annealing step might cause the segregation of the impurities of which Fe is the most common. When the amount of impurities is too large, the crystal can be hardly used as a clean substrate. Thus, one has to be lucky to get mineral with less impurities. Cutting, orienting,

and polishing of natural stones are needed as the surface of as-obtained minerals at mines has a rough surface with scratching. Oriented anatase substrates made from natural stones with the above treatments are also available at mineral substrate shops. These substrates have contaminations on the surface and rough surfaces due to chemical physical polishing. Thus, low energy electron diffraction (LEED) measurements do not show any patterns for these substrates. To obtain well oriented smooth surfaces and clear patterns of LEED for both cleaved and polished surfaces, additional cleaning cycles of sputtering and annealing are required[11].

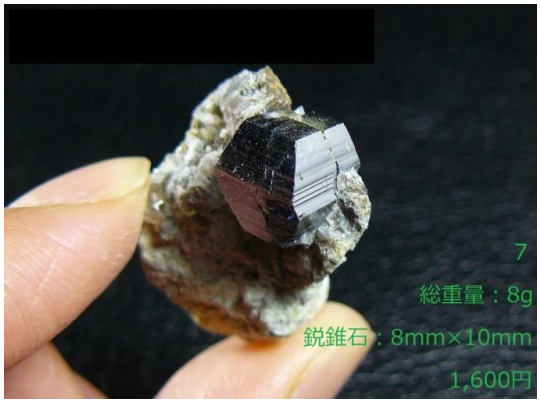


Figure 2.3. Photograph of anatase mineral from Pakistan. The top and bottom of the bipyramid structure are truncated. The top surface which appears after truncation is the (001) surface, and the side of the pyramid is the (101) surface. 8 x 10 mm sized-crystal generally costs around 30 Euros.

Setvin *et al.*[11] recently suggested that additional oxidation treatment is required after cleaning cycles of sputtering and annealing as they introduce oxygen vacancies, but also might ruin the morphology and partially form amorphous phase. Annealing in a partial pressure of oxygen repairs the lattice oxygen. However, STM[12] and LEED[13] measurements revealed that this process formed iron oxides layer on the surface as a result of oxidation of iron contamination which was diffused from the anatase bulk. To avoid such contaminations on the surface and obtain smoother surface, epitaxial growth on the mineral surface can be an useful strategy. Kraus *et al*[14]. demonstrated homoepitaxial growth of highly ordered and pure layers of anatase on anatase natural stones using atomic layer deposition (ALD). This method is preferentially applicable for the (101) surface as the (001) surface has many candidates of substrates on which anatase growth is carried out while there are almost no substrates, the lattices of which have a similarity with the (101) surface due to its complex structure.

Anatase (001) and (101) surfaces prepared by the cleaning cycles of sputtering and annealing shows (1 x 4) reconstruction pattern and (1 x 1) unreconstructed patter in LEED, respectively, although there are some experimental reports which show an unreconstructed (001)-(1 x 1) surface[2, 5, 15]. The unstable (001)-(1 x 1)surface reconstructs when heated to elevated temperatures[16-17] and it is in agreement with theoretical calculations[18]. Herman *et al.*[16] found the (1 x 4) reconstruction after sputtering and annealing the (1 x 1) surface in vacuum and proposed three potential models to interpret the results; a) missing row model, b) added row model, and c) microfacet model (figure 2.4). On the other hand Lazzeri *et al.*[19] introduced a new concept of added molecule (ADM) structure for (1 x 4) reconstruction based on calculations as shown in figure 2.5. Their calculations indicate that the ADM structure is energetically more favourable than an unreconstructed (1 x 1) surface and other possible models. The ADM structure might form by periodically replacing rows of the surface

bridging oxygens of the (1 x 1) surface with rows of $TiO_3$ species in order to relieve the large surface tensile stress on the unreconstructed surface. High-resolution scanning tunnelling microscopy (STM) and non-contact atomic force microscopy (nc-AFM) images confirmed the ADM model[20].

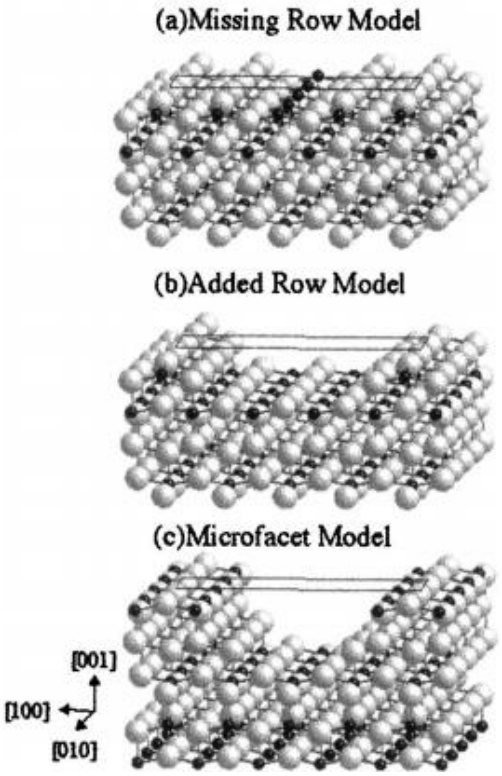


Figure 2.4. Three models of (001)-(1 x 4) reconstruction of anatase; a) The missing row model (MRM), b) The added row model (ARM), c) The microfacet model (MFM). Dark and light coloured circles represent Ti and O atoms, respectively. Reproduced from ref[6].

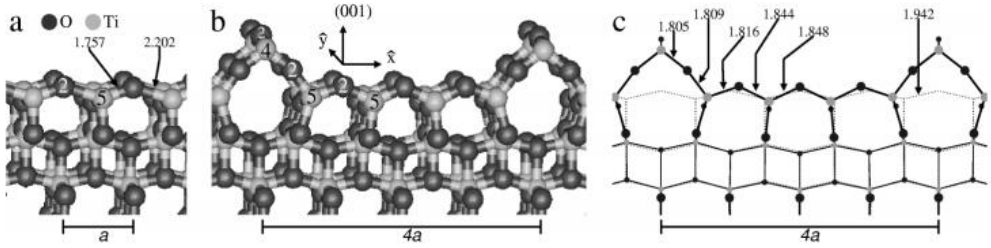


Figure 2.5. (a) Relaxed unreconstructed (001)-(1 x 1) surface of anatase. (b) Relaxed structure of the ADM (001)-(1 x 4) surface. (c) Projection of the atomic positions of the ADM model. Reproduced from ref[19].

Anatase single crystals were also grown from the gas phase by a chemical transport reaction employing $TeCl_4$ as the transporting agent[21]. However, its surface area is 1-4 $mm^2$ which would be too small to be used for measurements such as X-ray (XPS) and UV (UPS) Photoelectron Spectroscopy, and Scanning Tunneling Microscopy (STM). In addition, this preparation procedure is carried out outside the vacuum chamber and thus the resulting crystals need to be cleaned outside and inside the vacuum chamber, followed by transferring them to the measurement vacuum chambers without breaking vacuum. A heating process for cleaning the surface may cause a problem due to surface segregation of contaminated metal elements which are contained in the crystal, e,g, 0.22% of Al and traces of V, Zr, Nb, and La.

### 2.1.3 Surface and subsurface defects

$TiO_2$ is considered to be a n-type semiconductor owing to intrinsic oxygen vacancies. Oxygen vacancies can be easily introduced by annealing at elevated temperatures, bombarding with electrons and Ar ion, and hydrogenation[2, 22]. Cronemeyer *et al.*[23] was the first to determine the impurity level related to oxygen vacancies to be saturated 0.75–1.18 eV below the conduction band edge (figure 2.6). In photoelectron spectroscopy (PES), the $Ti^{3+}$ emission line in $Ti2p_{2/3}$ core level spectra is assigned to the presence of such defects. The binding energy of $Ti^{3+}$ is situated lower than that of the main emission line of $Ti^{4+}$ by 1.7 eV[24]. Defects in $TiO_2$ can also be identified with presence of so-called band gap states (BGS) in the band gap region [25-26]. BGS are believed to be associated with occupied Ti 3d states on $Ti^{3+}$ sites near the oxygen vacancy sites on the surface, but also due to $Ti^{3+}$ interstitial states in the subsurface region[25, 27-29]. Reckers *et al.* [25] proposed that BGS consist of shallow gap states (SGS) and deep gap states (DGS), which are situated at 0.5 and 1.6 eV below the conduction band edge, respectively. DGS are conventionally assigned to excess electrons localized on $Ti^{3+}$ interstitial and Ti atoms near oxygen vacancies[25, 30-32]. SGS have different origins. First, excess electrons at step edges or imperfect structures on the (101) surface might contribute to form SGS and its intensity is pronounced by increased amount of oxygen vacancies[25]. In addition, $Ti^{3+}$ interstitial and oxygen vacancy are also related to SGS. Remaining excess electrons produced by the formation of $Ti^{3+}$ interstitial and oxygen vacancy and exceeding the number of one electron per d band gap state would be delocalized on lattice Ti atoms due to electron-electron correlation, which are the components of the $TiO_6$ octahedra near the defect sites, and thus result in the shallow energy level near the conduction band edge[30-32]. However, the contribution of oxygen vacancy to SGS is negligible compared to the effect of $Ti^{3+}$ interstitial. The $Ti^{3+}$ emission line in $Ti2p_{2/3}$ and BGS are useful to determine the presence of defects. However, when the concentration of defects is small, it is difficult to detect these signals by XPS and UPS and such intensity attenuated emission is only detectable by surface sensitive resonant photoelectron spectroscopy[25, 27, 33].

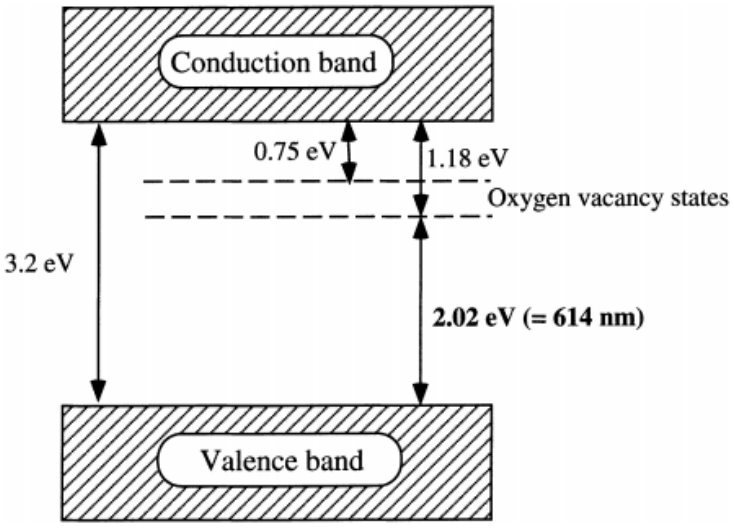


Figure 2.6. Band structure model of reduced $TiO_2$ with oxygen vacancies proposed by Cronemeyer *et al.*[23]. Reproduced from ref[34].

Based on DFT calculations, Cheng and Selloni[35] investigated the relative stabilities of oxygen vacancies at surface and subsurface sites of anatase (101), anatase (001), and rutile (110) surface. Their study revealed that defects are considerably more stable at the subsurface than on the surface for anatase surfaces while bridging oxygen sites on the surface are favoured for oxygen vacancies for rutile (110) surface (Table 2.1). This calculation was performed based on the simple generalized gradient approximation (GGA) which tends to underestimate the band gap and do not consider the Coulomb interaction in strongly correlated systems[36]. Thus, for $TiO_2$, GGA underestimates the d electron localization and the amount of lattice distortions at oxygen vacancy sites, causing a difficulty in comparing defect stability of surface, subsurface, and bulk. To overcome this issue, Li *et al*[37]. employed hybrid functional of screened exchange (sX) functional[38], which give good representations of the electronic structure. Their results showed the same trend to that obtained with GGA although sX function showed a higher energy than GGA for all the surfaces. These calculations can explain why the defect density observed for anatase surfaces is lower than that of the rutile surface. He *et al.*[39] performed STM measurements of reduced anatase (101) surface and found evidence for the predominance of subsurface defects. DFT calculations also predicted that the surface and subsurface of the (101) surface requires lower formation energy (enthalpy) to generate oxygen vacancies than the (001) surface. This is in agreement with experimental investigation showing that the (001) surface is more stable against defects than the (101) surface[27].

Table 2.1. Formation energies of oxygen vacancy defects at different surface and subsurface sites of anatase (101), anatase (001), and rutile (110). Lower formation energy means higher possibility of oxygen vacancy. Reproduced form ref[35].

| Defect site | **A**-$TiO_2$(101) | **A**-$TiO_2$(001) (1×4) | **R**-$TiO_2$(110) |
|---|---|---|---|
| $V_{O1}$ | 4.15(4.25) | 4.57(4.72) | **3.68**(4.01) |
| $V_{O2}$ | (5.40) | 5.17(5.52) | 4.50(4.56) |
| $V_{O3}$ | (4.73) | 4.29(5.05) | **3.99**(4.23) |
| $V_{O4}$ | **3.69**(4.03) | 4.78(5.08) | 5.23(5.22) |
| $V_{O5}$ | **3.65** | **4.10**(4.34) | 4.73(4.83) |
| $V_{O6}$ | | | 5.28(5.29) |
| $V_{O7}$ | | | 4.46 |
| $V_{O8}$ | | | 4.67 |
| $V_{O9}$ | | | 4.38 |

### 2.1.4 Adsorption of water on the surfaces

Most applications of $TiO_2$ such as water splitting, water purification, and self-cleaning involve an interaction with water molecules. Thus, the investigation of water adsorption on the surface is of importance and has focused on its state of adsorption; molecular, dissociative, or multilayer adsorption. Most calculations predicted that dissociative adsorption of water is energetically preferred than molecular adsorption on the rutile (110), which is the most studied surface and considered as the model surface[2]. However, there is a consensus established by a number of experimental evidence that for rutile (110) surface water dissociates only at the

vacancy site of so-called bridging oxygen row while only molecular adsorption takes place on the stoichiometric defect-free surface[2, 40-41]. On the other hand, in spite of the practical importance of anatase, experimental research on water adsorption on the well-defined surfaces of anatase is sparse. To the best of my knowledge, so far only limited experimental studies on the anatase (101) surface have been performed by temperature programmed desorption (TPD) [14], scanning tunnelling microscope (STM)[42-44], and different photoelectron spectroscopy techniques such as XPS, UPS, and two-photon (2PPE) photoelectron spectroscopy[24, 45-48]. It has been quite controversial whether a dominant state of water adsorption on the anatase (101) surface is molecular or dissociative. In 1998, Vittadini *et al.*[49] performed DFT calculations to predict that molecular adsorption is favoured on the anatase (101) surface while water dissociates on the anatase (001). Following the calculation, in 2000s experimental results supported molecular adsorption on the anatase (101). Herman *et al.*[45] observed desorption states for water adsorption at 160, 190, and 250 K, which are assigned to multilayer water, water adsorbed to 2 fold coordinated oxygen atom, and water adsorbed to 5 fold coordinated titanium atom. Furthermore, O 1s emission of high-resolution XPS showed a shoulder peak related to molecularly adsorbed water at a binding energy of 534.5 eV although it is noteworthy that the measurements were performed at low temperature of 130 K. STM images of the anatase (101) surface exposed to water also implied that molecular adsorption most likely took place on the surface[42-43]. Contrary to the above results, Walle *et al.*[47] demonstrated mixed dissociative and molecular water adsorption on the anatase (101) surface by high-resolution XPS at a range of temperature from 160-400 K. Dissociative adsorption is predominant at 160-230 K and the intensity of O 1s emission related to OH component decreases rapidly compared to that related to molecular water. As a result, molecular adsorption is negligible and only dissociative adsorption is observed at temperature higher than 300 K. This result has triggered further studies of water adsorption on the anatase (101) surface.

It was also proposed by DFT calculations that water would dissociate on the anatase (101) surface with subsurface defects[24, 46, 50]. Liu *et al.*[51] demonstrate dissociation of water on the surface of defective anatase (101) particles by diffuse reflectance infrared Fourier transform spectroscopy (DRIFTS). Aschauer *et al.*[46] showed that at room temperature no signature of water on the pristine anatase (101) surface was found while the water, which was dosed at low temperature, remained molecularly on the reduced surface. Their DFT calculation also predicted that the barrier for the water dissociation is decreased by subsurface oxygen vacancies and thus the dissociation would take place on the reduced surface. Although the dissociated state is not energetically favoured even with subsurface vacancies, dissociation is favourable with subsurface Ti interstitials. Li *et al.*[50] proposed two possible scenarios of the interplay between molecular water and the anatase (101) surface with subsurface oxygen vacancies, explaining the preferable dissociation of water on the surface (figure 2.7). First, subsurface oxygen vacancies interact with molecularly adsorbed water and then migrate to the surface layer, facilitating water dissociation. Another pathway is that molecular water dissociates via an interaction with subsurface oxygen vacancies, which subsequently migrate to the surface layer. Sencer *et al.*[52] also proposed a possibility of dissociation, which could be triggered by an excess electron at the water/anatase (101) interface. The excess electron would get trapped into a stable surface $Ti^{3+}$ - bridging OH complex. This interaction between molecular water and subsurface oxygen vacancies was suggested by STM[53] as well as an interplay

between oxygen molecules and the subsurface oxygen vacancies[44]. However, further experiments are required to confirm that. Patrick *et al.*[54] proposed by DFT calculation that even on the stoichiometric surface water would adsorb dissociatively with the H-bonded complex of OH and water. However, there is no experimental data supporting the concept. These studies apparently indicate that surface condition such as defects or adsorbates on the surface plays a crucial role in water adsorption.

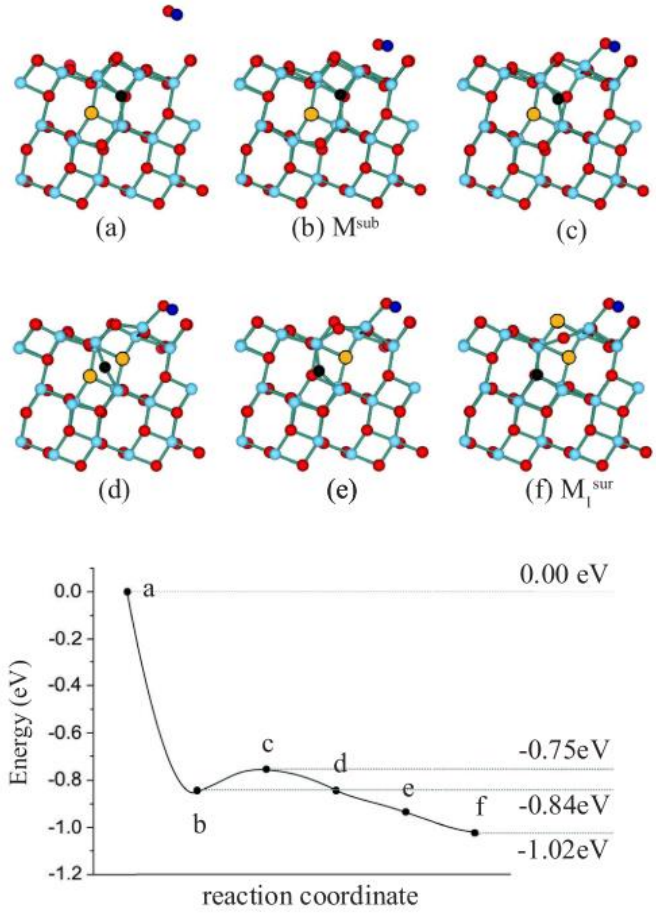


Figure 2.7. Different atomic configurations along the pathway for oxygen vacancy migration from the subsurface to the surface with molecularly adsorbed water on the anatase (101) surface. Dark blue, cyan, red, and yellow represent H, Ti, O, and oxygen vacancy, respectively. Reproduced from ref[50].

## 2.2 Principles of photocatalysis

Our society has been facing severe energy and environmental issues such as the depletion of fossil resources and pollution in air and water[55-56]. To approach such problems, researchers have explored new energy sources, which are sustainable and can replace thermal power generation using fossil fuels and nuclear power, and solutions by which contaminated air and water can be purified with cheap and abundant materials. Hydrogen has been focused on as an attractive alternative energy source. It can be used in a fuel cell to generate electricity with a high efficiency and just leave water instead of emitting greenhouse gases such as carbon dioxide. To generate hydrogen, there are various techniques employed nowadays. Steam reforming of methane is mostly used in industry. Liquids or gases containing hydrogen first form landfills, reacting with steam at elevated

temperature and producing hydrogen. In addition, gasification and electrolysis can be used to produce hydrogen. However, these methods require external energies such as heat and electricity. However electricity used for electrolysis can be generated from clean energy such as photovoltaic, wind, hydro, and biomass. A new era of the hydrogen society is dawning as hydrogen stations are replacing gas stations across the United States, Europe, and Japan led by Toyota. Since the discovery in 1972[57] that water splitting into hydrogen and oxygen can be achieved by $TiO_2$ under UV-light irradiation, photocatalysis has received considerable attentions as water can be directly split into hydrogen only using light. Photocatalysis is based on photoelectrochemical reactions induced by photo-generated charge carriers and involves three main steps: 1) excitation of electron-hole pairs by light irradiation, 2) charge carrier separation and transport to the photocatalyst surface, and 3) redox reactions using photo-generated charge carriers. For semiconductor photocatalysts, once excitation occurs under light irradiation the energy of which should be larger than the band gap of the photocatalyst, charge transfer of the photo-generated electron-hole pairs to adsorbed species on the photocatalyst surface takes place as shown in figure 2.8. When the photocatalysts are robust during the phenomena and the charge transfer is carried out continuously and exothermically, this process is called as heterogeneous photocatalysis.

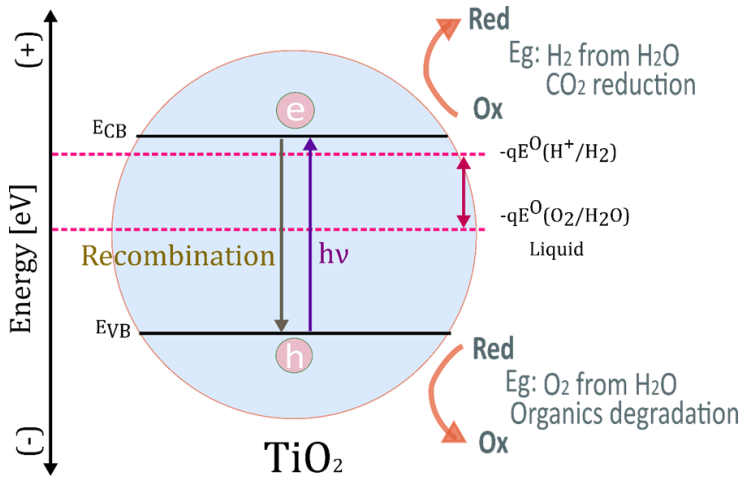


Figure 2.8. Scheme of photo-excitation of electron-hole pairs on the photocatalyst surface under light irradiation, following charge transfer to the surface, and redox reactions.

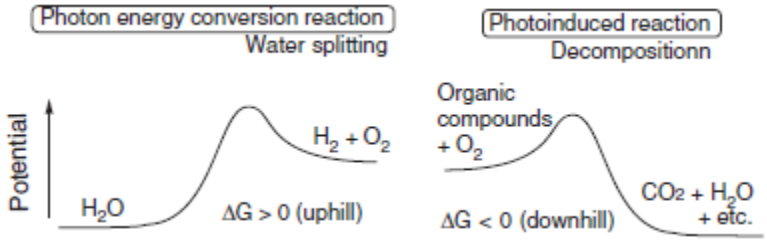


Figure 2.9. Different types of photocatalytic reactions. Water splitting (left) and organic decomposition (right). Reproduced from ref[58].

The photo-generated charge carriers can not only split water, but also lead to various beneficial phenomena such as decomposition of organic compounds, anti-virus, self-cleaning, and so on. Especially organic decomposition

by photocatalysis is relevant for environmental issues. Photocatalytic water splitting is a thermodynamically uphill reaction while photocatalytic decomposition is a downhill reaction as shown in figure 2.9[58]. Therefore, mechanisms of these different reactions are separately discussed in the following sections.

### 2.2.1 Water purification

One of the practical applications of photocatalysis is the degradation of the organic pollutants in water. Drastically developing world economy leads to the release of huge amounts of side products as pollutants in the environment. Cook predicted that tens of millions of dollars will be unavoidably spent to invest in new facilities to abate increasing water pollutants in the next decades[59]. In photocatalytic degradation reactions, generation of hydroxyl radicals ($OH^{\bullet}$) play a decisive role. Most photocatalytic degradation utilizes the strong oxidizing power of $OH^{\bullet}$ of 2.8 V versus Normal Hydrogen Electrode (NHE) in spite of its unclear nature[60]. Its oxidizing potential is quite high and just slightly lower than that of fluorine, i.e. 3.03 V[60]. It is capable of oxidizing most organic molecules, leaving carbon dioxide and inorganics. Mao *et al.* demonstrated that the oxidation rate of chlorinated ethanes is related to the C-H bond strengths of the organic molecules. This result indicates that the oxidation of organic molecules by $OH^{\bullet}$ would be the hydrogen atom abstraction from the organic molecules. Both electrons and holes are relevant although mainly holes contribute to the degradation. Photo-generated holes can indirectly oxidize organic compounds via $OH^{\bullet}$ produced by interaction with surface hydroxyl groups on the photocatalyst surface (reaction (1)) or molecule water (reaction (2)) as shown below.

$$h^+ + OH^- \rightarrow OH^{\bullet} \quad (1)$$

$$h^+ + H_2O \rightarrow OH^{\bullet} + H^+ \quad (2)$$

In typical photocatalytic reactions, holes oxidized compounds as described above while at the same time electrons reduce oxygen molecules, yielding the superoxide radical anion $O_2^{\bullet -}$ (reaction (3)). $O_2^{\bullet -}$ subsequently reacts with a water molecule to give hydroperoxyl radicals $HO_2^{\bullet}$ by protonation (reaction (4)), and finally transforms into $OH^{\bullet}$ along with hydrogen peroxide $H_2O_2$ as by-product (reaction (5)).

$$e^- + O_2 \rightarrow O_2^{\bullet -} \quad (3)$$

$$O_2^{\bullet -} + H_2O \rightarrow HO_2^{\bullet} + OH^- \quad (4)$$

$$HO_2^{\bullet} + H_2O \rightarrow HO^{\bullet} + H_2O_2 \quad (5)$$

$HO_2^{\bullet}$ can also result from reduction of oxygen molecules together with a proton (reaction (6)) and $H_2O_2$ can be also formed by reduction of dioxygen with the consumption of two electrons (reaction (7)).

$$O_2 + H^+ + e^- \rightarrow HO_2^{\bullet} \quad (6)$$

$$O_2 + 2H^+ + 2e^- \rightarrow H_2O_2 \quad (7)$$

Unstable $H_2O_2$ is believed to be decomposed into $OH^{\bullet}$ according to the following reaction

$$e^- + H_2O_2 \rightarrow OH^- + OH^{\bullet} \quad (8)$$

Tatsuma *et al.*[61] found that hydrogen peroxide generated on the photocatalysts via photocatalysis is transferred in air to the organic or inorganic substrates and there hydrogen peroxide is further converted into hydroxyl radicals, giving rise to oxidation reactions (Figure 2.10). This phenomenon is called as remote oxidation and confirms the indirect oxidation reactions by holes.

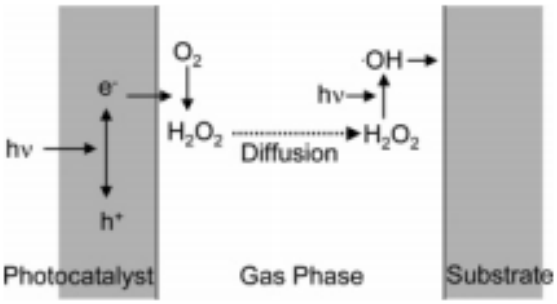


Figure 2.10. Schematic mechanism of remote oxidation by photocatalysts. Reproduced from ref[61].

Through above complicated pathways, electrons generate $OH^{\bullet}$ and oxidize organic compounds. However, it takes three electrons to produce one hydroxyl radical for the pathway of interaction with hydrogen peroxide (reaction (8)) while it takes only one hole to generate one hydroxyl radical from physisorbed water molecules or hydroxyl group (reaction (1) and (2), respectively). Therefore, most hydroxyl radicals contributing to organic oxidation reactions are originated from holes. Electrons are trapped at molecular oxygens, preventing the recombination of charge carriers and consuming electrons efficiently. Herein simultaneous consumption of electrons together with holes is a fatal factor since unreacted electrons are accumulated, recombine with holes, and decrease the total reaction rate.

The ability of semiconductor photocatalysts is ruled by its band energy positions and the redox potentials of organic compounds. Organic compounds can be reduced and oxidized by electrons and holes if their redox potentials are more positive than the flat band potential of the conduction band and more negative than the flat band potential of the valence band, respectively[62]. Thus, criteria for a good semiconductor photocatalyst for organic decomposition is that the redox potential of the $H_2O/OH^{\bullet}$ couple is located within the band gap of the photocatalyst. An ideal photocatalyst should be: 1) photoactive, 2) biologically and chemically inert, 3) physically robust, 4) stable against photo-corrosion, 5) inexpensive, 6) abundant on the earth, and 7) non-toxic. $TiO_2$ mostly meets these requirements, but its photocatalytic activity is not sufficient enough for practical use and it is only active under UV-light illumination. Therefore, the combination of the intrinsic properties of $TiO_2$ with the extrinsic modification provided by the deposition of co-catalysts is necessary for practical application[63].

## 2.2.2 Water splitting

Hydrogen is relevant not only as a new energy source, but also as a main source of ammonia. Ammonia can be produced by the Haber-Bosch process which is one of the most important invention in the last century for the prosperity of mankind. Nowadays it is used in various fields such as fertilizer and medicine, feeding and saving billions of people[64]. Thus, sustainable hydrogen evolution is of importance.

Photocatalytic water splitting into hydrogen and oxygen is an uphill reaction with a large positive change in the Gibbs free energy ($\Delta G° = +237$ kJ mol-1) which occurs according to the following reactions:

$$2H_2O + 4h^+ \rightarrow O_2 + 4H^+ \quad (9)$$

$$2H^+ + 2e^- \rightarrow H_2 \quad (10)$$

$$2H_2O \rightarrow 2H_2 + O_2 \quad (11)$$

According to Nernst equation, the Gibbs free energy of 237 kJ mol-1 corresponds to $\Delta E° = 1.23$ V per electron transferred. Therefore, to induce the water splitting reaction on a semiconductor surface, the semiconductor has to possess a large band gap which can absorb light with photons of energy higher than 1.23 eV. An ideal semiconductor photocatalyst has a band gap large enough to split water and its valence band and conduction band must be located at more negative and positive values than the electro chemical potentials $E°$ ($O_2/H_2O$) and $E°$ ($H^+/H_2$) to drive the oxygen evolution reaction (OER) and the hydrogen evolution reaction (HER) as shown in figure 2.11[65]. However, overpotentials of a few hundreds meV are required to drive both OER and HER at reasonable rates and need also to be taken into consideration.

Band edge positions vs NHE for different semiconductors are shown in figure 2.12[66]. Some materials have enough band gap energies to be excited by UV or visible light and their band edges straddle the potentials of both $O_2/H_2O$ and $H^+/H_2$ redox couples. However, due to the instability against water or photo-corrosion, very few semiconductors can meet the requirements for photocatalytic overall waters splitting by simultaneous water oxidation and reduction reactions.

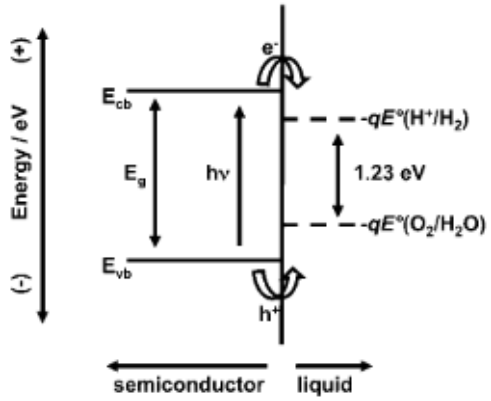


Figure 2.11. Overall water splitting with OER and HER on a semiconductor which has an appropriate band gap large enough. Reproduced from ref[65].

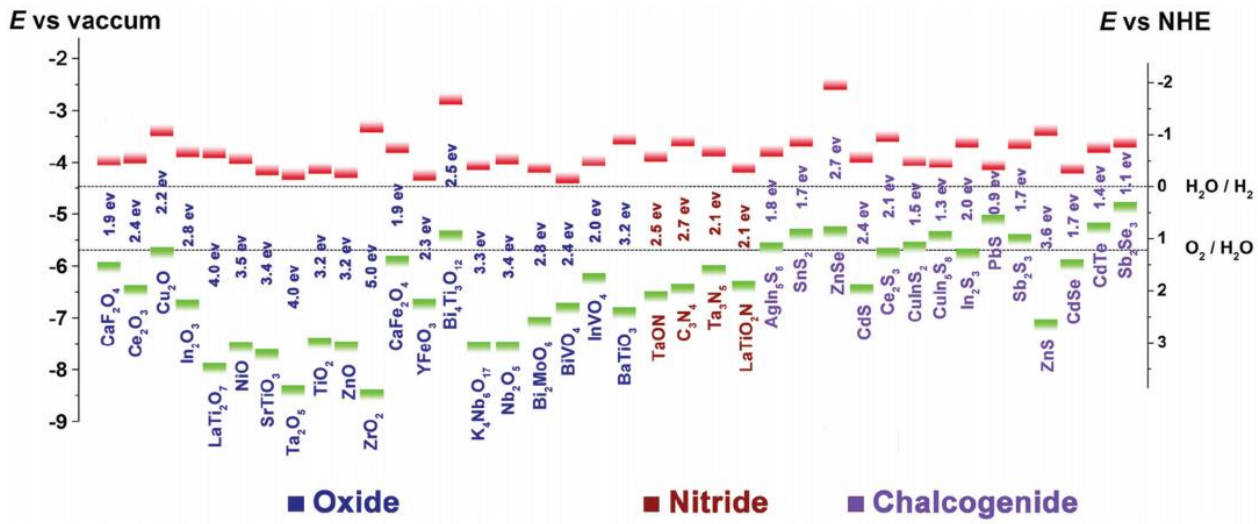


Figure 2.12. Bandgaps and band edge positions with respect to the vacuum level and NHE for different semiconductors. The red and blue lines represent the conduction and valence band edges, respectively. Reproduced by ref[66].

### 2.2.3 Other photocatalytic phenomena

There are many applications of $TiO_2$ photocatalysts in addition to water purification and water splitting. Self-cleaning has been already applied in industry. $TiO_2$ can decompose organic compounds as discussed above. A concept of this technique is keeping the surface clean without maintenance[67]. Its scheme is shown in figure 2.13[68]. This effect can be further enhanced when water flow such as a rain was applied to the surface. In Japan, self-cleaning has been practically used and one of the applications is to coat a surface of exterior building as shown in figure 2.14.

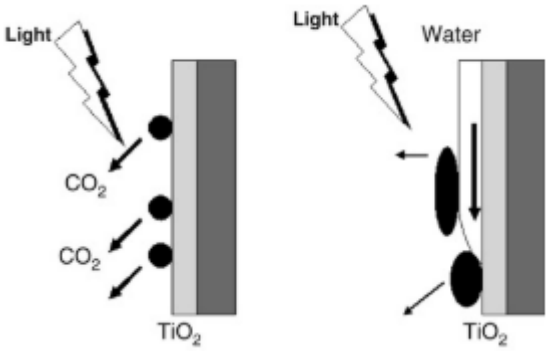


Figure 2.13. Scheme of self-cleaning by $TiO_2$ photocatalysts. Reproduced by ref[68].

Anti-fogging is also an applicable usage of $TiO_2$ photocatalysts. The fogging of the surfaces of mirrors and glass ruins visual clarity. $TiO_2$ surface becomes extremely hydrophilic under UV irradiation and thus water spreads across the surface. As a result, the water layer gets thinner and subsequently evaporates. When the amount of water is large, it forms a sheet-like layer which can also provide high visual clarity (figure 2.15)[69]. Recently biological applications such as photocatalytic anti-virus and anti-bacterial effects[70] and photocatalytic cancer treatment[71] have received more attentions, but their details are omitted here.


Figure 2.14. Application of self-cleaning building materials for a) self-cleaning tiles, b) self-cleaning glasses, c) self-cleaning sound proof wall on a highway, d) self-cleaning of tiles and glasses, and e) self-cleaning roof of a train station. Reproduced from ref[72].

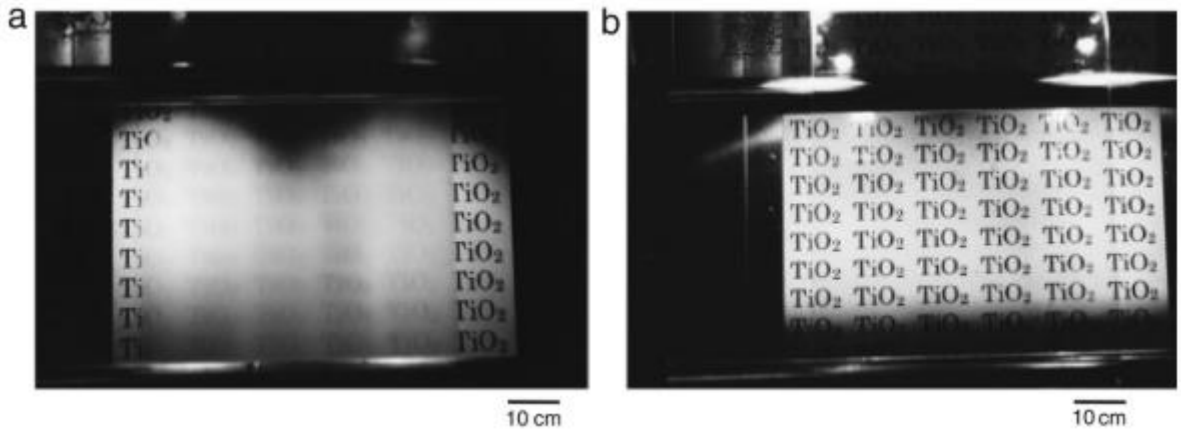


Figure 2.15. Pictures of fogged surfaces of a) uncoated glass and b) $TiO_2$ coated-glass after UV irradiation. Reproduced from ref[69].

## 2.3 Roles of co-catalysts: manipulation of charge transfer

The photocatalytic activities of semiconductors are still low and far from practical requirement although many materials such as $TiO_2$ are capable of evolving hydrogen and/or oxygen from water by photocatalytic reactions. This is mainly due to inefficient charge separation and transportation, and instability of photocatalysts related to their degradation by undesired side reactions of photocatalysis. Manipulation of the charge transfer and trapping apparently plays a key role in photocatalysis[63]. For this purpose, designing nanostructured composites have attracted attention as they possess unique physical and chemical properties different from the bulk properties[73-75]. Co-catalysts together with supporting semiconductor photocatalysts have been employed as the most promising strategies to boost the efficiency of photocatalytic reactions and stability of the photocatalysts by effectively controlling the transfer of charge carriers[76]. Generally, noble metals are selected as reduction co-catalysts and metal oxides are used as oxidation co-catalysts. Such co-catalysts offer three main benefits: (1) separation and trapping of photo-generated electrons and holes by Schottky barrier or p-n junction, (2) providing effective reaction sites catalyzing reduction or oxidation reactions by lowering overpotentials for photoelectrochemical reaction or activation energies for photocatalytic reaction, and (3) improving stability for photo-corrosion. Herein, fundamental concepts, influencing factors to determine physical properties, and recent progresses are reviewed regarding on above benefits of co-catalysts.

### 2.3.1 Charge separation by Schottky barrier and p-n junction

Co-catalysts can promote charge separation and transportation at the interface between semiconductor photocatalysts and metals or metal oxides as co-catalysts. In the case of semiconductor and metal with larger work function, as a result of thermodynamic equilibrium of electrons a Schottky barrier is formed at the interface as shown in figure 2.16. The internal electric field at the interface with the Schottky barrier facilitates the charge separation and subsequently traps the electrons on the metal side. Among noble metals, Pt is often chosen as a reduction co-catalyst as it has quite large work function forming a Schottky barrier which is large enough to separate and trap the charges. Usually it is assumed that electron scavenging by Pt is faster than charge recombination or reduction of reactants[77]. In addition to the Schottky barrier, the double-layer charging around the metal nanoparticles stores photo-excited electrons within the nanoparticles[78].

Kamat *et al.*[79] found that Fermi level equilibrium between Ag as a co-catalyst and $TiO_2$ as a semiconductor photocatlayst is dependent on irradiation condition. The charging and discharging of photo-excited electrons can be reversibly switched by on/off of UV irradiation as shown in figure 2.17. The electron storage in Ag induced by UV irradiation shifts the Fermi level to more negative potentials. Such a negative shift up to 100 meV has been also observed for $Au/TiO_2$ composites[80]. Electrons are trapped and stored at metals not only due to the Schottky barrier at the interface of metal and semiconductor, but also due to double layer charge that screens the stored electrons within the metal nanoparticles with size smaller than 10 nm diameter[78]. These electron storage effects should be considered to design photocatalytic systems of semiconductor and metal composites. When a n-type semiconductor and a p-type semiconductor are associated, a p-n junction is formed at the interface.

Photo-generated electrons and holes migrate to the n-type and p-type semiconductor, respectively, due to the electric field at the junction. Although defects could be formed at the interface between the co-catalysts and the photocatalyst and act as recombination sites, positive effects generally overcome such a drawback. Whereas the formation of Schottky or p-n junctions may be expected in many cases they have not been experimentally verified. In addition, very often the physical rules in charge carrier separation has not been considered in a straightforward manner.

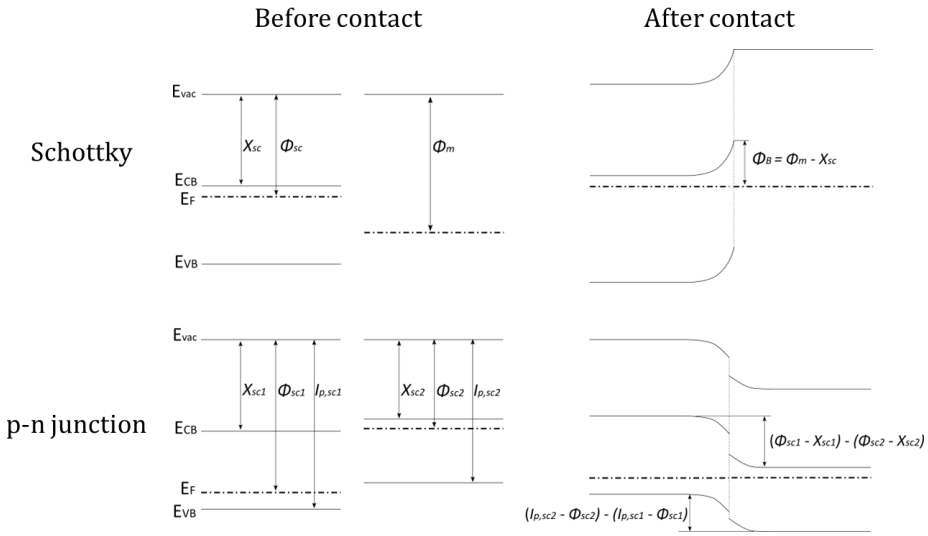


Figure 2.16. Schematic energy band diagrams of Schottky barrier and p-n junction.

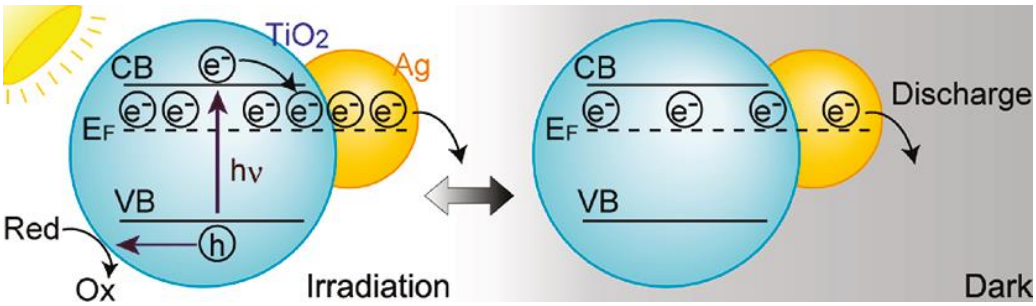


Figure 2.17. Fermi level position of Ag/$TiO_2$ nanoparticles under UV irradiation and in dark. Reproduced from ref.[79]

Above coupling of metal/semiconductor (Schottky barrier) or semiconductor/semiconductor (p-n junction) are generally constructed based on two structures: the core-shell configuration and the Janus structure[81] (Figure 2.18). Seh *et al.*[82] synthesized core-shell and Janus nanoparticles of Au(shell)/$TiO_2$(core) and compared their photocatalytic activities for hydrogen evolution. The Janus structure exhibited a 1.7 times higher activity than that of the core-shell structure. In the core-shell structure, electrons and holes are separated toward the shell (Au) and the core ($TiO_2$), respectively. The holes migrated to the core would not interact effectively with reactants on the surface of the nanocomposites. Unused holes in $TiO_2$ are accumulated which favours the recombination processes. On the other hand, in the Janus structure, both electrons and holes, which are also separated to Au and $TiO_2$, would be able to react directly with reactants. In such a condition, both carriers can be simultaneously consumed, hampering the recombination reactions. This result indicates that the morphology of heterostructures has to be carefully tuned for their optimal photocatalytic activities.

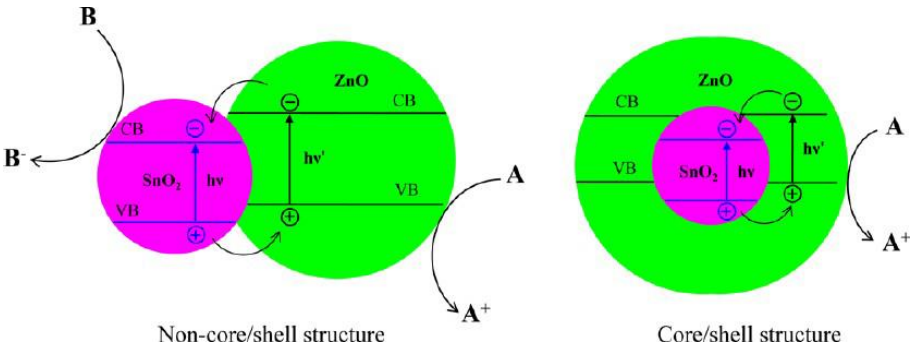


Figure 2.18. Band energy diagram of Janus and core-shell structure of $SnO_2$/ZnO. Reproduced from ref.[81]

## 2.3.2 Providing effective reaction sites

The main reason why most semiconductors need co-catalysts for reasonable photocatalytic activities is the recombination of the photo-generated electrons and holes before migrating to the surface and initiating redox reactions. The other reason of inefficient photocatalytic activities is a too slow surface redox reactions to efficiently consume both electrons and holes simultaneously. It is believed that the co-catalysts not only promote the charge separation by Schottky barriers or p-n junctions, but also catalyse redox reactions, decreasing the activation energy of photocatalysis and overpotential of photoelectrocatalytic water splitting. Generally noble metals are employed as co-catalysts for the reduction reaction and metal oxides are selected for the oxidation reaction.

Trassati *et al.*[83] reported a so-called volcano relationship between the exchange current for hydrogen evolution and the metal-hydrogen bond strength calculated from heat of hydride formation as shown in figure 2.19. Precious metals demonstrate exceptionally high activities. Especially, Pt is located at the top of the volcano, exhibiting the lowest activation energy for hydrogen evolution. In addition, Pt has the largest work function, forming a large Schottky barrier at the interface with semiconductors to facilitate the charge separation. Therefore, Pt has been conventionally considered as the best co-catalysts for the photocatalytic reduction reaction in terms of both catalytic and electronic properties. High catalytic activities have been achieved using Pt as co-catalysts on different semiconductor photocatalysts. Except for precious metals, Ni as an abundant non-precious metal shows the highest activity and thus is considered as a promising co-catalyst candidate for practical use of photocatalysis.

The catalytic activity of metal oxides for the oxidation reaction has been expected to be related to the ability of oxidation state transition between different valencies. For example, the oxidation state of Co changes from +2 to +4 for oxidizing reactants and collecting the holes[76]. Rasiyah *et al.*[84] proposed that oxygen evolution takes place with a redox reaction of metal oxides and thus catalysts, which show such transition reactions close to the reversible potential for oxygen evolution, would exhibit the higher catalytic activity. Based on the finding of a linear correlation between the minimum potential for oxygen evolution and the redox potentials of transition

reactions, Trasatti *et al.*[85] reported a relationship between the overpotential at a fixed current density for different metal oxides to the enthalpy of lower-to-higher oxide transition (figure 2.20). As well as the hydrogen evolution, precious metal oxides such as $RuO_2$ and $IrO_2$ are located at the top of the volcano and possess the optimal bond strength, showing the lowest over potential.

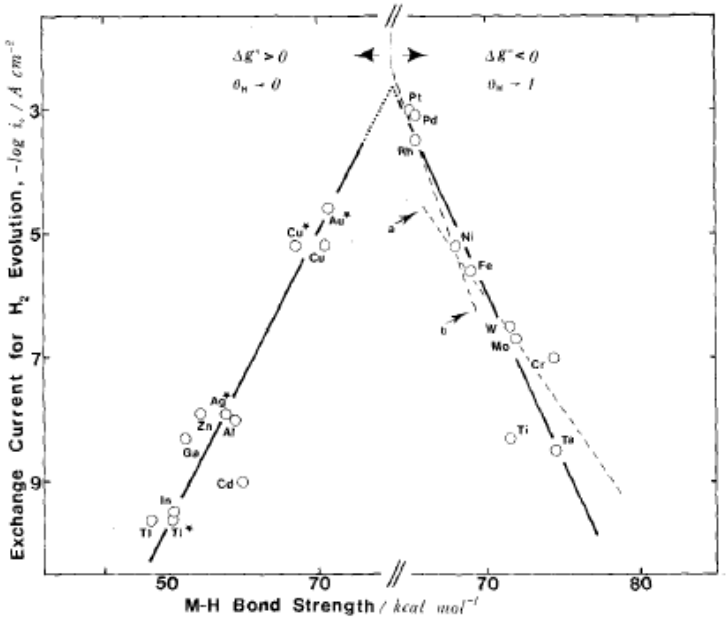


Figure 2.19. Volcano plot of metals for hydrogen evolution. Exchange currents for electrolytic hydrogen evolution is plotted as a function of strength of metal-hydrogen bond based on heat of hydride formation. Reproduced from ref.[83]

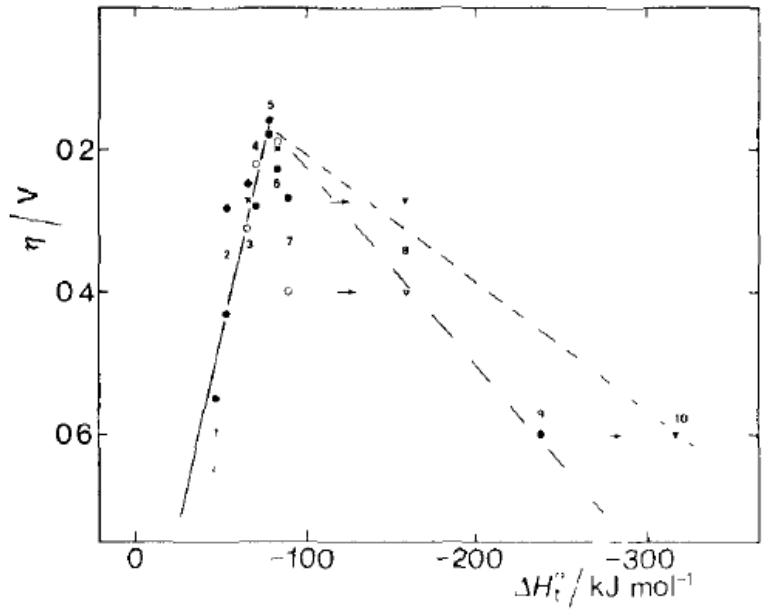


Figure 2.20. Volcano plot of metal oxides for oxygen evolution. Oxygen overpotential of metal oxides is plotted as a function of the enthalpy of lower-to-higher oxide transition. (1) $PbO_2$, (2) $Ni_2O_3$, (3) $PtO_2$, (4) $MnO_2$, (5) $RuO_2$, (6) $IrO_2$, (7, 8) $Co_3O_4$, and (9,10) $Fe_3O_4$. (•) acid and (o) alkaline solutions. Reproduced from ref.[85]

### 2.3.3 Exploring superior co-catalysts

Pt and Rh has been conventionally considered as the best reduction co-catalyst as discussed above since it possesses the largest work function among precious metals and is located at the top of the Trassati's volcano

map. However, Pt and Rh also catalyses the undesired back reaction of $H_2O$ formation from $H_2$ and $O_2$, limiting the photocatalytic activity. Although Au shows a negligible back reaction of $H_2O$ formation from $H_2$ and $O_2$, activities of Au is 10 times lower than that of Pt. To avoid the adverse reaction, transition metal oxides such as $Cr_2O_3$, $NiO_x$ and $RuO_2$ are often applied as co-catalysts for hydrogen evolution[86]. $MoS_2$ has been getting attention as the best reduction co-catalyst since $MoS_2$ co-catalysts deposited on CdSe exhibited an even higher efficiency for hydrogen evolution than that of Pt deposited on CdSe[87]. Recently, it was also demonstrated that $PtO_2$ can suppress the back reaction of $H_2O$ formation and performs as an excellent co-catalyst for hydrogen evolution[88].

$IrO_2$ has been conventionally employed as oxidation co-catalysts[89-90]. Ma *et al.*[91] deposited $IrO_x$, $CoO_x$, and $RuO_x$ co-catalysts onto $Zn_{2-x}GeO_{4x-3y}N_{2y}$ and compared photocatalytic activities for oxygen evolution. All the co-catalysts showed enhanced activities compared to $Zn_{2-x}GeO_{4x-3y}N_{2y}$ without co-catalysts and $CoO_x$ was the best one. Liu *et al.*[92] also reported that $CoO_x$ deposited on to $TiO_2$ nanosheets showed the best activity for oxygen evolution among $MnO_x$, $FeO_x$, $CoO_x$, $NiO_x$, and $CuO_x$. Today one of the most popular oxidation co-catalysts is cobalt-phosphate (CoPi), which was first employed in 2008[93]. Wang *et al.*[94] also employed CoPi as an oxidation co-catalyst deposited onto $BiVO_4$. 1 wt % of CoPi deposited onto $BiVO_4$ showed 6.8 times higher photocatalytic activities for oxygen evolution than that of the pristine $BiVO_4$. Furthermore, this group compared CoPi with other metal oxides co-catalysts such as $IrO_x$, $CoO_x$, $MnO_x$ and $RuO_x$. Of these co-cotalysts, CoPi was the best co-catalyst for oxygen evolution, followed by $CoO_x$ which showed a slightly lower activity than CoPi. Gerard *et al.* found that the kinetics of water oxidation by CoPi deposited onto $Fe_2O_3$ was slower than that of bare electrode, but the recombination rate of the former was much lower than that of latter, resulting in the enhanced oxidation activity by CoPi loading.

One has to consider morphology of the interface of co-catalysts and photocatalysts as well as selecting appropriate co-catalysts for specific reactions. It was found that $MoS_2$ deposited onto CdS showed much higer photocatalytic hydrogen evolution activity than Pt deposited onto CdS despite its superior performance of Pt compared with $MoS_2$ for the activation of hydrogen in electrochemical systems[95-96]. Chemically deposited $MoS_2$ onto CdS showed much higher activity than the simple mixture of $MoS_2$ and CdS. The better photocatalytic activity of $MoS_2$ co-catalyst would be attributed to the intimate contact between $MoS_2$ and CdS due to its chemical deposition. Smoother charge transfer is expected on the intimate contact at the interface. Similarly a lattice match of co-catalysts and photocatalyst would be crucial for the charge transfer. A lattice mismatch might give rise to defect levels in the band gap, increasing a ratio of recombination.

### 2.3.4 Balance of oxidation and reduction reactions

Both reduction and oxidation reactions are relevant to achieve the overall reactions. When it comes to water splitting, oxidation reaction might dictate the overall reaction. Oxidation reaction is slower than reduction

reaction and thus could be a bottleneck for the overall water splitting. Thus, developing oxidation reaction co-catalysts is a key step to apply photocatalysts for practical use. Furthermore, one has to carefully select photocatalysts and co-catalysts depending on reactions. Ohtani *et al.*[97] showed that some photocatalyst exhibited a high performance for water splitting which is an uphill reaction, but did not function at all for organic decomposition which is a downhill reaction, and vice versa. Especially careful optimization of an amount of co-catalysts is crucial. Uddin *et al.* prepared $RuO_2/TiO_2$ heterostructures and performed photocatalytic decomposition of methylene blue and methyl orange dyes, and hydrogen production by methanol photo-reforming under UV light illumination. 1 wt % $RuO_2/TiO_2$ showed best activities for degradation of both dyes while the best activity for hydrogen evolution was achieved by 5 wt % $RuO_2/TiO_2$[98-99].

## 2.4 Crystal facet engineering

Metal and semiconductor photocatalysts with specific crystallographic facets have attracted considerable attention in the last decade due to their facet-dependent properties in photocatalysis and solar energy conversion[75, 100-101]. These reactions are affected by surface atomic structures that can be finely defined since surface atomic arrangement and coordination determine the adsorption of molecules, surface transfer of charge carriers between the surface and the reactant molecules, and desorption of product molecules. Furthermore, when the photocatalysts are enclosed by multiple facets, photo-generated electrons and holes are transferred to different facets and they accumulate at the different facets for reduction and oxidation reactions, respectively. Therefore, photocatalytic activities sensitively vary on the crystallographic facets.

### 2.4.1 Roles of crystal facets in anatase

$TiO_2$ is known as the model surface and one of the most studied material with well-defined structures[2, 102-104]. Spherical anatase nanoparticles are commonly employed as photocatalysts because of the high surface-to-volume ratio, providing a great number of effective active sites on the surface. However, it has not reached to a level of practical applications mainly due to a low quantum efficiency originated from recombination of electrons and holes favoured by the small size of particles. Based on the rapid development of techniques to control the morphologies, research interest has shifted to tuning into the crystal facets to elucidate their roles in photocatalysis. So far, the morphology of $TiO_2$ has been investigated for sphere, cube, wire, tube, octahedron, belt and sheet structures. These structures are mainly exposed with (001), (101) and (010) facets. In 2002, Ohno *et al.*[105] reported the selective deposition of Pt and $PbO_2$ on the specific orientations of rutile and anatase via photo-deposition, indicating that the facets help in the separation of photoinduced electrons and holes. $Pt^{4+}$ ions were photocatalytically reduced on the rutile (110) and anatase (101) facet while $Pb^{2+}$ ions were oxidized on the rutile (011) and anatase (001) as shown in Figure 2.21, which suggests that rutile (110) and anatase (101) provide the effective reduction site and rutile (011) and anatase (001) work as the oxidation site. However, the role of crystal facets still remains under debate. In last decade, in-situ characterization methods have been developed considerably and provided indirect evidence with regard to the spatial charge separation on the (101)

and (001) facets of anatase. Tachikawa *et al.*[106] investigated facet dependent photocatalysis on anatase with single-molecule fluorescence imaging and kinetic analysis by using redox-responsive fluorogenic dyes. On the single crystal of anatase co-exposed with the (101) and (001) facets, the fluorogenic dyes are preferentially reduced on the (101) facet rather than on the (001) facet (Figure 2.22). This finding confirms the idea that the (101) facet functions as the reaction site for the effective reduction and indicates the selective electron trapping on the (101) facet. Furthermore, D'Arienzo *et al.*[107] performed electron spin resonance (ESR) measurements for shape-controlled nanoparticles exposed with specific crystal facets in order to correlate their photocatalytic activities to the charge trapping centres formed upon UV irradiation. Their results in Figure 2.23 verify that $O^-$ and $Ti^{3+}$ centres, which are assigned to oxidation and reduction sites where holes and electrons are trapped, respectively, are located on the (001) and (101) facets, respectively[108-111].

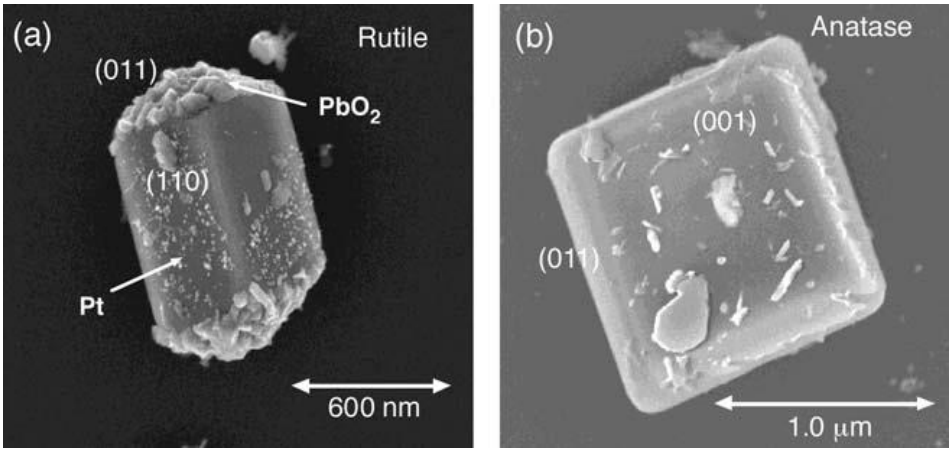


Figure 2.21. SEM images of a) rutile and b) anatase single crystalline nanocrystals. $PbO_2$ and Pt are selectively deposited onto rutile (011) and anatase (001) surfaces, and rutile (110) and anatase (011) via photo-deposition, respectively. Reproduced from ref[105].

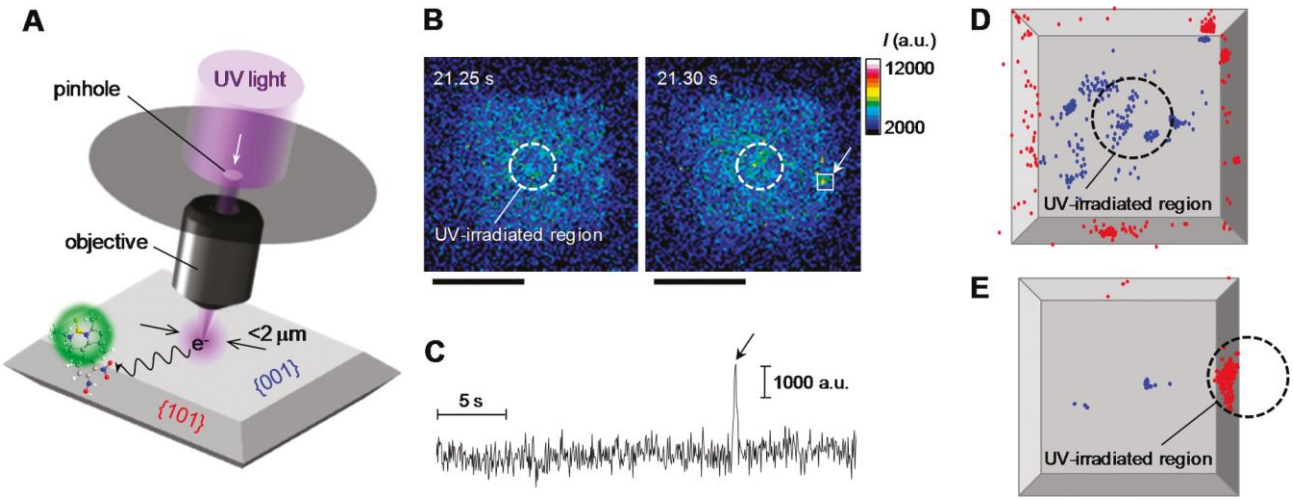


Figure 2.22. A) Scheme of the remote photocatalytic reaction on the anatase (101) surface with DN-BODIPY during illumination onto the anatase (001) surface. (B) Fluorescence image of $TiO_2$ crystals in DN-BODIPY solution under irradiation. The scale bars are 4 μm. (C) Fluorescence intensity over the square region of panel B. (D, E) Location of fluorescence bursts on the (001) and (101) surfaces. Reproduced from ref[106].

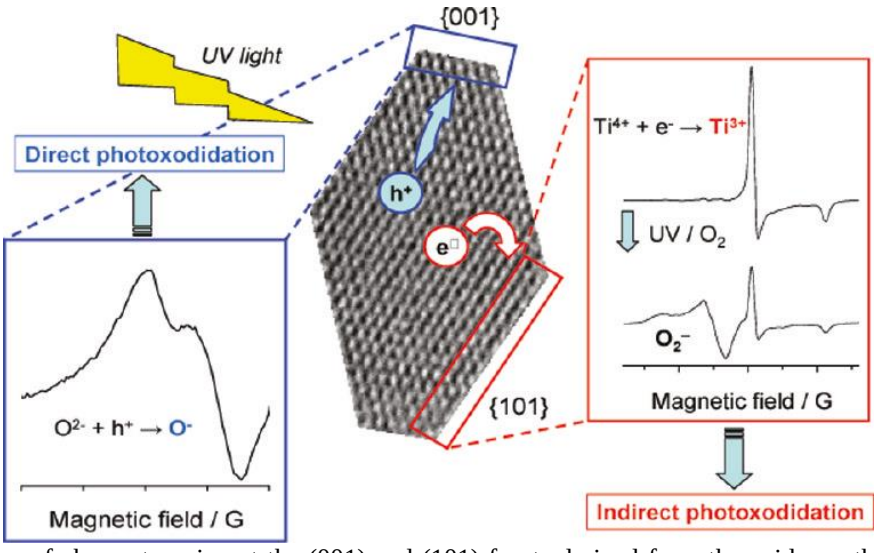


Figure 2.23. Scheme of charge trapping at the (001) and (101) facets derived from the evidence that the concentration of trapped holes ($O^-$ centers) increases with (001) surface area whereas the amount of $Ti^{3+}$ centers increases with (101) surface area. Insets represent ESR spectra. Reproduced from ref[107].

Charge separation and trapping are conventionally rationalized in terms of different energy levels of the conduction and valence bands of the different facets due to the surface atomic arrangement. DFT calculation predicts that the Fermi level of the (001) facet is located at a lower energy level than that of the (101) facet as shown in Figure 2.24[112]. Thus, the so-called surface heterojunction would be formed between the (101) and (001) facets due to the difference of their Fermi levels when both facets are exposed at the surface of the same crystallite. As a result, photo-generated electrons and holes could preferentially migrate to the (101) and (001) facets, leading thereby to different photocatalytic activities on these facets. Ye *et al.* investigated optical properties of anatase nanocrystals with (101), (001) and (010) single facets of 90 % exposure and found a difference in their absorption edge[113-114]. The order of their estimated band gaps is $E_g^{(010)} > E_g^{(101)} > E_g^{(001)}$ and the difference of the band gap would result in forming the surface heterojunction although the band alignment at the interface between facets could vary upon their Fermi level position. In addition, Pan *et al.*[115] and Xu *et al.*[116] found the same band gap order of $E_g^{(010)} > E_g^{(101)} > E_g^{(001)}$ and revealed that the distance between the top of the valence band and the Fermi level obtained from the XPS valence band spectra is the same for all the facets. However, in such electronic conditions, the electrons migrate to the (001) facet at the interface between the (001) and (101) facets, which is contrary to the prevailing consensus. As we discussed above, the origin of the charge separation and trapping induced by different facets is still under debate and further fundamental investigation are required for a deeper understanding and application purposes.

The difference in photocatalytic activities of different facets could be related not only to the electronic properties such as energy levels of valence and conduction bands, but also to the reaction mechanism at the molecular level on the surface. For instance, chemisorption properties of anatase strongly depend on the surface arrangements. According to both calculations and experimental results, the (101) facet is less favourable for dissociative adsorption of water and other typical probe molecules while these molecules are dissociatively

adsorbed on the (001) facet[45, 47, 49, 117-118]. It is generally admitted that the surface atomic structure exposed with facets containing under-coordinated atoms is more reactive. On the (001) surface, Ti and O atoms are coordinatively unsaturated and more importantly the configuration of the surface atoms are strained. The Ti-O-Ti bond angles are significantly larger at the surface, meaning that 2p states on the surface oxygen atoms are destabilized and quite reactive[18, 119]. Hence, the (001) facet has been believed to be superior to the (101) facet with regard to photocatalytic activities.

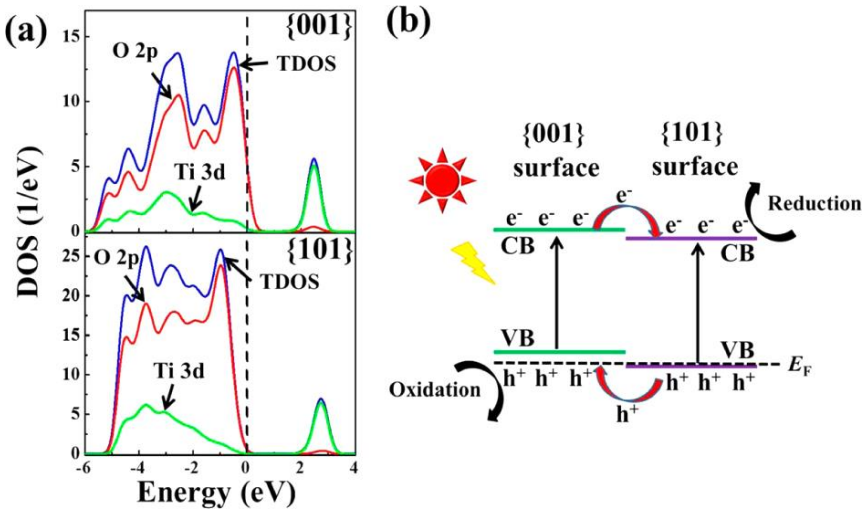


Figure 2.24. (a) Density of states plots for anatase (101) and (001) surfaces. (b) Energy junction at the interface between (101) and (001) surfaces described based on the calculation. Reproduced from ref[112].

Reaction selectivity is one of the main challenges in the field of photocatalysis. To achieve a high selectivity, strategies based on modifying environments have been developed such as controlling the surface electronic charge by adjusting the pH[120-124], and anchoring specific molecules onto the surface[125]. It is also possible to enhance the selectivity by using intrinsic surface properties of $TiO_2$. As discussed above, adsorption behaviour of reactant molecules is governed by the surface structures which affects the selectivity of photocatalytic reactions. It has been proposed that well-known dyes as methylene blue (MB) and methyl orange (MO) were selectively adsorbed and degraded by the (001) and (101) facets, respectively[126-127]. By contrast, Liu *et al.*[128] suggested a reverse role of the two facets. This might be due to effects of the pH of the solution or remaining organic species used as capping agents on the photocatalyst surface depending upon the synthetic methods used to prepare the photocatalysts. Indeed, these facets affect the adsorption behaviours of reactive molecules. Very recently, Zhou *et al.*[129] showed that the photocatalytic redox preferences of (001) and (101) facets can be modulated by the adsorbate-reconstructed surface structure, which can be controlled by surface protonation/deprotonation. The proposed scheme based on calculations is shown in Figure 2.25. Therefore, to elucidate the selectivity originated from the facets, some efforts still need to be made to investigate it by taking into account the above effects.

The photocatalytic order of the different facets has been a controversial topic. Pan *et al.*[115] compared photocatalytic activities in terms of generating $OH^{\cdot}$ radical and $H_2$ evolution of anatase micrometer-sized

crystals exposed with dominant (001), (010), and (101) facets. In contrast to the conventional interpretation telling that the (001) facet is more reactive than the (101) facet, it was found that the order of the photocatalytic activities for both generating the radical and $H_2$ evolution is (010)>(101)>(001). For (101) and (001) facets, the order for $H_2$ evolution activity is reasonable as the (101) facet acts as reduction reaction sites with accumulated photogenerated electrons, which are of course responsible for $H_2$ evolution. Furthermore, the (010) facets possess both a relatively high surface energy with undercoodinated atoms and the more negative conduction band edge which allows rationalizing its higher activity. Ye *et al.*[114] showed photocatalytic degradation of RhB and the photoreduction of $CO_2$ in contact to gaseous phase, revealing that the activity order for dye degradation is (001)>(101) while that for photoreduction is opposite. This could be explained by charge separation between the facets where photoexcited electrons and holes transfer to the (101) and (001) facets and provide effective reaction sites for gas reduction and dye oxidation, respectively. Dufour *et al.*[130-131] revealed that the acidity plays a crucial role in the RhB degradation. The absorption and degradation of the dye are favoured on the stronger acid sites. However, the acidity is not of importance for the phenol degradation. This is because the RhB degradation mainly takes place via direct oxidation on the photocatalyst surface while the degradation of phenol mainly occurs via hydroxyl radicals. As discussed above, understanding of the role of facets in photocatalytic activities is not that simple as different factors affect them. One should consider not only the number of undercoordinated atoms on the surface, but also the effect of charge carrier separation between the facets. In addition, the surfaces acidity of photocatalysts in the solution drastically affects their photocatalytic activities and has to be taken into consideration for practical use.

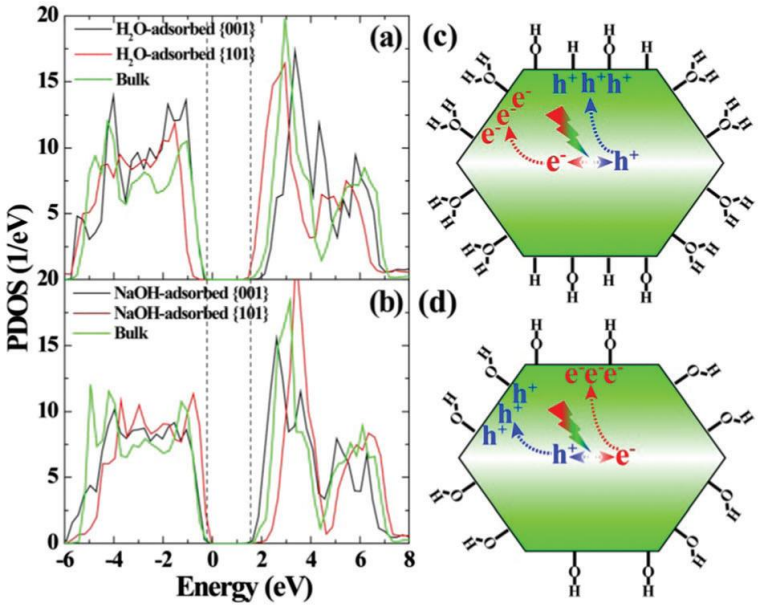


Figure 2.25. The partial density of states of the top O–Ti–O layer in a) $H_2O$ adsorbed and b) the deprotonated surfaces of (001) and (101) facets, and a proposed mechanism of the charge distribution on c) the $H_2O$ adsorbed and d) the deprotonated (001) and (101) surfaces. Reproduced from ref[129].

Since the (101) and (001) facets help to obtain the spatial charge separation due to the surface heterojunction and function as reduction and oxidation reaction sites, respectively, the relative ratio between the (101) and

(001) facets play a crucial role in photocatalysis[112]. To achieve a high photocatalytic efficiency, photoexcited electrons and holes should be consumed simultaneously at the same rate since excess carries (electrons or holes) which did not participate in the redox reactions would favour recombination phenomena of the charge carriers and would reduce the efficiency of total photocatalytic reactions. Thus, by a fine tuning of facet's ratio so that both reduction and oxidation reaction take place efficiently, which leeds to consuming both carriers, a synergetic effect of the charge separation and the effective reaction sites can be achieved. The aspect ratio of the (001) and (101) of anatase crystals is defined by the ratio between the side of the truncated facets of the top or bottom (*B*) and the side sandwiched by the two pyramids (*A*) as shown in Figure 2.26. For example, the typical value of *B/A* of 0.3 corresponds to about 4 % of the exposed (001) facets. An optimal ratio of the facets would depend on the kind of photocatalytic reactions. For instance, 50 % of the (001) facet has been reported as the best proportion for $CO_2$ reduction reaction[112, 132-133]. In the case of the $OH^{\cdot}$ radical formation and $H_2$ evolution, the optimal amount of the (001) facet is still under debate. However, there is a consensus that anatase crystallites exposing 70-80 % of the (001) facet exhibit inferior photocatalytic activities than one exposing 18-60 % of the (001) facet. This finding is in disagreement with the conventional understanding of the (001) facet as a more reactive facet than the (101) facet[115, 134-135]. This indicates that a dominant (001) facet on the surface is not always necessary to improve the photocatalytic activities. Furthermore, Wang *et al.*[136] synthesized single crystal nanoparticle with various amount of the (001) facet from 0 to nearly 100 % and it was revealed that the optimal amount of the (001) was 73 % for RhB degradation. On the other hand, particles with single facets of 100 % (101) and (001) exhibit worst activities, indicating that the co-existence of the (001) and (101) is crucial regardless of the ratio of the facets. Cao *et al.*[137] also performed dye degradation tests using MB, MO and RhB by anatase nanoparticles with various amount of the (001) facet and 77 % of the (001) was optimal for each dye checked.

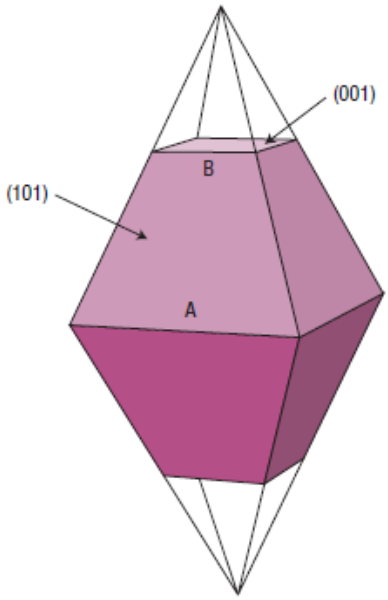


Figure 2.26. Truncated tetragonal bipyramid structure of single crystal anatase co-exposed with (101) and (001) facets. The aspect ratio is defined by a ratio between the side of the truncated facets of the top or bottom (*B*) and the side sandwiched by the two pyramids (*A*). Reproduced from ref[119].

In summary, the (101) and (001) facets function as reduction and oxidation sites, respectively, since photo-generated electrons and holes migrate to the (101) and (001) facets, respectively. Moreover, tuning the ratio of the two facets plays a crucial role to enhance photocatalytic activities. However, one also has to consider the number of the undercoordinated atoms on the surface, which has been conventionally understood as a key parameter since it would affect adsorption/desorption behaviours. In addition, other environmental conditions such as pH drastically change the surface properties and thus govern the photochemical activity. However, the role of facets is still controversial and any consensus has not been achieved so far that attention has not been paid carefully to the above effects. In order to elucidate the role of facets and its origin, some efforts still need to be made for fundamental investigations while considering not only surface properties of $TiO_2$ themselves, but also environmental parameters equally.

### 2.4.2 Synthetic approaches to control facets

Evolution of crystal structure during the crystal growth proceeds by continuously decreasing the total surface energy of the crystal and stops when the minimum surface energy is reached. To tailor the specific facets on the surface, there are two available strategies: bottom-up and top-down synthetic routes[100]. The bottom-up approach involves the nucleation and crystal growth from the solution. Two mechanisms have been proposed to explain the crystal growth process[138-144]. First of all, the conventional nucleation theory supports a single-step process where bulk nucleation and agglomeration take place. A second potent mechanism is a two-step nucleation. In this case, a nucleation might take place during crystallization, in which dense liquid nuclei are initially formed and subsequently the nucleuses start to crystallize as shown in figure 2.27[141]. On the other hand, the top-down synthesis route is the partial dissolution of mother-crystal particles and subsequent recrystallization on the surface in a solvent environment. Thus, a vital factor of this route is to select appropriate etching and morphology-controlling agents in order to achieve desired crystal structures.

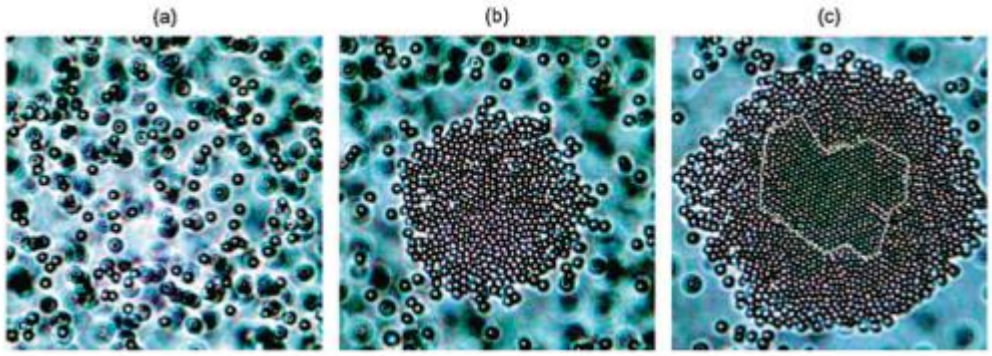


Figure 2.27. Two step nucleation observed for colloidal particles. a) Initial dilute liquid phase. b) Amorphous dense droplets. c) Crystalline nuclei created from the amorphous phase. Reproduced from ref[141].

For both cases, capping agents have been mainly employed to prepare well-defined crystals showing controlled exposed facets[75, 100-101, 107]. The capping agents are thought to be selectively adsorbed onto specific facets since their affinity to the surface of particles depends on the surface atomic arrangement. The interaction between adsorbates and facets would introduce impurities or additives on the surface of the particles. These modifications of the surface by adsorbates can change the surface stability of facets and thus affect the growth rates to the facets. Thus, tailoring of the specific facets can be achievable by using capping agents and varying their ratio in a solution. In contrast to the bottom-up route, the top-down route involves directional chemical etching of specific facets[145-146]. For the top-down route, a role of the capping agents is not only suppressing the growth along axes of specific facets, but also preventing specific facets from getting attacked by etching agents. It is noteworthy that the organic capping agents would remain on the facets even after some efforts to remove them by annealing or cleaning with chemical reagents. The adsorption and activation of reactant molecules on the surface are definitely influenced by the remained capping agents. This is a common problem when using organic capping agents as one cannot evaluate appropriately the role of facets in photocatalysis. Small inorganic ions can also work as capping agents to be selectively adsorbed onto the crystal facets. It was found that this kind of capping agents not only allows reactants to access to the capped surface of crystals, but also can be easily removed to recover the clean surface.

As discussed above, the strategy using capping agents can achieve crystal growth of which controlled crystal facets are thermodynamically unstable. Kinetic control is another effective approach to synthesize thermodynamically disfavoured surface facets[145]. The alteration of growth environments by tunig precursor concentration plays a main role to manipulate the growth rate of specific facets. In addition to kinetic control, the facets of semiconductor can be controlled in the thermodynamic regime. A polyhedron enclosed by a single kind of facet is preferentially created thermodynamically when its surface energy is sufficiently lower than that of other facets. According to the Thomson-Gibbs equation, the surface energy is proportional to the supersaturation during the crystal growth[147]. Therefore, it would be possible to control the exposed facets on the surface by changing the supersaturation[148-149].

#### 2.4.2.1 Anatase (101)

The order of the average surface energies of anatase is reported as 1.61, 0.90, 0.53, and 0.44 J $m^{-2}$ for (111), (001), (010), and (101) facets, respectively[2-3, 116, 150-151]. Anatase crystal is primarily dominated by the most naturally appearing, less reactive, and thermodynamically stable (101) facet, which occupies 94 % of the total exposed surface based on the Wuff construction[3-4]. Therefore, generally the common shape of anatase in nature is the truncated octahedral bipyramid consisting of eight (101) facets on the sides and two (001) facets on the top and bottom. During the crystal growth under equilibrium conditions, the high energy facets of the (001) diminish rapidly and thus the crystal transforms into a specific structure with exposed facets, which minimize the total surface free energy[152-153]. Therefore, (101) facets might dominate the surface of most anatase particles

synthesized by conventional methods. Highly oriented (101) facets could be obtained by coarsening. Penn and Banfield[154] synthesized slightly truncated bipyramid crystals with well defined (101) facets by coarsening pristine $TiO_2$ particles from sol-gel route under different hydrothermal conditions. Amano *et al.*[155] demonstrated a hydrothermal transformation directly from titanate nanowires into bipyramid single crystals with nearly 100 % dominant (101) facets with less truncation (Figure 2.28). Dai *et al.*[156] reported slightly truncated bipyramid crystals with 90 % of (101) facets via a hydrothermal route by employing small particles of amorphous $TiO_2$ prepared by electrospinning. D'Arienzo *et al.*[107] employed titanium tetrabutoxide as a metallo-organic precursor using a hydrothermal route to obtain well defined anatase single crystal with slight truncation at the top and bottom of pyramids. All these procedures use pre-synthesized amorphous $TiO_2$ particles or titanates as precursors. Contrary to these methods, Liu *et al.*[157] developed a new strategy to synthesize anatase with dominant (101) facets by using crystalline titanium diboride as precursor via an acidic hydrothermal method. Interestingly, Wu *et al.*[158] obtained anatase nanobelts with two large (101) facets by modifying pre-synthesized $TiO_2$ powder in NaOH solution, subsequently washing the resulting powder with hydrochloric acid, and finally annealing the cleaned particle (Figure 2.29). The beneficial effect of nanobelt structures in photocatalysis was attributed to suppressed recombination of charge carriers due to the superior charge mobility, fewer localized states in band gap, and effective trapping of oxygen on the surface.

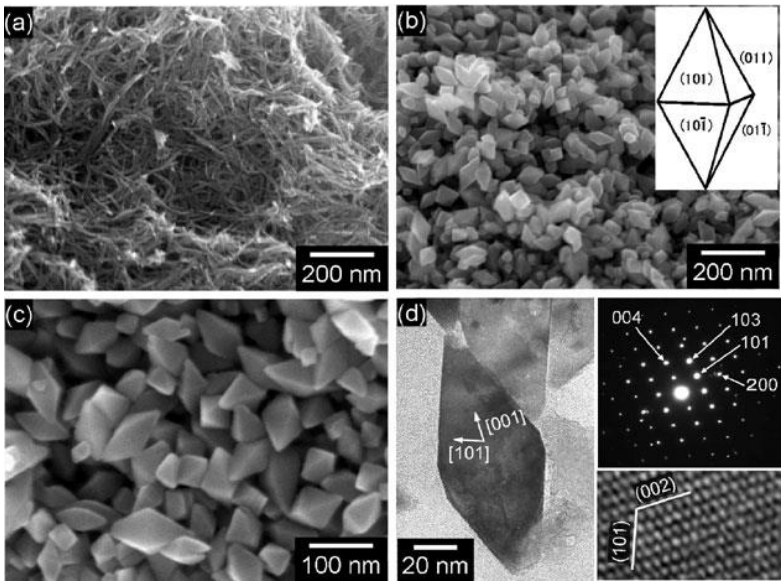


Figure 2.28. SEM images of (a) titanate nanowires as precursors and (b,c) anatase nanoparticles with dominant (101) facets after hydrothermal reaction of titanate nanowires. (d) TEM image and electron diffraction pattern of anatase nanoparticles with dominant (101) facets. Reproduced from ref[155].

The percentage of (101) facets in anatase crystals can reach to almost 100 % by using various synthetic methods. However, it is thermodynamically inevitable to form a few percent of (001) facets as this surface is required to minimize the total surface energy of whole crystals. Indeed, if (001) facets were completely eliminated, the

intersection of (101) planes would result in an acute angle, exhibiting higher energy than even the high energy surface of (001) facets[154].

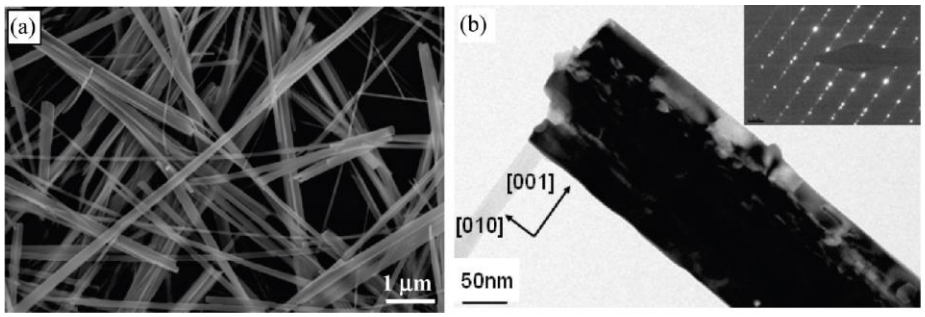


Figure 2.29. (a) SEM image and (b) bright-field TEM image of anatase nanobelts. The inset is a selected area electron diffraction pattern taken along the [100] direction of the nanobelt. Reproduced from ref[158].

In summary, it is relatively easy to obtain anatase single crystals with dominant (101) facets in the bipyramid structure as it is the most thermodynamically stable shape under usual preparation conditions. The percentage of (101) facets could vary by tuning the truncation of the edge at the top and bottom of bipyramids. Contrary to thermodynamically stable bipyramids, unique structures such as nanobelts exposing mostly (101) facets can also be achieved.

### 2.4.2.2 Anatase (001)

A large percentage of (001) facets in anatase crystallites has attracted significant attention over the last decade since facets with high surface energy were expected to show high photocatalytic activities. Unfortunately, such surfaces with high surface energy usually diminish rapidly during the crystal growth process due to the minimization of surface energy. Yang *et al.*[159] systematically explored the effect of 12 non-metallic adsorbate atoms (H, B, C, N, O, F, Si, P, S, Cl, Br, and I) on the surface energies of both (001) and (101) surfaces by the means of first-principle quantum chemical calculations. The calculations predicted that a surface terminated F atom not only yields the lowest values of the surface energy for both (001) and (101) surfaces, but also reverses the stabilities as shown in figure 2.30. In the presence of F atoms, the (001) is energetically preferable to (101) facet. The largest percentage of (001) facet was calculated to be more than 90 %. Based on these theoretical calculations, a micro-sized crystal with 47 % of (001) exposed facets was first synthesized by using $TiF_4$ and HF as the raw material and capping agents providing fluoride ions, respectively (figure 2.31). The percentage of the (001) facets can be increased by the synergetic effects of F and alcohol capping agents. For instance, the percentage was increased up to 69 % by using 2-propanol together with HF[160]. The addition of 2-propanol strengthens the stabilization effect associated with F adsorption on the (001) surface and thus stimulates its preferred growth. In addition to 2-propanol, ethanol, tert-butanol, isobutyl alcohol, benzyl alcohol, and 1-butanol have been successfully employed to increase the percentage of the (001) facets[161-163]. Especially by

employing 1-butanol, a paper-like nanosheets with nearly 100 % of (001) facets was successfully synthesized (figure 2.31)[163]. Another advantage of additional alcohol is the greater flexibility in synthesizing anatase crystals with uniform shapes and sizes.

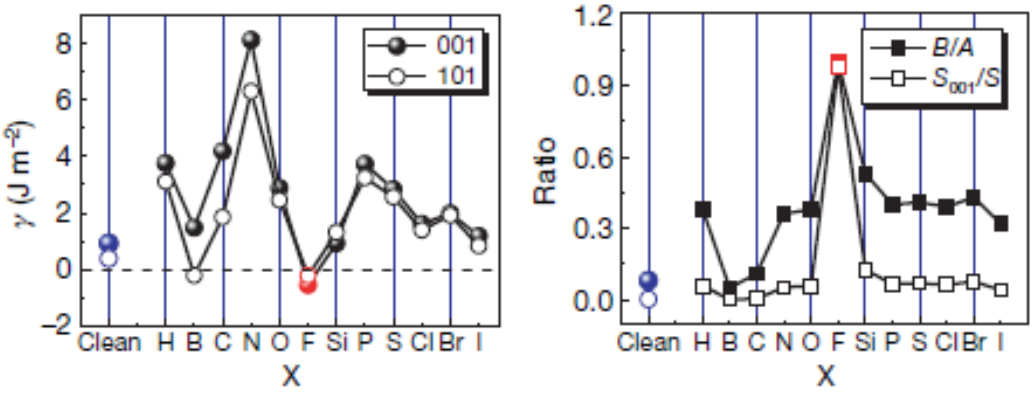


Figure 2.30. Calculated surface energies of (001) and (101) facets surrounded by adsorbate X atoms (left) and optimized value of *B/A* when anatase crystals are surrounded by adsorbate X atoms (right). X represents H, B, C, N, O, F, Si, P, S, Cl, Br, and I. Reproduced from ref[159].

As HF is extremely toxic, corrosive and environmentally undesirable, environmentally friendly HF-free routes to obtain (001) facets are required. The fluorine, which plays a key role in stabilizing the (001) facets, would be released from different sources. In addition to most frequently used HF, ammonium bifluoride[164], ammonium fluoride[165], titanium tetrafluoride[153], and ionic liquids[166] have been reported to be suitable fluorine sources. The reaction mechanism is well-summarized in different reports[100, 167]. These compounds containing fluorine are still toxic and corrosive when they are released into nature. Therefore, efforts have been made to develop methodologies using fluorine-free capping agents for practical mass production. In this context, mesoporous anatase spheres with (001) facets were synthesized using a hydrothermal route without fluorine[168]. $H_2SO_4$ was employed as mineralizer to hydrolyze and condense tetrabutyl titanate, which functioned as a phase inducer for the anatase phase and a capping agent stabilizing only (001) facets. $H_2SO_4$ adsorbed on the (001) surface can be easily removed due to its weak interactions with the (001) facet. Anatase nanosheets with (001) facets were prepared by chemical vapor deposition[169]. Silicon was selected as a morphology-directing agent instead of fluorine. Silicon vapor could suppress the growth of anatase crystals into the [001] direction and thus two-dimensional (001) nanosheets were formed. Roy *et al.*[170] reported that the fine control of different facets of anatase crystals can be achieved by varying the reaction duration using diethanolamine as a fluorine-free shape controlling reagent. In addition to the (001) facets, the (100) facets were also obtained simultaneously. Chen *et al.*[152] also synthesized hierarchical spheres consisting of ultrathin anatase nanosheets with nearly 100 % (001) facets in an amine-mediated environment. In this case, diethylenetriamine was used as an amine-capping agent to stabilize the (001) facet. Amano *et al.*[171] developed an original gas-phase process using $TiCl_4$ as a titanium source to synthesize faceted decahedral anatase single crystals. Cheng *et al.*[172] fabricated anatase nanosheets exposing 82% of (001) facets through a facile toluene-water biphasic interfacial reaction method. The nanosheets could only be synthesized through the two-phase interface reaction at high HCl concentration. Dinh

*et al.*[173] developed a pragmatic route to synthesize anatase crystals in various shapes such as rhombic, truncated rhombic, spherical, dog-bone, truncated and elongated rhombic, bar, and dots, by using a simple solvothermal technique employing oleic acid (OA) and oleylamine (OM) as capping agents in the presence of water vapor. The scheme is illustrated in figure 2.32. OA binds strongly to the (001) faces[174], whereas OM is adsorbed preferentially on the (101) facets[175]. The selective bindings of OA and OM to different facets of anatase prevent the growth in the corresponding direction. OA and OM act not only as capping agents but also as an acid base pair catalyst, which could increase the condensation rate without affecting the hydrolysis rate. Therefore, the shape of anatase crystals can be controlled by tuning the molar ratio of OA/OM. However, there is a drawback due to the fact it is difficult to remove the remaining capping agents on the surface of anatase and thus it is tricky to evaluate photocatalytic activities of the contaminated crystals.

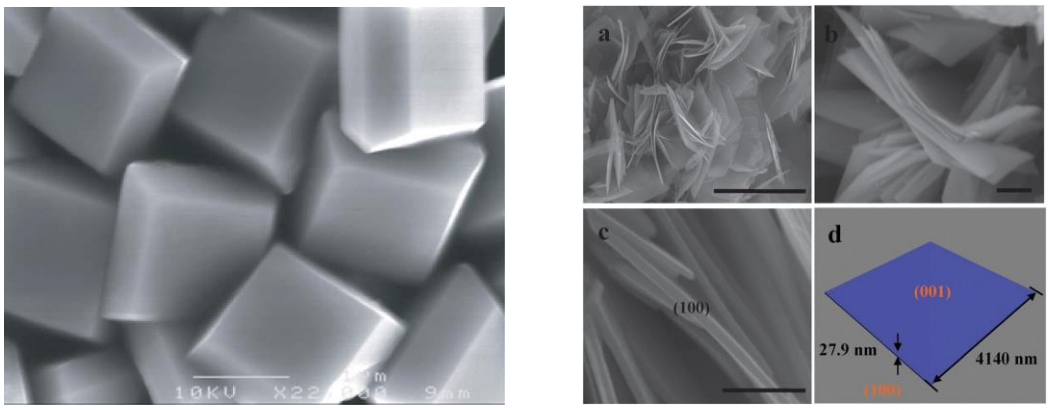


Figure 2.31. The first anatase single crystal with 47 % (001) facets via a hydrothermal method using HF reported in 2008 (left)[159] and anatase nanosheet crystals with 98.7 % (001) facets via a developed hydrothermal method employing 1-butanol in addition to HF reported in 2011 (right)[163]. Reproduced from ref[159, 163].

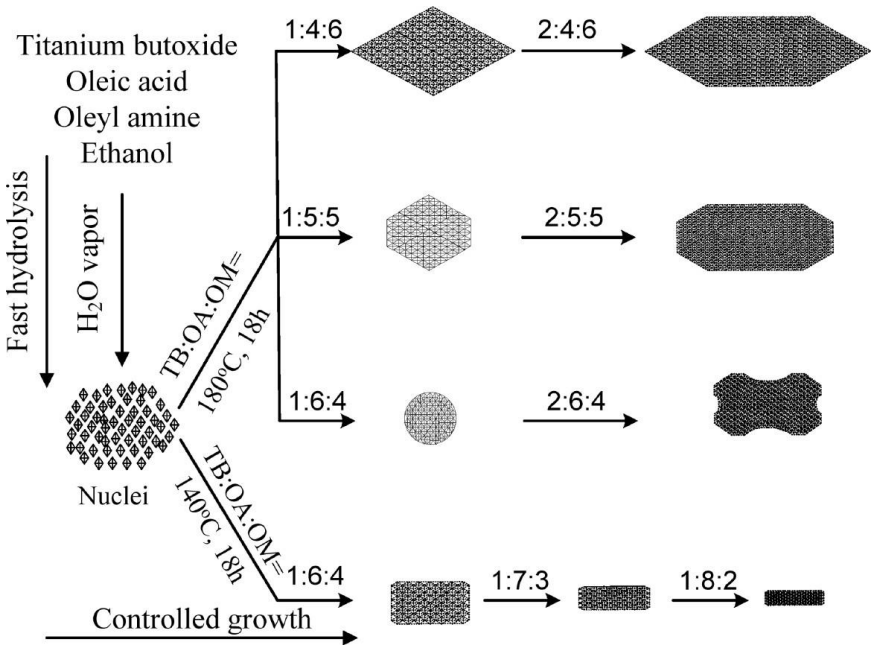


Figure 2.32. Schematic illustration of the overall formation and shape evolution of anatase single crystals. The shape controlling can be achieved by tuning a ratio of titanium butoxide (TB):oleic acid (OA):oleylamine (OM). Reproduced from ref[173].

Various techniques can be used to determine the percentage of (001) facets in anatase crystals such as FESEM, TEM, XRD, and Raman spectroscopy. In the case of FESEM and TEM, the dimensions of the crystals are measured to calculate the *A/B* ratio as mentioned above[115, 159]. XRD can also be employed to estimate the percentage of (001) facets even though this technique is not quantitatively precise. According to the Scherrer equation, the broadening of the (004) diffraction corresponds to the decrease of the crystallite size along the [001] axis vertical to the (001) facets, meaning that the top and bottom edges of the bipyramids of anatase crystals are truncated[176]. In addition, the sharpened peak of (101) diffraction represents the increased crystallite size along the [001] axis perpendicular to the (101) facets, indicating the increased (001) facets. Therefore, the percentage of the exposed (001) facets could be roughly estimated by calculating the FWHM of (004) and (101) diffraction peaks. Raman spectroscopy can also be used to estimate the percentage of (001) facets[177]. Figure 2.33 shows Raman spectra for anatase single crystalline particles with various percentages of (001) facets. The intensity of the Raman vibration modes would depend on the coverage of (001) facets on the surface as molecular bonds would behave differently on various facets. The percentage of (001) facets exposed in anatase crystals could be determined via the peak intensity ratio of the Eg and A1g peaks[115, 177-178]. The B1g peak is assigned to symmetric bending vibration of O-Ti-O at 394 $cm^{-1}$, the A1g peak is attributed to antisymmetric bending vibration of O Ti O at 514 $cm^{-1}$, and the Eg peak mainly belongs to the symmetric stretching vibration of O-Ti-O at 144 and 636 $cm^{-1}$.

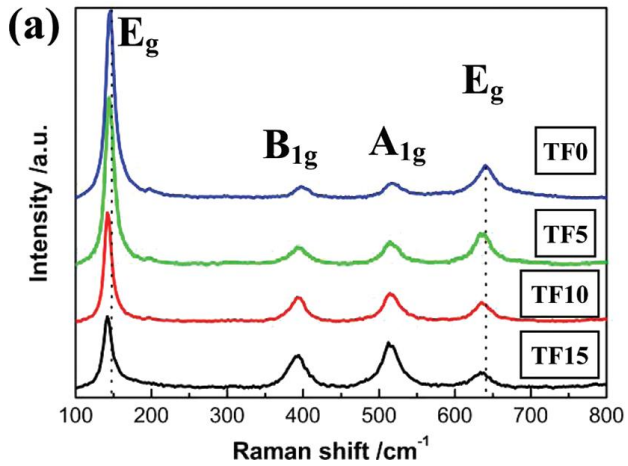


Figure 2.33. Raman spectra for anatase nanosheets with various percentages of (001) facets. TF0, TF5, TF10, and TF15 contain 8, 20, 53, and 78 % of (001) facets, respectively. Reproduced from ref[177].

### 2.4.2.3 Other facets of anatase

The (010) facet has been also considered as one of the most reactive facets. Although the surface energy of (010) was predicted to be between that of (001) and (101) facets, the equilibrium structure of anatase crystal exhibits no (010) facets according to calculations based on the Wuff construction and the calculated surface energy[3]. Barnard *et al.*[179] found that the shape of anatase nanoparticles is highly dependent on the surface chemistry by employing a thermodynamic model (capable of describing the free energy of nanoparticles as a

function of size, shape and surface chemistry), and surface energies and surface tension calculated for anatase surfaces terminated by adsorbates with varying amount of hydrogen and oxygen. The predicted shapes for various surface chemistries are shown in figure 2.34. A shape of an anatase crystal for hydrogen rich and hydrated surfaces was predicted to be same to the equilibrium structure whereas that for hydrogen poor and oxygenated surfaces was predicted to exhibit an elongated structure so that the (010) facets would appear. In addition, the surface chemistry also affects the aspect ratio of *B/A* (figure 2.26) as shown in figure 2.35.

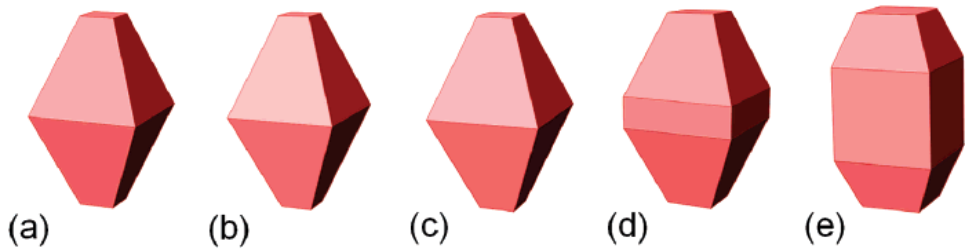


Figure 2.34. Predicted morphologies with (a) hydrogenated surfaces (b) with hydrogen-rich surface adsorbates, (c) hydrated surfaces, (d) hydrogen-poor adsorbates, and (e) oxygenated surfaces. Reproduced from ref[179].

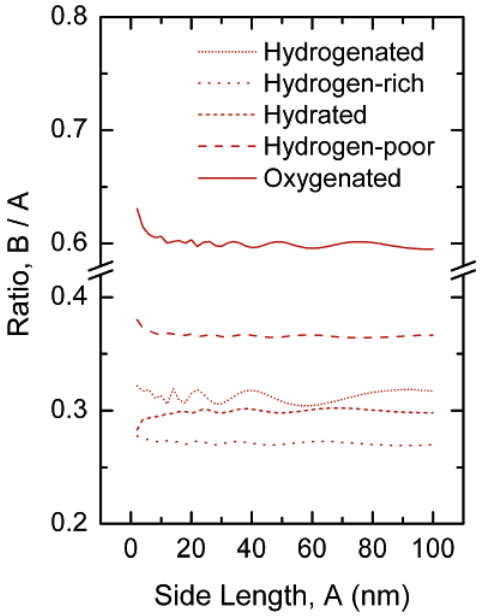


Figure 2.35. The optimized ratio of *B/A* of anatase with various surface chemistries: hydrogenated, hydrogen-rich, hydrated, hydrogen-poor, and oxygenated. Reproduced from ref[179].

### 2.4.3 Synergetic effects of facet controlling and co-catalysts

In addition to the facet engineering technique, the enhancement of the photocatalytic activity can be achieved by using co-catalysts. Recently efforts have been made to combine the above two techniques by depositing selectively oxidation and reduction co-catalysts onto oxidation and reduction sites, respectively. In such system, the photocatalytic activities can be drastically enhanced by the synergetic effects of the charge separation

between different facets and dual co-catalysts deposited onto different facets where co-catalysts can fully function.

In most cases, co-catalysts are deposited by an impregnation or adsorption method resulting in their random distribution on the photocatalyst surface without controlling the location. Li *et al.*[180] first demonstrated the selective deposition of Pt and different metal oxides co-catalysts onto the electron rich (010) and hole rich (110) facets of $BiVO_4$ via photo-deposition, respectively. Indeed, they had previously found that photo-generated electrons and holes were spatially separated into the (010) and (110) facets as already reported for $TiO_2$[181]. The scheme of selective deposition of dual co-catalysts and SEM images of $BiVO_4$ with selectively deposited dual co-catalysts via photo-deposition are shown in figure 2.36. It is known that noble metals are used as efficient reduction co-catalysts while metal oxides act as oxidation co-catalysts. Regardless of the co-catalysts, the heterojunction photocatalyst with selective deposition of co-catalysts on the corresponding sites exhibits superior photocatalytic activities compared to the system with the randomly distributed co-catalysts. In addition, a simultaneous deposition of both reduction and oxidation co-catalysts on appropriate facets resulted in 4 times higher photocatalytic activities than those observed for the case of a single (reduction or oxidation) co-catalyst deposition on appropriate facets. A combination of Pt as a reduction co-catalyst and $MnO_x$ as an oxidation co-catalyst was the best for the photocatalytic dye degradation of MO and RhB whereas Pt as a reduction co-catalyst and $Co_3O_4$ as an oxidation co-catalyst exhibited the best activity for the photocatalytic water oxidation. These results validate the idea that the enhanced photocatalytic activities are originated from not only the intrinsic nature of charge separation between the (010) and (110) facets of $BiVO_4$, but also the synergetic effect of dual co-catalysts deposited on different facets of $BiVO_4$. Moreover, the suitable selection of a combination of dual co-catalysts should be considered depending on the photocatalytic reactions.

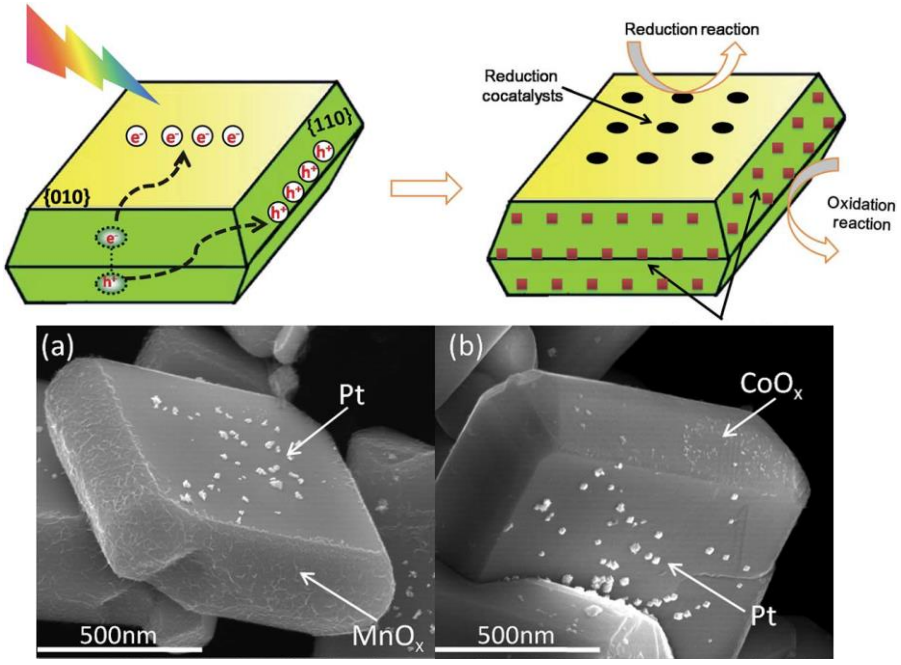


Figure 2.36. (Top) Schematic representation of the selective deposition of reduction and oxidation co-catalysts on (010) and (110) facets, respectively, via photo-deposition. SEM images of (a) $BiVO_4$ with selectively deposited Pt and $MnO_x$ and (b) $BiVO_4$ with selectively deposited Pt and $CoO_x$. Reproduced from ref[180].

The concept of dual co-catalysts should be valid for other anisotropic semiconductor photocatalysts and efficient photocatalytic systems could be achieved by a rational design where suitable co-catalysts are deposited onto the appropriate facets of the semiconductor crystals. To the best of my knowledge, the enhanced photocatalytic activities by dual co-catalysts on different facets of crystals have been demonstrated for anatase $TiO_2$[182-183], $Cu_2O$[184], BiOI[185], $SrTiO_3$[186], and $WO_3$[187]. In the cases of anatase, Liu *et al.*[182] prepared a $Fe_2O_3$-$TiO_2$-Pt system where α- $Fe_2O_3$ and Pt are selectively deposited onto (001) and (101) facets of anatase via photo-deposition, respectively. This system showed an enhanced photocatalytic $H_2$ production with selective co-catalysts deposition by 2.2 and 30 times higher than those delivered with photocatalysts with a random deposition and without co-catalysts, respectively. Meng *et al.*[183] deposited $Co_3O_4$ and Pt onto the (001) and (101) facets of anatase as shown in figure 2.37 and the designed system showed a higher photocatalytic $H_2$ production activity than anatase with single co-catalysts of $Co_3O_4$ or Pt by 9.4 and 1.8 times, respectively. These results again support the concept of the dual co-catalyst system where intrinsic electronic properties of different facets would suppress the recombination of charge carriers and dual co-catalysts deposited onto appropriate facets could not only provide effective reaction sites, but also trap the charge carriers and further prevent the recombination. To achieve more efficient photocatalytic activities, further efforts have to be made to explore an optimal ratio of different facets of support photocatalysts, suitable combinations of dual co-catalysts, and their amount for different reactions such as bacteria inactivation, dye decomposition, and hydrogen and oxygen evolution from water splitting.

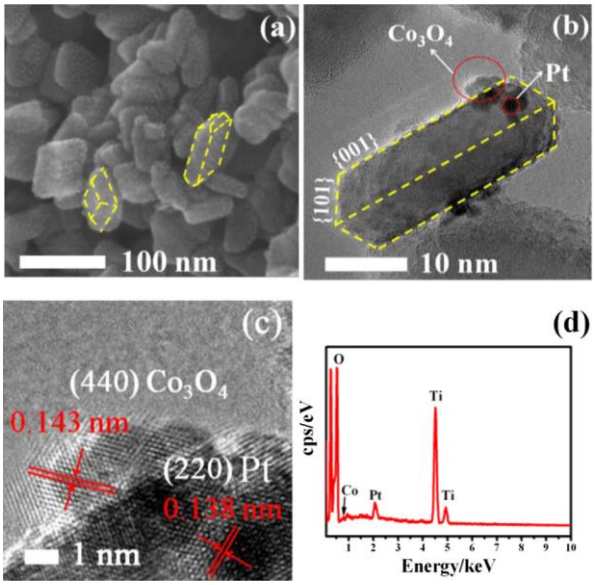


Figure 2.37. (a)FESEM, (b)TEM, (c)HRTEM, and EDS patterns of anatase crystals with $Co_3O_4$ and Pt selectively deposited onto (001) and (101) facets via photo-deposition, respectively. Reproduced from ref[180].

While for the above cases selective deposition of dual co-catalysts were performed with specific facets induced by intrinsic charge separation between different well-defined facets, very recently Li *et al.*[188] demonstrated that photo-generated electrons and holes can be regularly separated on ferroelectric $PbTiO_3$ photocatalysts without

regular facets. The reduction and oxidation co-catalysts were selectively deposited on different sites via an in-situ photochemical deposition method as shown in figure 2.38. The photocatalytic hydrogen production for $PbTiO_3$ with spatially separated dual co-catalysts is more than 100 times higher than that measured for the as-prepared $PbTiO_3$, which is much higher than that with dual co-catalysts with a random distribution. They proposed that the intrinsic electric fields and spontaneous electric polarization in the bulk of $PbTiO_3$ would trigger the spatial distribution of active sites on irregular $PbTiO_3$ crystals.

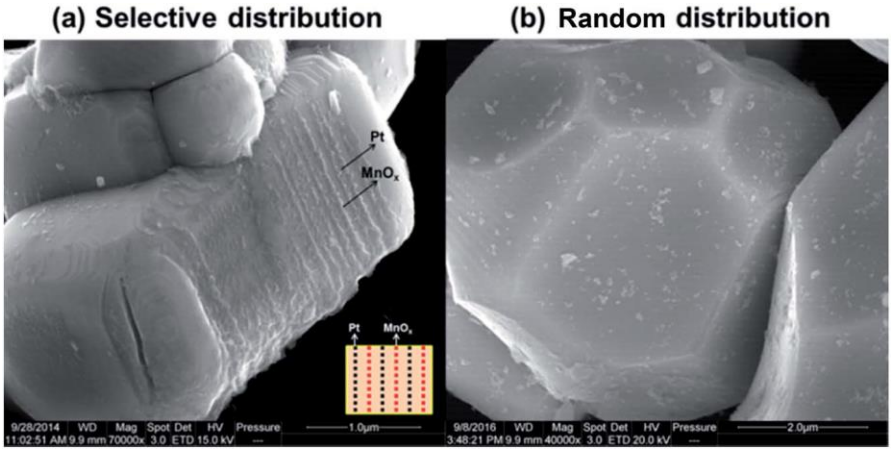


Figure 2.38. SEM images of (a)$PbTiO_3$ with selectively deposited Pt and $MnO_x$ via photo-deposition and (b) $PbTiO_3$ with randomly deposited Pt and $MnO_x$ via impregnation. Reproduced from ref[188].

To summarize the chapter 2, in a last decade both fundamental and practical investigations of photocatalyst especially employing $TiO_2$ have been intensively conducted. In terms of surface science, although single crystal rutile surfaces the (110) surface of which is considered as a model of metal oxides, have been intensively studied, reports on single crystal anatase surfaces are sparse despite their practical advantages as photocatalysts. Recently, the role of crystal graphic facets and effects of surface/subsurface defects and their interaction with simple molecules got started to be investigated. In addition, synergetic effects of crystal facets and co-catalysts selectively deposited on specific facets have drawn attention as this technique has a potential to drastically improve photocatalytic activities. However, the mechanistic details of these phenomena and systems are still under debate and thus further investigation are required to elucidate the mechanisms and achieve optimal photocatalysts especially using cheap and abundant materials such as $TiO_2$ and NiO for practical use.

The objective of this thesis is to reveal the origin of intrinsic charge carrier transfer between different facet of single crystalline $TiO_2$ and further enhance the charge carrier separation by establishing p-n junction via depositing p-type NiO selectively onto specific facets of $TiO_2$ nanocrystals. In the chapter 3, we prepared differently oriented anatase and rutile substrates with various surface states and compared their electronic properties by PES to elucidate the mechanisms of charge trapping and separation between different facets. Then we experimentally determined the band allignments of $NiO/TiO_2$ by interface experiments to rationalize the improved photocatalytic activities of $NiO/TiO_2$ heterostructured photocatalysts. Furthermore, by employing a

supercritical fluid route and a photo-deposition method, we synthesized $NiO/TiO_2$ heterostructed nanoparticles where NiO is selectively deposited onto specific facets of the single crystallite $TiO_2$ and found the superior photocatlytic activities of these systems in photocatlytc dye decompositions.


1. Barteau, M. A. Site requirements of reactions on oxide surfaces. *Journal of Vacuum Science & Technology A: Vacuum, Surfaces, and Films* **1993,** *11* (4), 2162-2168.
2. Diebold, U. The surface science of titanium dioxide. *Surface Science Reports* **2003,** *48* (5-8), 53-229.
3. Lazzeri, M.; Vittadini, A.; Selloni, A. Structure and energetics of stoichiometricTiO2anatase surfaces. *Physical Review B* **2001,** *63* (15).
4. Ramamoorthy, M.; Vanderbilt, D.; King-Smith, R. D. First-principles calculations of the energetics of stoichiometricTiO2surfaces. *Physical Review B* **1994,** *49* (23), 16721-16727.
5. Chen, S.; Mason, M.; Gysling, H.; Paz - Pujalt, G.; Blanton, T.; Castro, T.; Chen, K.; Fictorie, C.; Gladfelter, W.; Franciosi, A. Ultrahigh vacuum metalorganic chemical vapor deposition growth and in situ characterization of epitaxial TiO2 films. *Journal of Vacuum Science & Technology A: Vacuum, Surfaces, and Films* **1993,** *11* (5), 2419-2429.
6. Herman, G. S.; Gao, Y.; Tran, T. T.; Osterwalder, J. X-ray photoelectron diffraction study of an anatase thin film: TiO2(001). *Surface Science* **2000,** *447* (1-3), 201-211.
7. Sugimura, W.; Yamazaki, A.; Shigetani, H.; Tanaka, J.; Mitsuhashi, T. Anatase-type TiO2 thin films produced by lattice deformation. *Japanese journal of applied physics* **1997,** *36* (12R), 7358.
8. Murakami, M.; Matsumoto, Y.; Nakajima, K.; Makino, T.; Segawa, Y.; Chikyow, T.; Ahmet, P.; Kawasaki, M.; Koinuma, H. Anatase TiO 2 thin films grown on lattice-matched LaAlO 3 substrate by laser molecular-beam epitaxy. *Applied Physics Letters* **2001,** *78* (18), 2664-2666.
9. Gao, W.; Klie, R.; Altman, E. Growth of anatase films on vicinal and flat LaAlO3 (110) substrates by oxygen plasma assisted molecular beam epitaxy. *Thin Solid Films* **2005,** *485* (1-2), 115-125.
10. Dulub, O.; Diebold, U. Preparation of a pristine TiO2 anatase (101) surface by cleaving. *J Phys Condens Matter* **2010,** *22* (8), 084014.
11. Setvín, M.; Daniel, B.; Mansfeldova, V.; Kavan, L.; Scheiber, P.; Fidler, M.; Schmid, M.; Diebold, U. Surface preparation of TiO2 anatase (101): Pitfalls and how to avoid them. *Surface Science* **2014,** *626*, 61-67.
12. Onishi, H.; Iwasawa, Y. Dynamic visualization of a metal-oxide-surface/gas-phase reaction: Time-resolved observation by scanning tunneling microscopy at 800 K. *Phys Rev Lett* **1996,** *76* (5), 791-794.
13. Nie, S.; Starodub, E.; Monti, M.; Siegel, D. A.; Vergara, L.; El Gabaly, F.; Bartelt, N. C.; de la Figuera, J.; McCarty, K. F. Insight into magnetite's redox catalysis from observing surface morphology during oxidation. *Journal of the American Chemical Society* **2013,** *135* (27), 10091-10098.
14. Kraus, T. J.; Nepomnyashchii, A. B.; Parkinson, B. A. Templated homoepitaxial growth with atomic layer deposition of single-crystal anatase (101) and rutile (110) TiO2. *ACS Appl Mater Interfaces* **2014,** *6* (13), 9946-9.
15. Durinck, G.; Poelman, H.; Clauws, P.; Fiermans, L.; Vennik, J.; Dalmai, G. Observation of surface phonons on the (001) and (100) surfaces of anatase minerals. *Solid State Communications* **1991,** *80* (8), 579-581.
16. Herman, G. S.; Sievers, M. R.; Gao, Y. Structure determination of the two-domain ( 1x4) anatase TiO2(001) surface. *Phys Rev Lett* **2000,** *84* (15), 3354-7.
17. Hengerer, R.; Kavan, L.; Krtil, P.; Grätzel, M. Orientation Dependence of Charge - Transfer Processes on TiO2 (Anatase) Single Crystals. *Journal of the Electrochemical Society* **2000,** *147* (4), 1467-1472.
18. Gong, X. Q.; Selloni, A. Reactivity of anatase TiO(2) nanoparticles: the role of the minority (001) surface. *J Phys Chem B* **2005,** *109* (42), 19560-2.
19. Lazzeri, M.; Selloni, A. Stress-driven reconstruction of an oxide surface: the anatase TiO 2 (001)−(1× 4) surface. *Physical review letters* **2001,** *87* (26), 266105.
20. Tanner, R. E.; Sasahara, A.; Liang, Y.; Altman, E. I.; Onishi, H. Formic acid adsorption on anatase TiO2 (001)−(1× 4) thin films studied by NC-AFM and STM. *The Journal of Physical Chemistry B* **2002,** *106* (33), 8211-8222.
21. Kavan, L.; Grätzel, M.; Gilbert, S.; Klemenz, C.; Scheel, H. Electrochemical and photoelectrochemical investigation of single-crystal anatase. *Journal of the American Chemical Society* **1996,** *118* (28), 6716-6723.
22. Chen, X.; Liu, L.; Peter, Y. Y.; Mao, S. S. Increasing solar absorption for photocatalysis with black hydrogenated titanium dioxide nanocrystals. *Science* **2011,** *331* (6018), 746-750.

23. Cronemeyer, D. Infrared Absorption of Reduced Rutile Ti O 2 Single Crystals. *Physical Review* **1959,** *113* (5), 1222.
24. Jackman, M. J.; Thomas, A. G.; Muryn, C. Photoelectron Spectroscopy Study of Stoichiometric and Reduced Anatase TiO2(101) Surfaces: The Effect of Subsurface Defects on Water Adsorption at Near-Ambient Pressures. *The Journal of Physical Chemistry C* **2015,** *119* (24), 13682-13690.
25. Reckers, P.; Dimamay, M.; Klett, J.; Trost, S.; Zilberberg, K.; Riedl, T.; Parkinson, B. A.; Brötz, J.; Jaegermann, W.; Mayer, T. Deep and Shallow TiO2 Gap States on Cleaved Anatase Single Crystal (101) Surfaces, Nanocrystalline Anatase Films, and ALD Titania Ante and Post Annealing. *The Journal of Physical Chemistry C* **2015,** *119* (18), 9890-9898.
26. Wendt, S.; Sprunger, P. T.; Lira, E.; Madsen, G. K.; Li, Z.; Hansen, J. O.; Matthiesen, J.; Blekinge-Rasmussen, A.; Laegsgaard, E.; Hammer, B.; Besenbacher, F. The role of interstitial sites in the Ti3d defect state in the band gap of titania. *Science* **2008,** *320* (5884), 1755-9.
27. Thomas, A.; Flavell, W.; Mallick, A.; Kumarasinghe, A.; Tsoutsou, D.; Khan, N.; Chatwin, C.; Rayner, S.; Smith, G.; Stockbauer, R. Comparison of the electronic structure of anatase and rutile TiO 2 single-crystal surfaces using resonant photoemission and X-ray absorption spectroscopy. *Physical Review B* **2007,** *75* (3), 035105.
28. Kodaira, S.; Sakisaka, Y.; Maruyama, T.; Haruyama, Y.; Aiura, Y.; Kato, H. Angle-resolved photoemission study of an in-gap state in TiO2. *Solid State Communications* **1994,** *89* (1), 9-12.
29. Finazzi, E.; Di Valentin, C.; Pacchioni, G.; Selloni, A. Excess electron states in reduced bulk anatase TiO2: comparison of standard GGA, GGA+U, and hybrid DFT calculations. *J Chem Phys* **2008,** *129* (15), 154113.
30. Morgan, B. J.; Watson, G. W. Intrinsic n-type Defect Formation in TiO2: A Comparison of Rutile and Anatase from GGA+U Calculations. *The Journal of Physical Chemistry C* **2010,** *114* (5), 2321-2328.
31. Finazzi, E.; Di Valentin, C.; Pacchioni, G. Nature of Ti Interstitials in Reduced Bulk Anatase and Rutile TiO2. *The Journal of Physical Chemistry C* **2009,** *113* (9), 3382-3385.
32. Mattioli, G.; Filippone, F.; Alippi, P.; Amore Bonapasta, A. Ab initiostudy of the electronic states induced by oxygen vacancies in rutile and anataseTiO2. *Physical Review B* **2008,** *78* (24).
33. Thomas, A. G.; Flavell, W. R.; Kumarasinghe, A. R.; Mallick, A. K.; Tsoutsou, D.; Smith, G. C.; Stockbauer, R.; Patel, S.; Grätzel, M.; Hengerer, R. Resonant photoemission of anataseTiO2(101) and (001) single crystals. *Physical Review B* **2003,** *67* (3).
34. Nakamura, I.; Negishi, N.; Kutsuna, S.; Ihara, T.; Sugihara, S.; Takeuchi, K. Role of oxygen vacancy in the plasma-treated TiO2 photocatalyst with visible light activity for NO removal. *Journal of Molecular Catalysis A: Chemical* **2000,** *161* (1-2), 205-212.
35. Cheng, H.; Selloni, A. Surface and subsurface oxygen vacancies in anataseTiO2and differences with rutile. *Physical Review B* **2009,** *79* (9).
36. Mori-Sánchez, P.; Cohen, A. J.; Yang, W. Localization and delocalization errors in density functional theory and implications for band-gap prediction. *Physical review letters* **2008,** *100* (14), 146401.
37. Li, H.; Guo, Y.; Robertson, J. Calculation of TiO2 Surface and Subsurface Oxygen Vacancy by the Screened Exchange Functional. *The Journal of Physical Chemistry C* **2015,** *119* (32), 18160-18166.
38. Peverati, R.; Truhlar, D. G. Screened-exchange density functionals with broad accuracy for chemistry and solid-state physics. *Physical Chemistry Chemical Physics* **2012,** *14* (47), 16187-16191.
39. He, Y.; Dulub, O.; Cheng, H.; Selloni, A.; Diebold, U. Evidence for the predominance of subsurface defects on reduced anatase TiO2(101). *Phys Rev Lett* **2009,** *102* (10), 106105.
40. Lun Pang, C.; Lindsay, R.; Thornton, G. Chemical reactions on rutile TiO2(110). *Chem Soc Rev* **2008,** *37* (10), 2328-53.
41. Hussain, H.; Tocci, G.; Woolcot, T.; Torrelles, X.; Pang, C. L.; Humphrey, D. S.; Yim, C. M.; Grinter, D. C.; Cabailh, G.; Bikondoa, O.; Lindsay, R.; Zegenhagen, J.; Michaelides, A.; Thornton, G. Structure of a model TiO2 photocatalytic interface. *Nat Mater* **2017,** *16* (4), 461-466.
42. He, Y.; Tilocca, A.; Dulub, O.; Selloni, A.; Diebold, U. Local ordering and electronic signatures of submonolayer water on anatase TiO2(101). *Nat Mater* **2009,** *8* (7), 585-9.
43. Setvin, M.; Daniel, B.; Aschauer, U.; Hou, W.; Li, Y. F.; Schmid, M.; Selloni, A.; Diebold, U. Identification of adsorbed molecules via STM tip manipulation: CO, H(2)O, and O(2) on TiO(2) anatase (101). *Phys Chem Chem Phys* **2014,** *16* (39), 21524-30.
44. Setvin, M.; Aschauer, U.; Hulva, J.; Simschitz, T.; Daniel, B.; Schmid, M.; Selloni, A.; Diebold, U. Following the Reduction of Oxygen on TiO2 Anatase (101) Step by Step. *J Am Chem Soc* **2016,** *138* (30), 9565-71.

45. Herman, G. S.; Dohnálek, Z.; Ruzycki, N.; Diebold, U. Experimental Investigation of the Interaction of Water and Methanol with Anatase−TiO2(101). *The Journal of Physical Chemistry B* **2003,** *107* (12), 2788-2795.
46. Aschauer, U.; He, Y.; Cheng, H.; Li, S.-C.; Diebold, U.; Selloni, A. Influence of Subsurface Defects on the Surface Reactivity of TiO2: Water on Anatase (101). *The Journal of Physical Chemistry C* **2009,** *114* (2), 1278-1284.
47. Walle, L. E.; Borg, A.; Johansson, E. M. J.; Plogmaker, S.; Rensmo, H.; Uvdal, P.; Sandell, A. Mixed Dissociative and Molecular Water Adsorption on Anatase TiO2(101). *The Journal of Physical Chemistry C* **2011,** *115* (19), 9545-9550.
48. Payne, D.; Zhang, Y.; Pang, C.; Fielding, H.; Thornton, G. Creating Excess Electrons at the Anatase TiO2 (101) Surface. *Topics in Catalysis* **2017,** *60* (6-7), 392-400.
49. Vittadini, A.; Selloni, A.; Rotzinger, F. P.; Grätzel, M. Structure and Energetics of Water Adsorbed atTiO2Anatase \(101\) and \(001\) Surfaces. *Physical Review Letters* **1998,** *81* (14), 2954-2957.
50. Li, Y.; Gao, Y. Interplay between Water andTiO2Anatase (101) Surface with Subsurface Oxygen Vacancy. *Physical Review Letters* **2014,** *112* (20).
51. Liu, L.; Zhao, H.; Andino, J. M.; Li, Y. Photocatalytic CO2 Reduction with H2O on TiO2 Nanocrystals: Comparison of Anatase, Rutile, and Brookite Polymorphs and Exploration of Surface Chemistry. *ACS Catalysis* **2012,** *2* (8), 1817-1828.
52. Selcuk, S.; Selloni, A. Facet-dependent trapping and dynamics of excess electrons at anatase TiO2 surfaces and aqueous interfaces. *Nat Mater* **2016,** *15* (10), 1107-12.
53. Nadeem, I. M.; Harrison, G. T.; Wilson, A.; Pang, C. L.; Zegenhagen, J. r.; Thornton, G. Bridging Hydroxyls on Anatase TiO2 (101) by Water Dissociation in Oxygen Vacancies. *The Journal of Physical Chemistry B* **2017**.
54. Patrick, C. E.; Giustino, F. Structure of a water monolayer on the anatase TiO 2 (101) surface. *Physical Review Applied* **2014,** *2* (1), 014001.
55. Höök, M.; Tang, X. Depletion of fossil fuels and anthropogenic climate change—A review. *Energy Policy* **2013,** *52*, 797-809.
56. Seinfeld, J. H.; Pandis, S. N. *Atmospheric chemistry and physics: from air pollution to climate change*. John Wiley & Sons: 2016.
57. Fujishima, A.; Honda, K. Electrochemical Photolysis of Water at a Semiconductor Electrode. *Nature* **1972,** *238* (5358), 37-38.
58. Kudo, A.; Kato, H.; Tsuji, I. Strategies for the Development of Visible-light-driven Photocatalysts for Water Splitting. *Chemistry Letters* **2004,** *33* (12), 1534-1539.
59. Revivals, R. Water Pollution**2017**.
60. Legrini, O.; Oliveros, E.; Braun, A. Photochemical processes for water treatment. *Chemical reviews* **1993,** *93* (2), 671-698.
61. Kubo, W.; Tatsuma, T. Mechanisms of photocatalytic remote oxidation. *Journal of the American Chemical Society* **2006,** *128* (50), 16034-16035.
62. Linsebigler, A. L.; Lu, G.; Yates, J. T. Photocatalysis on TiO2 Surfaces: Principles, Mechanisms, and Selected Results. *Chemical Reviews* **1995,** *95* (3), 735-758.
63. Kamat, P. V. Manipulation of Charge Transfer Across Semiconductor Interface. A Criterion That Cannot Be Ignored in Photocatalyst Design. *J Phys Chem Lett* **2012,** *3* (5), 663-72.
64. Erisman, J. W.; Sutton, M. A.; Galloway, J.; Klimont, Z.; Winiwarter, W. How a century of ammonia synthesis changed the world. *Nature Geoscience* **2008,** *1* (10), 636.
65. Walter, M. G.; Warren, E. L.; McKone, J. R.; Boettcher, S. W.; Mi, Q.; Santori, E. A.; Lewis, N. S. Solar water splitting cells. *Chem Rev* **2010,** *110* (11), 6446-73.
66. Lu, Q.; Yu, Y.; Ma, Q.; Chen, B.; Zhang, H. 2D Transition - Metal - Dichalcogenide - Nanosheet - Based Composites for Photocatalytic and Electrocatalytic Hydrogen Evolution Reactions. *Advanced Materials* **2016,** *28* (10), 1917-1933.
67. Folli, A.; Pade, C.; Hansen, T. B.; De Marco, T.; Macphee, D. E. TiO2 photocatalysis in cementitious systems: Insights into self-cleaning and depollution chemistry. *Cement and concrete research* **2012,** *42* (3), 539-548.
68. Fujishima, A.; Zhang, X. Titanium dioxide photocatalysis: present situation and future approaches. *Comptes Rendus Chimie* **2006,** *9* (5-6), 750-760.
69. Watanabe, T.; Nakajima, A.; Wang, R.; Minabe, M.; Koizumi, S.; Fujishima, A.; Hashimoto, K. Photocatalytic activity and photoinduced hydrophilicity of titanium dioxide coated glass. *Thin solid films* **1999,** *351* (1-2), 260-263.

70. Liu, M.; Sunada, K.; Hashimoto, K.; Miyauchi, M. Visible-light sensitive Cu (ii)–TiO 2 with sustained anti-viral activity for efficient indoor environmental remediation. *Journal of Materials Chemistry A* **2015,** *3* (33), 17312-17319.
71. Chen, W.; Zhang, J. Using nanoparticles to enable simultaneous radiation and photodynamic therapies for cancer treatment. *Journal of nanoscience and nanotechnology* **2006,** *6* (4), 1159-1166.
72. Fujishima, A.; Zhang, X.; Tryk, D. TiO2 photocatalysis and related surface phenomena. *Surface Science Reports* **2008,** *63* (12), 515-582.
73. Osterloh, F. E. Inorganic nanostructures for photoelectrochemical and photocatalytic water splitting. *Chem Soc Rev* **2013,** *42* (6), 2294-320.
74. Qu, Y.; Duan, X. Progress, challenge and perspective of heterogeneous photocatalysts. *Chem Soc Rev* **2013,** *42* (7), 2568-80.
75. Bai, S.; Yin, W.; Wang, L.; Li, Z.; Xiong, Y. Surface and interface design in cocatalysts for photocatalytic water splitting and CO2 reduction. *RSC Advances* **2016,** *6* (62), 57446-57463.
76. Yang, J.; Wang, D.; Han, H.; Li, C. Roles of cocatalysts in photocatalysis and photoelectrocatalysis. *Acc Chem Res* **2013,** *46* (8), 1900-9.
77. Maeda, K.; Eguchi, M.; Lee, S.-H. A.; Youngblood, W. J.; Hata, H.; Mallouk, T. E. Photocatalytic hydrogen evolution from hexaniobate nanoscrolls and calcium niobate nanosheets sensitized by ruthenium (II) bipyridyl complexes. *The Journal of Physical Chemistry C* **2009,** *113* (18), 7962-7969.
78. Chen, S.; Ingram, R. S.; Hostetler, M. J.; Pietron, J. J.; Murray, R. W.; Schaaff, T. G.; Khoury, J. T.; Alvarez, M. M.; Whetten, R. L. Gold nanoelectrodes of varied size: transition to molecule-like charging. *Science* **1998,** *280* (5372), 2098-2101.
79. Takai, A.; Kamat, P. V. Capture, store, and discharge. Shuttling photogenerated electrons across TiO2-silver interface. *ACS Nano* **2011,** *5* (9), 7369-76.
80. Subramanian, V.; Wolf, E. E.; Kamat, P. V. Catalysis with TiO2/gold nanocomposites. Effect of metal particle size on the Fermi level equilibration. *J Am Chem Soc* **2004,** *126* (15), 4943-50.
81. Uddin, M. T.; Nicolas, Y.; Olivier, C.; Toupance, T.; Servant, L.; Muller, M. M.; Kleebe, H. J.; Ziegler, J.; Jaegermann, W. Nanostructured SnO2-ZnO heterojunction photocatalysts showing enhanced photocatalytic activity for the degradation of organic dyes. *Inorg Chem* **2012,** *51* (14), 7764-73.
82. Seh, Z. W.; Liu, S.; Low, M.; Zhang, S. Y.; Liu, Z.; Mlayah, A.; Han, M. Y. Janus Au - TiO2 Photocatalysts with Strong Localization of Plasmonic Near - Fields for Efficient Visible - Light Hydrogen Generation. *Advanced Materials* **2012,** *24* (17), 2310-2314.
83. Trasatti, S. Work function, electronegativity, and electrochemical behaviour of metals. *Journal of Electroanalytical Chemistry and Interfacial Electrochemistry* **1972,** *39* (1), 163-184.
84. Rasiyah, P.; Tseung, A.; Hibbert, D. A Mechanistic Study of Oxygen Evolution on NiCo2 O 4 I. Formation of Higher Oxides. *Journal of the Electrochemical Society* **1982,** *129* (8), 1724-1727.
85. Trasatti, S. Electrocatalysis by oxides — Attempt at a unifying approach. *Journal of Electroanalytical Chemistry and Interfacial Electrochemistry* **1980,** *111* (1), 125-131.
86. Maeda, K.; Domen, K. Photocatalytic Water Splitting: Recent Progress and Future Challenges. *The Journal of Physical Chemistry Letters* **2010,** *1* (18), 2655-2661.
87. Frame, F. A.; Osterloh, F. E. CdSe-MoS2: A quantum size-confined photocatalyst for hydrogen evolution from water under visible light. *The Journal of Physical Chemistry C* **2010,** *114* (23), 10628-10633.
88. Li, Y. H.; Xing, J.; Chen, Z. J.; Li, Z.; Tian, F.; Zheng, L. R.; Wang, H. F.; Hu, P.; Zhao, H. J.; Yang, H. G. Unidirectional suppression of hydrogen oxidation on oxidized platinum clusters. *Nat Commun* **2013,** *4*, 2500.
89. Meekins, B. H.; Kamat, P. V. Role of Water Oxidation Catalyst IrO2 in Shuttling Photogenerated Holes Across TiO2 Interface. *The Journal of Physical Chemistry Letters* **2011,** *2* (18), 2304-2310.
90. Kalyanasundaram, K.; Grätzel, M. Cyclic cleavage of water into H2 and O2 by visible light with coupled redox catalysts. *Angewandte Chemie International Edition* **1979,** *18* (9), 701-702.
91. Ma, B.; Yang, J.; Han, H.; Wang, J.; Zhang, X.; Li, C. Enhancement of Photocatalytic Water Oxidation Activity on IrO x− ZnO/Zn2− x GeO4− x− 3 y N2 y Catalyst with the Solid Solution Phase Junction. *The Journal of Physical Chemistry C* **2010,** *114* (29), 12818-12822.
92. Liu, L.; Ji, Z.; Zou, W.; Gu, X.; Deng, Y.; Gao, F.; Tang, C.; Dong, L. In Situ Loading Transition Metal Oxide Clusters on TiO2 Nanosheets As Co-catalysts for Exceptional High Photoactivity. *ACS Catalysis* **2013,** *3* (9), 2052-2061.
93. Kanan, M. W.; Nocera, D. G. In situ formation of an oxygen-evolving catalyst in neutral water containing phosphate and Co2+. *Science* **2008,** *321* (5892), 1072-1075.

94. Wang, D.; Li, R.; Zhu, J.; Shi, J.; Han, J.; Zong, X.; Li, C. Photocatalytic water oxidation on BiVO4 with the electrocatalyst as an oxidation cocatalyst: essential relations between electrocatalyst and photocatalyst. *The Journal of Physical Chemistry C* **2012,** *116* (8), 5082-5089.
95. Zong, X.; Yan, H.; Wu, G.; Ma, G.; Wen, F.; Wang, L.; Li, C. Enhancement of photocatalytic H2 evolution on CdS by loading MoS2 as cocatalyst under visible light irradiation. *Journal of the American Chemical Society* **2008,** *130* (23), 7176-7177.
96. Hinnemann, B.; Moses, P. G.; Bonde, J.; Jørgensen, K. P.; Nielsen, J. H.; Horch, S.; Chorkendorff, I.; Nørskov, J. K. Biomimetic hydrogen evolution: MoS2 nanoparticles as catalyst for hydrogen evolution. *Journal of the American Chemical Society* **2005,** *127* (15), 5308-5309.
97. Ohtani, B.; Abe, R. Mechanism of photocatalytic oxygen reduction reaction. *Chemistry (Japanese)* **2008,** *63* (9), 19-23.
98. Uddin, M. T.; Babot, O.; Thomas, L.; Olivier, C. l.; Redaelli, M.; D'Arienzo, M.; Morazzoni, F.; Jaegermann, W.; Rockstroh, N.; Junge, H. New insights into the photocatalytic properties of RuO2/TiO2 mesoporous heterostructures for hydrogen production and organic pollutant photodecomposition. *The Journal of Physical Chemistry C* **2015,** *119* (13), 7006-7015.
99. Uddin, M. T.; Nicolas, Y.; Olivier, C.; Toupance, T.; Müller, M. M.; Kleebe, H.-J.; Rachut, K.; Ziegler, J.; Klein, A.; Jaegermann, W. Preparation of RuO2/TiO2 Mesoporous Heterostructures and Rationalization of Their Enhanced Photocatalytic Properties by Band Alignment Investigations. *The Journal of Physical Chemistry C* **2013,** *117* (42), 22098-22110.
100. Liu, G.; Yu, J. C.; Lu, G. Q.; Cheng, H. M. Crystal facet engineering of semiconductor photocatalysts: motivations, advances and unique properties. *Chem Commun (Camb)* **2011,** *47* (24), 6763-83.
101. Bai, S.; Wang, L.; Li, Z.; Xiong, Y. Facet - Engineered Surface and Interface Design of Photocatalytic Materials. *Advanced Science* **2017,** *4* (1).
102. Thompson, T. L.; Yates, J. T., Jr. Surface science studies of the photoactivation of TiO2--new photochemical processes. *Chem Rev* **2006,** *106* (10), 4428-53.
103. Chen, W.; Kuang, Q.; Wang, Q.; Xie, Z. Engineering a high energy surface of anatase TiO2 crystals towards enhanced performance for energy conversion and environmental applications. *RSC Advances* **2015,** *5* (26), 20396-20409.
104. Sajan, C. P.; Wageh, S.; Al-Ghamdi, A. A.; Yu, J.; Cao, S. TiO2 nanosheets with exposed {001} facets for photocatalytic applications. *Nano Research* **2015,** *9* (1), 3-27.
105. Ohno, T.; Sarukawa, K.; Matsumura, M. Crystal faces of rutile and anatase TiO2 particles and their roles in photocatalytic reactions. *New Journal of Chemistry* **2002,** *26* (9), 1167-1170.
106. Tachikawa, T.; Yamashita, S.; Majima, T. Evidence for crystal-face-dependent TiO2 photocatalysis from single-molecule imaging and kinetic analysis. *J Am Chem Soc* **2011,** *133* (18), 7197-204.
107. D'Arienzo, M.; Carbajo, J.; Bahamonde, A.; Crippa, M.; Polizzi, S.; Scotti, R.; Wahba, L.; Morazzoni, F. Photogenerated defects in shape-controlled TiO2 anatase nanocrystals: a probe to evaluate the role of crystal facets in photocatalytic processes. *J Am Chem Soc* **2011,** *133* (44), 17652-61.
108. Hurum, D. C.; Gray, K. A.; Rajh, T.; Thurnauer, M. C. Recombination pathways in the Degussa P25 formulation of TiO2: surface versus lattice mechanisms. *The Journal of Physical Chemistry B* **2005,** *109* (2), 977-980.
109. Hurum, D.; Agrios, A.; Crist, S.; Gray, K.; Rajh, T.; Thurnauer, M. Probing reaction mechanisms in mixed phase TiO2 by EPR. *Journal of Electron Spectroscopy and Related Phenomena* **2006,** *150* (2-3), 155-163.
110. Berger, T.; Sterrer, M.; Diwald, O.; Knözinger, E.; Panayotov, D.; Thompson, T. L.; Yates, J. T. Light-induced charge separation in anatase TiO2 particles. *The Journal of Physical Chemistry B* **2005,** *109* (13), 6061-6068.
111. Berger, T.; Diwald, O.; Knözinger, E.; Sterrer, M.; Yates Jr, J. T. UV induced local heating effects in TiO 2 nanocrystals. *Physical Chemistry Chemical Physics* **2006,** *8* (15), 1822-1826.
112. Yu, J.; Low, J.; Xiao, W.; Zhou, P.; Jaroniec, M. Enhanced photocatalytic CO(2)-reduction activity of anatase TiO(2) by coexposed {001} and {101} facets. *J Am Chem Soc* **2014,** *136* (25), 8839-42.
113. Ye, L.; Mao, J.; Liu, J.; Jiang, Z.; Peng, T.; Zan, L. Synthesis of anatase TiO2 nanocrystals with {101}, {001} or {010} single facets of 90% level exposure and liquid-phase photocatalytic reduction and oxidation activity orders. *Journal of Materials Chemistry A* **2013,** *1* (35).
114. Ye, L.; Mao, J.; Peng, T.; Zan, L.; Zhang, Y. Opposite photocatalytic activity orders of low-index facets of anatase TiO(2) for liquid phase dye degradation and gaseous phase CO(2) photoreduction. *Phys Chem Chem Phys* **2014,** *16* (29), 15675-80.

115. Pan, J.; Liu, G.; Lu, G. Q.; Cheng, H. M. On the true photoreactivity order of {001}, {010}, and {101} facets of anatase TiO2 crystals. *Angew Chem Int Ed Engl* **2011,** *50* (9), 2133-7.
116. Xu, H.; Reunchan, P.; Ouyang, S.; Tong, H.; Umezawa, N.; Kako, T.; Ye, J. Anatase TiO2 single crystals exposed with high-reactive {111} facets toward efficient H2 evolution. *Chemistry of materials* **2013,** *25* (3), 405-411.
117. Blomquist, J.; Walle, L. E.; Uvdal, P.; Borg, A.; Sandell, A. Water dissociation on single crystalline anatase TiO2 (001) studied by photoelectron spectroscopy. *The Journal of Physical Chemistry C* **2008,** *112* (42), 16616-16621.
118. Li, Y.-F.; Liu, Z.-P.; Liu, L.; Gao, W. Mechanism and activity of photocatalytic oxygen evolution on titania anatase in aqueous surroundings. *Journal of the American Chemical Society* **2010,** *132* (37), 13008-13015.
119. Selloni, A. Crystal growth: Anatase shows its reactive side. *Nat Mater* **2008,** *7* (8), 613-5.
120. Yan, X.; Ohno, T.; Nishijima, K.; Abe, R.; Ohtani, B. Is methylene blue an appropriate substrate for a photocatalytic activity test? A study with visible-light responsive titania. *Chemical Physics Letters* **2006,** *429* (4-6), 606-610.
121. Mills, A.; Wang, J. Photobleaching of methylene blue sensitised by TiO2: an ambiguous system? *Journal of Photochemistry and Photobiology A: Chemistry* **1999,** *127* (1-3), 123-134.
122. Rochkind, M.; Pasternak, S.; Paz, Y. Using dyes for evaluating photocatalytic properties: a critical review. *Molecules* **2014,** *20* (1), 88-110.
123. Lazar, M. A.; Daoud, W. A. Selective adsorption and photocatalysis of low-temperature base-modified anatase nanocrystals. *RSC Adv.* **2012,** *2* (2), 447-452.
124. Robert, D.; Piscopo, A.; Weber, J. V. Selective solar photodegradation of organopollutant mixtures in water. *Solar Energy* **2004,** *77* (5), 553-558.
125. Makarova, O. V.; Rajh, T.; Thurnauer, M. C.; Martin, A.; Kemme, P. A.; Cropek, D. Surface modification of TiO2 nanoparticles for photochemical reduction of nitrobenzene. *Environmental science & technology* **2000,** *34* (22), 4797-4803.
126. Zhang, J.; Chen, W.; Xi, J.; Ji, Z. {001} Facets of anatase TiO2 show high photocatalytic selectivity. *Materials Letters* **2012,** *79*, 259-262.
127. Liu, B.; Huang, Y.; Wen, Y.; Du, L.; Zeng, W.; Shi, Y.; Zhang, F.; Zhu, G.; Xu, X.; Wang, Y. Highly dispersive {001} facets-exposed nanocrystalline TiO2 on high quality graphene as a high performance photocatalyst. *Journal of Materials Chemistry* **2012,** *22* (15).
128. Liu, S.; Yu, J.; Jaroniec, M. Tunable photocatalytic selectivity of hollow TiO2 microspheres composed of anatase polyhedra with exposed {001} facets. *J Am Chem Soc* **2010,** *132* (34), 11914-6.
129. Zhou, P.; Zhang, H.; Ji, H.; Ma, W.; Chen, C.; Zhao, J. Modulating the photocatalytic redox preferences between anatase TiO2 {001} and {101} surfaces. *Chem Commun (Camb)* **2017,** *53* (4), 787-790.
130. Pigeot-Rémy, S.; Dufour, F.; Herissan, A.; Ruaux, V.; Maugé, F.; Hazime, R.; Foronato, C.; Guillard, C.; Chaneac, C.; Durupthy, O. Bipyramidal anatase TiO2 nanoparticles, a highly efficient photocatalyst? Towards a better understanding of the reactivity. *Applied Catalysis B: Environmental* **2017,** *203*, 324-334.
131. Dufour, F.; Pigeot-Remy, S.; Durupthy, O.; Cassaignon, S.; Ruaux, V.; Torelli, S.; Mariey, L.; Maugé, F.; Chanéac, C. Morphological control of TiO2 anatase nanoparticles: What is the good surface property to obtain efficient photocatalysts? *Applied Catalysis B: Environmental* **2015,** *174*, 350-360.
132. Xiong, Z.; Luo, Y.; Zhao, Y.; Zhang, J.; Zheng, C.; Wu, J. C. Synthesis, characterization and enhanced photocatalytic CO 2 reduction activity of graphene supported TiO 2 nanocrystals with coexposed {001} and {101} facets. *Physical Chemistry Chemical Physics* **2016,** *18* (19), 13186-13195.
133. Cao, Y.; Li, Q.; Li, C.; Li, J.; Yang, J. Surface heterojunction between (001) and (101) facets of ultrafine anatase TiO2 nanocrystals for highly efficient photoreduction CO2 to CH4. *Applied Catalysis B: Environmental* **2016,** *198*, 378-388.
134. Liu, G.; Sun, C.; Yang, H. G.; Smith, S. C.; Wang, L.; Lu, G. Q.; Cheng, H. M. Nanosized anatase TiO2 single crystals for enhanced photocatalytic activity. *Chem Commun (Camb)* **2010,** *46* (5), 755-7.
135. Zheng, Z.; Huang, B.; Lu, J.; Qin, X.; Zhang, X.; Dai, Y. Hierarchical TiO2 microspheres: synergetic effect of {001} and {101} facets for enhanced photocatalytic activity. *Chemistry* **2011,** *17* (52), 15032-8.
136. Wang, W.; Fang, J.; Zhou, Y.; Zhang, W.; Lu, C. New insight on facet-dependent physicochemical properties of anatase TiO 2 nanostructures for efficient photocatalysis. *RSC Advances* **2016,** *6* (72), 67556-67564.
137. Cao, Y.; Zong, L.; Li, Q.; Li, C.; Li, J.; Yang, J. Solvothermal synthesis of TiO2 nanocrystals with {001} facets using titanic acid nanobelts for superior photocatalytic activity. *Applied Surface Science* **2017,** *391*, 311-317.

138. Kashchiev, D.; Vekilov, P. G.; Kolomeisky, A. B. Kinetics of two-step nucleation of crystals. *The Journal of chemical physics* **2005,** *122* (24), 244706.
139. Vekilov, P. G. Dense liquid precursor for the nucleation of ordered solid phases from solution. *Crystal Growth & Design* **2004,** *4* (4), 671-685.
140. Pan, W.; Kolomeisky, A. B.; Vekilov, P. G. Nucleation of ordered solid phases of proteins via a disordered high-density state: Phenomenological approach. *The Journal of chemical physics* **2005,** *122* (17), 174905.
141. Zhang, T. H.; Liu, X. Y. How does a transient amorphous precursor template crystallization. *Journal of the American Chemical Society* **2007,** *129* (44), 13520-13526.
142. Schöpe, H. J.; Bryant, G.; van Megen, W. Two-step crystallization kinetics in colloidal hard-sphere systems. *Physical review letters* **2006,** *96* (17), 175701.
143. Savage, J.; Dinsmore, A. Experimental evidence for two-step nucleation in colloidal crystallization. *Physical review letters* **2009,** *102* (19), 198302.
144. Tóth, G. I.; Pusztai, T.; Tegze, G.; Tóth, G.; Gránásy, L. Amorphous nucleation precursor in highly nonequilibrium fluids. *Physical review letters* **2011,** *107* (17), 175702.
145. Kuang, Q.; Wang, X.; Jiang, Z.; Xie, Z.; Zheng, L. High-energy-surface engineered metal oxide micro- and nanocrystallites and their applications. *Accounts of chemical research* **2013,** *47* (2), 308-318.
146. Huang, Z.; Geyer, N.; Werner, P.; De Boor, J.; Gösele, U. Metal - assisted chemical etching of silicon: a review. *Advanced materials* **2011,** *23* (2), 285-308.
147. Lin, H.-x.; Lei, Z.-c.; Jiang, Z.-y.; Hou, C.-p.; Liu, D.-y.; Xu, M.-m.; Tian, Z.-q.; Xie, Z.-x. Supersaturation-dependent surface structure evolution: From ionic, molecular to metallic micro/nanocrystals. *Journal of the American Chemical Society* **2013,** *135* (25), 9311-9314.
148. Ouyang, J.; Pei, J.; Kuang, Q.; Xie, Z.; Zheng, L. Supersaturation-controlled shape evolution of α-Fe2O3 nanocrystals and their facet-dependent catalytic and sensing properties. *ACS applied materials & interfaces* **2014,** *6* (15), 12505-12514.
149. Zhang, J.; Brehm, M.; Grydlik, M.; Schmidt, O. G. Evolution of epitaxial semiconductor nanodots and nanowires from supersaturated wetting layers. *Chemical Society Reviews* **2015,** *44* (1), 26-39.
150. Sun, L.; Zhao, Z.; Zhou, Y.; Liu, L. Anatase TiO 2 nanocrystals with exposed {001} facets on graphene sheets via molecular grafting for enhanced photocatalytic activity. *Nanoscale* **2012,** *4* (2), 613-620.
151. Xu, H.; Ouyang, S.; Li, P.; Kako, T.; Ye, J. High-active anatase TiO2 nanosheets exposed with 95%{100} facets toward efficient H2 evolution and CO2 photoreduction. *ACS applied materials & interfaces* **2013,** *5* (4), 1348-1354.
152. Chen, J. S.; Tan, Y. L.; Li, C. M.; Cheah, Y. L.; Luan, D.; Madhavi, S.; Boey, F. Y. C.; Archer, L. A.; Lou, X. W. Constructing hierarchical spheres from large ultrathin anatase TiO2 nanosheets with nearly 100% exposed (001) facets for fast reversible lithium storage. *Journal of the American Chemical Society* **2010,** *132* (17), 6124-6130.
153. Liu, B.; Aydil, E. S. Anatase TiO2 films with reactive {001} facets on transparent conductive substrate. *Chemical Communications* **2011,** *47* (33), 9507-9509.
154. Penn, R. L.; Banfield, J. F. Morphology development and crystal growth in nanocrystalline aggregates under hydrothermal conditions: Insights from titania. *Geochimica et cosmochimica acta* **1999,** *63* (10), 1549-1557.
155. Amano, F.; Yasumoto, T.; Prieto-Mahaney, O.-O.; Uchida, S.; Shibayama, T.; Ohtani, B. Photocatalytic activity of octahedral single-crystalline mesoparticles of anatase titanium (IV) oxide. *Chemical Communications* **2009,** (17), 2311-2313.
156. Dai, Y.; Cobley, C. M.; Zeng, J.; Sun, Y.; Xia, Y. Synthesis of anatase TiO2 nanocrystals with exposed {001} facets. *Nano letters* **2009,** *9* (6), 2455-2459.
157. Liu, G.; Yang, H. G.; Sun, C.; Cheng, L.; Wang, L.; Lu, G. Q. M.; Cheng, H.-M. Titania polymorphs derived from crystalline titanium diboride. *CrystEngComm* **2009,** *11* (12), 2677-2682.
158. Wu, N.; Wang, J.; Tafen, D. N.; Wang, H.; Zheng, J.-G.; Lewis, J. P.; Liu, X.; Leonard, S. S.; Manivannan, A. Shape-enhanced photocatalytic activity of single-crystalline anatase TiO2 (101) nanobelts. *Journal of the American Chemical Society* **2010,** *132* (19), 6679-6685.
159. Yang, H. G.; Sun, C. H.; Qiao, S. Z.; Zou, J.; Liu, G.; Smith, S. C.; Cheng, H. M.; Lu, G. Q. Anatase TiO2 single crystals with a large percentage of reactive facets. *Nature* **2008,** *453* (7195), 638-41.
160. Yang, H. G.; Liu, G.; Qiao, S. Z.; Sun, C. H.; Jin, Y. G.; Smith, S. C.; Zou, J.; Cheng, H. M.; Lu, G. Q. Solvothermal synthesis and photoreactivity of anatase TiO(2) nanosheets with dominant {001} facets. *J Am Chem Soc* **2009,** *131* (11), 4078-83.

161. Zhu, J.; Wang, S.; Bian, Z.; Xie, S.; Cai, C.; Wang, J.; Yang, H.; Li, H. Solvothermally controllable synthesis of anatase TiO 2 nanocrystals with dominant {001} facets and enhanced photocatalytic activity. *CrystEngComm* **2010,** *12* (7), 2219-2224.
162. Fang, W. Q.; Zhou, J. Z.; Liu, J.; Chen, Z. G.; Yang, C.; Sun, C. H.; Qian, G. R.; Zou, J.; Qiao, S. Z.; Yang, H. G. Hierarchical Structures of Single - Crystalline Anatase TiO2 Nanosheets Dominated by {001} Facets. *Chemistry-A European Journal* **2011,** *17* (5), 1423-1427.
163. Wen, C. Z.; Zhou, J. Z.; Jiang, H. B.; Hu, Q. H.; Qiao, S. Z.; Yang, H. G. Synthesis of micro-sized titanium dioxide nanosheets wholly exposed with high-energy {001} and {100} facets. *Chemical Communications* **2011,** *47* (15), 4400-4402.
164. Alivov, Y.; Fan, Z. A method for fabrication of pyramid-shaped TiO2 nanoparticles with a high {001} facet percentage. *The Journal of Physical Chemistry C* **2009,** *113* (30), 12954-12957.
165. Yu, J.; Xiang, Q.; Ran, J.; Mann, S. One-step hydrothermal fabrication and photocatalytic activity of surface-fluorinated TiO 2 hollow microspheres and tabular anatase single micro-crystals with high-energy facets. *CrystEngComm* **2010,** *12* (3), 872-879.
166. Zhang, D.; Li, G.; Yang, X.; Yu, J. C. A micrometer-size TiO2 single-crystal photocatalyst with remarkable 80% level of reactive facets. *Chem Commun (Camb)* **2009,** (29), 4381-3.
167. Ong, W. J.; Tan, L. L.; Chai, S. P.; Yong, S. T.; Mohamed, A. R. Highly reactive {001} facets of TiO2-based composites: synthesis, formation mechanism and characterization. *Nanoscale* **2014,** *6* (4), 1946-2008.
168. Zhao, Z.; Sun, Z.; Zhao, H.; Zheng, M.; Du, P.; Zhao, J.; Fan, H. Phase control of hierarchically structured mesoporous anatase TiO 2 microspheres covered with {001} facets. *Journal of Materials Chemistry* **2012,** *22* (41), 21965-21971.
169. Lee, W.-J.; Sung, Y.-M. Synthesis of anatase nanosheets with exposed (001) facets via chemical vapor deposition. *Crystal Growth & Design* **2012,** *12* (11), 5792-5795.
170. Roy, N.; Sohn, Y.; Pradhan, D. Synergy of low-energy {101} and high-energy {001} TiO(2) crystal facets for enhanced photocatalysis. *ACS Nano* **2013,** *7* (3), 2532-40.
171. Amano, F.; Prieto-Mahaney, O.-O.; Terada, Y.; Yasumoto, T.; Shibayama, T.; Ohtani, B. Decahedral Single-Crystalline Particles of Anatase Titanium(IV) Oxide with High Photocatalytic Activity. *Chemistry of Materials* **2009,** *21* (13), 2601-2603.
172. Cheng, X. L.; Hu, M.; Huang, R.; Jiang, J. S. HF-free synthesis of anatase TiO2 nanosheets with largely exposed and clean {001} facets and their enhanced rate performance as anodes of lithium-ion battery. *ACS Appl Mater Interfaces* **2014,** *6* (21), 19176-83.
173. Dinh, C. T.; Nguyen, T. D.; Kleitz, F.; Do, T. O. Shape-controlled synthesis of highly crystalline titania nanocrystals. *ACS Nano* **2009,** *3* (11), 3737-43.
174. Jun, Y.-w.; Casula, M. F.; Sim, J.-H.; Kim, S. Y.; Cheon, J.; Alivisatos, A. P. Surfactant-assisted elimination of a high energy facet as a means of controlling the shapes of TiO2 nanocrystals. *Journal of the American Chemical Society* **2003,** *125* (51), 15981-15985.
175. Joo, J.; Kwon, S. G.; Yu, T.; Cho, M.; Lee, J.; Yoon, J.; Hyeon, T. Large-Scale Synthesis of TiO2 Nanorods via Nonhydrolytic Sol− Gel Ester Elimination Reaction and Their Application to Photocatalytic Inactivation of E. c oli. *The Journal of Physical Chemistry B* **2005,** *109* (32), 15297-15302.
176. Wang, J.; Zhang, P.; Li, X.; Zhu, J.; Li, H. Synchronical pollutant degradation and H2 production on a Ti3+-doped TiO2 visible photocatalyst with dominant (0 0 1) facets. *Applied Catalysis B: Environmental* **2013,** *134*, 198-204.
177. Tian, F.; Zhang, Y.; Zhang, J.; Pan, C. Raman spectroscopy: a new approach to measure the percentage of anatase TiO2 exposed (001) facets. *The Journal of Physical Chemistry C* **2012,** *116* (13), 7515-7519.
178. Ye, L.; Liu, J.; Tian, L.; Peng, T.; Zan, L. The replacement of {101} by {010} facets inhibits the photocatalytic activity of anatase TiO2. *Applied Catalysis B: Environmental* **2013,** *134-135*, 60-65.
179. Barnard, A.; Curtiss, L. Prediction of TiO2 nanoparticle phase and shape transitions controlled by surface chemistry. *Nano letters* **2005,** *5* (7), 1261-1266.
180. Li, R.; Han, H.; Zhang, F.; Wang, D.; Li, C. Highly efficient photocatalysts constructed by rational assembly of dual-cocatalysts separately on different facets of BiVO4. *Energy Environ. Sci.* **2014,** *7* (4), 1369-1376.
181. Li, R.; Zhang, F.; Wang, D.; Yang, J.; Li, M.; Zhu, J.; Zhou, X.; Han, H.; Li, C. Spatial separation of photogenerated electrons and holes among {010} and {110} crystal facets of BiVO4. *Nat Commun* **2013,** *4*, 1432.

182. Liu, C.; Tong, R.; Xu, Z.; Kuang, Q.; Xie, Z.; Zheng, L. Efficiently enhancing the photocatalytic activity of faceted TiO 2 nanocrystals by selectively loading α-Fe 2 O 3 and Pt co-catalysts. *RSC Advances* **2016,** *6* (35), 29794-29801.
183. Meng, A.; Zhang, J.; Xu, D.; Cheng, B.; Yu, J. Enhanced photocatalytic H2-production activity of anatase TiO2 nanosheet by selectively depositing dual-cocatalysts on {101} and {001} facets. *Applied Catalysis B: Environmental* **2016,** *198*, 286-294.
184. Li, R.; Tao, X.; Chen, R.; Fan, F.; Li, C. Synergetic Effect of Dual Co - catalysts on the Activity of p - Type Cu2O Crystals with Anisotropic Facets. *Chemistry-A European Journal* **2015,** *21* (41), 14337-14341.
185. Bai, Y.; Ye, L.; Wang, L.; Shi, X.; Wang, P.; Bai, W. A dual-cocatalyst-loaded Au/BiOI/MnO x system for enhanced photocatalytic greenhouse gas conversion into solar fuels. *Environmental Science: Nano* **2016,** *3* (4), 902-909.
186. Mu, L.; Zhao, Y.; Li, A.; Wang, S.; Wang, Z.; Yang, J.; Wang, Y.; Liu, T.; Chen, R.; Zhu, J. Enhancing charge separation on high symmetry SrTiO 3 exposed with anisotropic facets for photocatalytic water splitting. *Energy & Environmental Science* **2016,** *9* (7), 2463-2469.
187. Gong, H.; Cao, Y.; Zhang, Y.; Zhang, Y.; Liu, K.; Cao, H.; Yan, H. The synergetic effect of dual co-catalysts on the photocatalytic activity of square-like WO 3 with different exposed facets. *RSC Advances* **2017,** *7* (31), 19019-19025.
188. Li, R.; Zhao, Y.; Li, C. Spatial distribution of active sites on a ferroelectric PbTiO3 photocatalyst for photocatalytic hydrogen production. *Faraday discussions* **2017,** *198*, 463-472.

## 3.1 Fermi level positions and induced band bending at single crystalline anatase (101) and (001) surfaces: Origin of the enhanced photocatalytic activity of facet engineered crystals.

Shun Kashiwaya conducted experiments, data analysis and preparation of the manuscript. Jan Morasch and Verena Streibel participated in the experimental work. Thierry Toupance, Wolfram Jaegermann and Andreas Klein participated in the discussions of the results and revised the manuscript.

ADVANCED ENERGY MATERIALS
www.advenergymat.de

# Fermi Level Positions and Induced Band Bending at Single Crystalline Anatase (101) and (001) Surfaces: Origin of the Enhanced Photocatalytic Activity of Facet Engineered Crystals

*Shun Kashiwaya, Thierry Toupance, Andreas Klein, and Wolfram Jaegermann**

**Single crystalline anatase is used to prepare well defined (001) and (101) surfaces in ultrahigh vacuum (UHV) in different states: sputtered, annealed, stoichiometric, and oxidized. The electronic properties of the well-defined surfaces are investigated by X-ray photoelectron spectroscopy and ultraviolet photoelectron spectroscopy after UHV transfer. The Fermi level of (001) facets for all applied surface conditions is lower than that of the (101) facets by 150–450 meV. The energy difference leads to a potential difference (band bending) at the interface between the (101) and (001) facets, resulting in the migration of photogenerated electrons and holes to different directions namely to the (101) and (001) facets, respectively. Photoelectron spectroscopy measurements clearly indicate for the first time that differences in the surface electronic structure and related potential of different facets explain a vectorial electron–hole pair separation to different reaction sites providing design criteria for enhanced photocatalysis.**

Titanium dioxide ($TiO_2$) has been intensively investigated for a range of applications such as solar energy conversion and photocatalysis already for decades.[1] Among different polymorphs, anatase $TiO_2$ is generally considered as a superior photocatalyst due to its longer carrier lifetime and higher electron mobility.[2] However, for homogeneous spherical particles the achieved quantum efficiencies of photochemical reactions are usually quite low.[3] Since the crystallographic orientation and the surface termination of metal oxides determine the electronic properties, there has been an increasing interest in facet engineered $TiO_2$ particles as well as in fundamental investigation on the different surfaces of single crystalline anatase.[3] For instance, Ohno et al.[4] discovered the selective deposition of Pt and $PbO_2$ on the specific orientations of rutile and anatase via photodeposition, indicating that the facets help in the separation of photoinduced electrons and holes. It was found that electrons tend to be transferred to the (101) facets, whereas the holes are driven to the (001) surfaces. This result suggests that anatase (101) surface provides the effective reduction site, whereas anatase (001) works as the oxidation site. Tachikawa et al.[5] investigated facet dependant photocatalysis on anatase with single-molecule fluorescence imaging and kinetic analysis by using redox-responsive fluorogenic dyes. On the single crystal of anatase coexposed with the (101) and (001) facets, the fluorogenic dyes are preferentially reduced on the (101) facet rather than the (001) facet. This finding confirms that photogenerated electrons preferentially migrate to and are trapped at the (101) facet. Such a charge carrier separation was observed for different metal oxides such as $Cu_2O$, $WO_3$, and $BiVO_4$.[3,6] Furthermore, based on the charge separation between different facets in the crystal, Li et al.[7] demonstrated a drastic enhancement of photocatalytic activities by selectively depositing reduction and oxidation cocatalysts onto the reductive and oxidative facets of $BiVO_4$ crystals. In summary, there is a strong need of deeper understanding of the mechanism of charge separation between different crystal facets.

Surface properties of the $TiO_2$ anatase have been studied by a number of experimental and theoretical investigations without providing a clear reason for different photocatalytic efficiencies.[8] However, the charge separation and trapping are conventionally explained by the different energy levels of different facets due to the surface atomic arrangement and coordination.[9] Recently, a first-principles calculation predicted that the Fermi level of the (001) facet is located at a lower energy level than that of the (101) facet.[9a] Thus, a so-called surface heterojunction would be formed between the (101) and (001) facets due to the original difference of their surface Fermi levels in a crystal exposed with both facets. As a result, photogenerated electrons and holes could preferentially migrate to the (101) and (001) facets, thereby exhibiting different photocatalytic activities on these facets. However, the Fermi level shown in the density of states is located near valence band maximum for the (101) and enters even into valence band for the (001) surface meaning that the (101) surface is a p-type semiconductor and

S. Kashiwaya, Prof. T. Toupance
Institut des Sciences Moléculaires
ISM UMR 5255 CNRS
Université de Bordeaux
351 Cours de la Libération F-33405 Talence Cédex, France
S. Kashiwaya, Prof. A. Klein, Prof. W. Jaegermann
Materials Science Department
Technische Universität Darmstadt
Otto Berndt Strasse 3, D-64287 Darmstadt, Germany
E-mail: jaegermann@surface.tu-darmstadt.de
The ORCID identification number(s) for the author(s) of this article can be found under https://doi.org/10.1002/aenm.201802195.

DOI: 10.1002/aenm.201802195

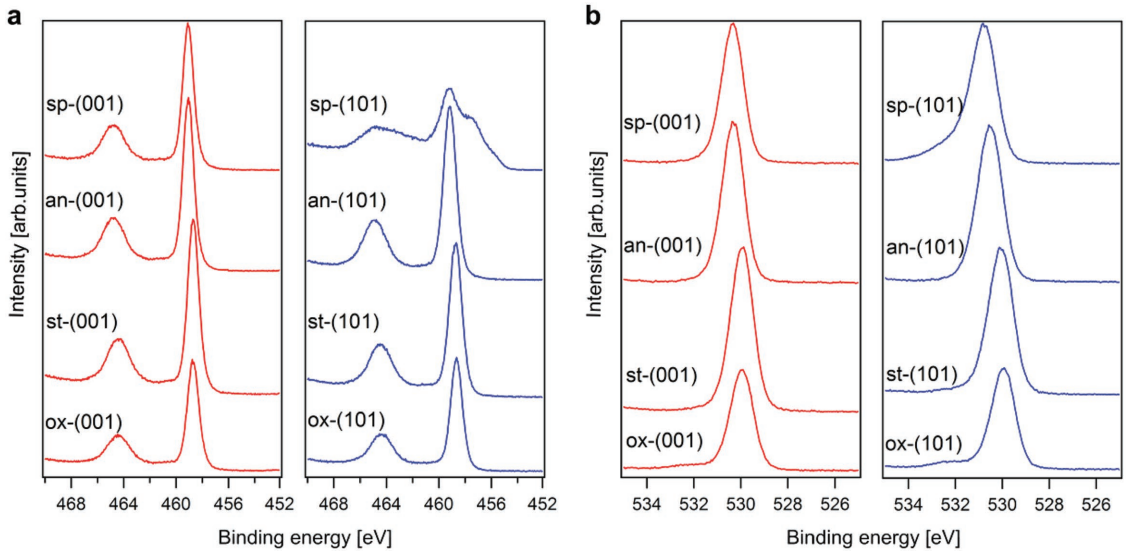


**Figure 1.** XP core level spectra of anatase (001) and (101) in different surface states. a) Ti2p and b) O1s core level emission for sputtered (st-(001) and st-(101)), annealed (an-(001) and an-(101)), stoichiometric (st-(001) and st-(101)), and oxidized (ox-(001) and ox-(101)).

the (001) surface is metallic although $TiO_2$ is considered as an insulator or a n-type semiconductor. This might be due to oversimplified approximations used during the calculation. However, this paper does not provide any details about the calculations, making this comparison of Fermi level positions questionable. In addition, a recent simulation[2] revealed that an excess electron at the (101) surface and aqueous interface would lead to water dissociation and get trapped into a stable surface $Ti^{3+}$-bridging OH complex, whereas the (001) surface is strongly repulsive for electrons and subsequently attracts holes. Thus, the origin of the role of the different facets has not been elucidated by experimental evidence and is still under debate. Although scanning tunnelling macroscopy studies have been intensively performed for single crystalline anatase,[10] detailed information on the surface electronic properties is sparse. One detrimental factor is the need to prepare well defined surface termination layers for the different surfaces without defects or adsorbates, which may strongly interfere with the precise evaluation of the electronic surface properties. Especially the amount of O vacancies and related $Ti3d^1$ surface states situated about 1 eV below the conduction band edge will strongly interfere with a detailed analysis of differences in the surface electronic properties.[8,11] Herein, we report on a systematic study of the electronic properties of single crystalline anatase (101) and (001) surfaces with various well-defined surface conditions by using X-ray photoelectron spectroscopy (XPS) and ultraviolet photoelectron spectroscopy (UPS). Our results help to enlighten the surface properties of facetted anatase $TiO_2$ crystals to conclude on the mechanism of charge separation based on intrinsic properties of anatase facets.

(101) and (001) surfaces are in situ prepared inside the vacuum chamber to expose different well-defined stoichiometries: sputtered (sp-(001) and sp-(101)), annealed (an-(001) and an-(101)), oxidized (ox-(001) and ox-(101)), and stoichiometric (st-(001) and st-(101)). As-is samples without any surface treatments show several contaminations such as carbon, calcium, silicon, and molybdenum and were treated by repeating the cycle of Ar ion sputtering and annealing in vacuum till the contamination disappears in XPS surface spectra, as shown in Figure S1 (Supporting Information). Fe contamination, which is the most relevant contamination in natural crystals,[12] was not found. Figure S2 (Supporting Information) shows sharp (1 × 1) low-energy electron diffraction (LEED) patterns for both an-(001) and an-(101), which were reoxidized and recrystallized after treated by cycles of Ar sputtering and annealing in ultrahigh vacuum (UHV). The LEED patterns for an-(001) and an-(101) were obtained for beam energies of 90.5 and 90.0 eV, respectively. It was reported that a two-domain (1 × 4) reconstruction was observed for the (001) surface when the surface was sputtered and annealed in UHV conditions or O background pressure.[13] In our work, the an-(001) does not form this reconstruction, since the lattice O was incorporated again by the O plasma treatment.[13a,14]

XP spectra of O1s and Ti2p core level for all prepared surface states are shown in **Figure 1**. The emission of Ti2p spectra for sp-(101) shows a strong low binding energy emission of $Ti^{3+}$ and $Ti^{2+}$ shifted to the main emission line of $Ti^{4+}$ by around 1.7 and 3.5 eV, respectively, while sp-(001) exhibits sharp symmetric main lines consisting of a $Ti^{4+}$ oxidation state. This indicates that the sp-(001) surface would contain much less O vacancies than the sp-(101) in agreement with literature data, as the (001) surface is extremely stable compared to the (101) surface.[15] The low binding energy shoulder related to defects for an-(101) was not observed after reoxidation by O plasma and recrystallization by annealing in vacuum for sp-(101). Although an-(001) and an-(101) are expected to contain low concentration of O vacancies due to annealing in vacuum at the elevated temperature, emissions related to O vacancies were not detected probably due to the limited resolution and surface sensitivity of XPS. The attenuated shoulder corresponding to $Ti^{3+}$ and the related emissions of $Ti^{3+}$ deep bandgap states (DGS) below the conduction band edge are detectable only by surface sensitive resonant photoelectron spectroscopy.[11,15a] Exposing an-(001) and an-(101) to an O plasma results in a shoulder emission

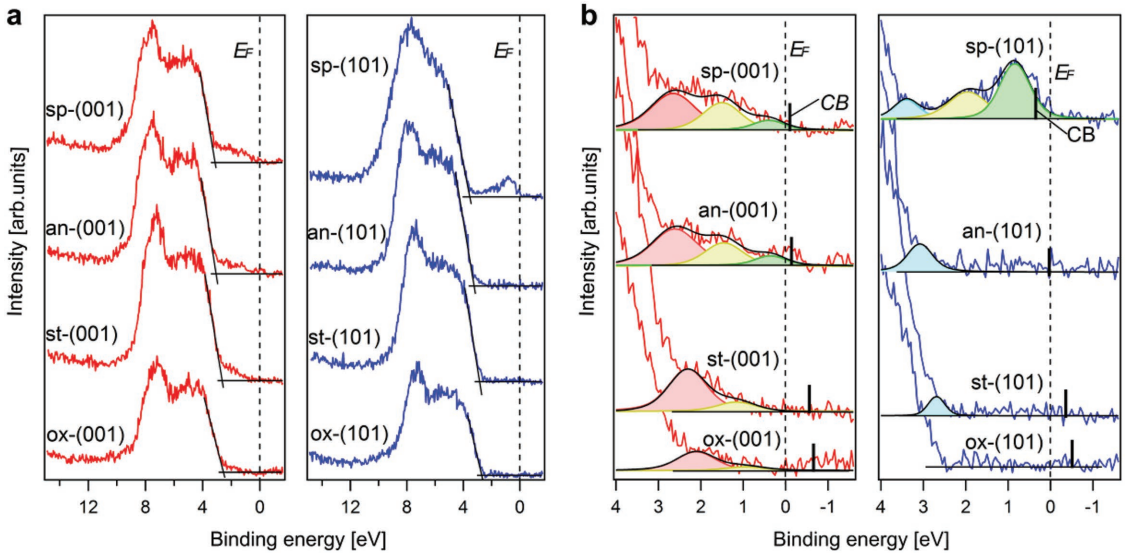


**Figure 2.** XP valence band spectra of anatase (001) and (101) in different surface states. a) Wide valence band region and b) its focused area of the bandgap region by a factor of 3 for sputtered (st-(001) and st-(101)), annealed (an-(001) and an-(101)), stoichiometric (st-(001) and st-(101)), and oxidized (ox-(001) and ox-(101)). The spectra in the bandgap region are combinations of VBSS (shaded magenda for (001) surface and shaded cyan for the (101) surface), DGS (shaded yellow), and SGS (shaded green).

at 3 eV higher than the main peak corresponding to Ti—O bonding. The shoulder might be attributed to mainly peroxo species and also to bridging dimers. The Ti atom on the surface is prone to form peroxo complexes with excited O atoms from the O plasma.[16] Furthermore, peroxo species on the surface were found to transform to a so-called bridging dimer at the lattice site via interaction with surface or subsurface O vacancies.[10a,17] St-(001) and st-(101) show no shoulder emission after annealing in vacuum at 473 K, which indicates the removal of the surface peroxo species from the ox-(001) and ox-(101) surfaces.

XP and UP valence band spectra for all prepared surface states are shown in **Figure 2** and Figure S3 (Supporting Information), respectively. The XP valence band spectra show at a first glance the typical valence band emission of $TiO_2$ bulk material with the typical double layer structure of the O2p $\pi$ and $\sigma$ bonding states at binding energy of about 5 and 8 eV, respectively.[15a] A more detailed inspection, however, indicates additional emissions of different intensity in the bandgap region of XPS and UPS depending on the surface treatment. The sputtered $TiO_2$ surfaces show the well-known Ti3d$^1$ emission lines in the bandgap region. It is accepted that the so-called bandgap surface state (BGS) would form due to occupied Ti 3d states on $Ti^{3+}$ sites near the O vacancy sites on the surface, but also due to $Ti^{3+}$ interstitial states in the subsurface region.[11,15a,18] BGS consists of shallow gap states (SGS) and DGS located at 0.5 and 1.6 eV below conduction band minimum, respectively,[11b] even though recent calculations using screened exchange functional, which gives accurate bandgaps and correct localization of charge near vacancies, implied that O vacancies would introduce a gap state above conduction band minimum for the (001) and (101) surfaces.[19] DGS are conventionally assigned to excess electrons localized on $Ti^{3+}$ interstitial and also Ti atoms near O vacancies.[11b,20] SGS would be originated from different factors. First, excess electrons at step edges or imperfect structures on the (101) surface contribute to form SGS and its intensity could be pronounced by increased amount of O vacancies.[11b] In addition, $Ti^{3+}$ interstitial and O vacancy also contribute to SGS. Remaining excess electrons produced by the formation of $Ti^{3+}$ interstitial and O vacancy and exceeding the number of one electron per d bandgap state would be delocalized on lattice Ti atoms due to electron–electron correlation, which are the components of the $TiO_6$ octahedra near the defect sites, and thus result in the shallow energy level near the conduction band edge.[20] However, the contribution of O vacancy to SGS is negligible compared to the effect of $Ti^{3+}$ interstitial.

(001) and (101) surfaces exhibit different distribution of DGS and SGS as shown in **Figure 3** derived from XP valence band spectra in Figure 2. The peaks of XP valence band region were fitted with Voigt functions using Gaussian and Lorentzian mixed line shapes. For the fits, we have assumed three contributions to the bandgap emissions including the DGS and SGS states and a so called valence band surface state (VBSS). The SGS and DGS states are well-established from experimental and theoretical studies,[11,15a,18] while the latter, which is of O 2p character, has been reported in theoretical studies only.[19] For estimating the concentration of the different states, we have used the XPS data as these are mostly determined by the initial state density, whereas for He UPS data final state density of states cannot be neglected for intensity analysis. Although the emissions in the bandgap region in the XP valence band spectra (Figure 2b) are rather noisy, the different intensities of the gap states can clearly be discerned from the background intensity, which is achieved for the annealed, stoichiometric, and oxidized (101) surface. In any case, the different intensities of the involved gap states are also reflected in the UP spectra, which are shown in Figure S3, Supporting Information. Regardless of surface conditions, DGS of the (001) surface is significantly larger than that of the (101) surface for XPS

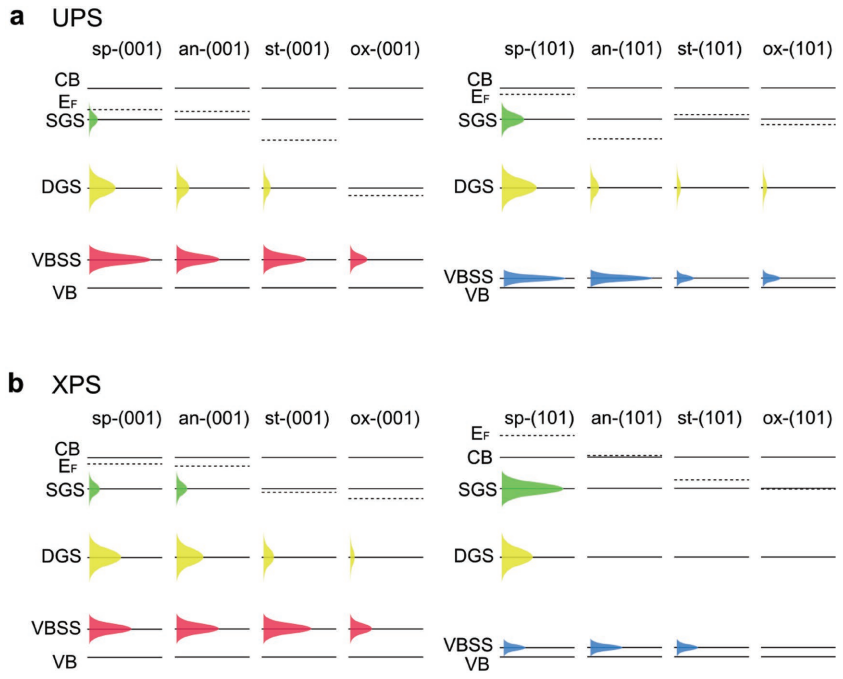


**Figure 3.** Distribution of SGS, DGS, and VBSS of anatase (001) and (101) in different surface states. Distribution derived from a) UPS and b) XPS for sputtered (st-(001) and st-(101)), annealed (an-(001) and an-(101)), stoichiometric (st-(001) and st-(101)), and oxidized (ox-(001) and ox-(101)) surfaces.

and however has a similar intensity to that of the (101) surface for UPS. UPS is more surface sensitive allowing to measure a shallow surface depth of 1–2 nm, whereas the X-ray reaches to 4–5 nm as an inelastic mean free pass of UPS is shorter than that of XPS. Therefore, this difference of DGS indicates that the defects ($Ti^{3+}$ interstitial and/or O vacancy) are located below the surface to deep subsurface or bulk for the (001) surface while they are situated on the surface or only at a shallow subsurface for the (101) surface. On the other hands, SGS of sp-(101) is intense compared with sp-(001) for both XPS and UPS. This implies that excess electrons of the (001) surface induced by Ar ion sputtering and annealing are largely localized on $Ti^{3+}$ interstitial or Ti atoms neighbouring O vacancies while those of the (101) surface are not only localized on the defects sites, but also widely delocalized on lattice Ti atoms.

The VBSS is located close to the valence and edge especially for the (001) surfaces. Comparing the energetic position of this feature, its relative intensity in the XP versus UP valence band spectra to recent surface electronic structure versus bulk electronic structure calculations, we assign this feature to the modified density of states (DOS) distribution of the (001) and (101) surface versus the bulk DOS. In the former case, the (001) surface, a thin surface layer with a reduced gap and energetically upward shifted O 2p states are formed, which for XPS will lead to a shoulder in the valence band edge due to increased depth (≈2 nm) and for UPS to a shifted band edge position due to reduced surface sensitivity (≈0.5 nm). DGS and SGS as well as VBSS of the (001) surface for XPS gradually attenuate with decrease of the Fermi level position but still remain even after O plasma treatment. By contrast, DGS and SGS of sp-(101) for XPS disappear immediately after reoxidation by O plasma treatment and subsequent annealing in vacuum. Defects in a deep subsurface position of the (001) surface are rather stable and tend to remain even in the oxidative atmosphere while those of the (101) surface could be repaired by O molecules or peroxo species even though it is expected that O radical of the O plasma cannot penetrate the surface and reach to deep subsurface unlike Ar plasma. Setvín et al. demonstrated that $O_2$ molecules on the surface react with subsurface O vacancies of the (101) surface.[10a,17] $O_2$ molecules are adsorbed as superoxo species at fivefold-coordinated Ti sites on the surface, transform into peroxo species, and finally are inserted into an anion surface lattice site as a bridging dimer via interaction with surface O vacancy as well as subsurface O vacancy.

As discussed above, we have achieved well-controlled different surface conditions with different distribution of defects/surface states for anatase (001) and (101) surfaces. Considering different surface states is a precondition for comparing the dependence of Fermi level on surface orientation. The Fermi level positions ($E_{VBM} - E_F$) with respect to the valence band maximum (VBM) were determined by applying a linear extrapolation of the valence band emission edge. The determination of the Fermi level from the XP valence band spectra is hardly affected by the distribution of surface/gap states due to their low intensity. This is confirmed by the shifts of the Ti and O binding energies, which follow the same order and are of similar magnitude (see **Table 1**). Fermi level positions obtained from XP valence band spectra are summarized in Table 1. For both the (001) and (101) facets, the order of Fermi level positions is ox-$TiO_2$ < st-$TiO_2$ < an-$TiO_2$ < sp-$TiO_2$ and is related to the different surface electronic structures due to the changed concentration of the different surface states of the different surfaces leading to band bending (space charge layer) effects. The variation range in the Fermi level, which are 560 and 860 meV for the (001) and (101) surfaces, respectively, was achieved by controlling surface terminations and the amount of intrinsic defects of $Ti^{3+}$ interstitial and O vacancy. As $Ti^{3+}$ interstitial and O vacancy give rise to the localized impurity level below the lower end of the conduction band,

**Table 1.** Binding energy of O1s and Ti2$p_{3/2}$ and Fermi level positions ($E_{VBM} - E_F$) of the (001) and (101) facets.

| | O1s [eV] | | Ti2$p_{3/2}$ [eV] | | $E_{VBM} - E_F$ [eV] | |
|---|---|---|---|---|---|---|
| | 001 | 101 | 001 | 101 | 001 | 101 |
| Sputtered | 530.35 | 530.81 | 459.08 | 459.21 | 3.10 | 3.55 |
| Annealed | 530.33 | 530.52 | 459.07 | 459.17 | 3.06 | 3.23 |
| Stoichiometric | 529.95 | 530.07 | 458.70 | 458.73 | 2.64 | 2.84 |
| Oxidized | 529.93 | 529.93 | 458.64 | 458.69 | 2.54 | 2.69 |

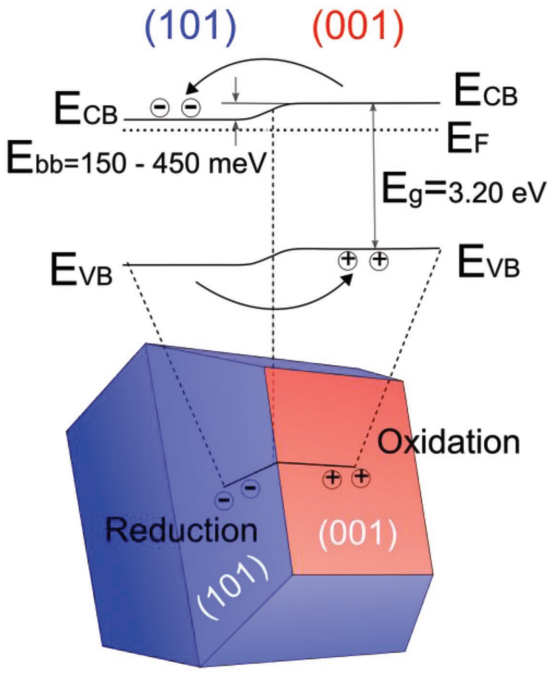


**Figure 4.** Scheme of charge separation on the anatase crystal coexposed with the (101) and (001) facets. Band alignment at the interface of the (101) and (001) facet was described based on the obtained Fermi level difference between these facets.

the amount of these intrinsic defects as well as the surface termination is directly related to the Fermi level position.[21]

Most importantly, we consistently found a difference in the Fermi level positions between the (001) and (101) facets. As shown in Table 1, the Fermi level position of the (001) facet is lower than that of the (101) facet by 150–450 meV for any surface conditions. The work function $\phi$ of st-(101) and st-(001) were determined to be 5.23 and 5.35 eV, respectively, from the binding energies of the secondary electron edge $E_{SE}$ according to $\Phi = h\nu - E_{SE}$. Thus, we conclude that the difference of the Fermi level position between the (001) and (101) facets originates from the difference in their work function. This difference in the Fermi level positions leads to a space charge layer between the interfaces of the two facets as schematically shown in **Figure 4** as a result of electronic equilibrium formation. As a consequence, photogenerated electrons and holes preferentially migrate to the (101) and (001) surface, respectively, which thus function as effective reaction sites for reduction and oxidation reactions, respectively. We do not have a direct measure of the Fermi level position inside the crystal and therefore cannot exclude an additional space charge layer from the surface into the bulk. But as $TiO_2$ is known to be n-doped from experimental transport measurements, such additional space charge effects will not strongly affect our conclusion on the orientation dependant surface potentials.

This difference of the Fermi level position between the (001) and (101) facets can be mainly related to a difference in the formation energy of O vacancies for the two facets. Density functional theory (DFT) calculation[15b,19] predicted that the surface and subsurface of the (101) facet require lower formation energy to create O vacancies than the (001) facet, which is in good agreement with experimental investigation.[15a] Therefore, the concentration of O vacancies on the (101) facet is higher and thus the Fermi level position on the (101) facet is raised higher by the defect impurity level than on the (001) facet. In addition, Li et al.[19] found that O vacancies are shallow donors with a donor level even above the conduction band minimum at the (101) surface, whereas the donor level at the (001) surface is slightly lower in energy than the calculated gap. Therefore, the (001) surface has a lower electron concentration and thus a lower Fermi energy than the (101) surface. The lower Fermi level position of the (001) surface is attributed not only to the lower formation energy of O vacancies, but also to its lower donor level. Although perfectly oxidized and stoichiometric surfaces would nominally contain no O vacancies on the surface, real samples under operation condition in UHV but also X-ray irradiation during XPS measurements will possess O vacancies on these surfaces, validating the difference in Fermi level positions.

The difference in Fermi level positions is found also to exist even on defect-free clean surfaces. It was reported based on a theoretical calculation that the top surfaces of the (001) and (101) facets have surface states above the bulk VBM and below the bulk conduction band minimum. (CBM).[19] The surface states of the (001) facet near the bulk CBM are lower than those of the (101) facet. Therefore, the Fermi level at the (001) surface is lower than that at the (101) surface even at defect-free conditions. The surface states near VBM for the (001) and (101) surface are located at 0.2–0.7 eV above VBM and at 0.3 eV up to VBM, respectively. These surface states near VBM were observed in XP and UP valence band spectra, as shown in Figure 2 and Figure S3 (Supporting Information), respectively, while those near CBM are rather weak as expected from calculation and could not be detected by XPS and UPS. The relative intensity of the surface states is shown in addition to SGS, DGS, and Fermi level from XP spectra in Figure 3. Regardless of surface condition, the surface state of the (001) surface is intense compared to that of the (101) surface in good agreement with calculation in literature.[19] The intensity of surface states for ox-(001) and ox-(101) is decreased, as these surfaces are covered by surface peroxo species. It is noted that the surface states of the (101) surface partially overlap with the VBM, thus resulting in underestimating the Fermi level position at a lower position than the actual value inside the bulk of the crystal.

So far, a large percentage of (001) facets in anatase photocatalysts has attracted significant attention over the last decade, as facets with high surface energy were expected to show high photocatalytic activities. The related importance of the (101) facets thus has been underestimated. Our result indicates that the both (001) and (101) facets are equally important in the photocatalytic performance, since a simultaneous presence of the two facets forms the energy junction which leads to a vectorial charge carrier separation of electron–hole pears and subsequently each facet has different roles in the photocatalytic reactions. It can also be expected that the deposition of different but correctly chosen cocatalysts with appropriate contact and catalytic properties on the different facets will further improve the photocatalytic properties.

In conclusion, we have compared the electronic properties of single crystal anatase (001) and (101) facet with various surface conditions: sputtered, annealed, oxidized, and stoichiometric.

The Fermi level position of the (001) and (101) facet in anatase was effectively manipulated in a variation range of 560 and 860 meV, respectively. Regardless of the different surface conditions, the Fermi level of (001) facets is always lower than that of the (101) facets by 150–450 meV due to the effect of surface states of different origin and concentrations. The energy difference forms an interfacial energy junction at the interface of the (101) and (001) facets, resulting in the spatial charge separation and enhancing the photocatalytic activities. Our results of XPS and UPS measurements of well-defined single crystal surfaces do not only reveal the intrinsic mechanism of the charge separation and different photocatalytic reaction sites in the anatase single crystal for the first time, but also suggest the same phenomena to be operative in other semiconductor photocatalysts as well. In addition, this study provides design rules for further enhancing the photocatalytic efficiencies. The preparation of "Janus" type structures by depositing cocatalysts of different work function and different catalytic selectivity will provide specifically designed nano-sized heterojunction photocatalysts with improved performances.[21]

## Experimental Section

Single crystals of anatase with epi-polished (101) and (001) surfaces with a specified surface roughness of less than a lattice constant were purchased from SurfaceNet GmbH (Rheine, Germany). The size of substrates is $5 \times 5 \times 1$ mm$^3$. The surface orientation has been confirmed by low energy electron diffraction (see Figure S2, Supporting Information). In addition to the as-is surfaces with contamination from air and polishing, unreconstructed (101) and (001) surfaces are in situ prepared inside the vacuum chamber to expose different well-defined stoichiometries: sputtered (sp-(001) and sp-(101)), annealed (an-(001) and an-(101)), oxidized (ox-(001) and ox-(101)), and stoichiometric (st-(001) and st-(101)). Sample preparations and measurements were carried out in the Darmstadt integrated system for materials research (Daisy-Mat)[22] equipped with a multitechnique surface analysis system Physical Electronics PHI 5700 capable of XPS and UPS, which is connected to different sample preparation chambers without breaking vacuum. The sputtered surfaces (sp-(001) and sp-(101)) were prepared by repeated cycles of $Ar^+$ ion sputtering with an energy of 1 keV for 15 min and annealing in UHV conditions at 873 K for 30 min until no remaining emissions from contaminations were observed by XPS. Although this procedure has been conventionally accepted to prepare clean surfaces of single crystal $TiO_2$,[8,23] Ar sputtering not only results in a highly reduced surface and thus leads to the formation of O vacancies and $Ti^{3+}$ surface states, but also partially destroys the crystallinity of the surface and introduces an amorphous phase.[12] The O vacancy concentration for the (101) and (001) surface prepared by the procedure is estimated to be $7 \pm 2$ and $1 \pm 2\%$, respectively.[15a] Therefore, the sputtered surface was oxidized by an O plasma at room temperature in an atmosphere of $7.5 \times 10^{-5}$ mbar $O_2$ for 15 min to reoxidized the surface, followed by annealing at 873 K in UHV to recrystallize the surface. This surface in a slight reduced state is referred to as an-(001) and an-(101). LEED measurements were performed with BDL 800 IR-LMX for the an-(101) and an-(001). Here the O plasma was selected to replenish the lattice O instead of annealing in $O_2$ atmosphere, which has been frequently used for oxidation, as the annealing procedure could form additional incomplete reconstructions.[24] It may also lead to iron oxide surface contaminations, as at elevated temperatures Fe surface segregation, which is a typical contamination of natural anatase crystals, may be triggered.[12] In addition, atomic O in the O plasma is more oxidative than a molecular $O_2$ during annealing in O atmosphere.[25] The an-(001) and an-(101) surfaces were treated with an O plasma at the same condition mentioned above without subsequent annealing and the resulting surfaces are referred to as ox-(001) and ox-(101). Finally, the stoichiometric surfaces, which are referred to as st-(001) and st-(101), were prepared by removing O atoms by annealing ox-(001) and ox-(101) in UHV condition at 473 K for 20 min.[26] The preparation procedure for the above different surfaces is described in Figure S4 (Supporting Information).

Characterization of the prepared surfaces were carried out in the Darmstadt integrated system for materials research (Daisy-Mat) equipped with a multitechnique surface analysis system Physical Electronics PHI 5700 capable of XPS and UPS. The XPS spectra were recorded with monochromatic Al K radiation at an emission angle of 45° and a pass energy of 5.85 eV, which gives a total energy resolution of 0.4 eV, as determined from the Gaussian broadening of the Fermi edge of a sputter-cleaned Ag sample. Binding energies of core levels and valence band maximum $E_{VB}$ can be determined with accuracies of 50 and 100 meV, respectively. For the determination of work function and ionization potentials, UPS spectra were recorded in normal emission with He I radiation ($h\nu = 21.2$ eV) from a He discharge lamp and a negative sample bias of 4.0 V. The total energy resolution is 0.2 eV. No charging problems were observed during the XPS and UPS measurements. Obtained binding energies were calibrated by the Fermi level energy of a sputter-cleaned Ag sample. Hence, all the binding energies are given with respect to the calibrated Fermi level set to 0 eV.

## Supporting Information

Supporting Information is available from the Wiley Online Library or from the author.

## Acknowledgements

The authors would like to thank Andreas Hajduk and Stephan Wagner for their assistance for performing the LEED measurements. This work was partly supported by the Erasmus Mundus Joint Doctoral program International Doctoral School in Functional Materials for Energy, Information Technology, and Health (Shun Kashiwaya fellowship) and the French-German University (UFA Doctoral College in Functional Materials for Energy and Information Technology) and was carried out within the framework of EMMI (European Multifunctional Material Institute).

## Conflict of Interest

The authors declare no conflict of interest.

## Keywords

anatase facet engineered photocatalysis, facet electronic structure, facet induced vectorial charge carrier separation, photoelectron spectroscopy

Received: July 16, 2018
Revised: September 12, 2018
Published online:

[1] a) F. Giordano, A. Abate, J. P. Correa Baena, M. Saliba, T. Matsui, S. H. Im, S. M. Zakeeruddin, M. K. Nazeeruddin, A. Hagfeldt, M. Graetzel, *Nat. Commun.* **2016**, *7*, 10379; b) M. G. Walter, E. L. Warren, J. R. McKone, S. W. Boettcher, Q. Mi, E. A. Santori, N. S. Lewis, *Chem. Rev.* **2010**, *110*, 6446; c) A. L. Linsebigler, G. Lu, J. T. Yates, *Chem. Rev.* **1995**, *95*, 735.

[2] S. Selcuk, A. Selloni, *Nat. Mater.* **2016**, *15*, 1107.
[3] G. Liu, J. C. Yu, G. Q. Lu, H. M. Cheng, *Chem. Commun.* **2011**, *47*, 6763.
[4] T. Ohno, K. Sarukawa, M. Matsumura, *New J. Chem.* **2002**, *26*, 1167.
[5] T. Tachikawa, S. Yamashita, T. Majima, *J. Am. Chem. Soc.* **2011**, *133*, 7197.
[6] a) L. Zhang, J. Shi, M. Liu, D. Jing, L. Guo, *Chem. Commun.* **2014**, *50*, 192; b) S. Wang, H. Chen, G. Gao, T. Butburee, M. Lyu, S. Thaweesak, J.-H. Yun, A. Du, G. Liu, L. Wang, *Nano Energy* **2016**, *24*, 94; c) R. Li, F. Zhang, D. Wang, J. Yang, M. Li, J. Zhu, X. Zhou, H. Han, C. Li, *Nat. Commun.* **2013**, *4*, 1432.
[7] R. Li, H. Han, F. Zhang, D. Wang, C. Li, *Energy Environ. Sci.* **2014**, *7*, 1369.
[8] U. Diebold, *Surf. Sci. Rep.* **2003**, *48*, 53.
[9] a) J. Yu, J. Low, W. Xiao, P. Zhou, M. Jaroniec, *J. Am. Chem. Soc.* **2014**, *136*, 8839; b) L. Ye, J. Liu, L. Tian, T. Peng, L. Zan, *Appl. Catal., B* **2013**, *134–135*, 60.
[10] a) M. Setvin, U. Aschauer, P. Scheiber, Y. F. Li, W. Hou, M. Schmid, A. Selloni, U. Diebold, *Science* **2013**, *341*, 988; b) M. Setvin, X. Hao, B. Daniel, J. Pavelec, Z. Novotny, G. S. Parkinson, M. Schmid, G. Kresse, C. Franchini, U. Diebold, *Angew. Chem., Int. Ed.* **2014**, *53*, 4714.
[11] a) T. Mayer, K. Schwanitz, B. Kaiser, A. Hajduk, M. V. Lebedev, W. Jaegermann, *J. Electron Spectrosc. Relat. Phenom.* **2017**, *221*, 116; b) P. Reckers, M. Dimamay, J. Klett, S. Trost, K. Zilberberg, T. Riedl, B. A. Parkinson, J. Brötz, W. Jaegermann, T. Mayer, *J. Phys. Chem. C* **2015**, *119*, 9890.
[12] M. Setvín, B. Daniel, V. Mansfeldova, L. Kavan, P. Scheiber, M. Fidler, M. Schmid, U. Diebold, *Surf. Sci.* **2014**, *626*, 61.
[13] a) G. S. Herman, M. R. Sievers, Y. Gao, *Phys. Rev. Lett.* **2000**, *84*, 3354; b) G. S. Herman, Y. Gao, T. T. Tran, J. Osterwalder, *Surf. Sci.* **2000**, *447*, 201.
[14] R. Hengerer, B. Bolliger, M. Erbudak, M. Grätzel, *Surf. Sci.* **2000**, *460*, 162.
[15] a) A. Thomas, W. Flavell, A. Mallick, A. Kumarasinghe, D. Tsoutsou, N. Khan, C. Chatwin, S. Rayner, G. Smith, R. Stockbauer, *Phys. Rev. B* **2007**, *75*, 035105; b) H. Cheng, A. Selloni, *Phys. Rev. B* **2009**, *79*, 092101.
[16] E. Yesodharan, M. Grätzel, *Helv. Chim. Acta* **1983**, *66*, 2145.
[17] M. Setvin, B. Daniel, U. Aschauer, W. Hou, Y. F. Li, M. Schmid, A. Selloni, U. Diebold, *Phys. Chem. Chem. Phys.* **2014**, *16*, 21524.
[18] a) S. Kodaira, Y. Sakisaka, T. Maruyama, Y. Haruyama, Y. Aiura, H. Kato, *Solid State Commun.* **1994**, *89*, 9; b) E. Finazzi, C. Di Valentin, G. Pacchioni, A. Selloni, *J. Chem. Phys.* **2008**, *129*, 154113.
[19] H. Li, Y. Guo, J. Robertson, *J. Phys. Chem. C* **2015**, *119*, 18160.
[20] a) B. J. Morgan, G. W. Watson, *J. Phys. Chem. C* **2010**, *114*, 2321; b) E. Finazzi, C. Di Valentin, G. Pacchioni, *J. Phys. Chem. C* **2009**, *113*, 3382; c) G. Mattioli, F. Filippone, P. Alippi, A. Amore Bonapasta, *Phys. Rev. B* **2008**, *78*, 241201.
[21] a) M. T. Uddin, Y. Nicolas, C. Olivier, T. Toupance, L. Servant, M. M. Muller, H. J. Kleebe, J. Ziegler, W. Jaegermann, *Inorg. Chem.* **2012**, *51*, 7764; b) M. T. Uddin, Y. Nicolas, C. Olivier, T. Toupance, M. M. Müller, H.-J. Kleebe, K. Rachut, J. Ziegler, A. Klein, W. Jaegermann, *J. Phys. Chem. C* **2013**, *117*, 22098; c) J. Yang, D. Wang, H. Han, C. Li, *Acc. Chem. Res.* **2013**, *46*, 1900.
[22] D. Ensling, A. Thißen, Y. Gassenbauer, A. Klein, W. Jaegermann, *Adv. Eng. Mater.* **2005**, *7*, 945.
[23] S. Wendt, P. T. Sprunger, E. Lira, G. K. Madsen, Z. Li, J. O. Hansen, J. Matthiesen, A. Blekinge-Rasmussen, E. Laegsgaard, B. Hammer, F. Besenbacher, *Science* **2008**, *320*, 1755.
[24] M. Li, W. Hebenstreit, U. Diebold, M. A. Henderson, D. R. Jennison, *Faraday Discuss.* **1999**, *114*, 245.
[25] C. C. Wu, C. I. Wu, J. C. Sturm, A. Kahn, *Appl. Phys. Lett.* **1997**, *70*, 1348.
[26] a) D. Klissurski, K. Hadjiivanov, M. Kantcheva, L. Gyurova, *J. Chem. Soc., Faraday Trans.* **1990**, *86*, 385; b) M. Iwamoto, Y. Yoda, N. Yamazoe, T. Seiyama, *J. Phys. Chem.* **1978**, *82*, 2564.

ADVANCED ENERGY MATERIALS

# Supporting Information

for *Adv. Energy Mater.,* DOI: 10.1002/aenm.201802195

# Fermi Level Positions and Induced Band Bending at Single Crystalline Anatase (101) and (001) Surfaces: Origin of the Enhanced Photocatalytic Activity of Facet Engineered Crystals

*Shun Kashiwaya, Thierry Toupance, Andreas Klein, and Wolfram Jaegermann**

# Supporting Information

**Title: Fermi level positions and induced band bending at single crystalline anatase (101) and (001) surfaces: Origin of the enhanced photocatalytic activity of facet engineered crystals.**

*Shun Kashiwaya, Thierry Toupance, Andreas Klein, Wolfram Jaegermann**

Surface contamination:

There were contaminations of various elements such as carbon, calcium, silicon, and molybdenum detected by XPS for both (001) and (101) single crystalline surfaces before cleaning by repeated cycles of $Ar^+$ ion sputtering and annealing in UHV as shown in Figure S1. Carbon is a typical contamination, which originates from air. Calcium and silicon would come from a remaining polishing suspension for chemical mechanical planarization, which is generally employed to obtain smooth surface topography. An origin of molybdenum is not clear, but this might be due to our annealing chamber where samples containing molybdenum were processed. Although iron is a typical contamination of natural anatase crystals and would be situated not only on the surface, but also in bulk, it was not detected by XPS. The cleaning procedure removed the contaminations while it slightly introduced argon as shown in Figure S1. However, an effect of argon is negligible as LEED images shown in figure S2 show clear patters, which can be observed for only well-oriented clean surfaces.

Valence band spectra of UPS:

An original valence band edge largely overlaps with valence band surfaces states in UPS as shown in Figure S3 compared to those of XPS as shown in Figure 2, causing a determination of VBM in UPS more complicated. Thus, the exploited values from UPS is quantitatively less

reliable than that from XPS, but qualitative comparison should be still valid as the binding energy of the two main emissions around 5 and 8 eV follow the shift of VBM.

Scheme of surface treatment steps

The experimental scheme of the different to preparation steps which were applied to obtain well defined surface terminations are summarized in Figure S4. Details are given in the Experimental Section of the main paper.

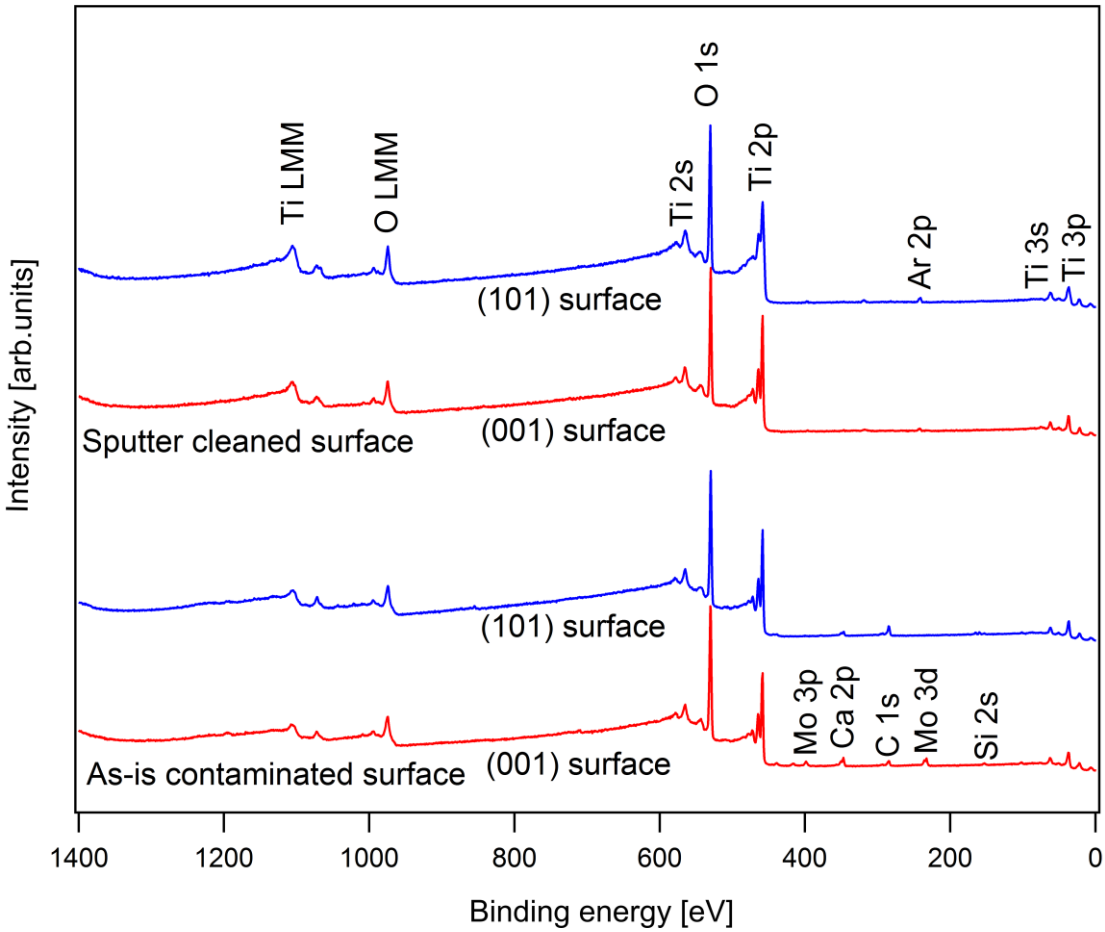


**Figure S1. Survey spectra of as-is contaminated and cleaned surfaces.** The cleaned surfaces were obtained by repeating the cycle of Ar sputtering and annealing in UHV.

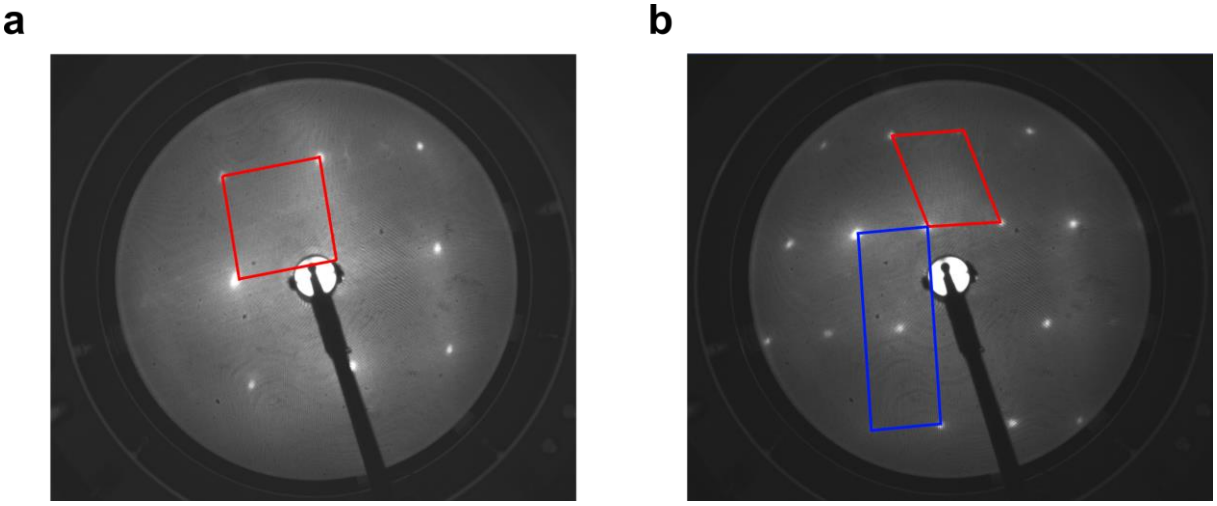


**Figure S2**. **Unreconstructed ($1 \times 1$) LEED patterns**. **a,b**, an-(001) (**a**) and an-(101) surface (**b**) for beam energies of 90.5 and 90.0 eV. (red: primitive unit cell and blue:centered unit cell)

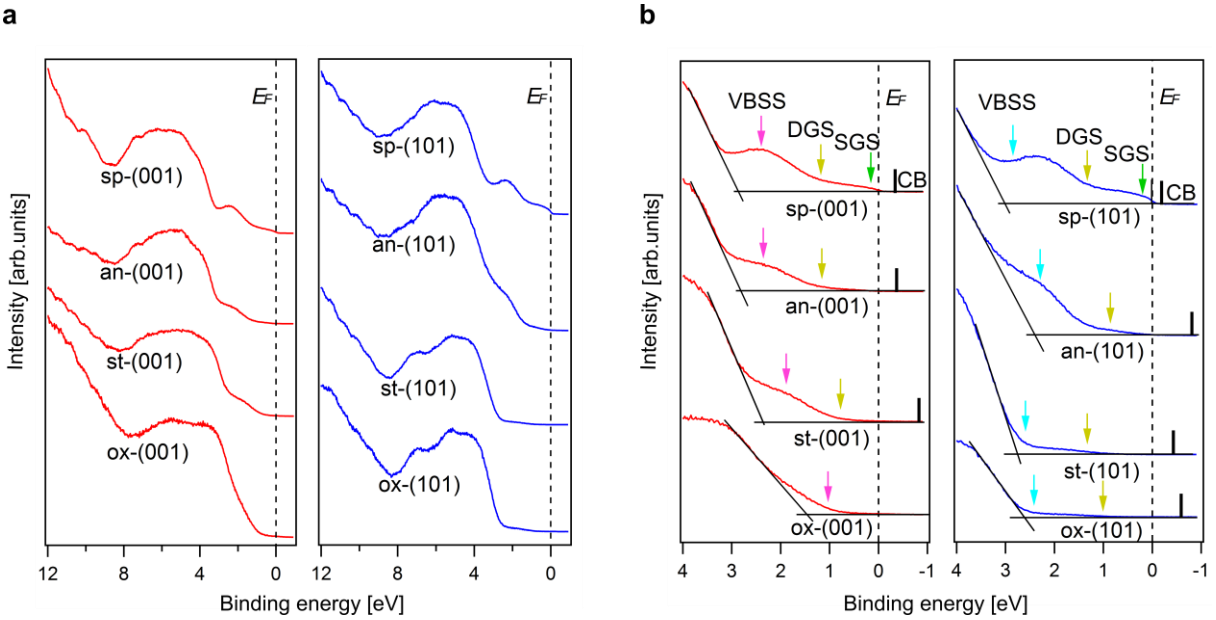


**Figure S3**. **UP valence band spectra of anatase (001) and (101) in different surface conditions. a,b**, wide valence band region (**a**) and its focused area **(b**) of the band gap region for sputtered (st-(001) and st-(101)), annealed (an-(001) and an-(101)), stoichiometric (st-(001) and st-(101)), and oxidized (ox-(001) and ox-(101)). The spectra in the band gap region are superpositions of (modified) valence band states as well as surface state contributions (magenda arrow for (001) surface and cyan allow for the (101) surface), DGS (yellow allow), and SGS (green allow).

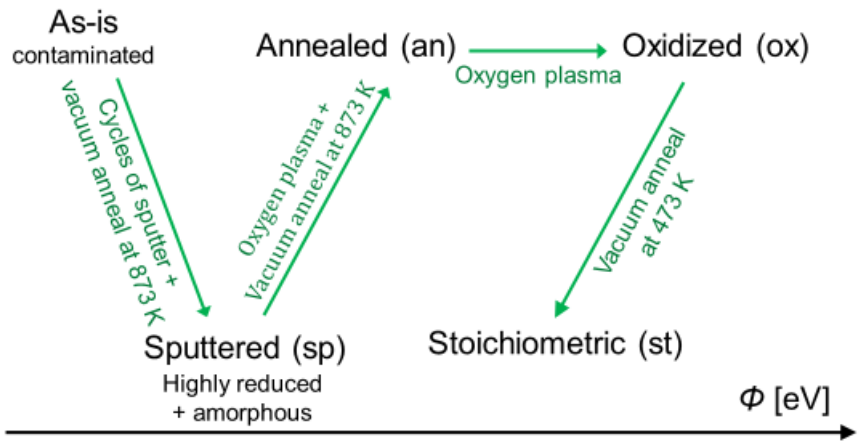


**Figure S4**. **A scheme of the preparation procedure of the different $TiO_2$ surface terminations:** As-is, sputtered, annealed, oxidized, and stoichiometric surfaces.

## 3.2 The Work function of single crystalline anatase and rutile with different surface states

Shun Kashiwaya conducted experiments, data analysis and preparation of the manuscript. Thierry Toupance, Andreas Klein and Wolfram Jaegermann participated in the discussions of the results and revised the manuscript.

This chapter is republished from [The work function of $TiO_2$, Shun Kashiwaya.; Thierry Toupance.; Andreas Klein.; Wolfram Jaegermann, *1*(1), 73, 2018].

surfaces

MDPI

Article

# The Work Function of $TiO_2$

**Shun Kashiwaya [1,2], Jan Morasch [1], Verena Streibel [1,†], Thierry Toupance [2], Wolfram Jaegermann [1] and Andreas Klein [1,*]**

[1] Department of Materials and Earth Sciences, Surface Science Division, Technische Universität Darmstadt, Otto-Berndt-Straße 3, 64287 Darmstadt, Germany; skashi@surface.tu-darmstadt.de (S.K.); j.morasch@web.de (J.M.); streibel@stanford.edu (V.S.); jaegerw@surface.tu-darmstadt.de (W.J.)

[2] Institute of Molecular Sciences, University of Bordeaux, CNRS UMR 5255, Bâtiment A12, 351 Cours de la Liberation, 33405 Talence CEDEX, France; thierry.toupance@u-bordeaux.fr

* Correspondence: aklein@surface.tu-darmstadt.de; Tel.: +49-6151-16-20772

† Current address: SUNCAT Center for Interface Science and Catalysis, SLAC National Accelerator Laboratory, 2575 Sand Hill Road, Menlo Park, CA 94025, USA.

Received: 13 July 2018; Accepted: 1 September 2018; Published: 7 September 2018


**Abstract:** Polycrystalline anatase thin films, (001)- and (101)-oriented anatase $TiO_2$ single crystals and (001)- and (110)-oriented rutile $TiO_2$ single crystals with various surface treatments were studied by photoelectron spectroscopy to obtain their surface potentials. Regardless of orientations and polymorph, a huge variation of the Fermi level and work function was achieved by varying the surface condition. The most strongly oxidized surfaces are obtained after oxygen plasma treatment with a Fermi level ~2.6 eV above the valence band maximum and ionization potentials of up to 9.5 eV (work function 7.9 eV). All other treated anatase surfaces exhibit an ionization potential independent of surface condition of $7.96 \pm 0.15$ eV. The Fermi level positions and the work functions vary by up to 1 eV. The ionization potential of rutile is ~0.56 eV lower than that of anatase in good agreement with recent band alignment studies.

**Keywords:** $TiO_2$; anatase; rutile; work function; electron spectroscopy; photocatalysis

## 1. Introduction

Titanium dioxide ($TiO_2$) is widely applied in photocatalysis [1] and as electrode in solar cells [2], and has been considered to be a promising material owing to its physical and chemical properties. Among the different polymorphs of $TiO_2$, mostly fundamental properties of rutile have been studied experimentally and theoretically despite a superior photocatalytic activity of anatase as compared to rutile, which is associated with its longer charge carrier life time and higher carrier mobility [3]. Oriented rutile substrates, of which the rutile (110) is the most stable and can be easily prepared, have been thoroughly investigated as model surfaces for fundamental surface phenomena [4]. In contrast, information about oriented anatase is sparse because of their difficult preparation [5]. Only recently novel techniques to prepare oriented anatase substrates have been developed [6]. In 2008 Yang et al. [7] synthesized anatase single crystals with 47% of the minority (001) facet via a hydrothermal route employing fluoric acid. This successful synthesis has surged further fundamental investigations of both anatase (101) and (001) facets [8–11]. However, although the electronic structure of anatase bulk and surfaces including band gaps and surface states are well known due a wide range of experimental and theoretical studies using complementary techniques, particularly using electron spectroscopy (see e.g., [11–21]), the surface potentials—Fermi level position, work function and ionization potential—have not yet been studied systematically.

The work function $\varphi$ of materials is especially relevant for photocatalysis and solar cells as it governs the band alignments of interfaces such as $TiO_2$/metal contacts forming Schottky barriers,

$TiO_2$/p-type semiconductor interfaces forming p-n junctions, and $TiO_2$/liquid junctions related to redox potentials. Despite its importance for $TiO_2$, only few work function data have been reported [22–24]. The work function is affected by the Fermi energy $E_F$ and by the vacuum energy $E_{vac}$, which can be manipulated separately by doping, surface space charge layers, or the surface dipole, respectively [25]. The latter depends on surface polarity and termination [26]. Changes in the surface dipole directly affect the ionization potential $I_P$, which is the difference between vacuum energy and valence band maximum $E_{VB}$ and which does not depend on the Fermi energy.

The ionization potential of metal oxide surfaces depends on surface orientation and surface termination, where the latter can vary with the oxygen activity during preparation [25,27–31]. Due to a strong electronegativity of oxygen, less oxygen results in a lower negative surface charge and thus in a lower $I_P$ and $\varphi$. The oxygen activity also affects the Fermi energy in oxides. A lower oxygen activity, i.e., more reducing conditions, generally results in a higher Fermi energy and thereby in a lower $\varphi = E_{vac} - E_F$. Detailed data on the interplay between the surface potentials and oxygen activity for most $TiO_2$ surfaces are still lacking.

Figure 1 displays a ball-and-stick model of bulk-terminated surfaces of rutile (110) and (001), and anatase (101) and (001) without structural relaxations. At the rutile (110) surface bridging oxygen atoms missing one bond to Ti can be easily removed by thermal annealing, whereas at the rutile (001) surface, oxygen vacancies $V_O$ are believed to easily form at a twofold-coordinated surface O atom [4,32]. It was theoretically predicted and experimentally shown that the point defect is located at the bridging oxygen row on the rutile (110) surface whereas for the anatase (101) surface $V_O$ are favored to be situated in the subsurface rather than on the surface [18,33–35]. At anatase (101) and (001) surfaces, the $V_O$ has a lower formation energy in the subsurface than on the surface while the rutile (110) surface exhibits an inverse trend. Thus, at anatase (101) and (001) surfaces, $V_O$ are energetically stable in the subsurface or even in the bulk whereas at rutile (110) and (001) surfaces, the $V_O$ form most likely at the bridging oxygen site on the top surface. This difference in oxygen vacancy distribution is expected to lead to different electronic properties.

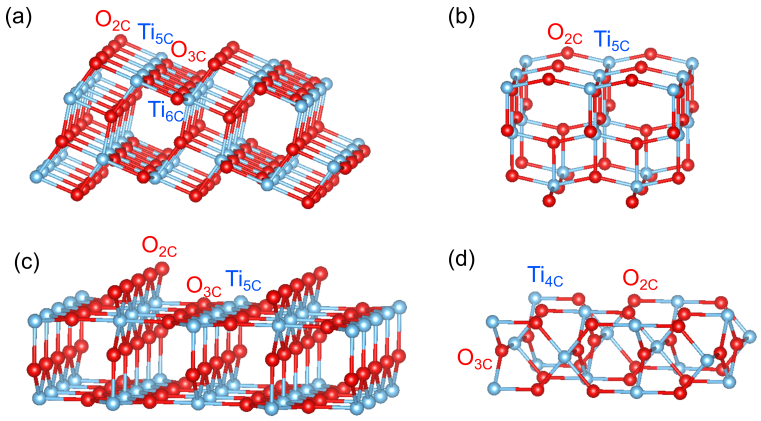


**Figure 1.** Bulk-terminated surfaces of (**a**) anatase (101), (**b**) anatase (001), (**c**) rutile (110) and (**d**) rutile (001), illustrated using VESTA.

Many applications of $TiO_2$ such as water splitting, water purification and self-cleaning, undergo an interaction with water [36–39]. Thus, the investigation of water adsorption on the surface is important. Water adsorption has therefore been investigated intensively by many groups with different techniques (see e.g., [4,40–50] and references therein). Studies of water adsorption on $TiO_2$ are usually performed at liquid nitrogen or lower temperature, where multilayers of molecular water can be adsorbed in a vacuum system [51]. Many studies have focused on the initial state of adsorption: molecular, dissociative, or multilayer adsorption. Most calculations have predicted that on rutile (110) surfaces dissociative adsorption of water is energetically preferred over molecular adsorption [4]. However,

there is a consensus established by several experiments that water dissociates only at the vacancy sites of so-called bridging oxygen rows while only molecular adsorption takes place on the stoichiometric defect-free rutile (110) surface [4,40,41]. For anatase, it was found that water adsorbs dissociatively on the surface in the presence of subsurface $V_O$, although it has also been reported that water would adsorb only molecularly on the anatase surfaces [42–46]. Based on these reports, we assume that the distribution of $V_O$ influences the interface of $TiO_2$ and water, which affects photocatalytic redox reactions. Despite the wealth of studies on this subject, it remains largely unknown how water adsorption affects the work function of different surfaces.

In this work, (001)- and (101)-oriented and polycrystalline anatase surfaces in different oxidation conditions were studied. The same treatments were applied to rutile (110)- and (001)-oriented surfaces. Polycrystalline anatase thin films prepared by spray pyrolysis are also included in this study. The chemical and electronic surface properties were accessed using X-ray und UV photoelectron spectroscopy (XPS and UPS). The reported results provide the variation of the surface potentials of $TiO_2$, i.e., the Fermi level position ($E_F$) with respect to the valence band maximum ($E_{VB}$) and the work function $\varphi$, with surface condition. For anatase, we have also studied the variation of surface properties after exposure to water vapor at room temperature without breaking vacuum. Furthermore, we compare anatase and rutile surfaces and discuss differences in their electronic properties. Overall, the work provides guidance towards manipulating the work function of $TiO_2$ surfaces.

## 2. Materials and Methods

Natural anatase crystals were employed for both (101) and (001) surfaces (SurfaceNet GmbH, Rheine, Germany). Polycrystalline anatase substrates were prepared by spray pyrolysis. Epitaxially polished rutile (110) and (001) substrates were purchased from CrysTec GmbH (Berlin, Germany). The size of the substrates is $5 \times 5 \times 1$ mm$^3$. A surface roughness less than a lattice constant was achieved after epi-polishing the single crystal substrates. For anatase, in addition to the ex-situ surfaces (ex-a(001), ex-a(101), and ex-a-poly) with contamination from air and polishing, unreconstructed (101) and (001), and polycrystalline surfaces were in situ prepared inside an integrated vacuum system to expose different well-defined stoichiometries: sputtered (sp-a(001), sp-a(101), and sp-a-poly), annealed (an-a(001), an-a(101), and an-a-poly), oxidized (ox-a(001), ox-a(101), and ox-a-poly), and stoichiometric (st-a(001), st-a(101), and st-a-poly). For rutile, annealed (an-r(110) and an-r(001)) and oxidized (ox-r(110) and ox-r(001)) were prepared.

Sample preparations and measurements were carried out in the Darmstadt integrated system for materials research (Daisy-Mat) [52] equipped with a multitechnique surface analysis system Physical Electronics PHI 5700, which is connected to different sample preparation chambers via a sample transfer system. The sputtered surfaces were prepared by repeated cycles of $Ar^+$ ion sputtering with an energy of 1 keV for 15 min and annealing under ultrahigh vacuum (UHV) conditions at 873 K for 30 min until no remaining emissions from contaminations were observed by X-ray photoelectron spectroscopy (XPS). Although this procedure has been conventionally accepted to prepare clean surfaces of single crystal $TiO_2$, Ar sputtering not only results in a highly reduced surface and thus leads to the formation of oxygen vacancies and $Ti^{3+}$ surface states, but also partially destroys the crystallinity of the surface and introduces an amorphous phase [4,6,53].

After Ar ion etching, the sputtered surfaces were oxidized in an Oxygen plasma at room temperature in an atmosphere of $7.5 \times 10^{-5}$ mbar $O_2$ for 15 min to re-oxidize the surface, followed by annealing at 873 K in UHV to re-crystallize the surface. Here the O plasma was selected to replenish the lattice O instead of annealing in $O_2$ atmosphere, which has been frequently used for oxidation, as annealing in $O_2$ could form additional incomplete reconstructions [54]. Furthermore, annealing in $O_2$ may lead to iron oxide layer formation since elevated temperatures may trigger the surface segregation of Fe, which is a typical contamination of natural anatase crystals [6]. In addition, atomic O in the O plasma is more oxidative than molecular $O_2$ during annealing in $O_2$ atmosphere, which leads to partially remaining $V_O$ [18,55].

The surfaces, which are in this work referred to as *annealed*, (The term *annealing* might be used differently in literature) were prepared by an oxygen plasma treatment and a subsequent reduction by annealing in vacuum at 873 K. Low energy electron diffraction (LEED) patterns recorded for these surfaces are shown in Figure A1. They show unreconstructed $1 \times 1$ patterns with low background intensity, indicating well-ordered surfaces. Finally, the stoichiometric surfaces were prepared by removing O adatoms by annealing the oxidized (plasma treated) surfaces in UHV at 473 K for 20 min [56,57]. An overview of the preparation procedures for the above described different surfaces is given in Figure 2. It is noted that the color of rutile substrates, which are less conductive than anatase, changed from transparent into dark blue after the reduction procedure, making the surfaces sufficiently conductive to avoid charging during photoemission measurements.

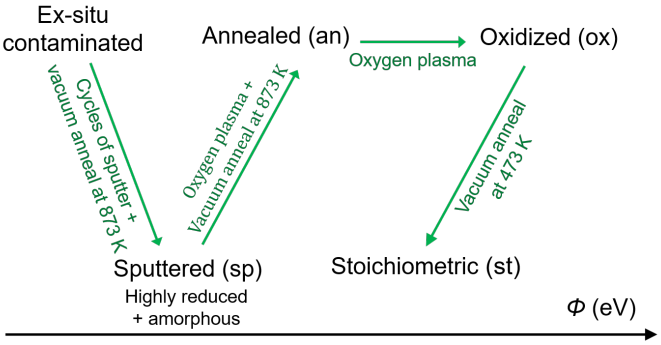


**Figure 2.** Scheme of the preparation procedure for ex-situ (ex), sputtered (sp), annealed (an), oxidized (ox), and stoichiometric (st) surfaces of the $TiO_2$ surfaces.

To further understand the electronic structures of different surfaces in a practical situation for photocatalytic reactions, water was dosed through a diaphragm valve for atomic layer deposition in a vacuum chamber [58] onto the annealed, oxidized, and stoichiometric surfaces for the anatase (001) and (101), and polycrystalline anatase. The water exposure at room temperature was completed using 15 water pulses of 0.5 s duration followed by evacuation for 60 s. The amount of exposed water molecules in this process depends on the pumping speed and the chamber geometry. We estimate the exposure to $10^6$–$10^8$ Langmuir. The resulting $TiO_2$ substrates were transferred to the XPS chamber and investigated immediately after this adsorption procedure. XPS analysis revealed a small C 1s emission after water exposure.

X-ray photoelectron spectra were recorded with monochromatic Al K$\alpha$ radiation at an emission angle of 45° and a pass energy of 5.85 eV, which gives a total energy resolution of 0.4 eV, as determined from the Gaussian broadening of the Fermi edge of a sputter-cleaned Ag sample. Binding energies of core levels and the valence band maximum $E_{VB}$ can be determined with an accuracy of 50 meV, and 100 meV, respectively. For the determination of work function $\varphi$ and ionization potentials $I_P$, ultraviolet photoelectron spectra were recorded in normal emission with He I radiation ($h\nu = 21.2$ eV) from a He discharge lamp and a negative sample bias of 4.0 V. The total energy resolution is 0.2 eV. No charging problems were observed during the XPS and UPS measurements. Obtained binding energies for XPS and UPS were calibrated by the Fermi level energy of a sputter-cleaned Ag sample. Hence, all binding energies are given with respect to the calibrated Fermi level at 0 eV. More details of the experimental setup and approach in performing the experiments may be found elsewhere [52,59].

## 3. Results and Discussion

The Ti $2p_{3/2}$ and O 1s core level spectra of the differently treated surfaces are shown in Figure 3. The Ti $2p_{3/2}$ emission of the sputtered anatase (101) surface shows a strong low binding energy emission associated with $Ti^{3+}$ and $Ti^{2+}$ shifted relative to the main emission line of $Ti^{4+}$ by ~1.7 and ~3.5 eV, respectively [45,60,61]. All other samples, including the sputtered anatase (001), exhibit sharp

and symmetric lines consisting of a single $Ti^{4+}$ oxidation state. Evidently, the anatase (101) surface is much easier reduced than the (001) surface. The low binding energy Ti $2p_{3/2}$ emissions related to surface reduction of anatase (101) are neither observed after re-oxidation by O plasma treatment nor after re-crystallization by annealing in vacuum.

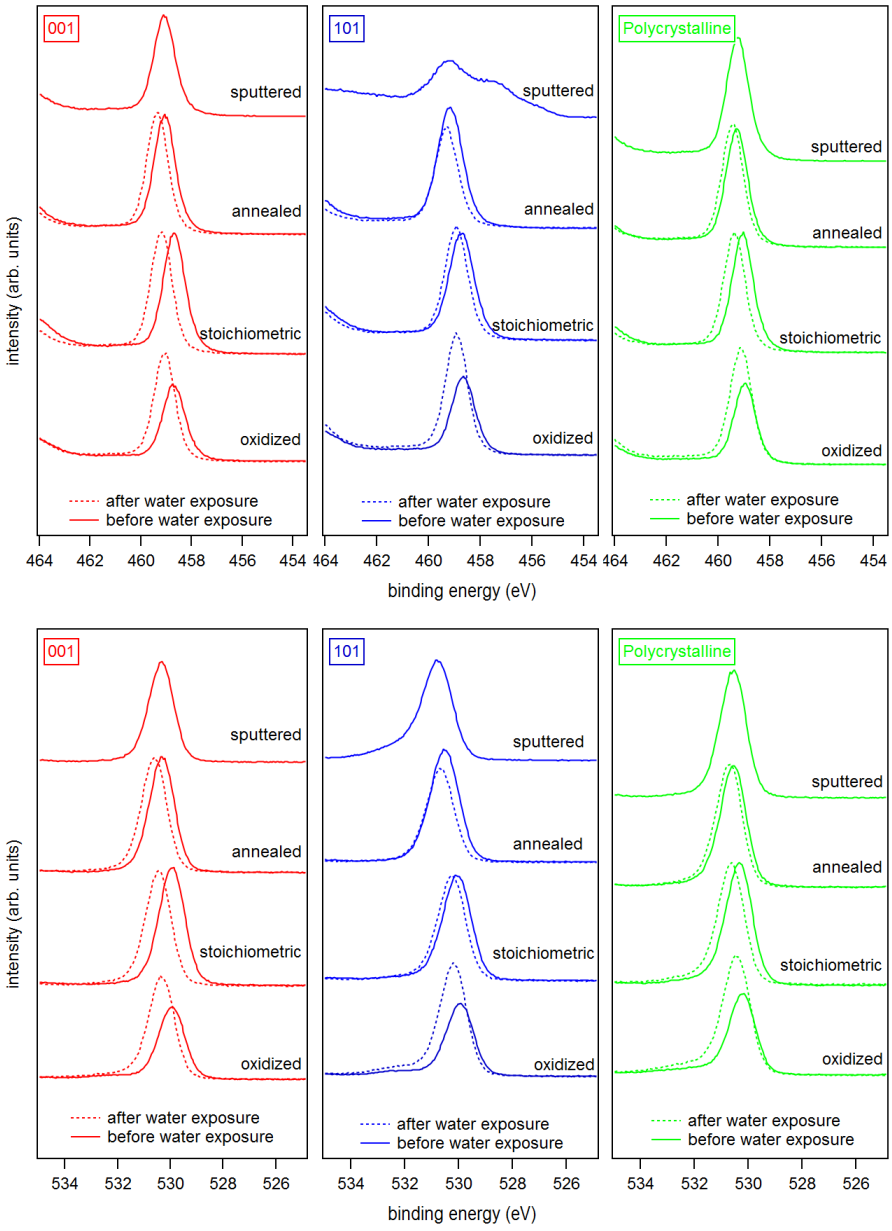


**Figure 3.** X-ray photoelectron spectra of the Ti $2p_{3/2}$ (**top**) and the O 1s (**bottom**) core level emissions of (**left**) anatase (001), (**middle**) anatase (101), and (**right**) polycrystalline anatase substrates with sputtered, annealed, stoichiometric, and oxidized surfaces. Solid and dash lines represent spectra before and after water exposure, respectively.

Exposing an-a(001) and an-a(101) to an O plasma results in a shoulder in the O 1s emission at 3 eV higher binding energy compared to the O 1s emission related to $TiO_2$ (see bottom row of Figure 3). This shoulder is likely attributed to peroxo ($O_2^{2-}$) surface species, like for example in bridging oxygen dimers [62]. The stoichiometric anatase (001) and (101) surfaces show no shoulder in the O 1s emission

after annealing in vacuum at 473 K. The surface peroxo species observed after oxygen plasma treatment at ox-a(001) and ox-a(101) is therefore effectively removed by annealing.

X-ray and ultraviolet valence band spectra are shown in Figure 4. UP spectra are usually more sensitive to surface defects than XP spectra, which is mostly due to the higher surface sensitivity of UPS and the higher intensities. It is accepted that the so-called band gap surface states would form due to occupied Ti 3d states ($Ti^{3+}$) near the O vacancy sites on the surface, but also due to $Ti^{3+}$ interstitials in the subsurface region [4,11,18,63,64]. It is clear from Figure 4 that all sputtered $TiO_2$ surfaces show the well-known Ti $3d^1$ emission lines in the band gap region.

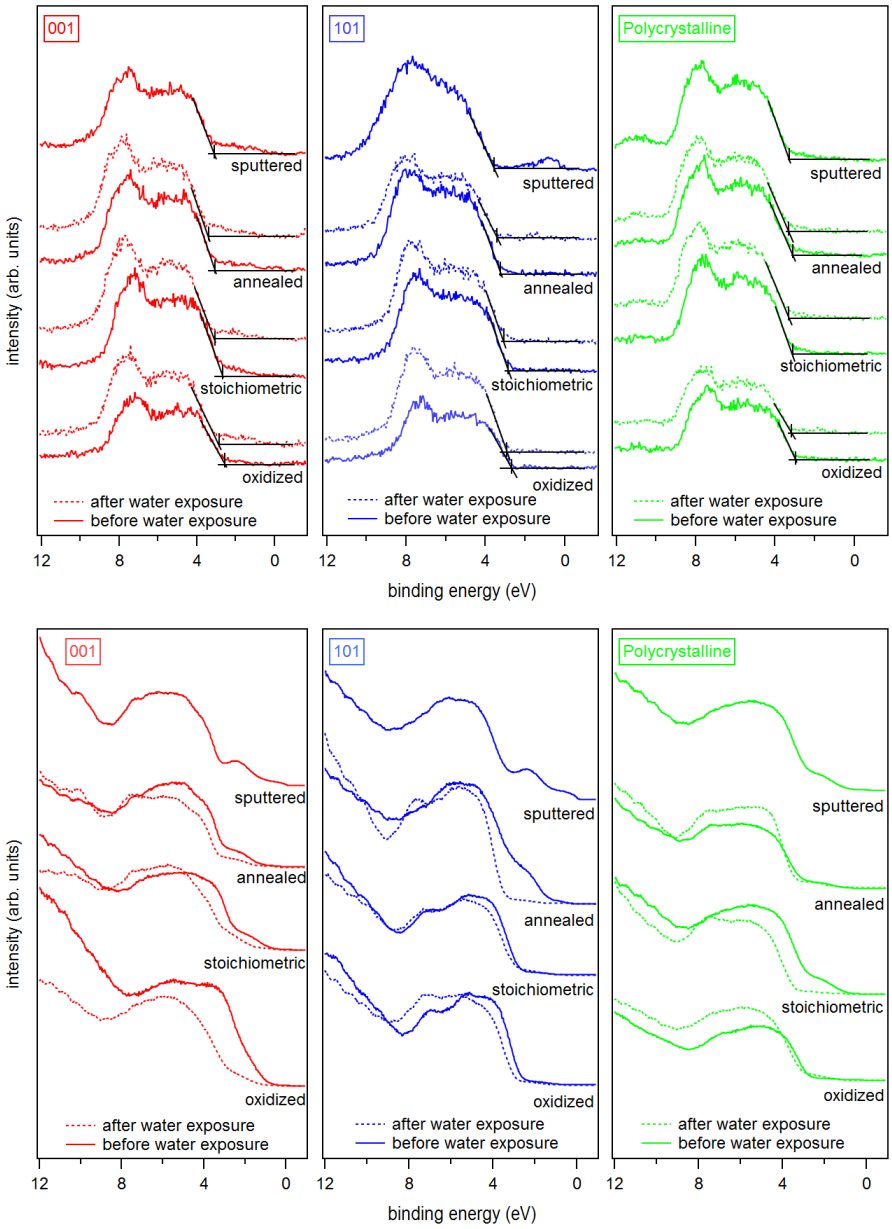


**Figure 4.** X-ray (**top**) and ultraviolet (**bottom**) valence band spectra of sputtered, annealed, stoichiometric, and oxidized surfaces for (**left**) anatase (001), (**middle**) anatase (101), and (**right**) polycrystalline anatase substrates before and after water exposure.

The emission of the gap states is different for the (001) and (101) surface orientation of anatase. The state energically closer to the Fermi energy at a binding energy of ~0.5 eV is more pronounced for

the (101) surface. As this emission is clearly observed only for the sputtered (101) surface, this shallow gap state is likely related to the observation of the reduced Ti species.

The intensity of the band gap states is generally reduced with surface oxidation for both orientations and all treatments. However, the deep gap state, which is closer to the onset of the valence band maximum at 1.5–2.0 eV binding energy, is still observed in the XP and the UP valence spectra for the (001) surface even after O plasma treatment. In contrast, the deep gap state is completely attenuated for the oxidized and the stoichiometric (101) surface.

The valence band maximum binding energies $E_F - E_{VB}$ are determined by a linear extrapolation of the low binding energy valence band emission edge. Only XPS data are used here as they are less affected by the gap state emissions. The extracted values are summarized in Table 1 together with the core level binding energies, which are determined from the spectra shown in Figure 3.

**Table 1.** Binding energies (Ti 2p and O 1s), Fermi level position $E_F - E_{VB}$, work function $\varphi$, and ionization potential $I_P$ for anatase (001), anatase (101), and polycrystalline anatase, as well as for rutile (001) and rutile (110) with different surface stoichiometries: sputtered, annealed, stoichiometric, oxidized and ex-situ prepared surfaces. Number in brackets are obtained after in situ exposure to water vapor at room temperature.

| | **Sputtered** | **Annealed** | **Stoichiometric** | **Oxidized** | **Ex-Situ** |
|---|---|---|---|---|---|
| | | | Ti $2p_{3/2}$ (eV) | | |
| a-(001) | 459.08 | 459.07 (459.36) | 458.70 (459.20) | 458.64 (459.06) | 459.27 |
| a-(101) | 459.21 | 459.17 (459.31) | 458.73 (458.93) | 458.69 (458.91) | 459.28 |
| a-poly | 459.25 | 459.28 (459.44) | 459.06 (459.37) | 458.95 (459.09) | |
| r-(001) | | 459.38 | | 458.78 | |
| r-(110) | | 459.35 | | 458.95 | |
| | | | O 1s (eV) | | |
| a-(001) | 530.35 | 530.33 (530.62) | 529.95 (530.47) | 529.93 (530.32) | 530.60 |
| a-(101) | 530.81 | 530.52 (530.68) | 530.07 (530.27) | 529.93 (530.19) | 530.62 |
| a-poly | 530.57 | 530.56 (530.71) | 530.35 (530.64) | 530.20 (530.44) | |
| r-(001) | | 530.69 | | 530.04 | |
| r-(110) | | 530.62 | | 530.21 | |
| | | | $E_F - E_{VB}$ (eV) | | |
| a-(001) | 3.10 | 3.06 (3.39) | 2.64 (3.06) | 2.53 (2.87) | 3.44 |
| a-(101) | 3.55 | 3.23 (3.40) | 2.84 (3.08) | 2.69 (2.91) | 3.35 |
| a-poly | 3.23 | 3.09 (3.37) | 3.12 (3.31) | 2.94 (3.16) | |
| r-(001) | | 3.07 | | 2.57 | |
| r-(110) | | 3.12 | | 2.68 | |
| | | | $\varphi$ in (eV) | | |
| a-(001) | 4.70 | 4.72 (4.36) | 5.35 (4.34) | 6.44 (4.97) | 3.61 |
| a-(101) | 4.62 | 4.72 (4.36) | 5.23 (4.40) | 6.76 (5.03) | 3.65 |
| a-poly | 4.51 | 4.23 (4.22) | 5.16 (4.38) | 5.62 (4.94) | |
| r-(001) | | 4.29 | | 6.08 | |
| r-(110) | | 4.31 | | 5.96 | |
| | | | $I_P$ (eV) | | |
| a-(001) | 7.80 | 7.78 (7.75) | 7.99 (7.40) | 8.97 (7.84) | 7.05 |
| a-(101) | 8.17 | 7.95 (7.76) | 8.07 (7.48) | 9.45 (7.94) | 7.00 |
| a-poly | 7.74 | 7.32 (7.59) | 8.28 (7.69) | 8.56 (8.10) | |
| r-(001) | | 7.36 | | 8.65 | |
| r-(110) | | 7.43 | | 8.64 | |

Independent of surface orientations, the valence band maximum binding energy decreases in the order sputtered, annealed, stoichiometric, and oxidized treatment. The valence band maximum and the core levels show comparable binding energy shifts. In particular, the binding energy difference between the O 1s and the Ti 2p core level is $71.29 \pm 0.04$ eV, with the only exception of the sputtered anatase surface, where the binding energy of the Ti 2p core level is more uncertain due to the strong

reduction of the surface. The binding energy differences between the core levels and valence band maxima also remain within ±0.15 eV, which can also be considered to be constant considering the changes of the valence bands in dependence on treatment. The binding energy shifts can therefore be attributed to different Fermi energies. These are likely caused by different concentrations of oxygen vacancies at the surface or in the bulk. The former would cause binding energy shifts due to surface electron accumulation, the latter due to enhanced doping.

The overall variation of the Fermi energy is 0.46 eV for the (001) and 0.71 eV for the (101) surface orientation, respectively. It is noteworthy that $E_F - E_{VB}$ of the (101) surface is always higher than that of the (001) surface. This difference of $E_F - E_{VB}$ results in a variation of surface potential with orientation, which will drive photogenerated electrons and holes towards the (101) and (001) surfaces, respectively. This charge separation mechanism agrees with literature reports [65,66].

The secondary electron edges of the UP spectra of anatase are shown in Figure 5. Their energetic position is determined at the middle of the steep rise of the edge. (Most authors use the intersection of the secondary electron edge with the baseline to determine the work function. We take the middle of the steep rise instead as we assume that the onset is broadened by the resolution of the spectrometer system. We use this procedure when the width of the steep part of the edge is ≤0.2 eV, which is the case for all spectra in this manuscript. In this case, the difference between the two approaches is less than 0.1 eV.) The extracted work functions $\varphi$ and ionization potentials $I_P$ are summarized in Table 1 and the work function is plotted as a function of the Fermi energy in Figure 6. More extended data including polycrystalline and water exposed samples are provided in the appendix in Figure A2 and Table A1. The work functions are decreasing in the order oxidized > stoichiometric > annealed > sputtered for both single crystal anatase surface orientations. It therefore decreases monotonically with the increase of the Fermi level to valence band maximum distance, $E_F - E_{VB}$. This is to be expected as both depend on the oxidation state of the surface and subsurface. Similar dependencies have been reported for ZnO, $In_2O_3$ and $SnO_2$ [25].

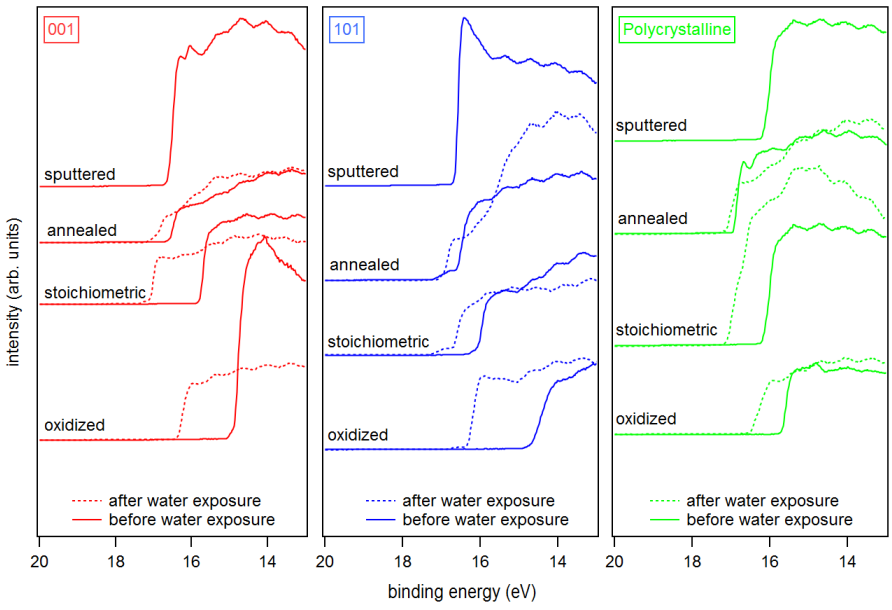


**Figure 5.** UP spectra of SEE of sputtered, annealed, stoichiometric, and oxidized surfaces for anatase (001), anatase (101), and polycrystalline anatase substrates before and after water exposure.

The overall variation of the work function is 1.74, 2.14 and 1.39 eV for anatase (001), anatase (101) and polycrystalline anatase, respectively. The change of $\varphi$ between stoichiometric, annealed, and sputtered single crystal surfaces is caused mainly by a change of $E_F - E_{VB}$ as the ionization potential is almost constant for these surface conditions with $I_P = 7.96 \pm 0.15$ eV. Such a behavior has also been

reported by Henrich et al. for rutile (110) surfaces [22]. The ionization potential of the polycrystalline surfaces varies more with preparation conditions than at the single crystalline surfaces. This is likely attributed to a less pure surface condition, as the surfaces typically show residual carbon contamination. Considerably higher ionization potentials of up to 9.45 eV are observed for the oxygen plasma treated surfaces. This matches with the assumed peroxo or bridging oxygen species on the surface, which are induced by radical oxygen atoms of the oxygen plasma. Electronegative oxygen accumulates with a negative charge, leading to high work functions and ionization potentials of oxidized surfaces due to an increase of the surface dipole [31,67].

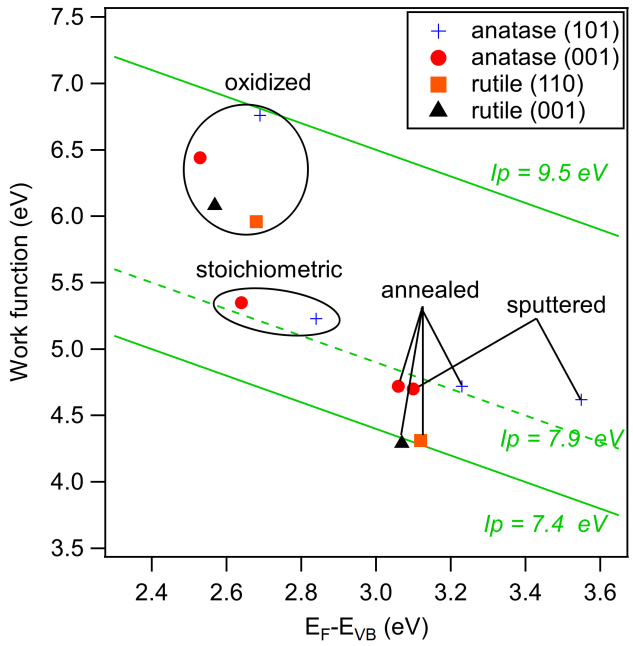


**Figure 6.** Work function versus Fermi level to valence band maximum distance, $E_F - E_{VB}$, of sputtered, annealed, stoichiometric, and oxidized surfaces for anatase (001), anatase (101), and polycrystalline anatase substrates before and after water exposure. Values for annealed and oxidized rutile (001) and (110) surfaces are added for comparison.

Water vapor was exposed to the surfaces at room temperature and the resulting electronic properties were investigated by XPS and UPS. Obtained core level binding energies and surface potentials of the surfaces exposed to water are included in brackets in Table 1. The chemical modification of the surface resulting from water exposure is not clear. During low temperature adsorption, a mixture of molecular and dissociative adsorption is reported [4,40–46]. The adsorption of water molecules is not expected at room temperature in ultra-high vacuum but formation of hydroxides is likely. However, we do not have a clear confirmation for this. The O 1s peaks do not show the high binding energy shoulder typical for hydroxides. Nevertheless, the O 1s spectra do exclude a low OH coverage. Further studies, which are beyond the scope of the present work, are required to resolve the interaction of water vapor with $TiO_2$ surfaces.

Irrespective of the uncertainty of the chemical state of the surface, water exposure reproducibly induces shifts of the Ti 2p and O 1s core levels and the valence band edge towards higher binding energies. The shifts can therefore be attributed to a downward band bending at the $TiO_2$ surface, resulting in an accumulation of electrons at the surface. This observation emphasizes the importance of adsorbates for the frequently reported electron accumulation layers at oxide surfaces [68–70]. The final Fermi level positions, which are extracted from the valence band maximum and the core level binding energies do not depend on surface orientation and are ∼3.4, ∼3.1 and ∼2.9 eV for the annealed, stoichiometric and oxidized (001) and (101) surfaces, respectively. The original difference in $E_F - E_{VB}$

between the anatase (101) and (001), which was present for all surface conditions, thus disappeared after water exposure.

The work function after water exposure is ∼4.4 eV for the annealed and stoichiometric surfaces, while it is significantly higher (∼5.0 eV) for the oxidized surface. Apparently, the adsorbed peroxo or bridging oxygen species, which cause the increased ionization potential, are not completely removed by water exposure. These species are therefore strongly enough bound to the surface to withstand the reduction of the sample by water exposure. The latter is indicated by the rise of the Fermi energy.

XP spectra of the valence band region, the Ti $2p_{3/2}$, and the O 1s core levels of annealed and oxidized rutile (001) and (110) surfaces are shown in Figure 7. Corresponding core level binding energies and surface potentials are included in Table 1. Obtained work functions and ionization potentials are plotted together with the anatase data in Figure 6. A large difference of $E_F - E_{VB}$ and $\varphi$ between the two treatments but no significant dependence on surface orientation are observed. The ionization potential of the annealed surfaces amounts to $7.40 \pm 0.04$ eV, which is 0.56 eV lower than that of the corresponding anatase surfaces.

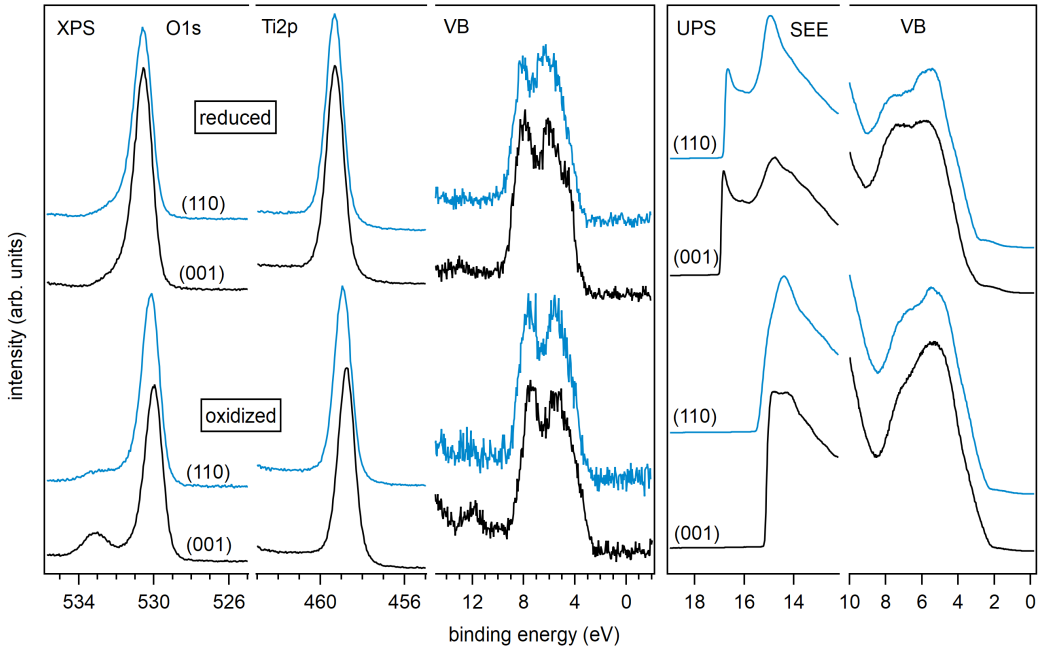


**Figure 7.** XP spectra of Ti 2p, O 1s, and valence band emission lines, and UP spectra of secondary electron edge and valence band region for rutile (001) and (110) substrates with reduced and oxidized surfaces.

The ionization potentials of the anatase and rutile surfaces (except for the ones treated in the O plasma), which are 7.96 and 7.40 eV, respectively, are comparable to those of ZnO surfaces exposed to oxidizing conditions (∼7.6 eV) [25,29]. Similar ionization potentials are also found for surfaces of Sn-doped $In_2O_3$ (∼7.7 eV) and reduced $SnO_2$ surfaces [25,29,71,72]. The latter are characterized by a $Sn^{2+}$ oxidation state [28,73–75]. Except for the sputtered anatase (101) surfaces, which exhibits substantial reduction of Ti, most of the Ti adopts a +IV oxidation state. One might therefore expect that the ionization potential is comparable to that of the stoichiometric $SnO_2$ surface, which amounts to ∼8.9 eV [25,29,71,72]. The deviation is quite substantial, even for rutile, which has the same crystal structure as $SnO_2$. The ionization potential of $TiO_2$ is therefore substantially lower than that of $SnO_2$. $TiO_2$ surfaces do also not show the variation of cation oxidation state and the associate change of $I_P$, which is characteristic for $SnO_2$. The origin of these remarkable differences remains to be resolved. Due to the similar ionization potentials and work functions of $TiO_2$, ZnO and $In_2O_3$, the superior

photocatalytic and solar cell properties of $TiO_2$ are probably not caused by an advantageous energy band alignment.

The difference in ionization potential between anatase and rutile amounts to ∼0.5 eV. Aligning the vacuum energies of the two polytypes does therefore result in a valence band maximum of anatase being ∼0.5 eV lower in energy than that of rutile. This is the same direction and of the same magnitude as the energy band alignment established recently by different experimental and theoretical approaches [19,76,77], supporting the conclusion that the energy bands of rutile are higher than those of anatase.

## 4. Summary and Conclusions

Chemical and electronic properties of anatase (001), anatase (101), polycrystalline anatase, rutile (110) and rutile (001) with different surface treatments were studied using XPS and UPS. The Fermi energy and work function depend drastically on surface conditions, which are characterized by different oxygen vacancy concentrations and surface adsorbates. We have shown how the surface Fermi energy, work function and ionization potentials are affected and can therefore be adjusted by different surface treatments.

For anatase, the Fermi level can be manipulated between $E_F - E_{VB} = 2.53$–$3.10$, $2.69$–$3.55$, and $2.94$–$3.23$ eV for the (001), (101) and polycrystalline surfaces, respectively. Along with the different Fermi energies goes a variation of work function between $\varphi = 4.70$–$6.44$, $4.62$–$6.76$, and $4.51$–$5.62$ eV for the (001), (101) and polycrystalline surfaces, respectively. Apart from the plasma treated samples, which have exceptionally high work functions likely due to the presence of peroxo species, the ionization potential is rather insensitive to the surface treatments and exhibits a value of $I_P = 7.96 \pm 0.15$ eV. This is approximately 0.5 eV higher than of rutile, which agrees with the band alignment obtained from other techniques. For the anatase samples, the Fermi energy at the (101) surface is furthermore higher than at the (001) surface for all surface treatments.

Exposure of the samples to water vapor at room temperature reproducibly causes a downward band bending on all surfaces (rise of the Fermi energy). For the anatase surfaces, the dependence of Fermi energy on surface orientation is removed by water exposure. Water exposure also affects the ionization potential. Together, both effects result in a lowering of the work function down to $4.34 \pm 0.06$ eV ($I_P = 7.61 \pm 0.15$ eV) for the annealed and the stoichimetric surfaces. The ionization potential of the plasma treated surfaces remains rather high ($7.96 \pm 0.13$ eV), resulting in work functions of $4.98 \pm 0.05$ eV after water exposure.

**Author Contributions:** Single and polycrystalline surfaces were prepared and analyzed by S.K. and J.M., supervised by A.K., W.J. and T.T.; Discussion and interpretation of results was conducted by S.K., A.K. and W.J.; The original draft has been composed by S.K., edited by A.K. and revised by all authors; Funding has been acquired by W.J. and T.T.

**Funding:** This work was partly supported by the European Commission within the Erasmus Mundus Joint Doctoral program International Doctoral School in Functional Materials for Energy, Information Technology, and Health (ids-funmat), the French-German University (UFA Doctoral College in Functional Materials for Energy and Information Technology) and was carried out within the framework of EMMI (European Multifunctional Material Institute). Further support was received from the European Commission under the FP7 project "Novel Composite Oxides by Combinatorial Material Synthesis for Next Generation All-Oxide-Photovoltaics," project number 309018.

**Acknowledgments:** Receipt of polycrystalline samples from Arie Zaban's group at Bar Ilan University, Israel, is also gratefully acknowledged.

**Conflicts of Interest:** The authors declare no conflict of interest. The founding sponsors had no role in the design of the study; in the collection, analyses, or interpretation of data; in the writing of the manuscript, and in the decision to publish the results.

## Abbreviations

The following abbreviations are used in this manuscript:

| | |
|---|---|
| XPS | X-ray photoelectron spectroscopy |
| UPS | ultraviolet photoelectron spectroscopy |
| UHV | ultra-high vacuum |
| LEED | low-energy electron diffraction |

## Appendix A. LEED Pattern for Annealed Anatase Surfaces

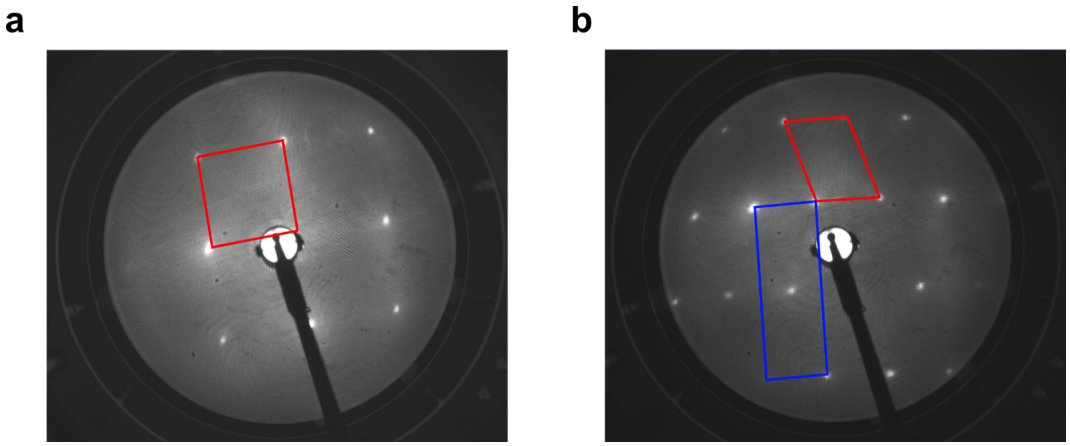


**Figure A1.** LEED pattern of the annealed anatase (001) (**a**) and (101) (**b**) surfaces. The unit cells are indicated.

## Appendix B. Further Work Function Data

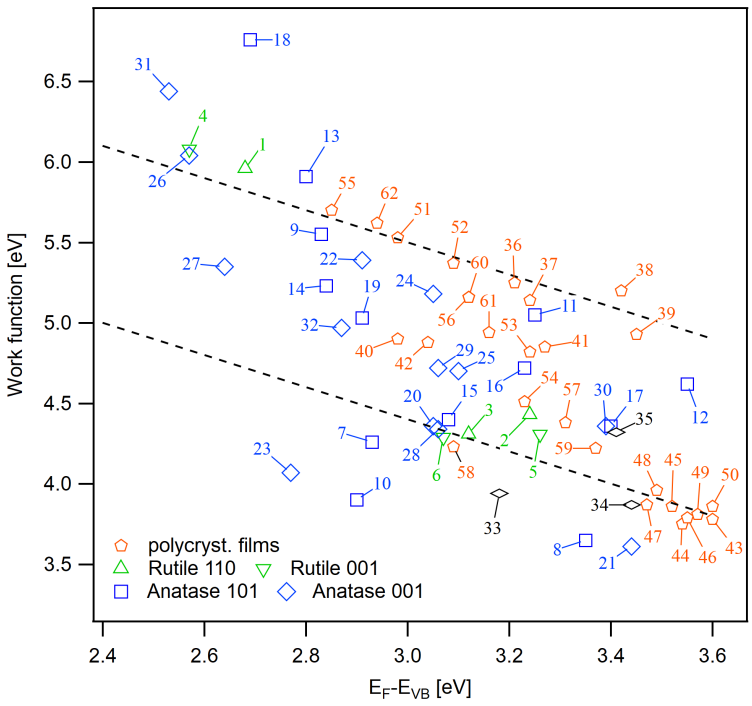


**Figure A2.** Extended set of work function and Fermi energy data. The description of the sample numbers are given in Table A1.

**Table A1.** Sample descriptions and surface potentials for Figure A2. All values are in eV with a typical uncertainty of ±0.1 eV.

| No. | Sample | Description | $E_F$ | $\varphi$ | $I_P$ |
|---|---|---|---|---|---|
| 1 | rutile (110) | (i) same as #2; (ii) $O_2$ plasma, RT, 15 min | 2.68 | 5.96 | 8.64 |
| 2 | rutile (110) | (i) 500 °C, 0.5 Pa $O_2$, 2h; (ii) 600 °C, $10^{-6}$ Pa, 1 h | 3.24 | 4.43 | 7.67 |
| 3 | rutile (110) | same as #2 | 3.12 | 4.31 | 7.43 |
| 4 | rutile (001) | same as #1 | 2.57 | 6.08 | 8.65 |
| 5 | rutile (001) | same as #2 | 3.26 | 4.31 | 7.57 |
| 6 | rutile (001) | same as #2 | 3.07 | 4.29 | 7.36 |
| 7 | anatase (101) | same as #2 | 2.93 | 4.26 | 7.19 |
| 8 | anatase (101) | same as #2 + air exposure | 3.35 | 3.65 | 7.00 |
| 9 | anatase (101) | $O_2$ plasma, RT, 15 min | 2.83 | 5.55 | 8.38 |
| 10 | anatase (101) | same as #9 + air exposure | 2.90 | 3.90 | 6.80 |
| 11 | anatase (101) | (i) same as #12; (ii) $O_2$ plasma, RT, 15 min; (iii) annealing in $10^{-6}$ Pa, 200 °C, 20 min | 3.25 | 5.05 | 8.30 |
| 12 | anatase (101) | cycles of sputtering + annealing 600 °C, $10^{-6}$ Pa, 1 h | 3.55 | 4.62 | 8.17 |
| 13 | anatase (101) | (i) same as #12; (ii) $O_2$ plasma, RT, 15 min | 2.80 | 5.91 | 8.71 |
| 14 | anatase (101) | stoichiometric as in manuscript | 2.84 | 5.23 | 8.07 |
| 15 | anatase (101) | (i) same as #14; (ii) $H_2O$ adsorption | 3.08 | 4.40 | 7.48 |
| 16 | anatase (101) | reduced as in manuscript | 3.23 | 4.72 | 7.95 |
| 17 | anatase (101) | (i) same #16; (ii) $H_2O$ adsorption | 3.4 | 4.36 | 7.76 |
| 18 | anatase (101) | oxidized as in manuscript | 2.69 | 6.76 | 9.45 |
| 19 | anatase (101) | (i) same as #18; (ii) $H_2O$ adsorption | 2.91 | 5.03 | 7.94 |
| 20 | anatase (001) | same as #7 | 3.05 | 4.36 | 7.41 |
| 21 | anatase (001) | same as #8 | 3.44 | 3.61 | 7.05 |
| 22 | anatase (001) | same as #9 | 2.83 | 5.55 | 8.38 |
| 23 | anatase (001) | same as #10 | 2.90 | 3.90 | 6.80 |
| 24 | anatase (001) | same as #11 | 3.25 | 5.05 | 8.30 |
| 25 | anatase (001) | same as #12 | 3.55 | 4.62 | 8.17 |
| 26 | anatase (001) | same as #13 | 2.80 | 5.91 | 8.71 |
| 27 | anatase (001) | same as #14 | 2.84 | 5.23 | 8.07 |
| 28 | anatase (001) | same as #15 | 3.08 | 4.4 | 7.48 |
| 29 | anatase (001) | same as #16 | 3.23 | 4.72 | 7.95 |
| 30 | anatase (001) | same as #17 | 3.40 | 4.36 | 7.76 |
| 31 | anatase (001) | same as #18 | 2.69 | 6.76 | 9.45 |
| 32 | anatase (001) | same as #19 | 2.91 | 5.03 | 7.94 |
| 33 | powder | sol-gel, as prepared | 3.18 | 3.94 | 7.12 |
| 34 | powder | hydrothermal, as prepared | 3.44 | 3.87 | 7.31 |
| 35 | nanocrystals | (101) facetted | 3.41 | 4.32 | 7.73 |
| 36 | sprayed film | 0.5 Pa $O_2$, 400 °C, 12 h | 3.21 | 5.25 | 8.46 |
| 37 | sprayed film | 0.5 Pa Ar, 400 °C, 12 h | 3.24 | 5.14 | 8.38 |
| 38–42 | sprayed film | same as #36 | 2.98–3.45 | 4.85–5.25 | 7.88–8.62 |
| 43–50 | sprayed film | as received | 3.47–3.60 | 3.75–3.96 | 7.29–7.46 |
| 51 | thin film | (i) in situ magnetron sputtering at RT; (ii) 0.5 Pa $O_2$, 600 °C, 1 h | 2.98 | 5.53 | 8.51 |
| 52 | thin film | (i) in situ magnetron sputtering at RT; (ii) 0.5 Pa $O_2$, 400 °C, 1 h | 3.09 | 5.37 | 8.46 |
| 53 | sprayed film | same as #11 | 3.24 | 4.82 | 8.06 |
| 54 | sprayed film | same as #12 | 3.23 | 4.51 | 7.74 |
| 55 | sprayed film | same as #13 | 2.85 | 5.70 | 8.55 |
| 56 | sprayed film | stoichiometric as in manuscript | 3.12 | 5.16 | 8.28 |
| 57 | sprayed film | (i) same as #58; (ii) $H_2O$ adsorption | 3.31 | 4.23 | 7.32 |
| 58 | sprayed film | reduced as in manuscript | 3.09 | 4.23 | 7.32 |
| 59 | sprayed film | (i) same as #60; (ii) $H_2O$ adsorption | 3.37 | 4.22 | 7.59 |
| 60 | sprayed film | stoichiometric as in manuscript | 3.12 | 5.16 | 8.28 |
| 61 | sprayed film | (i) same as #62; (ii) $H_2O$ adsorption | 3.16 | 4.94 | 8.10 |
| 62 | sprayed film | oxidized as in manuscript | 2.94 | 5.62 | 8.56 |

## References


1. Linsebigler, A.L.; Lu, G.; Yates, J.T. Photocatalysis on $TiO_2$ Surfaces: Principles, Mechanisms, and Selected Results. *Chem. Rev.* **1995**, *95*, 735–758. [CrossRef]
2. Grätzel, M. Solar Energy Conversion by Dye-Sensitized Photovoltaic Cells. *Inorg. Chem.* **2005**, *44*, 6841–6851. [CrossRef] [PubMed]
3. Selcuk, S.; Selloni, A. Facet-dependent trapping and dynamics of excess electrons at anatase $TiO_2$ surfaces and aqueous interfaces. *Nat. Mater.* **2016**, *15*, 1107. [CrossRef] [PubMed]
4. Diebold, U. The surface science of titanium dioxide. *Surf. Sci. Rep.* **2003**, *48*, 53–229. [CrossRef]
5. Herman, G.S.; Gao, Y. Growth of epitaxial anatase (001) and (101) films. *Thin Solid Films* **2001**, *397*, 157–161. [CrossRef]
6. Setvin, M.; Daniel, B.; Mansfeldova, V.; Kavan, L.; Scheiber, P.; Fidler, M.; Schmid, M.; Diebold, U. Surface preparation of $TiO_2$ anatase (101): Pitfalls and how to avoid them. *Surf. Sci.* **2014**, *626*, 61–67. [CrossRef]
7. Yang, H.G.; Sun, C.H.; Qiao, S.Z.; Zou, J.; Liu, G.; Smith, S.C.; Cheng, H.M.; Lu, G.Q. Anatase $TiO_2$ single crystals with a large percentage of reactive facets. *Nature* **2008**, *453*, 638. [CrossRef] [PubMed]
8. Chen, W.; Kuang, Q.; Wang, Q.; Xie, Z. Engineering a high energy surface of anatase $TiO_2$ crystals towards enhanced performance for energy conversion and environmental applications. *RSC Adv.* **2015**, *5*, 20396–20409. [CrossRef]
9. Liu, G.; Yu, J.C.; Lu, G.Q.M.; Cheng, H.M. Crystal facet engineering of semiconductor photocatalysts: motivations, advances and unique properties. *Chem. Commun.* **2011**, *47*, 6763–6783. [CrossRef] [PubMed]
10. Scheiber, P.; Fidler, M.; Dulub, O.; Schmid, M.; Diebold, U.; Hou, W.; Aschauer, U.; Selloni, A. (Sub)Surface Mobility of Oxygen Vacancies at the $TiO_2$ Anatase (101) Surface. *Phys. Rev. Lett.* **2012**, *109*, 136103. [CrossRef] [PubMed]
11. Reckers, P.; Dimamay, M.; Klett, J.; Trost, S.; Zilberberg, K.; Riedl, T.; Parkinson, B.A.; Brötz, J.; Jaegermann, W.; Mayer, T. Deep and Shallow $TiO_2$ Gap States on Cleaved Anatase Single Crystal (101) Surfaces, Nanocrystalline Anatase Films, and ALD Titania Ante and Post Annealing. *J. Phys. Chem. C* **2015**, *119*, 9890–9898. [CrossRef]
12. Baldini, E.; Chiodo, L.; Dominguez, A.; Palummo, M.; Moser, S.; Yazdi-Rizi, M.; Auböck, G.; Mallett, B.P.; Berger, H.; Magrez, A. Strongly bound excitons in anatase $TiO_2$ single crystals and nanoparticles. *Nat. Commun.* **2017**, *8*, 13. [CrossRef] [PubMed]
13. Moser, S.; Moreschini, L.; Jaćimović, J.; Barišić, O.S.; Berger, H.; Magrez, A.; Chang, Y.J.; Kim, K.S.; Bostwick, A.; Rotenberg, E.; et al. Tunable Polaronic Conduction in Anatase $TiO_2$. *Phys. Rev. Lett.* **2013**, *110*, 196403. [CrossRef] [PubMed]
14. Emori, M.; Sakino, A.; Ozawa, K.; Sakama, H. Polarization-dependent ARPES measurement for valence band of anatase $TiO_2$. *Solid State Commun.* **2014**, *188*, 15–18. [CrossRef]
15. Sandell, A.; Sanyal, B.; Walle, L.; Richter, J.; Plogmaker, S.; Karlsson, P.; Borg, A.; Uvdal, P. Probing and modifying the empty-state threshold of anatase $TiO_2$: Experiments and ab initio theory. *Phys. Rev. B* **2008**, *78*, 075113. [CrossRef]
16. Tuan, A.C.; Kaspar, T.C.; Droubay, T.; Rogers , J.W., Jr.; Chambers, S.A. Band offsets for the epitaxial $TiO_2/SrTiO_3/Si(001)$ system. *Appl. Phys. Lett.* **2003**, *83*, 3734–3736. [CrossRef]
17. Thomas, A.G.; Flavell, W.R.; Kumarasinghe, A.R.; Mallick, A.K.; Tsoutsou, D.; Smith, G.C.; Stockbauer, R.; Patel, S.; Grätzel, M.; Hengerer, R. Resonant photoemission of anatase $TiO_2$ (101) and (001) single crystals. *Phys. Rev. B* **2003**, *67*, 035110. [CrossRef]
18. Thomas, A.G.; Flavell, W.R.; Mallick, A.K.; Kumarasinghe, A.R.; Tsoutsou, D.; Khan, N.; Chatwin, C.; Rayner, S.; Smith, G.C.; Stockbauer, R.L.; et al. Comparison of the electronic structure of anatase and rutile $TiO_2$ single-crystal surfaces using resonant photoemission and X-ray absorption spectroscopy. *Phys. Rev. B* **2007**, *75*, 035105. [CrossRef]
19. Pfeifer, V.; Erhart, P.; Li, S.; Rachut, K.; Morasch, J.; Brötz, J.; Reckers, P.; Mayer, T.; Rühle, S.; Zaban, A.; et al. Energy Band Alignment Between Anatase and Rutile $TiO_2$. *J. Phys. Chem. Lett.* **2013**, *4*, 4182–4187. [CrossRef]
20. Schwanitz, K.; Weiler, U.; Hunger, R.; Mayer, T.; Jaegermann, W. Synchrotron-induced photoelectron spectroscopy of the dye-sensitized nanocrystalline $TiO_2$/electrolyte interface: Band gap states and their interaction with dye and solvent molecules. *J. Phys. Chem. C* **2007**, *111*, 849–854. [CrossRef]

21. Liu, G.; Schulmeyer, T.; Thissen, A.; Klein, A.; Jaegermann, W. In situ preparation and interface characterization of $TiO_2/Cu_2S$ heterointerface. *Appl. Phys. Lett.* **2003**, *82*, 2269–2271. [CrossRef]
22. Henrich, V.E.; Dresselhaus, G.; Zeiger, H.J. Observation of Two-Dimensional Phases Associated with Defect States on the Surface of $TiO_2$. *Phys. Rev. Lett.* **1976**, *36*, 1335–1339. [CrossRef]
23. Thompson, T.L.; Diwald, O.; Yates, J.T. $CO_2$ as a Probe for Monitoring the Surface Defects on $TiO_2$(110)Temperature-Programmed Desorption. *J. Phys. Chem. B* **2003**, *107*, 11700–11704. [CrossRef]
24. Borodin, A.; Reichling, M. Characterizing $TiO_2$(110) surface states by their work function. *Phys. Chem. Chem. Phys.* **2011**, *13*, 15442–15447. [CrossRef] [PubMed]
25. Klein, A.; Körber, C.; Wachau, A.; Säuberlich, F.; Gassenbauer, Y.; Schafranek, R.; Harvey, S.P.; Mason, T.O. Surface Potentials of Magnetron Sputtered Transparent Conducting Oxides. *Thin Solid Films* **2009**, *518*, 1197–1203. [CrossRef]
26. Goniakowski, J.; Finocchi, F.; Noguera, C. Polarity of oxide surfaces and nanostructures. *Rep. Prog. Phys.* **2008**, *71*, 016501. [CrossRef]
27. Ishii, H.; Sugiyama, K.; Ito, E.; Seki, K. Energy Level Alignment and Interfacial Electronic Structures at Organic/Metal and Organic/Organic Interfaces. *Adv. Mater.* **1999**, *11*, 605–625. [CrossRef]
28. Batzill, M.; Diebold, U. The surface and materials science of tin oxide. *Prog. Surf. Sci.* **2005**, *79*, 47–154. [CrossRef]
29. Klein, A.; Körber, C.; Wachau, A.; Säuberlich, F.; Gassenbauer, Y.; Harvey, S.P.; Proffit, D.E.; Mason, T.O. Transparent Conducting Oxides for Photovoltaics: Manipulation of Fermi Level, Work Function, and Energy Band Alignment. *Materials* **2010**, *3*, 4892–4914. [CrossRef] [PubMed]
30. Hohmann, M.V.; Ágoston, P.; Wachau, A.; Bayer, T.J.M.; Brötz, J.; Albe, K.; Klein, A. Orientation Dependent Ionization Potential of $In_2O_3$: A Natural Source for Inhomogeneous Barrier Formation at Electrode Interfaces in Organic Electronics. *J. Phys. Condens. Matter* **2011**, *23*, 334203. [CrossRef] [PubMed]
31. Wardenga, H.; Klein, A. Surface Potentials of (111), (110) and (100) oriented $CeO_{2-x}$ thin films. *Appl. Surf. Sci.* **2016**, *377*, 1–8. [CrossRef]
32. Morgan, B.J.; Watson, G.W. A Density Functional Theory + U Study of Oxygen Vacancy Formation at the (110), (100), (101), and (001) Surfaces of Rutile $TiO_2$. *J. Phys. Chem. C* **2009**, *113*, 7322–7328. [CrossRef]
33. Cheng, H.; Selloni, A. Surface and subsurface oxygen vacancies in anatase $TiO_2$ and differences with rutile. *Phys. Rev. B* **2009**, *79*, 092101. [CrossRef]
34. Li, H.; Guo, Y.; Robertson, J. Calculation of $TiO_2$ Surface and Subsurface Oxygen Vacancy by the Screened Exchange Functional. *J. Phys. Chem. C* **2015**, *119*, 18160–18166. [CrossRef]
35. He, Y.; Dulub, O.; Cheng, H.; Selloni, A.; Diebold, U. Evidence for the Predominance of Subsurface Defects on Reduced Anatase $TiO_2(101)$. *Phys. Rev. Lett.* **2009**, *102*, 106105. [CrossRef] [PubMed]
36. Bahnemann, D. Photocatalytic water treatment: solar energy applications. *Solar Energy* **2004**, *77*, 445–459. [CrossRef]
37. Fujishima, A.; Zhang, X.; Tryk, D.A. $TiO_2$ photocatalysis and related surface phenomena. *Surf. Sci. Rep.* **2008**, *63*, 515–582. [CrossRef]
38. De Angelis, F.; Valentin, C.D.; Fantacci, S.; Vittadini, A.; Selloni, A. Theoretical Studies on Anatase and Less Common $TiO_2$ Phases: Bulk, Surfaces, and Nanomaterials. *Chem. Rev.* **2014**, *114*, 9708–9753. [CrossRef] [PubMed]
39. Bourikas, K.; Kordulis, C.; Lycourghiotis, A. Titanium Dioxide (Anatase and Rutile): Surface Chemistry, Liquid-Solid Interface Chemistry, and Scientific Synthesis of Supported Catalysts. *Chem. Rev.* **2014**, *114*, 9754–9823. [CrossRef] [PubMed]
40. Pang, C.L.; Lindsay, R.; Thornton, G. Chemical reactions on rutile $TiO_2$(110). *Chem. Soc. Rev.* **2008**, *37*, 2328–2353. [CrossRef] [PubMed]
41. Hussain, H.; Tocci, G.; Woolcot, T.; Torrelles, X.; Pang, C.L.; Humphrey, D.S.; Yim, C.M.; Grinter, D.C.; Cabailh, G.; Bikondoa, O.; et al. Structure of a model $TiO_2$ photocatalytic interface. *Nat. Mater.* **2017**, *16*, 461. [CrossRef] [PubMed]
42. Vittadini, A.; Selloni, A.; Rotzinger, F.P.; Grätzel, M. Structure and Energetics of Water Adsorbed at $TiO_2$ Anatase (101) and (001) Surfaces. *Phys. Rev. Lett.* **1998**, *81*, 2954–2957. [CrossRef]
43. Aschauer, U.; He, Y.; Cheng, H.; Li, S.C.; Diebold, U.; Selloni, A. Influence of Subsurface Defects on the Surface Reactivity of $TiO_2$: Water on Anatase (101). *J. Phys. Chem. C* **2010**, *114*, 1278–1284. [CrossRef]

44. Li, Y.; Gao, Y. Interplay between Water and $TiO_2$ Anatase (101) Surface with Subsurface Oxygen Vacancy. *Phys. Rev. Lett.* **2014**, *112*, 206101. [CrossRef]
45. Jackman, M.J.; Thomas, A.G.; Muryn, C. Photoelectron Spectroscopy Study of Stoichiometric and Reduced Anatase $TiO_2$(101) Surfaces: The Effect of Subsurface Defects on Water Adsorption at Near-Ambient Pressures. *J. Phys. Chem. C* **2015**, *119*, 13682–13690. [CrossRef]
46. Liu, L.; Zhao, H.; Andino, J.M.; Li, Y. Photocatalytic $CO_2$ Reduction with $H_2O$ on $TiO_2$ Nanocrystals: Comparison of Anatase, Rutile, and Brookite Polymorphs and Exploration of Surface Chemistry. *ACS Catal.* **2012**, *2*, 1817–1828. [CrossRef]
47. Duncan, D.; Allegretti, F.; Woodruff, D. Water does partially dissociate on the perfect $TiO_2$ (110) surface: A quantitative structure determination. *Phys. Rev. B* **2012**, *86*, 045411. [CrossRef]
48. Walle, L.E.; Borg, A.; Uvdal, P.; Sandell, A. Experimental evidence for mixed dissociative and molecular adsorption of water on a rutile $TiO_2$ (110) surface without oxygen vacancies. *Phys. Rev. B* **2009**, *80*, 235436. [CrossRef]
49. Mu, R.; Zhao, Z.J.; Dohnálek, Z.; Gong, J. Structural motifs of water on metal oxide surfaces. *Chem. Soc. Rev.* **2017**, *46*, 1785–1806. [CrossRef] [PubMed]
50. Patrick, C.E.; Giustino, F. Structure of a water monolayer on the anatase $TiO_2$ (101) surface. *Phys. Rev. Appl.* **2014**, *2*, 014001. [CrossRef]
51. Henrion, O.; Klein, A.; Pettenkofer, C.; Jaegermann, W. Low temperature adsorption of water on cleaved GaAs(110) surfaces. *Surf. Sci. Lett.* **1996**, *366*, L685. [CrossRef]
52. Klein, A. Interface Properties of Dielectric Oxides. *J. Am. Ceram. Soc.* **2016**, *99*, 369–387. [CrossRef]
53. Wendt, S.; Sprunger, P.T.; Lira, E.; Madsen, G.K.H.; Li, Z.; Hansen, J.O.; Matthiesen, J.; Blekinge-Rasmussen, A.; Lægsgaard, E.; Hammer, B.; et al. The Role of Interstitial Sites in the Ti3d Defect State in the Band Gap of Titania. *Science* **2008**, *320*, 1755–1759. [CrossRef] [PubMed]
54. Li, M.; Hebenstreit, W.; Gross, L.; Diebold, U.; Henderson, M.A.; Jennison, D.R.; Schultz, P.A.; Sears, M.P. Oxygen-induced restructuring of the $TiO_2$(110) surface: A comprehensive study. *Surf. Sci.* **1999**, *437*, 173–190. [CrossRef]
55. Wu, C.C.; Wu, C.I.; Sturm, J.C.; Kahn, A. Surface modification of indium tin oxide by plasma treatment: An effective method to improve the efficiency, brightness, and reliability of organic light emitting devices. *Appl. Phys. Lett.* **1997**, *70*, 1348. [CrossRef]
56. Klissurski, D.; Hadjiivanov, K.; Kantcheva, M.; Gyurova, L. Study of peroxide-modified titanium dioxide (anatase). *J. Chem. Soc. Faraday Trans.* **1990**, *86*, 385–388. [CrossRef]
57. Iwamoto, M.; Yoda, Y.; Yamazoe, N.; Seiyama, T. Study of metal oxide catalysts by temperature programmed desorption. 4. Oxygen adsorption on various metal oxides. *J. Phys. Chem.* **1978**, *82*, 2564–2570. [CrossRef]
58. Bayer, T.J.M.; Wachau, A.; Fuchs, A.; Deuermeier, J.; Klein, A. Atomic layer deposition of $Al_2O_3$ onto Sn-doped $In_2O_3$: Absence of self-limited adsorption during initial growth by oxygen diffusion from the substrate and band offset modification by Fermi level pinning in $Al_2O_3$. *Chem. Mater.* **2012**, *24*, 4503–4510. [CrossRef]
59. Klein, A. Transparent Conducting Oxides: Electronic Structure - Property Relationship from Photoelectron Spectroscopy with in-situ Sample Preparation. *J. Am. Ceram. Soc.* **2013**, *96*, 331–345. [CrossRef]
60. Idriss, H.; Barteau, M.A. Characterization of $TiO_2$ surfaces active for novel organic syntheses. *Catal. Lett.* **1994**, *26*, 123–139. [CrossRef]
61. Moulder, J.F.; Stickle, W.F.; Sobol, P.E.; Bomben, K.D. *Handbook of X-ray Photoelectron Spectroscopy*; Physical Electronics, Inc.: Eden Prairie, MN, USA, 1995.
62. Yesodharan, E.; Grätzel, M. Photodecomposition of Liquid Water with $TiO_2$? Supported Noble Metal Clusters. *Helv. Chim. Acta* **1983**, *66*, 2145–2153. [CrossRef]
63. Kodaira, S.; Sakisaka, Y.; Maruyama, T.; Haruyama, Y.; Aiura, Y.; Kato, H. Angle-resolved photoemission study of an in-gap state in $TiO_2$. *Solid State Commun.* **1994**, *89*, 9–12. [CrossRef]
64. Finazzi, E.; Valentin, C.D.; Pacchioni, G.; Selloni, A. Excess electron states in reduced bulk anatase $TiO_2$: Comparison of standard GGA, GGA+U, and hybrid DFT calculations. *J. Chem. Phys.* **2008**, *129*, 154113. [CrossRef] [PubMed]
65. Ohno, T.; Sarukawa, K.; Matsumura, M. Crystal faces of rutile and anatase $TiO_2$ particles and their roles in photocatalytic reactions. *New J. Chem.* **2002**, *26*, 1167–1170. [CrossRef]

66. Yu, J.; Low, J.; Xiao, W.; Zhou, P.; Jaroniec, M. Enhanced Photocatalytic $CO_2$-Reduction Activity of Anatase $TiO_2$ by Coexposed 001 and 101 Facets. *J. Am. Chem. Soc.* **2014**, *136*, 8839–8842. [CrossRef] [PubMed]
67. Dette, C.; Pérez-Osorio, M.A.; Kley, C.S.; Punke, P.; Patrick, C.E.; Jacobson, P.; Giustino, F.; Jung, S.J.; Kern, K. $TiO_2$ Anatase with a Bandgap in the Visible Region. *Nano Lett.* **2014**, *14*, 6533–6538. [CrossRef] [PubMed]
68. King, P.D.C.; Veal, T.D.; Fuchs, F.; Wang, C.Y.; Payne, D.J.; Bourlange, A.; Zhang, H.; Bell, G.R.; Cimalla, V.; Ambacher, O.; et al. Band gap, electronic structure, and surface electron accumulation of cubic and rhombohedral $In_2O_3$. *Phys. Rev. B* **2009**, *79*, 205211. [CrossRef]
69. Berthold, T.; Rombach, J.; Stauden, T.; Polyakov, V.; Cimalla, V.; Krischok, S.; Bierwagen, O.; Himmerlich, M. Consequences of plasma oxidation and vacuum annealing on the chemical properties and electron accumulation of $In_2O_3$ surfaces. *J. Appl. Phys.* **2016**, *120*, 245301. [CrossRef]
70. Vasheghani Farahani, S.K.; Veal, T.D.; Mudd, J.J.; Scanlon, D.O.; Watson, G.W.; Bierwagen, O.; White, M.E.; Speck, J.S.; McConville, C.F. Valence-band density of states and surface electron accumulation in epitaxial $SnO_2$ films. *Phys. Rev. B* **2014**, *90*, 155413. [CrossRef]
71. Körber, C.; Ágoston, P.; Klein, A. Surface and Bulk Properties of Sputter Deposited Intrinsic and Doped $SnO_2$ Thin Films. *Sens. Actuators B* **2009**, *139*, 665–672. [CrossRef]
72. Rachut, K.; Körber, C.; Brötz, J.; Klein, A. Growth and Surface Properties of Epitaxial $SnO_2$. *Phys. Stat. Sol. (A)* **2014**, *211*, 1997–2004. [CrossRef]
73. Batzill, M.; Katsiev, K.; Burst, J.M.; Diebold, U.; Chaka, A.M.; Delley, B. Gas-phase-dependent properties of $SnO_2$ (110), (100), and (101) single-crystal surfaces: Structure, composition, and electronic properties. *Phys. Rev. B* **2005**, *72*, 165414. [CrossRef]
74. Cox, D.F.; Fryberger, T.B.; Semancik, S. Oxygen vacancies and defect electronic states on the $SnO_2$(110)-1$\times$1 surface. *Phys. Rev. B* **1988**, *38*, 2072–2083. [CrossRef]
75. Ágoston, P.; Albe, K. Disordered reconstructions of the reduced $SnO_2$-(110) surface . *Surf. Sci.* **2011**, *605*, 714–722. [CrossRef]
76. Deák, P.; Aradi, B.; Frauenheim, T. Band Lineup and Charge Carrier Separation in Mixed Rutile-Anatase Systems. *J. Phys. Chem. C* **2011**, *115*, 3443–3446. [CrossRef]
77. Scanlon, D.O.; Dunnill, C.W.; Buckeridge, J.; Shevlin, S.A.; Logsdail, A.J.; Woodley, S.M.; Catlow, C.R.A.; Powell, M.J.; Palgrave, R.G.; Parkin, I.P.; et al. Band alignment of rutile and anatase $TiO_2$. *Nat. Mater.* **2013**, *12*, 798. [CrossRef] [PubMed]


## 3.3 Dependence of crystallographic surface orientation of rutile $TiO_2$ on band alignments of NiO/ $TiO_2$

Shun Kashiwaya conducted experiments, data analysis and preparation of the manuscript. Thierry Toupance, Andreas Klein and Wolfram Jaegermann participated in the discussions of the results and revised the manuscript.

**Title: Dependence of crystallographic surface orientation of rutile $TiO_2$ surfaces on band alignments of NiO/$TiO_2$**

*Shun Kashiwaya, Thierry Toupance, Andreas Klein, Wolfram Jaegermann**

Shun Kashiwaya
Institut des Sciences Moléculaires, ISM UMR 5255 CNRS, Université de Bordeaux,
351 Cours de la Libération, F-33405 Talence Cédex, France
Materials Science Department, Technische Universität Darmstadt, Otto Berndt Strasse 3, D-64287 Darmstadt, Germany

Prof. Dr. Thierry Toupance
Institut des Sciences Moléculaires, ISM UMR 5255 CNRS, Université de Bordeaux,
351 Cours de la Libération, F-33405 Talence Cédex, France

Prof. Dr. Andreas Klein
Materials Science Department, Technische Universität Darmstadt, Otto Berndt Strasse 3, D-64287 Darmstadt, Germany

E-mail: jaegermann@surface.tu-darmstadt.de
Prof. Dr. Wolfram Jaegermann
Materials Science Department, Technische Universität Darmstadt, Otto Berndt Strasse 3, D-64287 Darmstadt, Germany

Abstract:

$TiO_2$ is a promising material to address the energy and environmental issues in terms of photoelectrochemical reactions. Electronic properties of $TiO_2$ surfaces which play a crucial role in such reactions are drastically affected by surface stoichiometries. The surface states of $TiO_2$ are also of importance as it might govern energy band alignments of n-type $TiO_2$ and p-type NiO as a highly reactive co-catalyst among non-precious metals, which may form a p-n junction and help in separating photo-generated charge carriers. In this work, well-defined reduced and oxidized surfaces of oriented rutile (001) and (110) are prepared and their electronic properties are compared. A variation of the Fermi level is 2.6 to 3.3 eV depending upon the stoichiometry. Furthermore, energy band alignments of p-NiO/n- $TiO_2$ with above surfaces are experimentally established by in-situ photoelectron spectroscopy during stepwise deposition of NiO onto the $TiO_2$. The Fermi level of NiO is pinned a value of $E_F - E_{VB}$ between 0.5 and 0.9 eV. A steep bending on the (001) surface occurs at the thinner layer of

NiO than that on the (110) surface and completes already within a thin layer of a few nm, helping in separating the charge carriers in the nanoparticle photocatalysts.

## 1. Introduction

Among the metal oxides semiconductors, titanium dioxide ($TiO_2$) is one of the most often studied material, which has been applied in photocatalysis[1], solar energy conversion[2], and gas sensing[3]. However, the given variations in the electronic properties of different surface orientation have not been systematically investigated yet despite the expected decisive influence on device performance. Epitaxially polished $TiO_2$ substrates of different phases and orientations are commercially available. Especially the most stable rutile (110) surface has often been used to study fundamental phenomena. Hence, this well-defined surface of rutile $TiO_2$ is well known and has been often employed as the model system for the investigation of fundamental physical and chemical properties in the surface science of metal oxides[4, 5].

Oxygen vacancies have been considered as a key factor in the surface chemistry of $TiO_2$ as vacancy sites form reactive centers that dissociate adsorbed molecules on the generally inert oxides surface[6, 7]. Despite its high importance, detailed information of the interplay between the electronic properties and the oxygen vacancies at the surface of $TiO_2$ is still lacking at this point[8, 9]. Of the structural phases of $TiO_2$, anatase and rutile have attracted most attentions in view of applications. **Figure 1** displays a ball-and-stick model of the rutile (110) and (001) bulk-terminated surface without structural relaxations[10]. The (110) and (001) surfaces have the lowest and highest surface energy, respectively[11]. At rutile (110) the so-called bridging oxygen atoms miss one bond to Ti atom in the missing layer and thus can be easily removed by thermal annealing, whereas at rutile (001), oxygen vacancies are believed to be easily formed at a twofold-coordinated surface O atom similar to the (110) surface though this is still subject of debate[4, 12]. The energetic position of surface or subsurface defect states can be

deduced from experimental and theoretical studies[9, 12, 13]. Also, there are variations in ionization potential and work function. The surface and subsurface distribution of oxygen vacancies in anatase is different from that in rutile. At anatase (101) and (001), oxygen vacancies have lower formation energy in the subsurface than at the surface and thus energetically prefer to reside in the subsurface and bulk, whereas at rutile (110), oxygen vacancies form most likely at the bridging oxygen site on the surface[14]. Therefore, at anatase (101) and (001) surfaces, which are the two dominant surface orientations, a lower vacancy concentration has been found and they are more difficult to be reduced than the rutile (110)[15]. Hence, one could assume that oxygen vacancies in rutile would have more crucial impact on the electronic surface and interface properties than that in anatase. The surface electronic properties of $TiO_2$ anatase has been recently studied in our group[16]. Despite the importance of the surfaces of rutile and anatase, a clear correlation between the electronic properties and oxygen vacancies on the different surfaces of rutile and anatase cannot be given yet.

One of the dominant application of $TiO_2$ is the use as a photocatalyst due to its relatively high photocatalytic activity, low cost, nontoxicity, and chemical and physical stability against photo-corrosion and thus it has been intensively investigated[1, 4]. The photocatalytic activity is however still limited by the recombination of photogenerated electron and hole pairs probably on surface defects[17]. Ohno *et al.*[18] investigated the selective deposition of Pt and $PbO_2$ on specific facets of rutile and anatase particles. These studies indicate that the different crystal facets of $TiO_2$ possess different electronic properties and help to separate photoinduced electrons and holes[18]. This effect seems to be stronger for rutile than for anatase. Heterostructures of $TiO_2$ to metals or semiconductors have been developed for many oxide semiconductors in order to separate the charge carriers efficiently at the interface, resulting in more effective photocatalysis[19, 20]. Recently many efforts have been extended to elucidate the effect of co-catalysts selectively deposited onto the surfaces of semiconductor

photocatalysts forming Schottky or p-n junction at the interface, which may help in separating the photoexcited charge carriers[20, 21, 22]. Also here different facets are considered to influence the contact properties[22]. However, little information on the role of specific orientations in the contact formation of heterostructures is available yet. The work function and related Fermi level position are a crucial property when two materials form a contact since it governs the band alignment at the interface. For metal oxides, the value of the work function can be controlled effectively by determining surface density of states and the related surface potentials of a specific surface orientation[23]. With contact formation the relative influence of the surface dipole or local space charge layers will determine charge carrier flow. Among these factors, the oxygen stoichiometry plays a crucial role. Hence, the conditions of the metal oxide surface should be taken into consideration in contact formation. However, both experimental and theoretical studies on the interplay between the surface condition and resulting band alignments at the interface of metal oxides are still sparse despite some recent results from our group[20, 24].

In this work, as a first step we have investigated reduced and oxidized surfaces of rutile (110) and (001) substrates by X-ray photoelectron spectroscopy (XPS) and Ultraviolet photoelectron spectroscopy (UPS) measurements. The electronic properties of heterostructures consisting of p-type NiO and n-type rutile (110) and (001) interfaces, where a p-n junction may form and contribute to separating the photo-excited charge carriers vectorially, are investigated in order to determine the energy band alignment of the NiO/rutile junction and elucidate the effect of the surface condition. Interface experiments [25, 26] are carried out by XPS and UPS measurements during in-situ stepwise NiO film deposition using DC sputtering on reduced and oxidized rutile substrates. Thus, four band alignments of NiO/reduced rutile (110), NiO/reduced rutile (001), NiO/oxidized rutile (110), and NiO/oxidized rutile (001) are experimentally established.

## 2. Result and discussion

### 2.1. Reduced and oxidized rutile substrates

For reduced and oxidized surfaces of the rutile (110) and (001) substrates, XPS spectra of the Ti2$p_{3/2}$ and O1s core level emission lines and valence band region, and UPS spectra of a secondary electron edge and the valence band region are shown in Figure 2 and 3, respectively. The work function $\Phi$ and ionization potential $I_P$ of the rutile substrates were determined from the binding energies of the secondary electron edge $E_{SE}$ according to $\Phi = h\nu - E_{SE}$ and valence band maximum $E_{VBM}$ according to $I_P = E_{Vac} - E_{VBM,}$ respectively. Table 1 summarizes the obtained values of binding energies of Ti2$p_{3/2}$ and O1s, valence band maximum, work function, and ionization potential.

The values of the $E_{VBM}$ onsets are determined by applying a linear extrapolation for the edge of the valence band emission obtained by XPS. The valence band spectra of XPS show that the Fermi level of 3.12 eV of the reduced rutile (110) is decreased to 2.68 eV with surface oxidation. A similar shift was observed for the (001) surface. The lower Fermi level position of the oxidized rutile can be attributed to the removal of intrinsic oxygen vacancies on the surface after the annealing step. Generally, oxygen vacancies give rise to so called band gap states (BGS), which forms at a binding energy of around 1 eV due to occupied Ti 3d states on $Ti^{3+}$ sites near the surface vacancy sites, but also $Ti^{3+}$ interstitial states in the subsurface region[15, 16, 27, 28]. For the reduced rutile of both orientations, the valence band spectra of UPS show a shoulder peak corresponding to the BGS in the band gap region even though no evident emission from the $Ti^{3+}$ related BGS are found in the valence band spectra of XPS. More pronounced emissions from oxygen vacancies located within the bandgap of $TiO_2$ is clearly evident only from the very sensitive resonant photoelectron spectroscopy[15, 16].

The secondary electron cut off exhibits steep slopes in all UPS spectra shown in Figure 3. Hence, its energetic position was determined accurately. It is noteworthy that there are two intense peaks at 16.8 and 15.1 eV near the secondary electron cutoff in UPS spectra and the one at the higher binding energy disappears after oxidation. The oxidized rutile exhibits a drastically higher work function of 6.0-6.1 eV compared to 4.3-4.4 eV of the reduced surfaces. The huge shift of work function is attributed to clearly different surface terminations. Electronegative oxygen accumulates with a negative charge on the O plasma treated surface, resulting in the low and high value of work function of reduced and oxidized surfaces, respectively[29]. Note that previously reported highest values of the work function determined by UPS and two-photon photoemission spectroscopy are between 5.3-5.5 eV[9, 30] and 5.5-5.8 eV[7], respectively. This indicates a high density of adsorbed oxygen ions, which is expected to be peroxo species, on the oxidized surface after oxygen plasma treatment. Peroxo species formed at the surface after oxygen plasm treatment are also expected to explain the additional O1s emission line at binding energy of 533.1 eV. The Ti atom on the surface is prone to form peroxo complexes with excited oxygen atoms from the plasma[31]. Characteristics of such peroxo species on rutile are not well understood. Pesoxo species on anatase were found to transform to a so-called bridging dimer via reaction with surface or subsurface oxygen vacancies[32]. We tend to exclude $H_2O$ or OH adsorbates because of our in-situ UHV approach even though it was found based on STM works that residual moisture in UHV chamber can adsorb on the surface[33], which however could not increase the work function. The work function of the reduced rutile (001) is lower than that of reduced rutile (110) by 120 meV. This might be due to more oxygen vacancies at the (001) than at the (110) surface. It has been expected that oxygen vacancies form more likely on the (001) surface rather than the (110) surface[12]. Band diagrams of different $TiO_2$ substrates obtained by above XPS and UPS are shown in figure 4.

The Ti2p and O1s core levels of reduced rutile, which show a binding energy at 459.4 and 530.7 eV, respectively, also shift in parallel after oxidation towards lower binding energy by 0.4-0.6 eV corresponding to Fermi level shifts for the both (110) and (001) surfaces (Figure 2). It is widely accepted that a shoulder peak related to $Ti^{3+}$ at the lower binding energy of the main peak of the $Ti^{4+}$ emission shifted by around 1.7 eV appears with the oxygen deficiencies[15, 28]. However, in our case the $Ti2p_{3/2}$ line show sharp and symmetric shapes consisting of dominant $Ti^{4+}$ oxidation state even after reduction. No clear emission from the shoulder peaks is observed, indicating rather low $Ti^{3+}$ concentrations.

### 2.2. NiO/rutile $TiO_2$ heterostructures

To get an improved understanding of the interface properties of NiO/rutile heterojunction, in-situ interface experiments were carried out by XPS and UPS measurements after each deposition steps of NiO with increasing thickness onto the reduced and oxidized rutile (110) and (001) substrates. Figure 5 presents the core level photoelectron spectra recorded during the stepwise deposition for the oxidized rutile (110) (spectra for other substrates are shown in figure S1 in supplementary information). The emission of Ti2p shows the typical doublet peak and but only the $Ti2p_{3/2}$ line is used to follow the peak shift during the deposition. The identification and interpretation of the NiO spectra are complicated due to complex main line splitting caused by multiplet contributions and satellite structures at higher binding energies. Binding energies of 852.6, 854.6, and 856.1 eV are assigned to $Ni2p_{3/2}$ spectra for Ni, $Ni^{2+}$, and $Ni^{3+}$, respectively[34]. The spectral feature within the main satellite at binding energy of around 861 eV indicates that mostly NiO is deposited already from the very beginning of the deposition sequence. The shoulder appearing at 1.5 eV higher binding energy compared to the main emission is related to a satellite emission of the $Ni^{2+}$ rather than $Ni^{3+}$ species. This satellite is known as a nonlocal screening satellite and appears by a screening process due to oxygen atoms belonging to the octahedral $NiO_6$ coordination clusters[35]. However, at a low

coverage of NiO, a broad emission is evident and can be related to the nonlocal satellite emissions associated with imperfect octahedra due to surface effects[36]. For thicker layers, the typical NiO emission signature is obtained. The contribution of both the nonlocal and surface effect results in difficulties to determine the exact binding energy peak position. Therefore, the main satellite peak of $Ni2p_{3/2}$ at about 7 eV higher binding energy from the main line of $Ni2p_{3/2}$, which is characteristic for $Ni^{2+}$, is adopted instead of the main peak for following the peak shift in the course of NiO deposition.

The $Ti2p_{3/2}$ peak in Figure 5 is rather sharp and symmetric indicating a mostly stoichiometric surface with dominant $Ti^{4+}$ oxidation state. However, there is a clear tendency of an increase of the asymmetry of the Ti2p line to lower binding energy for all heterointerfaces, which may indicate a slight increase of $Ti^{3+}$ states during NiO deposition. A reduction of $TiO_2$ substrates is often accompanied by oxidation of the overlayer metals or metal oxides when the overlayer is deposited onto the $TiO_2$ substrates[4]. However, the heat of formation of the most stable Ni oxides (NiO) indicate that such a substrate reduction is not thermodynamically preferable as the heat of NiO formation of -250 kJ/mol is more positive than the change in the standard free energy of -364 or -483 kJ/mol at room temperature for the formation of lower oxidation states as $Ti^{3+}$ or $Ti^{2+}$, respectively[37]. In the O1s region, there are two shoulder peaks observed. The first shoulder at a higher binding energy than the main peak of 3.0 eV is assigned to peroxo species on the top of the rutile substrates, which disappears immediately after the first NiO deposition. The second one at a higher binding energy than the main peak by 2.3 eV might be attributed to the initial formation of the O poor surface species, which should show a higher binding energy.

For all the four cases of NiO and different rutile heterostructures, the spectral changes of the $TiO_2$ substrates and growing NiO films are very similar to each other (see figure S1 in

supplementary information). The evolution of the Fermi level ($E_F - E_{VBM}$) of NiO and rutile substrates obtained by following the core level of Ni2p satellite and Ti2p$_{3/2}$, respectively, is shown in Figure 6. The values of $E_F - E_{VBM}$ of uncovered rutile substrates and the NiO top layer correspond to the values of $E_{VB}$ as determined from the valence band spectra. The Fermi level of both NiO and rutile shifts to lower binding energy in parallel. This indicates that band bending occurs only in the rutile substrates and the emission line of Ni2p just follows the band bending in rutile. For the reduced samples, the Fermi level of $TiO_2$ shifts in two steps for both orientations. A first and immediate Fermi level shift of about 0.6 eV occurs after the first deposition step. We assign this to the oxidation of the rutile substrates, which is caused by the sputter conditions. This shift corresponds to the Fermi level difference $E_F - E_{VBM}$ of reduced and oxidized rutile substrates. A second Fermi level shift occurs due to a contact formation between NiO and rutile forming the p-n junction leading to band bending in contact. For the oxidized samples, both orientations do not show the initial Fermi level shifts. Only the Fermi level shifts, which are induced by the contact formation between NiO and rutile, were observed. As is clear from Figure 6, the band bending saturates at a thinner NiO thickness for the rutile (001) compared to the rutile (110) for both reduced and oxidized substrates. This might be related to higher oxygen vacancy concentration as these are expected to form easily at the (001) surface. These electrons containing defects states are related to the $O^{2-}$ vacancies, which are correlated with $Ti^{3+}$ $3d^1$ electron states of $Ti^{3+}$ surface sites. It has been shown by resonance photoelectron spectroscopy that these states do also exist on $TiO_2$ surface up to 1/3 of a monolayer even when they can hardly be identified by standard XPS[15, 38]. Thermal equilibrium of electrons with the Fermi level of the growing NiO could thus be easily completed for the (001) surface. Therefore, the bending on the (001) surface starts and completes at the thinner layer of NiO. It is worth mentioning that the Fermi level of rutile finally reaches the same value of about 1.6 eV independent of surface orientation and treatment.

The work function of the uncovered rutile substrates and top layers of deposited NiO was derived from the binding energies of the secondary electron edge $E_{SE}$ according to $\Phi = h\nu - E_{SE}$. The work function of NiO on the reduced rutile (110) and (001) substrates is 5.15 and 5.10 eV whereas that on the oxidized rutile (110) and (001) substrates is 5.31 and 5.38 eV, respectively. The higher value of the work function of NiO on the oxidized rutile might be attributed to mainly the formation of $O_2^{2-}$ surface adsorbates of which the value of work function is higher than that of NiO without surface adsorbates, and possibly a change in the ionization potential of NiO that corresponds to a change of the $O_2^{2-}$ induced surface dipole related to the stoichiometric surface termination.

Finally, the band alignments at the interface of NiO/reduced rutile (110) and NiO/oxidized rutile (110) as experimentally established using above data are shown in Figure 7 (band alignments for the rutile (001) are shown in figure S2 in supplementary information). As is evident from these diagrams, the overall trend of the development of space charge layers in the two materials in contact of p-doped NiO and n-doped $TiO_2$ are hardly affected by the pre-treatment induced differences. Evidently in p-NiO the Fermi level is pinned by a high concentration of defect states ($Ni^{3+}$ related states) in the bulk of the material as there is no additional band bending found in the NiO layers. The pinning level is found at a value of $E_F - E_{VBM}$ between 0.5 and 0.9 eV.

The Fermi level of n-$TiO_2$ is shifted downward with the deposition of p-NiO as it is expected for the contact formation between a p-doped and a n-doped semiconductor. However, the distribution of the original differences in work function $\Phi_{NiO} - \Phi_{TiO2}$ shows two different distribution. At first for the low NiO coverage a strong interfacial dipole $\delta$ develops and its

value is larger for the oxidized $TiO_2$ of both surface orientations. This surface dipole is evidently due to the peroxo induced increase of work function of the oxidized surfaces. Also, on the band alignment a difference of valence band levels between NiO and the different $TiO_2$ surfaces is found to be reduced for the oxidized $TiO_2$. We attribute these facts to a modification of the NiO deposition in the low coverage regime, which is also related to the later onset of a well-defined overlayer Fermi level formation (see Figure 6). The band bending in the $TiO_2$ is found to be larger for the higher doped $n^+$-$TiO_2$ (reduced rutile) as to be expected from its original Fermi level position within the conduction band. There are additional small deviations in the interfacial surface potential differences of the four different cases. However, if these are mostly due to intrinsic differences in band alignment or extrinsic differences to different concentration of interfacial defects related to processing effects cannot be concluded from the given set of experiments. Despite these facts there is a still a dominant factor valid for all interfaces. The deposition of NiO leads to strong band bending within the $TiO_2$ substrates already for thin NiO layers, which would contribute to charge carrier separation in photocatalytic particles.

## 3. Conclusion

We have compared the surface potentials of rutile $TiO_2$ (001) and (110) surfaces with reduced and oxidized conditions. The Fermi position varies from 2.6-2.7 to 3.1 eV upon the amount of oxygen vacancies introduced by different surface pre-treatment to prepare clean surfaces. Work function exhibits an even larger variation from 4.3 to 6.0-6.1 eV due to the surface adsorbate of poroxo species in addition to the difference of the Fermi level position. However, no noticeable difference in the Fermi level position and work function between the two facets are observed.

We have also experimentally established energy band diagrams of p-NiO and n-type rutile $TiO_2$ (001) and (110) with reduced and oxidized surfaces. The results indicate that one has to take into account the surface condition when considering the band alignments. The Fermi level of NiO is pinned at a value of $E_F - E_{VB}$ between 0.5 and 0.9 eV. Although there is no difference in the final energy band alignments between the two facets, the bending on the (001) surface occurs at the thinner layer of NiO than that on the (110) surface. The steep band bending on the (001) surface completes already within a thin layer of a few nm and help in separating the charge carriers in the nanoparticle photocatalysts.

## 4. Experimental Section

### 4.1. Reduced rutile substrate preparation

Epitaxially polished rutile (110) and (001) substrates were purchased from Crystec GmbH (Berlin, Germany). The size of the substrates is 5 x 5 x 1 mm. Surface defect states can be controlled by annealing temperature. The most reduced surface is expected for annealing in vacuum, which can be performed up to at temperatures of 900 K without ruining the morphology[8]. In this work, reduced rutile (110) and (001) substrates were prepared by annealing at 773 K and oxygen partial pressure of 0.5 Pa for 2 hours, followed by annealing at 873 K in vacuum for 1 hour. The colour of the substrates changes from transparent into dark blue after reduction. As well known, thermal annealing in vacuum at an elevated temperature generates surface oxygen vacancies, which are mostly located in the bridging oxygen row for the rutile surface[39]. The n-type doping by introduction of bulk oxygen vacancies results in a high conductivity, which avoids a charging problem with XPS and UPS.

### 4.2. Oxidized rutile substrate preparation

Oxidized surfaces were prepared by the above reduction procedure at first in order to make them conductive. The samples were subsequently exposed to an oxygen plasma for 15

minutes at room temperature. The resulting surface is expected to be a quasi-stoichiometric surface as it is nearly impossible to avoid oxygen vacancies completely. We use the oxygen plasma to oxidize the surface instead of annealing them at an elevated temperature in oxygen. Imperfect complex features such as rosettes or strands can form when reduced $TiO_2$ substrates are re-oxidized at high temperature in oxygen[40]. Moreover, the competition of bulk vacancy formation and surface oxidation cannot be easily controlled[4, 41].

### 4.3. NiO/rutile heterostructure preparation

NiO was grown on reduced and oxidized rutile (110) and (001) substrates using a direct current (DC) reactive magnetron sputter deposition from a metallic Ni target with 40 W of DC power under 20 % $O_2$/ 80 % Ar mixture atmosphere at 0.5 Pa pressure and room temperature. The gas flow of oxygen and argon is kept of 4 and 16 sccm, respectively, during the deposition. The target-to-substrate distance was set to 8.4 cm. The deposition rate is about 2.0 nm/min. We are aware of possibly additional defect states induced by sputter deposition of oxides. However, a number of systematic studies on different oxides have proven that for our experimental conditions this approach seems applicable[26].

### 4.4. Characterization method

The experiments were carried out in the Darmstadt integrated system for materials research (Daisy-Mat) equipped with a multitechnique surface analysis system (Physical Electronics PHI 5700) capable of XPS and UPS and different deposition chambers. This system allows the in-situ characterization of the prepared surfaces and interfaces. XPS spectra were recorded with monochromatic Al Kα radiation at an emission angle of 45° and a pass energy of 5.85 eV, which gives a total energy resolution of 0.4 eV, as determined from the Gaussian broadening of the Fermi edge of a sputter-cleaned Ag sample. Binding energies of core levels and valence band maximum can be determined with an accuracy of 50 meV and 100 meV,

respectively. For the determination of work function and ionization potentials, UPS spectra were recorded in normal emission with He I radiation ($h\nu$ =21.2 eV) from a He discharge lamp and a negative sample bias of 4.0 V. The total energy resolution is 0.2 eV. No charging problems were observed during the XPS and UPS measurement. Binding energies obtained by XPS and UPS were calibrated by the Fermi level energy of the sputter-cleaned Ag sample. Hence, all the binding energies are given with respect to the calibrated Fermi level position set to 0 eV. More details of the Daisy-Mat system, which unfortunately does not contain a LEED setup, and the experimental approach in performing the experiments may be found elsewhere[25, 26].

The reduced and oxidized rutile (110) and (001) surfaces were studied by in-situ XPS and UPS measurements without breaking the vacuum. Afterwards, in order to obtain the band alignment of NiO and the rutile substrates, interface experiments were performed in Daisy-M at. After each stepwise deposition of NiO onto the rutile substrates, XPS spectra were recorded without breaking vacuum to follow shifts of the binding energies of core level emission lines and the evolution of peak shapes. Thus, the energy band alignments of NiO/reduced rutile(110), NiO/reduced rutile(001), NiO/oxidized rutile(110), and NiO/oxidized rutile(001) heterostructures were experimentally established.

**Acknowledgements**

This work was performed within the framework of EMMI (European Multifunctional Material Institute) and was partially funded by the “Université Franco-allemande” (German-French Doctoral College in Functional Materials) and the European Commission (S. K. Fellowship, Erasmus Mundus IDS-FunMat).

References

[1] A. Fujishima, X. Zhang, D. Tryk, *Surface Science Reports* **2008**, 63, 515.

[2] M. Gratzel, *Inorg Chem* **2005**, 44, 6841.

[3] D. Kohl, *J Phys D Appl Phys* **2001**, 34, R125.

[4] U. Diebold, *Surface Science Reports* 2003, 48, 53.

[5] V. E. Henrich, P. A. Cox, *The surface science of metal oxides*, Cambridge University Press, Cambridge **1996**.

[6] M. A. Henderson, W. S. Epling, C. L. Perkins, C. H. F. Peden, U. Diebold, *The Journal of Physical Chemistry B* **1999**, 103, 5328.

[7] K. Onda, B. Li, H. Petek, *Physical Review B* **2004**, 70.

[8] T. L. Thompson, O. Diwald, J. T. Yates, *The Journal of Physical Chemistry B* **2003**, 107, 11700.

[9] A. Borodin, M. Reichling, *Phys Chem Chem Phys* **2011**, 13, 15442.

[10] K. Momma, F. Izumi, *Journal of Applied Crystallography* **2008**, 41, 653.

[11] M. Ramamoorthy, D. Vanderbilt, R. D. King-Smith, *Physical Review B* **1994**, 49, 16721.

[12] B. J. Morgan, G. W. Watson, *The Journal of Physical Chemistry C* **2009**, 113, 7322.

[13] a) H. Cheng, A. Selloni, *Physical Review B* **2009**, 79; b) Z. Wang, B. Wen, Q. Hao, L. M. Liu, C. Zhou, X. Mao, X. Lang, W. J. Yin, D. Dai, A. Selloni, X. Yang, *J Am Chem Soc* **2015**, 137, 9146.

[14] Y. He, O. Dulub, H. Cheng, A. Selloni, U. Diebold, *Phys Rev Lett* **2009**, 102, 106105.

[15] A. Thomas, W. Flavell, A. Mallick, A. Kumarasinghe, D. Tsoutsou, N. Khan, C. Chatwin, S. Rayner, G. Smith, R. Stockbauer, *Physical Review B* **2007**, 75, 035105.

[16] P. Reckers, M. Dimamay, J. Klett, S. Trost, K. Zilberberg, T. Riedl, B. A. Parkinson, J. Brötz, W. Jaegermann, T. Mayer, *The Journal of Physical Chemistry C* **2015**, 119, 9890.

[17] P. V. Kamat, *J Phys Chem Lett* **2012**, 3, 663.

[18] T. Ohno, K. Sarukawa, M. Matsumura, *New Journal of Chemistry* **2002**, 26, 1167.

[19] a) A. L. Linsebigler, G. Lu, J. T. Yates, *Chemical Reviews* **1995**, 95, 735; b) F. E. Osterloh, *Chem Soc Rev* **2013**, 42, 2294.

[20] a) M. T. Uddin, Y. Nicolas, C. Olivier, T. Toupance, M. M. Müller, H.-J. Kleebe, K. Rachut, J. Ziegler, A. Klein, W. Jaegermann, *The Journal of Physical Chemistry C* **2013**, 117, 22098; b) M. T. Uddin, Y. Nicolas, C. Olivier, T. Toupance, L. Servant, M. M. Muller, H. J. Kleebe, J. Ziegler, W. Jaegermann, *Inorg Chem* **2012**, 51, 7764.

[21] a) R. Li, H. Han, F. Zhang, D. Wang, C. Li, *Energy Environ. Sci.* **2014**, 7, 1369; b) L. Ye, Y. Su, X. Jin, H. Xie, C. Zhang, *Environmental Science: Nano* **2014**, 1.

[22] G. Liu, J. C. Yu, G. Q. Lu, H. M. Cheng, *Chem Commun (Camb)* **2011**, 47, 6763.

[23] a) H. Ishii, K. Sugiyama, E. Ito, K. Seki, *Advanced Materials* **1999**, 11, 605; b) H. F. Wardenga, A. Klein, Applied Surface Science **2016**, 377, 1; c) M. Batzill, U. Diebold, *Progress in Surface Science* **2005**, 79, 47; d) E. L. Bruner, N. Koch, A. R. Span, S. L. Bernasek, A. Kahn, J. Schwartz, *Journal of the American Chemical Society* **2002**, 124, 3192; e) A. Klein, C. Körber, A. Wachau, F. Säuberlich, Y. Gassenbauer, R. Schafranek, S. P. Harvey, T. O. Mason, *Thin Solid Films* **2009**, 518, 1197.

[24] S. Li, F. Chen, R. Schafranek, T. J. M. Bayer, K. Rachut, A. Fuchs, S. Siol, M. Weidner, M. Hohmann, V. Pfeifer, J. Morasch, C. Ghinea, E. Arveux, R. Günzler, J. Gassmann, C. Körber, Y. Gassenbauer, F. Säuberlich, G. V. Rao, S. Payan, M. Maglione, C. Chirila, L. Pintilie, L. Jia, K. Ellmer, M. Naderer, K. Reichmann, U. Böttger, S. Schmelzer, R. C. Frunza, H. Uršič, B. Malič, W.-B. Wu, P. Erhart, A. Klein, *physica status solidi (RRL) - Rapid Research Letters* **2014**, 8, 571.

[25] A. Klein, *Thin Solid Films* **2012**, 520, 3721.

[26] D. Ensling, A. Thißen, Y. Gassenbauer, A. Klein, W. Jaegermann, *Advanced Engineering Materials* **2005**, 7, 945.

[27] S. Kodaira, Y. Sakisaka, T. Maruyama, Y. Haruyama, Y. Aiura, H. Kato, *Solid State Communications* **1994**, 89, 9.

[28] Z. Zhang, S.-P. Jeng, V. E. Henrich, *Physical Review B* **1991**, 43, 12004.

[29] C. Dette, M. A. Perez-Osorio, C. S. Kley, P. Punke, C. E. Patrick, P. Jacobson, F. Giustino, S. J. Jung, K. Kern, *Nano Lett* **2014**, 14, 6533.

[30] a) Y. W. Chung, W. J. Lo, G. A. Somorjai, *Surface Science* **1977**, 64, 588; b) H. Onishi, T. Aruga, C. Egawa, Y. Iwasawa, *Surface Science* **1988**, 193, 33.

[31] E. Yesodharan, M. Grätzel, *Helvetica Chimica Acta* **1983**, 66, 2145.

[32] a) M. Setvin, U. Aschauer, P. Scheiber, Y. F. Li, W. Hou, M. Schmid, A. Selloni, U. Diebold, *Science* **2013**, 341, 988; b) M. Setvin, B. Daniel, U. Aschauer, W. Hou, Y. F. Li, M. Schmid, A. Selloni, U. Diebold, *Phys Chem Chem Phys* **2014**, 16, 21524.

[33] S. Wendt, R. Schaub, J. Matthiesen, E. K. Vestergaard, E. Wahlström, M. D. Rasmussen, P. Thostrup, L. Molina, E. Lægsgaard, I. Stensgaard, *Surface Science* **2005**, 598, 226.

[34] A. P. Grosvenor, M. C. Biesinger, R. S. C. Smart, N. S. McIntyre, *Surface Science* **2006**, 600, 1771.

[35] M. A. van Veenendaal, G. A. Sawatzky, *Phys Rev Lett* **1993**, 70, 2459.

[36] L. Soriano, I. Preda, A. Gutiérrez, S. Palacín, M. Abbate, A. Vollmer, *Physical Review B* **2007**, 75.

[37] C. T. Campbell, *Surface Science Reports* **1997**, 27, 1.

[38] A. G. Thomas, W. R. Flavell, A. R. Kumarasinghe, A. K. Mallick, D. Tsoutsou, G. C. Smith, R. Stockbauer, S. Patel, M. Grätzel, R. Hengerer, *Physical Review B* **2003**, 67.

[39] a) J. M. Pan, B. L. Maschhoff, U. Diebold, T. E. Madey, *Journal of Vacuum Science & Technology A: Vacuum, Surfaces, and Films* **1992**, 10, 2470; b) C. Lun Pang, R. Lindsay, G. Thornton, *Chem Soc Rev* **2008**, 37, 2328; c) O. Bikondoa, C. L. Pang, R. Ithnin, C. A. Muryn, H. Onishi, G. Thornton, *Nature Materials* **2006**, 5, 189.

[40] a) M. Li, W. Hebenstreit, U. Diebold, M. A. Henderson, D. R. Jennison, *Faraday Discussions* **1999**, 114, 245; b) E. Asari, R. Souda, *Physical Review B* **1999**, 60, 10719.

[41] H. Onishi, Y. Iwasawa, *Phys Rev Lett* **1996**, 76, 791.

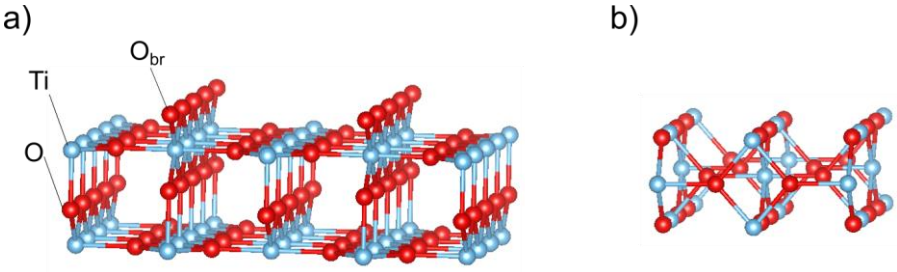


**Figure 1.** Ball and stick model of the unrelaxed bulk-terminated surface structures of a) rutile (110) and b) (001) surfaces

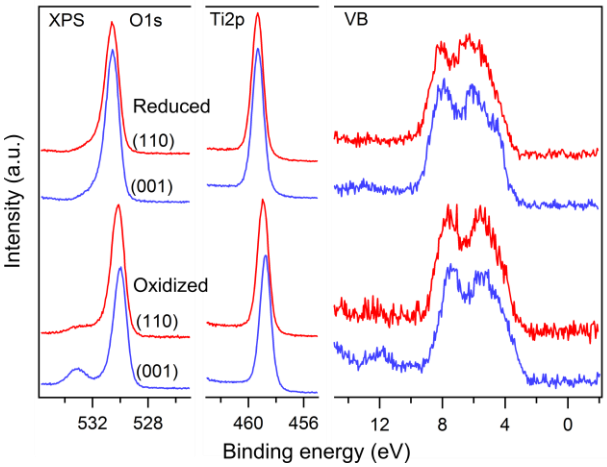


**Figure 2.** XP spectra on reduced and oxidized rutile (110) and (001): XPS $Ti2p_{3/2}$, O1s, and VB region

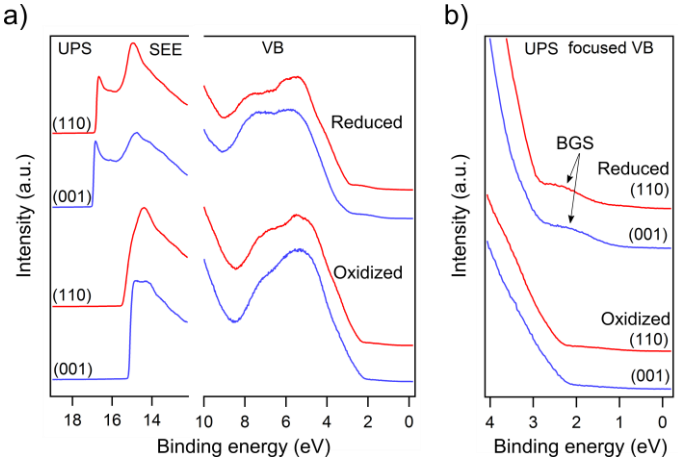


**Figure 3.** UP spectra on reduced and oxidized rutile (110) and (001): a) SEE and VB region and b) VB region focused by a factor of 5.

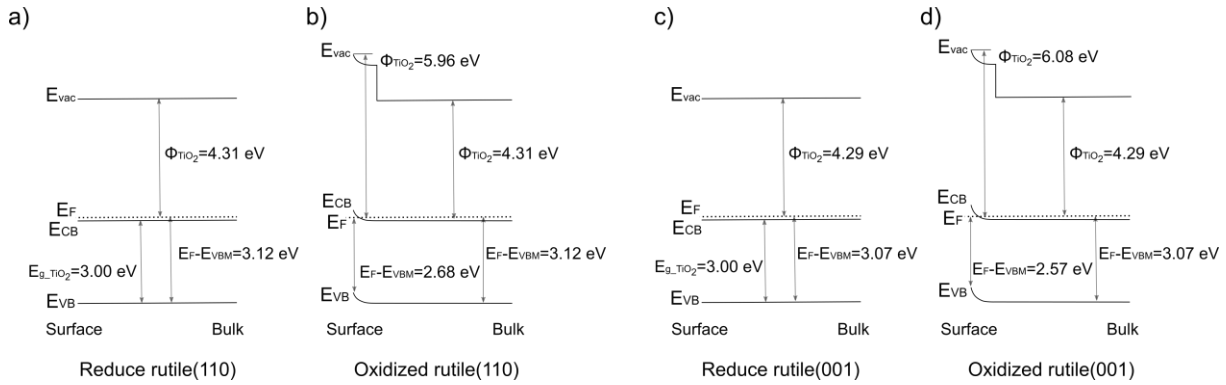


**Figure 4.** Band diagrams of different rutile substrates: a) reduced rutile (110), b) oxidized rutile (110), c) reduced rutile (001), and d) oxidized rutile (001).

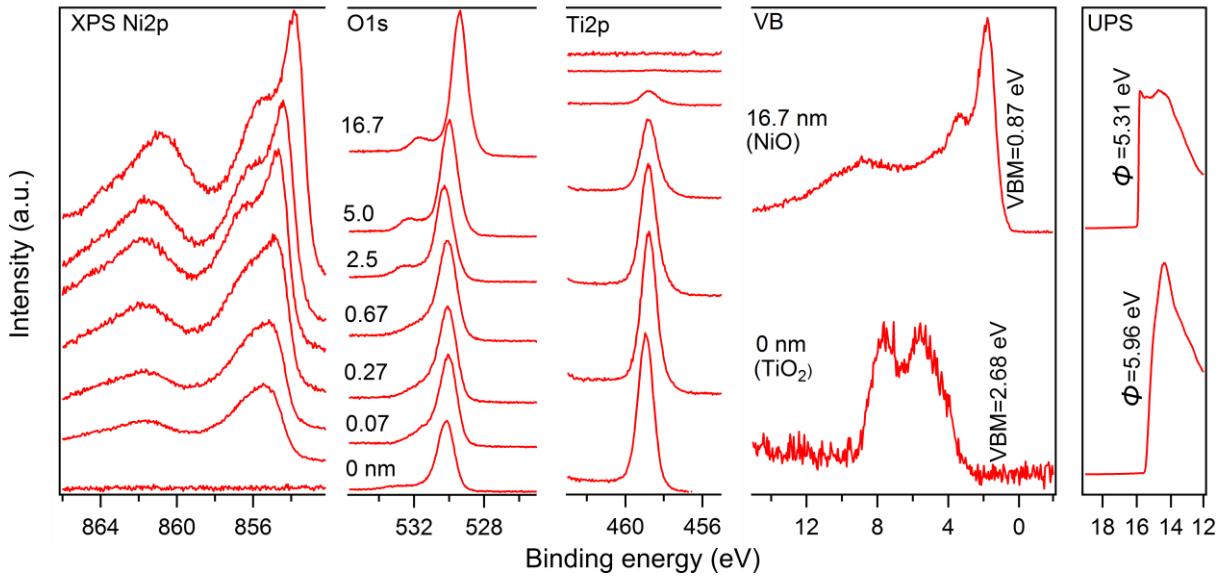


**Figure 5.** XP and UP spectra of the interface experiment performed by NiO deposition onto oxidized $TiO_2$ rutile (110) substrate.

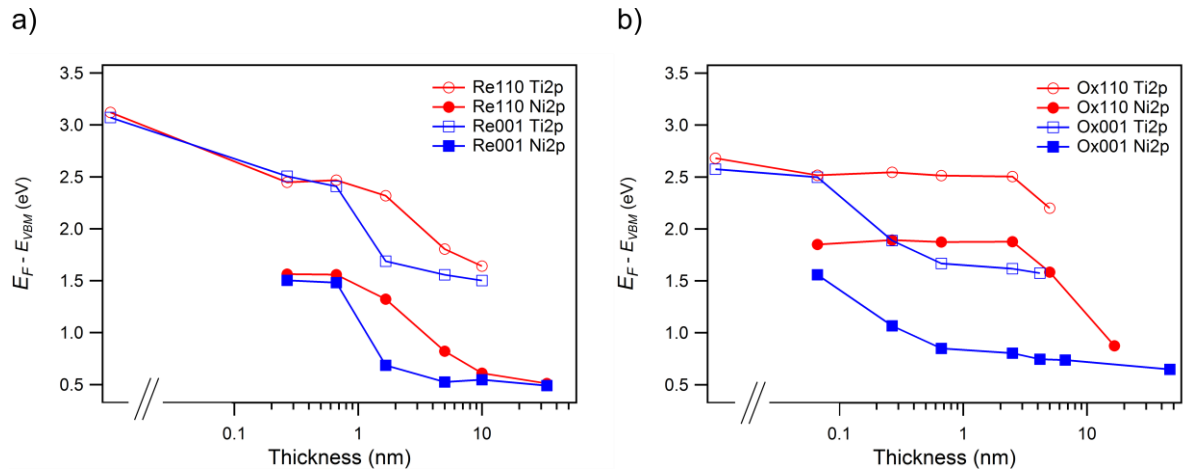


**Figure 6.** Fermi level ($E_F - E_{VBM}$) as measured by NiO/$TiO_2$ interface of a) reduced and b) oxidized $TiO_2$ rutile substrates for (001) and (110) surfaces.

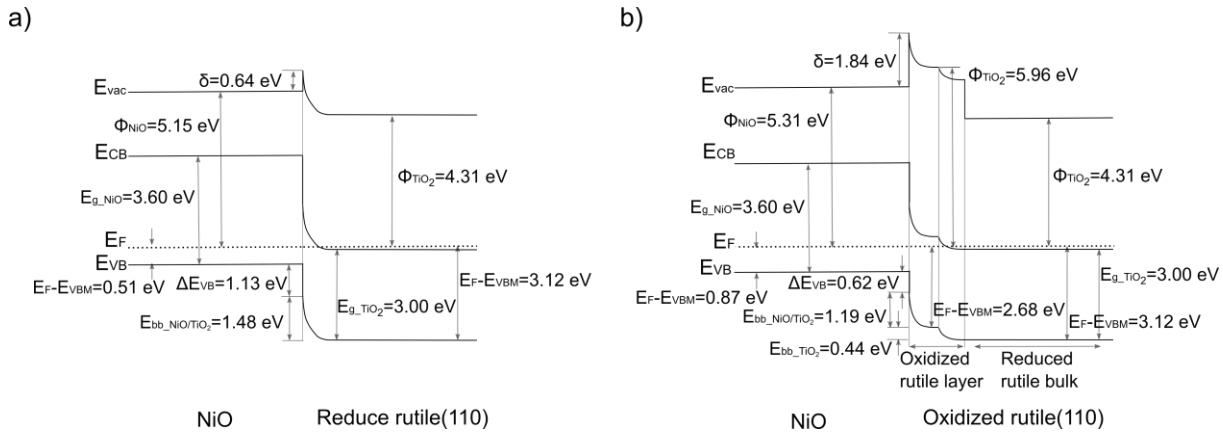


**Figure 7.** Band energy diagrams of p-NiO/n-$TiO_2$ for reduced and oxidized rutile (110) as determined from the experimental data. The important values are given in the figures. It is evidential that the Fermi level of p-NiO, as determined in the experiments, is pinned at a value of $E_F - E_{VB} \sim 0.5 - 0.9$ eV.

**Table 1.** Values of $\Phi$, $E_F$ - $E_{VBM}$, and $Ip$ of reduced and oxidized rutile substrates

| Sample | $Ti2p_{3/2}$ [eV] | O1s [eV] | $E_F$ - $E_{VBM}$ [eV] | $\Phi$ [eV] | $I_P$ [eV] |
|---|---|---|---|---|---|
| Reduced (110) | 459.35 | 530.62 | 3.12 | 4.31 | 7.43 |
| Reduced (001) | 459.38 | 530.69 | 3.07 | 4.29 | 7.36 |
| Oxidized (110) | 458.95 | 530.21 | 2.68 | 5.96 | 8.64 |
| Oxidized (001) | 458.78 | 530.04 | 2.57 | 6.08 | 8.65 |

# Supporting Information

**Dependence of crystallographic surface orientation of rutile $TiO_2$ surfaces on band alignments of NiO/$TiO_2$**

*Shun Kashiwaya, Thierry Toupance, Andreas Klein, Wolfram Jaegermann**

Photoelectron spectroscopy for i*nterface experiments*

XP and UP spectra of interface experiments performed by NiO deposition onto oxidized rutile (001), reduced rutile (110), and reduced rutile (001) are shown in figure S1.

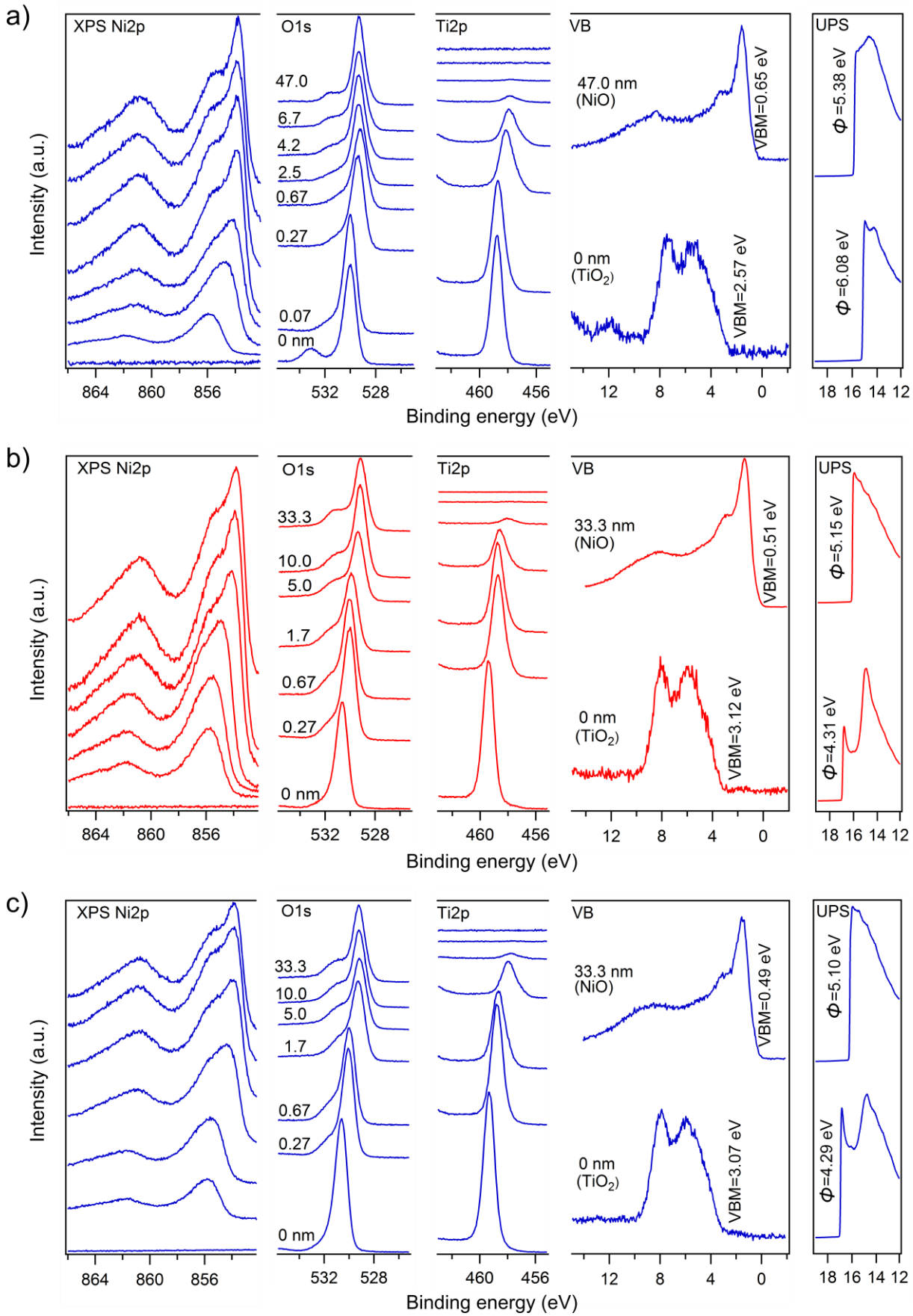


**Figure S1.** XP and UP spectra of the interface experiments performed by NiO deposition onto different $TiO_2$ rtuile substrates: a) oxidized rutile (001), b) reduced rutile (110), and c) reduced rutile (001).

*Energy band alignments*

Energy band alignments of NiO/reduced rutile (001) and NiO/oxidized rutile (001) are shown in figure S2.

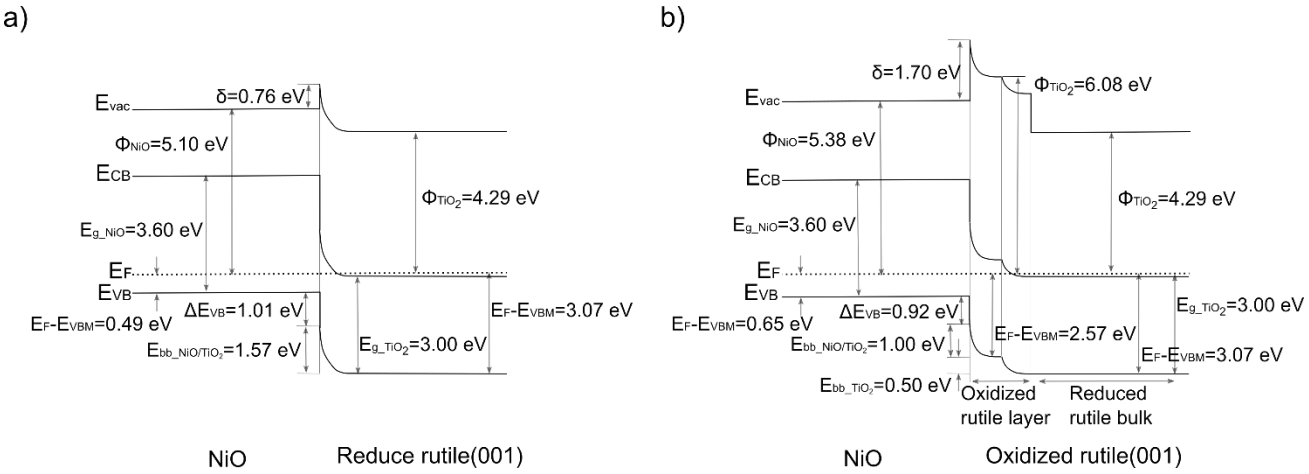


**Figure S2.** Band energy diagrams of p-NiO/n-$TiO_2$ for reduced and oxidized rutile (001)

## 3.4 Supercritical $CO_2$-assisted deposition of NiO on (101)-anatase-$TiO_2$ for efficient facet engineered photocatalysts

Shun Kashiwaya conducted experiments, data analysis and preparation of the manuscript. Jerome Majimel participated in experimental works and the discussions of the results. Cyril Aymonier provided the facilities and his expertises for SCFD experiments. Cyril Aymonier, Celine Olivier, Andreas Klein, Wolfram Jaegermann and Thierry Toupance participated in the discussions of the results and revised the manuscript.

NJC

PAPER



Cite this: *New J. Chem.*, 2018, **42**, 18649

# Supercritical $CO_2$-assisted deposition of NiO on (101)-anatase-$TiO_2$ for efficient facet engineered photocatalysts†

S. Kashiwaya,[ab] C. Aymonier,[c] J. Majimel,[c] C. Olivier,[a] A. Klein,[b] W. Jaegermann[b] and T. Toupance*[a]

Received 22nd August 2018,
Accepted 8th October 2018

DOI: 10.1039/c8nj04292f

rsc.li/njc

NiO/(101)-anatase-$TiO_2$ heterostructure nanoparticles were synthesized by depositing NiO onto the (101) facet of anatase crystals *via* the supercritical fluid chemical deposition (SFCD) route. Thorough characterization experiments performed by various techniques (XRD, UV-Vis DRS, $N_2$ sorption, HR-TEM, EDX, and XPS) indicate that the SFCD method allowed a good dispersion of NiO onto the $TiO_2$ nanoparticles for NiO amounts below 2 wt%. Compared to pure $TiO_2$, the 0.1–1 wt% NiO–$TiO_2$ nanocomposites showed enhanced photocatalytic properties for methylene blue (MB) and methyl orange (MO) decomposition under UV light irradiation, the 0.25 wt% NiO–$TiO_2$ system leading to the highest efficiencies. The photocatalytic properties were then rationalized in terms of the acidic properties and electronic structures of the NiO–$TiO_2$ nanocomposites. This higher photocatalytic activity was mainly related to the heterocontact at the interface of the NiO–$TiO_2$ crystallites and to the enhanced reaction rates at the $NiO_x$ surface.

## 1. Introduction

Since the pioneering work of Fujishima *et al.* in 1972 dealing with the photodecomposition of water on titanium dioxide ($TiO_2$) without any applied electric power,[1] photocatalytic reactions on $TiO_2$ surfaces have attracted worldwide attention due to their capability of decomposition of various air and water pollutants, $CO_2$ reduction, and water splitting.[2–4] Photocatalytic processes with semiconductors involve three main steps: (i) creation of electron–hole pairs upon light irradiation; (ii) diffusion and transfer of photo-generated carriers after charge separation and (iii) redox reactions at the semiconductor surface. However, owing to the highly preferred recombination of photo-generated carriers in photocatalysts and slow surface redox reactions, photocatalysis with pure $TiO_2$ materials is of no practical use.[5]

In this context, crystal facet engineering of $TiO_2$ has attracted much attention since Ohno *et al.* performed the selective deposition of Pt and $PbO_2$ on specific orientations of rutile and anatase, revealing the key role of facets in the separation of photoinduced electron–hole pairs.[6–10] The photocatalytic activities of semiconductors are drastically affected by their crystallographic surface orientation and structures as the surface atomic structures govern the adsorption of molecules, surface transfer and trapping of photo-generated carriers, and thus redox reactions.[11–13] In the past decade, main efforts have been devoted towards maximizing the surface area of the highest energy {001} facet to enhance the photocatalytic activity.[14] However, it was also found that the coexistence of both the high energy {001} facet as oxidation sites and the low energy {101} facet as reduction sites results in spatial charge separation because of a selective migration and/or trapping of electrons and holes to specific exposed crystal faces. This indicates that the {101} facet also plays a key role in photocatalytic processes.[15–17]

Another efficient strategy to enhance the photocatalytic activity is to combine $TiO_2$ nanoparticles with cocatalysts, thereby providing oxidation or reduction active sites and improving the kinetic rates by lowering the activation energies, trapping charge carriers and inhibiting the recombination of the photo-generated charge carriers.[18] Noble metals, such as Au or Pt particles, have been proven to be very efficient cocatalysts for the improvement of $TiO_2$ photocatalytic activity.[19,20] However, noble metals are scarce and expensive, and also catalyze the back reaction leading to the formation of water from

[a] *Institut des Sciences Moléculaires, ISM UMR 5255 CNRS, Université de Bordeaux, 351 Cours de la Libération, F-33405 Talence, Cédex, France. E-mail: thierry.toupance@u-bordeaux.fr*
[b] *Fachbereich Material- und Geowissenschaften, Technische Universität Darmstadt, Petersenstr. 23, 64287 Darmstadt, Germany*
[c] *CNRS, Univ. Bordeaux, Bordeaux INP, ICMCB, UMR 5026, F-33600 Pessac, France*

† Electronic supplementary information (ESI) available: FTIR spectra, complementary XRD, Raman, XPS, TEM-EDX and photocatalytic data. See DOI: 10.1039/c8nj04292f

hydrogen and oxygen, thus limiting their ability as cocatalysts for water splitting. To avoid this reverse reaction, transition metal oxides that show a negligible activity for water formation are conventionally chosen as cocatalysts. On the other hand, another approach to improve the photocatalytic activity is to load p-type semiconductors onto n-type $TiO_2$ nanostructures, establishing a p–n heterojunction at the interfacial contact between a n-type material such as $TiO_2$ and a p-type semiconductor. As a result, photo-generated electrons and holes are spatially separated to $TiO_2$ and the p-type semiconductor, respectively, thus hampering the recombination phenomena and leading to a longer charge carrier lifetime. Notably, p-type metal oxides such as NiO, $IrO_2$, and $Co_3O_4$ provide oxidation reaction sites, decrease the activation energy, and suppress reverse reactions.[18,21,22] Amongst p-type metal oxide semiconductors, nickel oxide (NiO) is one of the most reactive materials that is abundant on Earth and can act as both a reduction and oxidation cocatalyst. Thus, many reports deal with NiO/polycrystalline $TiO_2$ systems, usually prepared by impregnation,[23] precipitation,[24] hydrothermal[25] or sol–gel methods,[26,27] which show improved photocatalytic properties for organic pollutant decomposition[25,26] or hydrogen production.[23,24,27,28] Combining crystal facet engineering of $TiO_2$ and cocatalyst deposition would therefore provide promising heterostructures exhibiting synergetic effects for photocatalysis purposes. Although noble metals such as Pt have been selectively deposited onto the {101} facet, which is the most common and stable one, the selective deposition of NiO as the metal oxide onto the {101} facet has not been demonstrated.

In this context, we developed highly active NiO–$TiO_2$ photocatalysts obtained by the deposition of NiO at the {101} facet of anatase by employing the supercritical fluid chemical deposition (SFCD) route. SFCD using carbon dioxide ($scCO_2$) is indeed considered as a green and effective method for chemical deposition as no liquid or solvent residue is left on the particles after deposition.[29,30] $ScCO_2$ exhibits unique properties such as hybrid gas-like and liquid-like properties in which solutes can be dissolved like a liquid. The reaction environment such as density, viscosity, diffusivity or surface tension can be easily manipulated through the control of pressure and temperature. The deposition of transition metals onto different supports has already been achieved by this method but,[31–34] to the best of our knowledge, the use of SFCD for NiO deposition on $TiO_2$ has not been reported yet. The structural, morphological and textural properties of the obtained heterostructures were thoroughly characterized and their photocatalytic activity was examined by the degradation of methylene blue (MB) and methyl orange (MO) dye under UV irradiation. MB and MO, which can be positively and negatively charged in solution, respectively, were selected to investigate the dye sensitization effects of the $TiO_2$ photocatalyst.[35,36]

## 2. Experimental section

### 2.1. Materials preparation

Titanium(IV) butoxide ($Ti(OBu)_4$, 97%, company), oleic acid ($C_{18}H_{33}CO_2H$, 90%, Aldrich), oleylamine ($C_{18}H_{35}NH_2$, 70%, Aldrich), and a superhydride solution (1 M lithium triethylboronhydride, $LiEt_3BH$ in THF, Aldrich), and nickel(II) nitrate hexahydrate ($Ni(NO_3)_2{\cdot}6H_2O$, 98%, Acros organics) were employed without any further purification.

Oriented single crystalline anatase nanoparticles exposing {101} facets were synthesized by a solvothermal method adapting previously reported procedures based on the use of water vapor as the hydrolysis agent to accelerate the hydrothermal reaction and the use of oleic acid and oleylamine as capping agents, which exhibit different binding strengths to control the crystal growth of anatase $TiO_2$ nanoparticles.[37,38] Typically 2.5 g of $Ti(OBu)_4$ were added to a mixture of 9.2 g of oleic acid and 16.8 g of oleylamine in 6.6 mL of absolute ethanol, which corresponds to a molar ratio of 1 : 4 : 6 in $Ti(OBu)_4$, oleic acid, and oleylamine. The resulting solution was stirred for 30 min and transferred into a 225 mL autoclave containing 22.4 g of absolute ethanol and 1.17 g of deionized water. The autoclave was heated at 180 °C for 18 h to reach a pressure of about 1.8 MPa. A white powder was then recovered from the solution by centrifugation, washed with ethanol 4 times, and dried in air and then under vacuum for 2 h. Elimination of oleic acid molecules strongly bonded to the surface was achieved by treatment of $TiO_2$ powders with 10 mL of lithium triethylborohydride (1 M), a strong reducing agent,[38,39] under a nitrogen atmosphere. After sonication, the suspension was stirred overnight, and the resulting dark blue suspension was centrifuged and the powder obtained was washed with distilled water, acetone, and dichloromethane. The $TiO_2$ nanoparticles were finally dried in air and under vacuum for 2 h. To get rid of remaining oleylamine on the surface, the powders were finally treated by sonication in 70 mL of a 0.4 M $H_2SO_4$ solution. The powders recovered by centrifugation were washed with $CH_2Cl_2$, and dried in air and under vacuum for 2 h to yield 500 mg of a white powder, hereafter named pure $TiO_2$.

NiO deposition was then performed in a 30 mL custom-built reactor made of stainless steel and equipped with a magnetic stirrer. The pressure in the reactor was controlled using a high-pressure pump. In a typical procedure, an appropriate amount of nickel(II) nitrate hexahydrate was dissolved in 3 mL of ethanol, and 200 mg of $TiO_2$ nanoparticles were dispersed into the solution followed by sonication for 10 min. The mixture was then transferred into the reactor. The reactor was filled with $CO_2$ to reach a pressure of 5 MPa at room temperature, heated to 200 °C, pumped up to 22 MPa using the high-pressure pump, and kept under these conditions under stirring at 40 rpm for 30 min. To recover the dry and clean powders, the reactor was flushed under a $scCO_2$ flow at a pressure of 10–12 MPa and a temperature of 120 °C. $ScCO_2$ is an effective drying and cleaning solvent as it is nontoxic, nonflammable, and inert towards the obtained nanoparticles. The recovered NiO–$TiO_2$ samples were annealed in air at 400 °C for 1 h to achieve a high crystallinity of NiO and an intimate contact at the interface of NiO–$TiO_2$. The amounts of nickel nitrate hexahydrate to prepare NiO–$TiO_2$ photocatalysts containing 0.1, 0.25, 0.5, 1, 2 and 10 wt% of NiO were 0.8, 2.0, 4.0, 8.0, 15.9 and 79.5 mg, respectively. The resulting samples are hereafter named 0.1 wt% NiO–$TiO_2$, 0.25 wt% NiO–$TiO_2$, 0.5 wt% NiO–$TiO_2$, 1.0 wt% NiO–$TiO_2$, 2.0 wt% NiO–$TiO_2$, and 10 wt% NiO–$TiO_2$.

 

### 2.2. Materials characterization

Raman spectra were recorded using a Thermo Scientific DXR Raman microscope with a 633 nm wavelength excitation laser operating at 7 mW output power, 20 times with an exposure time of 1 s, between 50 and 3500 $cm^{-1}$ with 1 $cm^{-1}$ spectra resolution. XRD spectra were acquired with a Bruker AXS diffractometer (D2 PHASER A26-X1-A2B0D3A) using a Cu anode (Kα radiation). A continuous scan mode was used to collect $2\theta$ data from 5 to 80° with a sampling pitch of 0.02° and at a scan rate of 2.4° $min^{-1}$. The average crystallite size of the prepared nanoparticles was estimated by fwmh (full width at half maximum) according to Scherrer's formula (applied to the {101} reflection), $D = (0.9\lambda)/(\beta_{1/2}\cos\theta_B)$, where $D$, $\lambda$, $\beta_{1/2}$, and $\theta_B$ represent the average grain size, the wavelength of Cu Kα (=1.5405 Å), the fwhm, and the diffraction angle, respectively. UV-Vis diffuse reflectance spectra were measured at room temperature in the 200–800 nm wavelength range using an UV-Vis-NIR Cary 5000E spectrometer equipped with an integrating sphere. Samples were placed in a Suprasil1 cell equipped with a quartz window. Halon standard (6 mm deep and 1 g $cm^{-3}$ density) was used as a reference. The textural properties were evaluated by nitrogen sorption porosimetry using ASAP2010 Micromeritics equipment. The specific surface area (BET (Brunauer–Emmett–Teller) method applied in the 0.1–0.3 relative pressure range)[40] and the pore size distribution (BJH (Barrett–Joyner–Halenda) model applied to the adsorption branch)[41] were determined after degassing the samples at 120 °C to reach a constant pressure (<10 μmHg).[28] HR-TEM was carried out using a JEOL 2200FS (JEOL, Tokyo, Japan) microscope operating at an acceleration voltage of 200 kV (wavelength $\lambda$ = 2.51 pm) equipped with a Schottky type FEG and an EDX system (Oxford, Wiesbaden, Germany). For HR-TEM, HR-STEM and EDX studies, the photocatalyst nanoparticles were dispersed in ethanol by sonication and a few droplets of the suspension were deposited over holey carbon grids (Cu-300HD, Pacific Grid-Tech). Moreover, in order to be representative and statistically meaningful, many images from several regions of various samples were recorded and the most characteristic results are represented here.

The electronic properties of the prepared samples were investigated with DAISY-MAT,[42] which is an integrated surface science system consisting of a Physical Electronics PHI 5700 multi-technique surface analysis system and various technique deposition chambers with an ultrahigh vacuum sample transfer. XPS spectra were recorded using monochromatic Al Kα (1486.6 eV) radiation with an energy resolution of 0.4 eV as determined from the broadening of the Fermi edge of a sputter-cleaned Ag sample. The binding energies of core levels, and the valence band maximum $E_{VB}$ can be determined with an accuracy of 50 meV and 100 meV, respectively. The binding energies determined by XPS were calibrated by the Fermi level energy of the sputter-cleaned Ag sample. Hence, all the binding energies are given with respect to the calibrated Fermi level. The powder samples are pressed onto indium foil as a conductive substrate to avoid a charging problem, and transferred into the XPS chamber without any further treatment.

### 2.3. Photocatalytic tests

The photocatalytic properties of the as-synthesized samples were evaluated by the degradation of methylene blue (MB) or methyl orange (MO) dye (Alfa Aesar, reagent grade, used as supplied) under UV-light at room temperature. 50 mg of a photocatalyst were dispersed in 50 mL aqueous solution of MB or MO (10 mg $L^{-1}$) to obtain a photocatalyst concentration of 1.0 g $L^{-1}$. The experiments were performed in a Pyrex beaker illuminated with a 125 W high-pressure mercury lamp (Philips, HPL-N 125 W/542 E27) emitting UV light. The lamp was positioned above the beaker solution and the distance between the lamp and the top of the solution was 60 mm. The suspension was initially stirred in the dark for 30 min to reach the adsorption/desorption equilibrium. During the experiments, the solutions were continuously stirred at room temperature in open air. At given irradiation time intervals, 2 mL aliquots of the suspensions were collected and centrifuged (4000 rpm, 10 min) to remove the photocatalyst particles from the dye solution. Monitoring the absorption intensity of MB at 664 nm or MO at 515 nm using a UV-Visible spectrophotometer (Shimadzu, UV-1650 pc) led to the determination of the remaining amount of dyes. The intensity of the maximum absorption was investigated as the wavelength of the peak depends on the pH of the solution for MO. A calibration plot based on Beer–Lambert's law was established by relating the absorbance to the concentration. Blank experiments were also conducted with the catalysts in the absence of light and without the catalysts while the dye was illuminated.

## 3. Results and discussion

### 3.1. Materials characterization

Changes in the morphology and sizes of the pure $TiO_2$ particles depending on the chemical and thermal treatment employed were first evaluated by HRTEM as depicted in Fig. 1. Before treatment with superhydride and sulfuric acid solutions, the nanoparticles agglomerated along the [001] direction (Fig. 1A and B). The selected area electron diffraction patterns (SAED) shown in Fig. 1A (inset) confirm the formation of the highly oriented anatase phase. The first and second rings can be indeed assigned to the diffraction features originating from the (101) and (004) planes of anatase $TiO_2$, respectively. However, the well-ordered agglomeration has collapsed upon post-treatment with superhydride and sulphuric acid, forming partially isolated particles and mainly random agglomeration due to the small nanoparticle size, *i.e.* 7 nm, and possibly due to the surfactant molecules remaining on the surface (Fig. 1C and D). The nanoparticles exhibit a bipyramidal, *i.e.* rhombic, shape exposing only the {101} facet of anatase that remains unchanged after both reductive and acidic treatments. Interplanar spacings of 0.350 and 0.467 nm at an angle of 68.1° match very well with the (101) and (001) planes of anatase. As shown by Dinh *et al.*[37] and D'Arienzo *et al.*,[38] the use of an excess of oleylamine compared to oleic acid actually favours the formation of well-defined rhombic structures. Moreover, the supercritical fluid treatment (without a nickel precursor) does

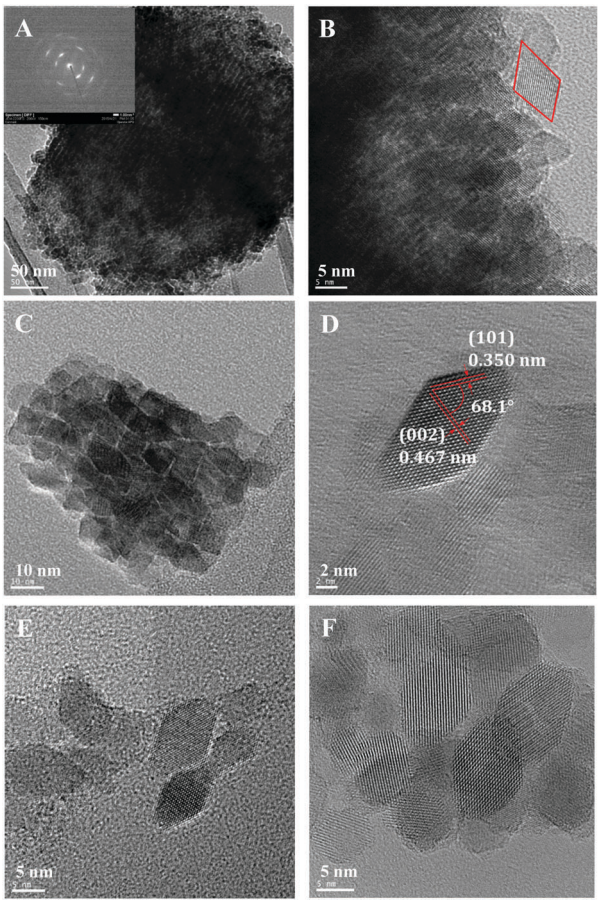


Fig. 1 HR-TEM images (SAED (inset)) of: (A and B) pure $TiO_2$ before treatment with superhydride and sulphuric acid; (C and D) pure $TiO_2$ after treatment with superhydride and sulphuric acid; (E) pure $TiO_2$ after treatment with superhydride and sulphuric acid followed by supercritical fluid treatment; (F) 0.25 wt% NiO–$TiO_2$.

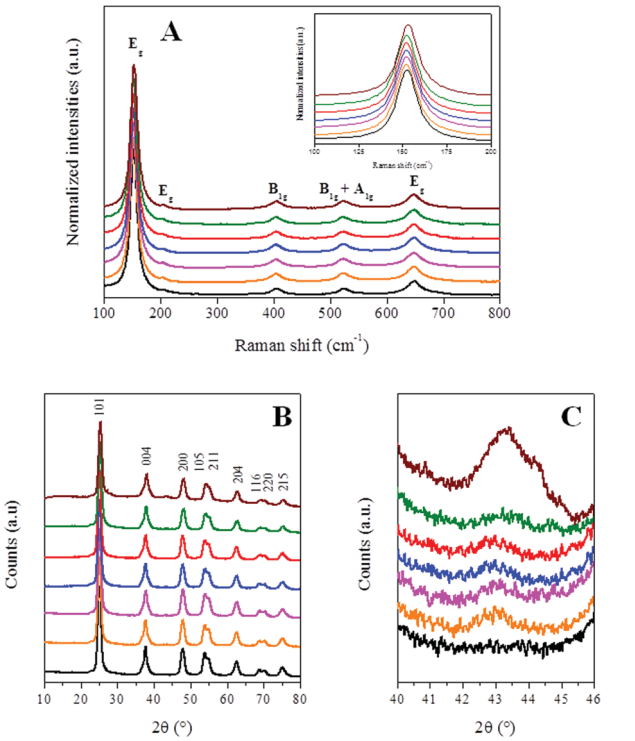


Fig. 2 (A) Raman spectra (inset: expansion of the 100–200 $cm^{-1}$ region); (B) XRD patterns; (C) expansion of the $2\theta$ region for the pure $TiO_2$ (black), 0.1 wt% NiO–$TiO_2$ (orange), 0.25 wt% NiO–$TiO_2$ (magenta), 0.5 wt% NiO–$TiO_2$ (blue), 1 wt% NiO–$TiO_2$ (red), 2 wt% NiO–$TiO_2$ (olive) and 10 wt% NiO–$TiO_2$ (brown) nanomaterials.

not affect both morphology and sizes of the $TiO_2$ nanoparticles exposing the {101} facets (Fig. 1E). As a consequence, NiO was then deposited on the oriented anatase $TiO_2$ rhombic particles employing a SFCD route with carbon dioxide and ethanol as solvents. Ethanol was chosen as a co-solvent for enhancing the solubility of the precursor in carbon dioxide.

Crystalline phase identification for the obtained NiO–$TiO_2$ nanocomposites was first performed by Raman spectroscopy and powder XRD analyses (Fig. 2). As depicted in Fig. 2A, the Raman spectra of the samples containing up to 2 wt% NiO exhibited main resonances at 152, 203, 405, 522 and 647 $cm^{-1}$, which can be ascribed to the $E_g$, $E_g$, $B_{1g}$, $A_{1g} + B_{1g}$ and $E_g$ modes of anatase $TiO_2$.[43] These data are fully consistent with the factor group analysis, which predicts six Raman-active modes ($A_{1g} + 2B_{1g} + 3E_g$) for anatase $TiO_2$.[43,44] The absence of energy shift and line-broadening of the Raman peaks as the NiO content was increased up to 2 wt% indicates that NiO deposition by the SFCD method did not lead to imperfections or alloying effect in the anatase $TiO_2$ nanocrystals (Fig. 2A, inset).[45] However, the Raman shifts detected were significantly different from those reported by Arsov *et al.* for anatase $TiO_2$ single crystals, *i.e.* 144 ($E_g$), 197 ($E_g$), 399 ($B_{1g}$), 516 ($A_{1g}$), 516 ($B_{1g}$), and 639 ($E_g$) $cm^{-1}$.[46] These differences could be rationalized on the basis of the size of the anatase $TiO_2$ nanocrystals. Indeed, according to previously reported works,[43,47] 8 $cm^{-1}$ shift towards a higher energy of the peak at 144 $cm^{-1}$ is consistent with a nanocrystal size of 7 ± 1 nm. As a consequence, nickel oxide deposition did not induce any significant change in the anatase nanocrystal size. It is also worth mentioning that the absence of typical features for the nickel oxide species is likely due to the combination of weak NiO loading and low crystallite size.[48] The crystalline structure was also confirmed by XRD (Fig. 2B). Thus, whatever the NiO amount XRD patterns showed main features, which can be indexed to the (101), (004), (200), (105), (211), (204), (116), (220) and (215) diffraction peaks of the pure anatase polymorph according to literature data (Joint Committee on Powder Diffraction Standards, JCPDS, card no. 21-1272). In addition, the Scherrer formula applied to the line width of the (101) diffraction peak led to an average crystallite size of 7.1 ± 0.4 nm for pure $TiO_2$ and between 7.5 ± 0.4 and 7.9 ± 0.4 nm for the NiO–$TiO_2$ heteronanostructures (Table 1), which is in good agreement with the TEM and Raman spectroscopy results. Furthermore, plotting the XRD patterns with the enhanced intensity in the $2\theta$ region from 40 to 46° revealed the presence of a broad extra line around $2\theta$ = 43° for the NiO–$TiO_2$ heteronanostructures (Fig. 2C), the intensity of which increases with the NiO amount. This feature can be assigned to the (200) diffraction line of the face-centered cubic (fcc) crystalline structure

 

Table 1 Crystallite size, textural properties and apparent rate constants for the degradation of MO and MB for the $TiO_2$ and NiO–$TiO_2$ photocatalysts

| Sample | Mean crystallite size XRD[a] (nm) | $S_{BET}$[b] ($m^2\ g^{-1}$) | Total pore volume[c] ($cm^3\ g^{-1}$) | Mean pore size[d] (nm) | Apparent rate constant $k_{app}$ MB[e] ($min^{-1}$) | Apparent rate constant $k_{app}$ MO[f] ($min^{-1}$) |
|---|---|---|---|---|---|---|
| $TiO_2$ | 7.1 ± 0.4 | 116.4 ± 3.2 | 0.096 ± 0.013 | 4.8 ± 0.6 | 0.0102 | 0.0340 |
| 0.1 wt% NiO–$TiO_2$ | 7.9 ± 0.4 | 109.2 ± 3.0 | 0.113 ± 0.015 | 4.5 ± 0.6 | 0.0341 | 0.0677 |
| 0.25 wt% NiO–$TiO_2$ | 7.6 ± 0.4 | 111.1 ± 3.1 | 0.101 ± 0.013 | 4.7 ± 0.6 | 0.0464 | 0.0742 |
| 0.5 wt% NiO–$TiO_2$ | 7.7 ± 0.4 | 105.1 ± 2.9 | 0.098 ± 0.013 | 5.0 ± 0.6 | 0.0263 | 0.0358 |
| 1 wt% NiO–$TiO_2$ | 7.6 ± 0.4 | 112.1 ± 3.1 | 0.118 ± 0.015 | 5.1 ± 0.7 | 0.0252 | 0.0356 |
| 2 wt% NiO–$TiO_2$ | 7.5 ± 0.4 | 116.1 ± 3.2 | 0.125 ± 0.016 | 4.9 ± 0.6 | 0.0225 | 0.0276 |
| 10 wt% NiO–$TiO_2$ | 7.6 ± 0.4 | 101.3 ± 2.8 | 0.103 ± 0.013 | 5.2 ± 0.7 | 0.0018 | 0.0246 |

[a] Calculated according to the Scherrer relationships using the full width at half-maximum of the (101) diffraction line. [b] Surface areas determined by BET. [c] Total pore volume determined at a relative pressure of 0.99. [d] Mean pore diameters calculated by the BJH theory (applied to the adsorption branch of the isotherm).[41] [e] MB: methylene blue dye. [f] MO: methyl orange dye.

of NiO (JCPDS, card no. 04-0835) and was also found in the XRD pattern of pure NiO prepared by the SFCD method (Fig. S1, ESI†). The broad and attenuated peak typical of cubic NiO is in favour of a high dispersion at NiO contents below 2 wt%, which provides small particles hardly detectable by XRD.[28] Finally it is worth underlining that the introduction of a high NiO loading by the SFCD route seems to induce some changes in the $TiO_2$ nanocrystals. Thus, the shift of the main Raman peak and new diffraction lines at $2\theta$ = 27.1 and 43.6° observed for the 10 wt% NiO–$TiO_2$ nanocomposite suggests a slight modification in the crystallite size and the formation of a small amount of a rutile polymorph.

On the other hand, the crystal morphology of the heterostructures does not change for NiO amounts up to 2 wt% (Fig. 1F and Fig. S2, ESI†). The uniform dispersion of NiO on the $TiO_2$ nanocrystallites was confirmed by the energy dispersive X-ray spectroscopic (EDX) elemental maps of titanium, oxygen and nickel elements as shown in Fig. 3 and Fig. S3 (ESI†) for 2 wt% NiO content. In this case, the semiquantitative electron mapping shows that 1.5 wt% NiO is dispersed on the $TiO_2$ crystallites, which is in good agreement with the nominal NiO content. By contrast, for 10 wt% NiO content, the NiO nanoparticles agglomerate and establish a micro heterostructure of NiO/$TiO_2$ according to the HR-STEM images and EDX element maps shown in Fig. S4 (ESI†). The $TiO_2$ and NiO regions are composed of individual nanocrystals, the sizes of which are about 7–10 nm and 2–3 nm, respectively (Fig. S2, ESI†). However, it is noteworthy that the $TiO_2$ agglomeration also contains Ni species homogeneously distributed onto the $TiO_2$ nanocrystals.

The textural properties of the different nanocomposites prepared were then scrutinized by $N_2$ sorption analysis. Regardless of the NiO loading, the adsorption–desorption isotherms exhibit characteristic type-IV sorption behavior with type-H2 hysteresis loops, which are typical of mesoporous solids according to the IUPAC classification (Fig. S5, ESI†).[49] Moreover, the mean pore size distributions are rather broad, indicating non-uniform channels in the mesoporous region. It is also worth mentioning that the isotherm's desorption branch is not very steep, $N_2$ desorption occurring in two main steps in certain cases as for 0.1 wt% NiO–$TiO_2$. This can be rationalized by considering that the type-H2 hysteresis loop arises, on the one hand, from capillary condensation in narrow-neck and wide-body, known as the single pore mechanism, and, on the other hand, from the pore network topology, often referred to as pore block effects.[26,49,50] This finding is fully consistent with the TEM images, indicating that the nanocomposites consist of a porous network of aggregated nanoparticles, and the mesoporosity detected is stemming from the interparticle voids. The Brunauer–Emmet–Teller (BET) specific areas, total pore volumes and average mesopore sizes are reported in Table 1. Whatever the NiO loading, the mean mesopore size is rather constant, *i.e.* ranges between 4.5 and 5.2 ± 0.2 nm. Furthermore, the BET surface areas of the NiO–$TiO_2$ nanocomposites containing less than 2 wt% NiO remain close to that of the pure $TiO_2$ nanoparticles, *i.e.* range between 105.1 ± 2.9 and 116.1 ± 3.2 $m^2\ g^{-1}$. As a result, the supercritical fluid deposition of NiO allowed high surface areas to be maintained, which was not the case for NiO–$TiO_2$ nanocomposites prepared by other methods such as sol–gel derived methods.[26,28]

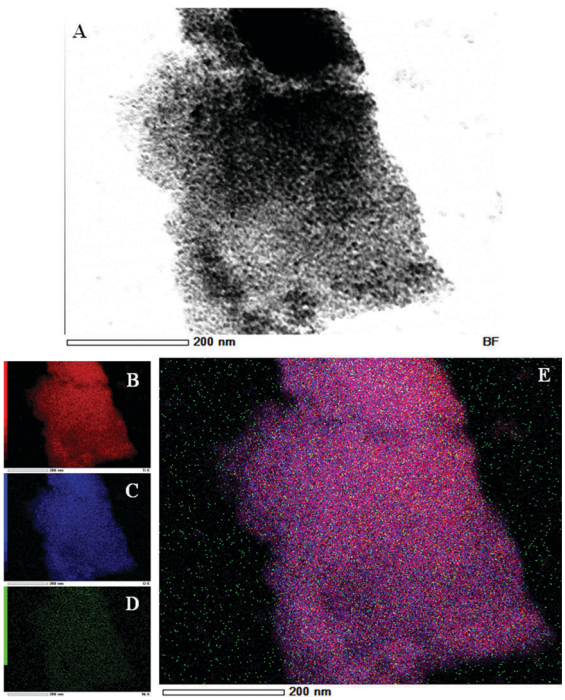


Fig. 3 (A) Bright field STEM micrograph of the 2 wt% NiO–$TiO_2$ nanomaterials and EDX elemental mapping of (B) Ti, (C) O, and (D) Ni. (E) 3-Colours image obtained by superimposed chemical elemental mapping.

### 3.2. Optical and electronic properties

The optical properties of the NiO–$TiO_2$ heteronanostructures were investigated by UV-Vis diffuse reflectance spectroscopy (Fig. 4). The steep absorption edge for pure $TiO_2$ at 385 nm stems from electron transitions between the valence band (mainly O 2p orbitals) and the conduction band (mainly Ti 3d orbitals) of the anatase $TiO_2$ nanoparticles.[11] The NiO–$TiO_2$ heteronanostructures showed visible light absorption, the edge of which shifts towards lower energies with increasing amount of NiO. To obtain deeper insight into the dependence of the optical properties on NiO amount, the band gap energy ($E_g$) of the different samples prepared was determined from their absorption spectra using the Kubelka–Munk theory.[51] In the case of powder materials, the optical band gap can be inferred from the plot of $[F(R)h\nu]^{1/n}$ *vs.* $h\nu$ where $F(R)$ is the remission function related to the reflectance $R$ ($F(R) = (1 - R)^2/2R$),[52] $h$ is the Planck constant, $\nu$ is the light frequency and $n = 2$ for an indirect transition semiconductor such as anatase $TiO_2$.[11,53] The intercept of the linear extrapolation for the main slope with the abscissa axis yields the energy band gap value (Fig. 4, inset). The band gaps decrease from 3.21 eV for pure $TiO_2$ to 3.19, 3.15, 3.16, 3.13, 3.07 and 2.98 eV for 0.1, 0.25, 0.5, 1, 2, and 10 wt% NiO/$TiO_2$, respectively. This trend cannot be interpreted as the simple addition of the anatase $TiO_2$ and NiO optical properties since the band gap of nickel oxide has been reported to range between 3.4 and 4.3 eV.[54,55] DFT calculations have shown that the modification of the anatase $TiO_2$ surface with NiO clusters leads to new states located above the valence band and just below the conduction band of $TiO_2$.[56] Thus, the valence band maximum of anatase $TiO_2$ increases due to mixing with the Ni 3d level, where new vacant levels appear close to the conduction band minimum of anatase $TiO_2$. This results in a narrowed band gap of the NiO–$TiO_2$ samples, and thus in visible light absorption. The evolution of the energy band gap with the NiO loading therefore reveals a strong interaction of the NiO particles with the anatase $TiO_2$ surface through the Ni–O–Ti bonds.[56]

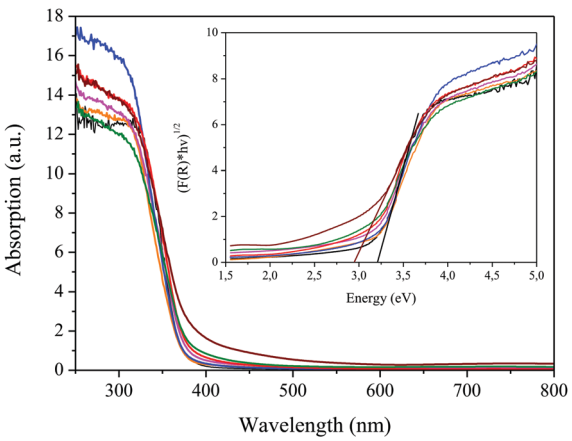


Fig. 4 UV-Visible diffuse reflectance spectra (DRS) and $(F(R)h\nu)^{1/2}$ *vs.* $h\nu$ plots (inset) for the pure $TiO_2$ (black), 0.1 wt% NiO–$TiO_2$ (orange), 0.25 wt% NiO–$TiO_2$ (magenta), 0.5 wt% NiO–$TiO_2$ (blue), 1 wt% NiO–$TiO_2$ (red), 2 wt% NiO–$TiO_2$ (olive) and 10 wt% NiO–$TiO_2$ (brown) nanocomposites.

The composition and electronic properties of the pure $TiO_2$ and hetereostructure NiO–$TiO_2$ nanocomposites were further investigated by XPS analyses. In addition to carbon, nitrogen, and calcium species, which are typical contaminants of *ex situ* samples synthesized chemically, emissions from titanium, oxygen, nickel, and indium were detected in the survey spectra (Fig. S6, ESI†). High resolution XPS spectra for the valence band region, Ti 2p, Ni 2p, and O 1s are depicted in Fig. 5A–D. The Fermi level shifts toward a lower energy level from 3.34 eV for pure $TiO_2$ to 3.31, 3.29, 3.26, 3.26, 3.23, and 2.54 eV for 0.1, 0.25, 0.5, 1, 2, and 10 wt% NiO–$TiO_2$, respectively. Except for 10 wt% NiO–$TiO_2$, the Fermi level is located above the conduction band minimum (Fig. 5A). The valence band spectrum of 10 wt% NiO–$TiO_2$ shows two edges at 2.54 and 0.54 eV, which would come from the NiO–$TiO_2$ heterostructure and the NiO agglomeration, respectively. For the pure anatase $TiO_2$, the emission from the Ti $2p_{3/2}$ doublet shows only the $Ti^{4+}$ line at 459.55 eV without the presence of $Ti^{3+}$ since no feature at about 457.5 eV was detected.[57] The peak shifts to a lower binding energy by 80–100 meV in the presence of various amounts of NiO (Fig. 5B). The O 1s spectra show an intense peak at 530.72 eV corresponding to the Ti–O bonds with a shoulder at a higher binding energy of 1.6 eV from the main emission line, which also shows an upward shift of 40–90 meV with NiO as well as Ti $2p_{3/2}$ peaks (Fig. 5C). The observed shift in the Ti 2p and O 1s core levels is relatively small. One reason may be that the particle size of the photocatalyst is too small to form a complete space charge layer enough to saturate the bending. Another reason could be that the NiO nano-deposits are too homogeneously distributed on the $TiO_2$ for small coverage or form a phase separated NiO cluster onto the $TiO_2$ nanocrystallites (Fig. S3 and S4, ESI†). The shoulder of the O 1s line mainly results from the hydroxide species due to the water molecules adsorbed on the $TiO_2$ surface and might partially come from a $Ni^{3+}$ oxidation state at the surface layers of NiO. No clear signal of NiO was found in XPS, which also indicates that the morphology of the composites was not very well developed. The spectra may be assigned to an overlap of the $Ni^{2+}$ and $Ni^{3+}$ oxides.[58] Using an energy band gap value of 3.58 eV for NiO as previously reported in the literature,[54] a band alignment of the NiO/$TiO_2$ photocatalysts derived from the Fermi levels and the optical band gaps determined by XPS and DR UV-Vis is shown in Fig. 6. We expected that a p–n junction would be formed between NiO and $TiO_2$ in the NiO/(101)-anatase–$TiO_2$ heterostructure and it would help in separation of electrons and holes, the former migrating towards the $TiO_2$ surface and the latter towards the NiO one. However, the experimental results show no indication of a well developed space charge layer in the $TiO_2$ substrates in contrast to similar experiments performed before with related heterostructures.[28] Therefore, it cannot be concluded that a space charge layer developed at the heterostructure contact contributes to charge carrier separation or that only the catalytic effects of the $NiO_x$ layers will contribute to the photocatalytic properties.

### 3.3. Photocatalytic properties

The photocatalytic activity of the pure $TiO_2$ and NiO–$TiO_2$ nanomaterials was examined by photodecomposition under

 

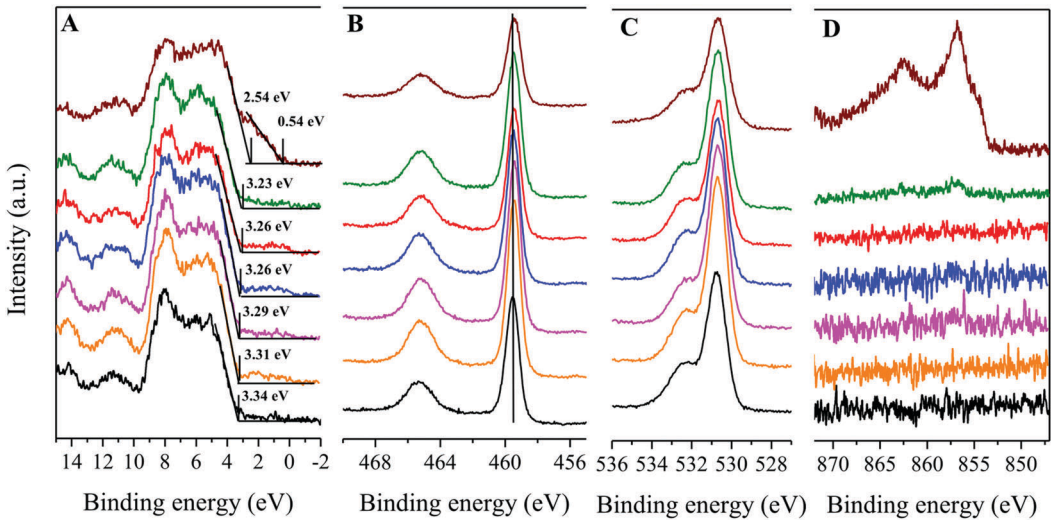


Fig. 5 High resolution XPS spectra of the valence band (A), Ti $2p_{3/2}$ (B), O 1s (C), and Ni $2p_{3/2}$ (D) for the pure $TiO_2$ (black), 0.1 wt% NiO–$TiO_2$ (orange), 0.25 wt% NiO–$TiO_2$ (magenta), 0.5 wt% NiO–$TiO_2$ (blue), 1 wt% NiO–$TiO_2$ (red), 2 wt% NiO–$TiO_2$ (olive) and 10 wt% NiO–$TiO_2$ (brown) nanocomposites.

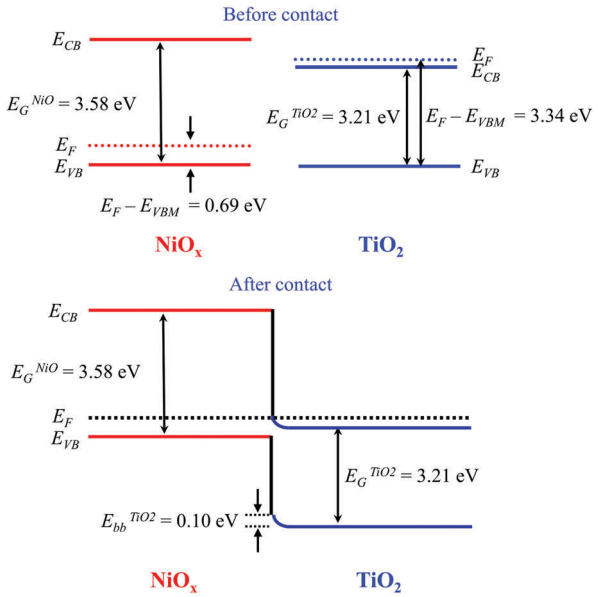


Fig. 6 Energy band alignment at the interface of $NiO_x$ and $TiO_2$. $E_F$, $E_{CB}$, $E_{VB}$, $E_G^{NiO}$, $E_G^{TiO_2}$, and $E_{bb}^{TiO_2}$ represent the Fermi level, the conduction band minimum, the valence band maximum, the band gap of $NiO_x$, band gap of $TiO_2$, and band bending, respectively.

UV-illumination of conventional cationic or anionic organic pollutants such as methylene blue (MB) and methyl orange (MO).[59,60] Before irradiating with UV light, the dye solution was stirred in the presence of the photocatalysts for 30 min in the dark. A significant decrease of the pH value down to 3.15–4.35 was observed for the 0–2 wt% NiO–$TiO_2$ nanomaterials, evidencing the acidic properties of the materials studied (Table S1, ESI†). This finding confirms that the $TiO_2$ nanobipyramids exposing mainly {101} facets are acidic as previously reported in the literature.[13] After taking into account the influence of the pH change upon the absorption properties of both dyes, no significant dye adsorption onto the photocatalysts was detected. While both MB and MO solutions remained unchanged under UV light irradiation without any catalyst, a stepwise attenuation of all characteristic absorption peaks in the wavelength range of 200–800 nm for both dyes was observed (Fig. 7A and C). It is worthwhile to mention that the main absorption peak of MB shifts progressively from 664 nm to 644 nm after 80 min of illumination, which can be related to the formation of Azur B and Azur A dye intermediates arising from the *N*-demethylation of MB.[61,62] Nonetheless, the collapse of the absorption bands in the UV region for both MO and MB solutions in the presence of the 0.25 wt% NiO–$TiO_2$ nanomaterials indicates complete decomposition of these dyes within 80 min (Fig. 7A, C and Fig. S7, ESI†). Moreover, as shown in Fig. 7B and D, the photodecomposition of MB and MO by the pure $TiO_2$ and NiO–$TiO_2$ nanomaterials followed a pseudo first-order law, $\ln(C/C_0) = -k_{app}t$, where $k_{app}$ is the pseudo first-order rate constant and, $C$ and $C_0$ represent the concentration of the dye in the solution at time $t$ and 0. The corresponding apparent rate constants are reported in Table 1. To take into account the specific surface areas, normalized rate constant ($K_{norm}$) defined as $K_{norm} = k_{app}/S_{BET}$ have been calculated and plotted as a function of the NiO loading (Fig. 8).

First of all, MO was preferentially decomposed in comparison to MB for a given NiO loading, all samples exposing only {101} anatase $TiO_2$ facets. The selective decomposition of MO might be related to the {101} facet as it has been previously proposed that MB and MO were selectively adsorbed and degraded by the (001) and (101) planes, respectively.[63,64] On the other hand, Liu *et al.* suggested a reverse role of the two facets and thus the origin of the selectivity stemming from the facet still remains controversial.[65] Herein, the amphoteric behaviour of the nanoparticles likely plays a key role in the selectivity for MO degradation. Indeed, the surface charge attracts the dyes with opposite charge from the solution and depends on the pH of the solution, which is affected by the surrounding of the nanoparticles.[35,36,59,60] Below the point of zero charge ($pH_{pzc}$) of anatase $TiO_2$, particles adsorb protons,

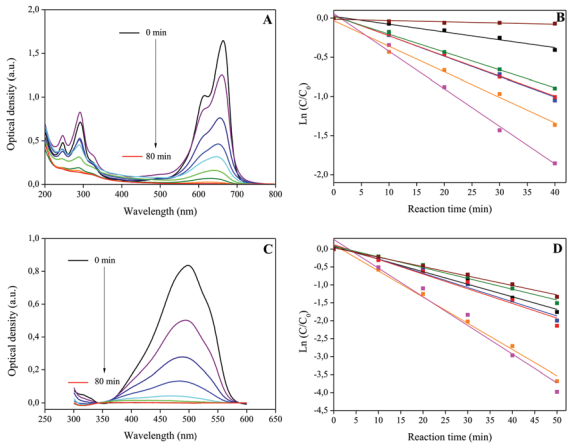


Fig. 7 (A) (resp. C) Absorbance changes of the MB (resp. MO) solution after different irradiation times in the presence of the 0.25 wt% NiO–$TiO_2$ nanocomposite: equilibrium (black), 10 min (purple), 20 min (royal), 30 min (blue), 40 min (cyan), 50 min (green), 60 min (olive), 70 min (orange) and 80 min (red). (B) (resp. D) $\ln(C/C_0)$ as a function of the irradiation time for MB (resp. MO) decomposition in the presence of pure $TiO_2$ (black), 0.1 wt% NiO–$TiO_2$ (orange), 0.25 wt% NiO–$TiO_2$ (magenta), 0.5 wt% NiO–$TiO_2$ (blue), 1 wt% NiO–$TiO_2$ (red), 2 wt% NiO–$TiO_2$ (olive) and 10 wt% NiO–$TiO_2$ (brown) nanomaterials.

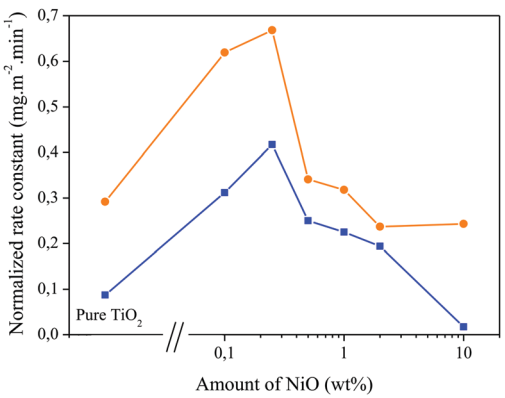


Fig. 8 Normalized rate constant $K_{norm}$ as a function of the NiO amount for the degradation of MB (squares, blue) and MO (circles, orange).

thus leading to a positive charge surface, whereas above the $pH_{pzc}$ they release protons resulting in a negative surface charge in the reaction medium. Ku *et al.* found that the $pH_{pzc}$ of pure $TiO_2$ was 5.3 and that of NiO–polycrystalline $TiO_2$ increased from 5.6 to 6.7 when the NiO amount was augmented from 0.1 to 5.0 wt%.[66] Due to the acidity of the sample studied, the pH of the solutions ranges between 3.15 and 4.35 resulting in a positively charged surface. As a result, the chemisorption of the positively charged MB dye is disfavoured, which precludes any dye sensitization processes for MB decomposition, whereas the anionic form of MO (according to the acidity constant of MO, *i.e.* 3.45, the anionic form of MO is present in a significant amount in the reaction medium) is preferentially adsorbed onto the photocatalysts due to the electrostatic interaction. This would explain the enhanced photodecomposition rate of MO compared to that of MB.

Nonetheless, pH effects and surface charges are not the only main factors governing the high photocatalytic activity of the materials prepared for dye decomposition. Indeed, the NiO–$TiO_2$ nanocomposites showed higher photocatalytic activities than pure $TiO_2$ for NiO loading in the 0.1–1 wt% range (Fig. 8). Moreover, the evolution of the photocatalytic activities as a function of the NiO amount is similar for both anionic and cationic dyes, the 0.25 wt% NiO/$TiO_2$ nanocomposite leading to the highest activities. Thus, the normalized rate constants for 0.25 wt% NiO–$TiO_2$ are 4.8 and 2.3 times higher than those of pure $TiO_2$ for MB and MO, respectively. The introduction of NiO therefore strongly influences the photocatalytic properties. As described above, the surface properties (specific surface area, adsorption properties for a given dye…) and light harvesting ability of the 0.1–1 wt% NiO–$TiO_2$ composites are similar. As a consequence, the change in the photocatalytic properties can either be attributed to the enhanced photo-generated charge-separation efficiency or to the catalytic effects of the homogeneously distributed $NiO_x$ surface layers. According to the energy diagram shown in Fig. 6, the photo-excited electron and holes may be transferred to $TiO_2$ and NiO, respectively. The electrons transferred to $TiO_2$ then take part in the reduction of dissolved oxygen, forming a superoxide radical, $O_2^{\bullet -}$. The $O_2^{\bullet -}$ radicals react with $H_2O$ to produce hydroxyl radicals $OH^{\bullet}$, which are strong oxidizing agents for the decomposition of the dyes. At the same time, the holes transferred to NiO directly react with the surface adsorbed dyes, leading to dye decomposition, and also oxidize the surface hydroxyl groups or physisorbed $H_2O$, forming $OH^{\bullet}$. Nonetheless, as the energy level differences reported in Fig. 6 are weak, the enhanced reaction rates at the $NiO_x$ surface can also account for the high photocatalytic activities.

## 4. Conclusions

Heterostructure NiO-(101)-anatase–$TiO_2$ nanoparticles were successfully synthesized by depositing NiO nanoparticles onto the {101} facet of the oriented $TiO_2$ nanoparticles using the supercritical fluid chemical deposition route. The materials characterization results reveal that the SFCD method allows a good dispersion of NiO at loadings below 2 wt% without affecting the textural and morphological properties of the starting bipyramid $TiO_2$ nanoparticles. Only small downward shifts of the core levels of the NiO–$TiO_2$ photocatalysts compared with that of the pure $TiO_2$ photocatalyst were observed by XPS, which does not allow conclusions about the presence of band bending at the p–n junction of the NiO–$TiO_2$ interface. Nonetheless, the nanocomposites containing NiO loadings below 1 wt% showed higher photocatalytic activity than pure anatase $TiO_2$ for the photodegradation of both anionic and cationic dyes. The 0.25 wt% NiO–$TiO_2$ nanocomposite was the most efficient system for MB and MO dye decomposition, with activities 4.8 and 2.3 times higher than those of pure $TiO_2$. The better performances were mainly attributed to the heterocontact at the interface of the NiO–$TiO_2$ crystallites and to the

 

improved reaction rates at the $NiO_x$ surface. However, the morphology is not yet ideal and needs further optimization. Finally, this work suggests a potential strategy to enhance photocatalytic activity by depositing co-catalysts onto specific facets of photocatalyst crystals.

## Conflicts of interest

There are no conflicts to declare.

## Acknowledgements

Marie-Anne Dourges (ISM) is thanked for recording the $N_2$ sorption data. This work was performed within the framework of the EMMI (European Multifunctional Material Institute) and was partially funded by the ''Université Franco-allemande'' (German-French Doctoral College in Functional Materials) and the European Commission (S. K. Fellowship, Erasmus Mundus IDS-FunMat). The authors also acknowledge the PLACAMAT structure for the electron microscopy structure.

## Notes and references

1 A. Fujishima and K. Honda, *Nature*, 1972, **238**, 37–38.
2 J. Schneider, M. Matsuoka, M. Takeuchi, J. Zhang, Y. Horiuchi, M. Anpo and B. W. Bahnemann, *Chem. Rev.*, 2014, **114**, 9919–9986.
3 J. Kou, C. Lu, J. Wang, Y. Chen, Z. Xu and R. S. Varma, *Chem. Rev.*, 2017, **117**, 1445–1514.
4 M. G. Walter, E. L. Warren, J. R. McKone, S. W. Boettcher, Q. Mi, E. A. Santori and N. S. Lewis, *Chem. Rev.*, 2010, **110**, 6446–6473.
5 P. V. Kamat, *J. Phys. Chem. Lett.*, 2012, **3**, 633–672.
6 T. Ohno, K. Sarukawa and M. Matsumura, *New J. Chem.*, 2002, **26**, 1167–1170.
7 T. Tachikawa, Y. Soichiro and T. Majima, *J. Am. Chem. Soc.*, 2011, **133**, 7197–7204.
8 G. Liu, J. C. Yu, G. Q. Lu and H.-M. Cheng, *Chem. Commun.*, 2011, **47**, 6763–6783.
9 D. Wang, P. Kanhere, M. Li, Q. Tay, Y. Tang, Y. Huang, T. C. Sum, N. Mathews, T. Shritharan and Z. Chen, *J. Phys. Chem. C*, 2013, **117**, 22894–22902.
10 M. D'Arienzo, M. V. Dozzi, M. Redaelli, B. Di Credico, F. Morazzoni, R. Scotti and S. Polizzi, *J. Phys. Chem. C*, 2015, **119**, 12385–12393.
11 U. Diebold, *Surf. Sci. Rep.*, 2003, **48**, 53–229.
12 C. Sun, L.-M. Liu, A. Selloni, G. Q. Lu and S. C. Smith, *J. Mater. Chem.*, 2010, **20**, 10319–10334.
13 F. Dufour, S. Pigeot-Remy, O. Durupthy, S. Cassaignon, V. Ruaux, S. Torelli, L. Mariey, F. Maugé and C. Chanéac, *Appl. Catal., B*, 2015, **174-175**, 350–360.
14 W. Chen, Q. Kuang, Q. Wang and Z. Xie, *RSC Adv.*, 2015, **5**, 20396–20409.
15 N. Murakami, Y. Kurihara, T. Tsubota and T. Ohno, *J. Phys. Chem. C*, 2009, **113**, 3062–3069.
16 N. Roy, Y. Sohn and D. Pradhan, *ACS Nano*, 2013, **7**, 2532–2540.
17 J. Yu, J. Low, W. Xiao, P. Zhou and M. Jaroniec, *J. Am. Chem. Soc.*, 2014, **136**, 8839–8842.
18 J. Yang, D. Wang, H. Han and C. Li, *Acc. Chem. Res.*, 2013, **46**, 1900–1909.
19 D. A. Panayotov, A. I. Frenkel and J. R. Morris, *ACS Energy Lett.*, 2017, **2**, 1223–1231.
20 Q. Zhang, R. Li, Z. Li, A. Li, S. Wang, Z. Liang, S. Liao and C. Li, *J. Catal.*, 2016, **337**, 36–44.
21 A. L. Linsebigler, G. Lu and J. T. Yates Jr., *Chem. Rev.*, 1995, **95**, 735–758.
22 B. H. Meekins and P. V. Kamat, *J. Phys. Chem. Lett.*, 2011, **2**, 2304–2310.
23 S.-I. Fujita, H. Kawamori, D. Honda, H. Yoshida and M. Arai, *Appl. Catal., B*, 2016, **181**, 818–824.
24 W.-T. Chen, A. Chan, D. Sun-Waterhouse, T. Moriga, H. Idriss and G. I. N. Waterhouse, *J. Catal.*, 2015, **326**, 43–53.
25 M. Wang, Y. Hu, J. Han, R. Guo, H. Xiong and Y. Yin, *J. Mater. Chem. A*, 2015, **3**, 20727–20735.
26 T. Sreethawong, Y. Suzuki and S. Yoshikawa, *Chem. Eng. J.*, 2012, **192**, 292–300.
27 S. A. Rawool, M. R. Pai, A. M. Banerjee, A. Arya, R. S. Ningthoujam, R. Tewari, R. Rao, B. Chalke, P. Ayyub, A. K. Tripathi and S. R. Bharadwaj, *Appl. Catal., B*, 2018, **221**, 443–458.
28 Md. T. Uddin, Y. Nicolas, C. Olivier, W. Jaegermann, N. Rockstroh, H. Junge and T. Toupance, *Phys. Chem. Chem. Phys.*, 2017, **19**, 19279–19288.
29 C. Aymonier, A. Loppinet-Serani, H. Reveron, Y. Garrabos and F. Cansell, *J. Supercrit. Fluids*, 2006, **38**, 242–251.
30 C. Aymonier, G. Philippot, A. Erriguible and S. Marre, *J. Supercrit. Fluids*, 2018, **134**, 184–196.
31 J.-L. Bobet, C. Aymonier, D. Mesguish, F. Cansell, K. Asano and E. Akika, *J. Alloys Compd.*, 2007, **429**, 250–254.
32 A. Denis, E. Sellier, C. Aymonier and J.-L. Bobet, *J. Alloys Compd.*, 2009, **476**, 152–159.
33 S. Couillaud, M. Kirikova, W. Zaïdi, J.-P. Bonnet, S. Marre, C. Aymonier, J. Zhang, F. Cuevas, M. Laroche, L. Aymard and J.-L. Bobet, *J. Alloys Compd.*, 2013, **429**, 6–12.
34 B. Motos-Pérez, C. Quilfen, D. Uzio and C. Aymonier, *ChemCatChem*, 2017, **9**, 2352–2357.
35 A. Mills and J. Wang, *J. Photochem. Photobiol., A*, 1999, **127**, 123–124.
36 X. Yan, T. Ohno, K. Nishijima, R. Abe and B. Ohtani, *Chem. Phys. Lett.*, 2006, **429**, 606–610.
37 C.-T. Dinh, T.-D. Nguyen, F. Kleitz and T.-O. Do, *ACS Nano*, 2009, **3**, 3737–3743.
38 M. D'Arienzo, J. Carbajo, A. Bahamonde, M. Crippa, S. Polizzi, R. Scotti, L. Wahba and F. Morazzoni, *J. Am. Chem. Soc.*, 2011, **133**, 17652–17661.
39 J. Joo, S. G. Kwon, T. Yu, M. Cho, J. Lee, J. Yoon and T. Hyeon, *J. Phys. Chem. B*, 2005, **109**, 15297–15302.
40 S. Brunauer, P. H. Emmett and E. Teller, *J. Am. Chem. Soc.*, 1938, **60**, 309–319.
41 F. Rouquerol, J. Rouquerol and K. Sing, *Adsorption by Powders and Porous Solids*, Acasemic Press, San Diego, 1999, p. 200.

42 A. Klein, T. Mayer, A. Thissen and W. Jaegermann, *Bunsenmagazin*, 2008, **10**, 124–139.
43 S. Sahoo, A. K. Arora and V. Sridharan, *J. Phys. Chem. C*, 2009, **113**, 16927–16933.
44 M. Rezaee, S. M. M. Khoie and K. H. Liu, *CrystEngComm*, 2011, **13**, 5055–5061.
45 L. C. Sim, K. W. Ng, S. Ibrahim and P. Saravanan, *Int. J. Photoenergy*, 2013, 659013.
46 L. D. Arsov, C. Kormann and W. Plieth, *J. Raman Spectrosc.*, 1991, **22**, 573–575.
47 S. Balaji, Y. Djaoued and J. Robichaud, *J. Raman Spectrosc.*, 2006, **37**, 1416–1422.
48 W. Hong, Y. Zhou, C. Lv, Z. Han and G. Chen, *ACS Sustainable Chem. Eng.*, 2018, **6**, 889–896.
49 K. S. W. Sing, *Pure Appl. Chem.*, 1985, **57**, 603–619.
50 C. K. Lee and S. L. Lee, *Heterog. Chem. Rev.*, 1996, **3**, 269–302.
51 T. Uddin, Y. Nicolas, C. Olivier, T. Toupance, M. M. Mûller, H.-J. Kleebe, K. Rachut, J. Ziegler, A. Klein and W. Jaegermann, *J. Phys. Chem. C*, 2013, **117**, 22098–22110.
52 F. Jahan, M. H. Islam and B. E. Smith, *Sol. Energy Mater. Sol. Cells*, 1995, **37**, 283–293.
53 Y.-F. Zhang, W. Lin, K.-N. Ding and J.-Q. Li, *J. Phys. Chem. B*, 2005, **109**, 19270–19277.
54 P. S. Patil and L. D. Kadam, *Appl. Surf. Sci.*, 2002, **199**, 211–221.
55 G. A. Sawatzky and J. W. Allen, *Phys. Rev. Lett.*, 1984, **53**, 2339–2347.
56 A. Iwaszuk, M. Nolan, Q. Jin, M. Fujishima and H. Tada, *J. Phys. Chem. C*, 2013, **117**, 2709–2718.
57 M. J. Jackman, A. G. Thomas and C. Muryn, *J. Phys. Chem. C*, 2015, **119**, 13682–13690.
58 S. Uhlenbrock, C. Scharfschwerdt, M. Neumann, G. Illing and H.-J. Freund, *J. Phys.: Condens. Matter*, 1992, **4**, 7973–7978.
59 M. A. Lazar and W. A. Daoud, *RSC Adv.*, 2012, **2**, 447–452.
60 M. Rochkind, S. Pasternak and Y. Paz, *Molecules*, 2015, **20**, 88–110.
61 T. Zhang, T.-K. Oyama, S. Horikoshi, H. Hidaka, J. Zhao and N. Serpone, *Sol. Energy Mater. Sol. Cells*, 2002, **73**, 287–303.
62 T. Zhang, T. Oyama, A. Aoshima, H. Hidaka, J. Zhao and N. Serpone, *J. Photochem. Photobiol., A*, 2001, **140**, 163–172.
63 B. Liu, Y. Huang, Y. Wen, L. Du, W. Zeng, Y. Shi, F. Zhang, G. Zhu, X. Xu and Y. Wang, *J. Mater. Chem.*, 2012, **22**, 7484–7491.
64 J. Zhang, W. Chen, J. Xi and Z. Ji, *Mater. Lett.*, 2012, **79**, 259–262.
65 S. Liu, J. Yu and M. Jaroniec, *J. Am. Chem. Soc.*, 2010, **132**, 11914–11916.
66 Y. Ku, C.-N. Lin and W.-M. Hou, *J. Mol. Catal. A: Chem.*, 2011, **349**, 20–27.

 

## 3.5 Photocatalytic activity and band alignment of NiO selectively deposited onto (101) facet of $TiO_2$ anatase co-exposed with (001) and (101) facets

Shun Kashiwaya conducted experiments, data analysis and preparation of the manuscript. Yannick Herman participated in the experimental work Jerome Majimel participated in experimental works and the discussions of the results. Celine Olivier, Andreas Klein, Wolfram Jaegermann and Thierry Toupance participated in the discussions of the results and revised the manuscript.

# Photocatalytic activity and band alignment of NiO selectively deposited onto {101} facet of $TiO_2$ anatase co-exposed with {001} and {101} facets


## Abstract

Facet-engineered anatase $TiO_2$ with NiO nanoparticles heterocontacts were successfully prepared by selective photodeposition of NiO nanoparticles onto the {101} facet of the top-truncated bipyramidal $TiO_2$ anatase nanocrystals co-exposed with {001} and {101} facets. The morphology and electronic properties of the resulting 0.1-10 wt% NiO-decorated $TiO_2$ were investigated by X-ray diffraction, high resolution electron microscopy, $N_2$ sorption analysis, and UV-vis spectroscopy. Furthermore, a careful determination of the energy band alignment diagram was conducted by a model experiment using XPS and UPS in order to verify charge separation at the interface of the NiO/$TiO_2$ heterostructure. The model experiment was performed by stepwise deposition of NiO onto oriented $TiO_2$ substrates and in-situ photoelectron spectroscopy measurements without breaking vacuum. Core levels showed shifts of 0.58 eV toward lower binding energies, meaning an upward band bending in $TiO_2$ at the NiO-$TiO_2$ interface. Furthermore, 0.1 wt % NiO-$TiO_2$ exhibited 50 % higher activities than the pure $TiO_2$ for methylene blue (MB) photodecomposition under UV irradiation. This enhanced photocatalytic activity of NiO-$TiO_2$ nanocomposites was related to the internal electric field developed at the p-n NiO/$TiO_2$ heterojunction, leading to vectorial charge separation. Finally, mechanistic studies conducted in the presence of carrier or radical scavengers revealed that holes dominantly contributed to the photocatalytic reactions in the case of NiO-$TiO_2$ photocatalysts while electrons played a main role in photocatalysis for the pure $TiO_2$ materials.


## I Introduction

Chemical reactions on titanium dioxide ($TiO_2$) surfaces have attracted worldwide attention in the fields of energy conversion,[1-3] energy storage[4-5] and photocatalysis[6-8] owing to the relatively high abundance, low cost, environmental friendliness, high chemical stability and, both outstanding optical and electronic properties of $TiO_2$-based systems. Thus, $TiO_2$ materials, mainly as anatase polymorph, showed great ability for decomposition of various pollutants in air or water,[7] carbon dioxide reduction,[9] and water splitting[6] under light illumination. Nonetheless, pure $TiO_2$ materials still suffer from some limitations for

practical use in photocatalysis stemming from too fast recombination of photogenerated electron-hole pairs and too slow redox reactions.[10] A first efficient way to improve the photocatalytic activity consists in coupling $TiO_2$ nanoparticles to noble metal co-catalysts with large work function, *e.g.* platinum and rhodium, in order to enhance the quantum yield in minority carrier photogenerating by separating electron-hole pairs with a Schottky barrier at the interface and subsequently transferring them to acceptor molecules.[7,11-12] Furthermore, along with providing reaction sites, these noble metals have beneficial effects on the kinetics of the photocatalytic reactions, for instance by decreasing the overpotential and the activation energy for hydrogen evolution from water according to Volcano plot for metal hydrogen bonding energy.[13] However, the use of noble metals led to further drawbacks such as their scarcity and cost, and their ability to catalyze the back reaction of the formation of water from hydrogen and oxygen, limiting the photocatalytic activity for water splitting. Thus, transition metal oxides that have a negligible activity for water formation have been chosen as co-catalysts to avoid back reactions.[14] Another conventional strategy for enhancing the photocatalytic activity is to deposit a p-type semiconductor onto a n-type semiconductor in order to establish a p-n heterojunction where photogenerated electrons and holes can be spatially separated to the n-type and the p-type components, respectively. Thus, oxidation reactions are promoted by p-type metal oxide co-catalysts such as nickel oxide (NiO), iridium oxide ($IrO_2$), and cobalt oxide ($Co_3O_4$) since these oxides provide oxidation reaction sites, decrease the activation energy, and suppress back reactions.[7,12,15-16]

On the other hand, the selective deposition of Pt and $PbO_2$ on specific orientations of rutile and anatase particles was first reported by Ohno *et al.,*[17] revealing that the different facets of a crystal exposed to the surface promote the separation of photoinduced electrons and holes.[18-21] This finding has therefore triggered crystal facet engineering of $TiO_2$ particles. Crystallographic surface orientation and structures indeed play a crucial role in photocatalysis with metal oxide semiconductors since the surface atomic structures rule the physi/chemisorption of reactive species, surface transfer and trapping of photoinduced charge carriers, and, as a consequence, redox processes.[22] Over the past decade, many efforts have been devoted to maximizing the surface area of the highest energy {001} facet of anatase crystals, which was believed to be the most reactive, to reach high photocatalytic efficiencies.[23-25] By contrast, improved photocatalytic efficiencies were reported for particles exposing both low energy facets {101} as reduction reaction sites and high energy facets {001} as oxidation reaction sites.[26-29] This was ascribed to the selective migration and/or trapping of electrons and positive holes to specific exposed crystal faces favoring spatial charge separation. As a result, the presence of both {101} and {001} facets in anatase nanocrystals are relevant to get high photocatalytic activities. Moreover, enhanced photocatalytic activities could be reached with $TiO_2$-based materials by combining appropriate co-catalysts together with facet engineering of $TiO_2$ nanocrystals for their synergetic effect. In this context, nickel oxide (NiO),

which is rather abundant and reactive, is one of the most investigated co-catalyst in combination with $TiO_2$, and can act as both reduction and oxidation co-catalysts. Even though various NiO-$TiO_2$ nanostructures with a random distribution of NiO onto $TiO_2$ have been previously studied,[30-35] the selective deposition of NiO onto oriented $TiO_2$ nanoparticles has never been achieved and both electronic and photocatalytic properties of the resulting heterostructures have not been investigated yet.

In the following, we described the selective deposition of NiO onto the {101} facet of anatase $TiO_2$ nanoparticles co-exposed with {001} and {101} facets by employing an original photodeposition method. The formation of cubic NiO particles on the {101} facet was clearly evidenced by high resolution transmission electron microscopy (HRTEM), high resolution scanning transmission electron microscopy (HRSTEM) and energy dispersive X-ray spectroscopy (EDX) mapping. Furthermore, a so-called interface experiment[36] was performed by in-situ X-ray (XPS) and ultraviolet (UPS) photoelectron spectroscopy measurements during stepwise NiO deposition via DC sputtering onto a stoichiometric single crystal anatase (101) surface. An energy band alignment of the NiO-anatase (101) interface was experimentally derived from the obtained XP and UP spectra of the interface experiment. Finally, photocatalytic activities of the obtained nanocomposites as a function of NiO loading were examined by degradation of methylene blue (MB) under UV irradiation and mechanistic aspects were investigated by comparing the degradation rate determined with those obtained in the presence of hole and radical scavengers. The main species ruling the photocatalytic properties of the NiO-$TiO_2$ nanomaterials appeared to be different from that governing those of pure $TiO_2$ nanocrystals.

## 2. Experimental section

### 2.1. Photocatalyst preparation

All the chemicals were purchased in analytical grade and used without any further purification. Single crystalline $TiO_2$ anatase particles co-exposed with {001} and {101} facets obtained by gas-phase reaction were provided by Prof. Ohtani's group.[27] NiO-$TiO_2$ anatse heterostructured photocatalysts were synthesized in two steps. First, Ni-B was selectively deposited onto the {101} facet of the anatase particles by photo-deposition.[37] 1.27 g of boric acid (Sigma-Aldrich) was added to 70 mL of distilled water under stirring. The solution was sonicated for 5 min. Potassium hydroxide was then progressively added to the solution until reaching pH = 9.2 under stirring and 30 mL of distilled water was added to the solution. The resulting solution is referred as a KBi buffer. The KBi buffer, deionized water, and nickel(II) nitrate hexahydrate solution (34 mM, Sigma-Aldrich) were stirred and subsequently centrifuged at 4000 rpm for 10 min to remove slight amount of precipitated nickel hydroxide, which has light green color. 500 mg of the single crystalline anatase particles were dispersed into the solution, treated with

sonication for 10 min, and stirred for 1 h. To realize the photo-deposition of Ni-B onto the anatase particles, the solution was irradiated by UV light under stirring for 3 h. After washing with distilled water for three times, the resulting particles were dried at 70 °C and dried in vacuum for 1 h to obtain Ni-B deposited onto the {101} facet of the anatase particles. The {101} facet of anatase crystals was found to accumulate photo-generated electrons,[18] and thus nickel nitrate ($Ni^{2+}$) is supposed to be reduced to Ni-B ($Ni^0$) selectively on the {101} facet of anatase crystals under UV irradiation. The resulting Ni-B/$TiO_2$ heterostructured particles were then annealed at 400 °C for 4 h to oxidize deposited Ni-B and achieve the target NiO-$TiO_2$ photocatalysts where NiO is selectively deposited onto the {101} facet of the anatase particles co-exposed with {001} and {101} facets. Photocatalysts containing 0.1, 0,2, 0.5, 1, and 10 wt % of NiO were obtained by adding 0.2, 0.4, 1, 2, 20 mL of nickel nitrate solution (34 mM), respectively, as a precursor added to 500 mg of anatase particles. The KBi buffer/nickel nitrate solution ratio was fixed at 2.5 and distilled water was also added to reach 100 mL of total volume of the precursor solution containing KBi buffer and nickel nitrate. The resulting photocatalyst are hereafter named as 0.1wt% NiO-$TiO_2$, 0.2wt% NiO-$TiO_2$, 0.5wt% NiO-$TiO_2$, 1wt% NiO-$TiO_2$, and 10wt% NiO-$TiO_2$.

### 2.2. Photocatalyst characterization

XRD analyses were carried out using a Bruker AXS diffractometer (D2 PHASER A26-X1-A2B0D3A) equipped with a Cu anode (Kα radiation).[38] DRS spectra were recorded with an UV-vis-NIR Cary 5000E spectrophotometer endowed with an integrating sphere and by using a Suprasil cell bearing a quartz window. Halon standard (6 mm deep and 1 $g.cm^{-3}$ density) was employed as a reference. Specific surface areas ($S_{BET}$) were determined by applying the BET (Brunauer−Emmett−Teller) equation[39] between 0.1 and 0.3 relative pressures of $N_2$ adsorption−desorption isotherms recorded at 77K with an ASAP2010 Micromeritics apparatus. HRTEM images were taken using a JEOL JEM 2200F (JEOL, Tokyo, Japan) operating at an acceleration voltage of 200 kV (wavelength $\lambda$ = 2.51 pm) equipped with a Schottky type FEG and an EDX system (Oxford, Wiesbaden, Germany). For the sample preparation for HRTEM, HRSTEM and EDX, the photocatalysts nanoparticles were dispersed in ethanol under ultrasound sonication and a few droplets of the suspension was placed on holey carbon grids (Cu-300HD, Pacific Grid-Tech).

Electronic properties of the synthesized photocatalysts were investigated with DAISY-MAT[40] consisting of a multi-technique surface analysis system (Physical Electronics PHI 5700). XP spectra were measured by using monochromatic Al Kα (1486.6 eV) radiation with an energy resolution of 0.4 eV as determined from the broadening of the Fermi edge of a sputter-cleaned Ag substrate. Binding energies of core levels, and valence band maximum $E_{VB}$ can be obtained with an accuracy of 50 meV, and 100 meV, respectively. Binding energies determined by XPS were calibrated by the Fermi level position of the sputter-cleaned Ag sample. Thus, all binding energies are provided with respect to the calibrated Fermi

level set to 0 eV. Photocatalysts samples were pressed onto indium foils as a conductive substrate to avoid a charging problem and transferred into the XPS chamber without any further treatments.

### 2.3. Photocatalytic experiments

Photocatalytic properties of the different NiO-$TiO_2$ nanocomposites were determined by decomposition of MB (Alfa Aesar) under UV-light illumination using a previously established procedure.[41] Typically, a suspension of photocatalyst (50 mg) in a MB aqueous solution (10 mg/L, 50 mL) was introduced into a Pyrex beaker and was then illuminated with a 125 W high-pressure mercury lamp (Philips, HPL-N 125 W/542 E27) positioned 60 mm above the solution. After stirring in the dark for 30 min to reach adsorption/desorption equilibrium and switching on the light, 2 mL of the suspensions were collected at given irradiation time intervals, and then centrifuged (4000 rpm, 10 min) to remove the photocatalyst particles from the MB solution. The remaining MB amount was monitored by UV-visible spectroscopy following the change in absorption at $\lambda_{max}$ = 664 nm using a Shimadzu, UV-1650 pc spectrophotometer. Blank experiments were also conducted with the catalysts in the absence of light and without the catalysts with light irradiation.

Furthermore, the same experiments were also conducted in the presence of different scavengers for charge carriers and radicals to investigate the role of radicals in the photocatalytic reactions. Potassium iodide (KI), isopropanol (IPA), and 1,4-benzoquinone (BQ) were selected as holes, hydroxyl radicals (OH), and superoxide radicals ($\bullet O^{2-}$) scavengers, respectively.[42-45] The concentration of KI, IPA, and BQ were 4 x $10^{-4}$, 1 x $10^{-3}$ and 1 x $10^{-3}$ M, respectively.

### 2.4. Interface model experiment

Natural anatase crystals were employed for both (101) and (001) surfaces (SurfaceNet GmbH, Germany). The size of substrates is 5 x 5 x 1 mm. A surface roughness less than a lattice constant was achieved after epi-polishing. As-it-is surfaces are contaminated from air and the polishing step. Cleaning cycles of $Ar^+$ ion sputtering with an energy of 1 keV for 15 min and annealing in vacuum at 873 K for 30 min were repeated until no remaining emissions from contaminations were observed by XPS. This cleaning procedure has been often employed to remove the contamination and achieve clean $TiO_2$ surfaces.[46] However, Ar sputtering not only leads to a highly reduced surface and thus forms O vacancies and $Ti^{3+}$ surface states, but also partially ruins the crystallinity of the surface and introduces an amorphous phase.[47] The O vacancy concentration for the (101) and (001) surface prepared by the procedure is expected to be $7\pm2$ and $1\pm2$ %, respectively.[48] Therefore, the sputtered surfaces were oxidized by an O plasma at room temperature in an atmosphere of 7.5 x $10^{-5}$ mbar $O_2$ for 15 min to re-oxidize the surface and subsequently annealed at 873 K in UHV to re-crystallize the surface. Here the O plasma was selected

to replenish the lattice O instead of annealing in $O_2$ atmosphere, which has been generally used for oxidation, as this annealing procedure can form additional incomplete reconstructions for rutile surfaces,[49] which could be also formed for anatase surfaces. It may also result in iron oxide surface contaminations as at elevated temperatures Fe surface segregation, which is a typical contamination in natural anatase crystals, may take place.[42] Furthermore, atomic O in the O plasma is more oxidative than a molecular $O_2$ during annealing in O atmosphere.[50] The re-oxidized and re-crystallized surfaces were treated with an O plasma at the same condition mentioned above to oxidized them as they were slightly reduced due to annealing in vacuum at the elevated temperature. This further oxidation procedure is expected to introduce adsorbed O atoms such as peroxo species adsorbed on the surfaces. Finally, the stoichiometric surfaces were obtained by removing adsorbed O atoms by annealing the oxidized surfaces in UHV condition at 473 K for 20 min.[51]

To experimentally determine energy band alignments of NiO and oriented anatase surfaces, the interface model experiments were carried out in DAISY-MAT capable of XPS and UPS and different deposition chambers in UHV without breaking vacuum. This system allows the in-situ characterization of the prepared surfaces and interfaces. NiO was grown on the stoichiometric anatase (001) and (101) substrates using a direct current (DC) reactive magnetron sputter deposition from a metallic Ni target with 40 W of DC power under 20 % $O_2$/ 80 % Ar mixture atmosphere at 0.5 Pa pressure and room temperature. The gas flow of oxygen and argon is kept of 4 and 16 sccm, respectively, during the deposition. The target-to-substrate distance was set to 8.4 cm. The deposition rate is about 2.0 $nm.min^{-1}$. We are aware of possibly additional defect states induced by sputter deposition of oxides. However, a number of systematic studies on different oxides have proven that for our experimental conditions this approach is applicable. After each stepwise deposition of NiO by DC sputtering onto the substrates, XPS spectra were recorded without breaking vacuum to follow shifts of the binding energies of core level emission lines and the evolution of peak shapes. To determine work function and ionization potentials of the stoichiometric anatase substrates and NiO films at the end of all the stepwise deposition, UPS spectra were recorded in normal emission with He I radiation ($h\nu = 21.2$ eV) from a He discharge lamp and a negative sample bias of 4.0 V. The total energy resolution of UPS is 0.2 eV. No charging problems were observed during the XPS and UPS measurements. Binding energies obtained by XPS and UPS were calibrated by the Fermi level energy of the sputter-cleaned Ag sample. Hence, all the binding energies are given with respect to the calibrated Fermi level position set to 0 eV. More details of the DAISY-MAT system and the experimental approach in performing the experiments may be found elsewhere.[36]

## 3. Results and Discussion

### 3.1. Characterization of photocatalysts

To prepare well-defined heterostructure NiO-$TiO_2$ particles, the electroless nickel plating strategy was adapted to deposit amorphous Ni-B catalyst on specific facets of $TiO_2$ nanocrystals.[37] Instead of using silver-based materials as a reducing agent, UV-light combined with the charge separation offered by the different redox properties of {101} and {001} facets were exploited for the selective deposition of amorphous Ni-B on the {101} facets which led to NiO particles after further calcination (Scheme 1).

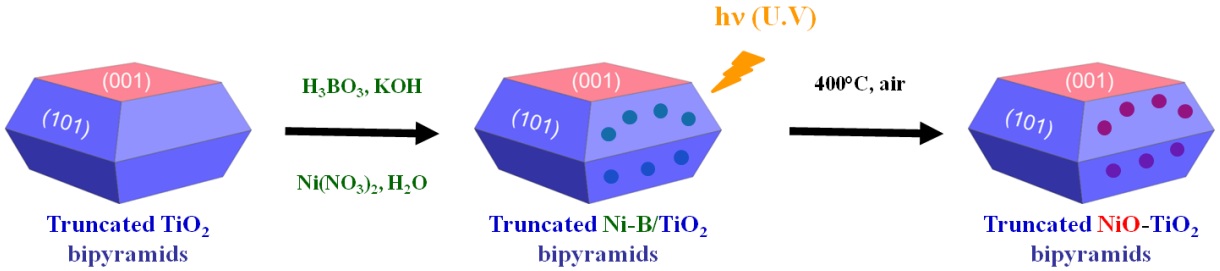


**Scheme 1.** Preparation strategy for selective deposition of NiO onto {101} anatase $TiO_2$ facets.

Regardless of the NiO loading, the main diffraction peaks observed in the XRD patterns can be indexed as the (101), (004), (200), (105), (211), (204), (116), (220), and (215) diffraction lines of the anatase phase of $TiO_2$ (Figure 1). The weak feature at 27.5° (2θ) can be attributed to the presence of small amounts of the rutile polymorph (110 diffraction line) due to the high temperature (1573 K) used to synthesize the oriented $TiO_2$ particles.[26] Peaks assigned to NiO were not observed clearly probably due to the small crystalline domain size (nm order) of the NiO species. It is indeed well-known that the crystallite size is inversely proportional to the full-width at half-maximum (FWHM) of each peak which yields broadened and attenuated signals in the XRD patterns.[52]

The morphology of the different materials was then studied by TEM, HR-TEM and EDX analyses (Figures 2 and 3). A square shape of the particle indicates that the {001} facet of the anatase single crystal is parallel to the sample carbon grid as anatase single crystals co-exposed with {001} and {101} facets have a bi-pyramidal shape with truncation of their top and bottom edges (Figure 2A). A gradation of the contrast observed at the edge of the particle can be caused by thinner parts of the sample and might represent a slope of the {101} facet. Figure 2B shows $TiO_2$ particles with other angle showing both {001} and {101} facets. STEM images, EDX elemental mapping, and HR-TEM images of 10wt% NiO-$TiO_2$ depicted in Figure 3 clearly indicate that Ni elements are selectively distributed at the {101} facets, which constitute the edge of the particle (Figure 3E and 3F). HR-TEM images confirm the selective deposition of 2-3 nm of NiO particles onto the {101} facet (Figure 3G and

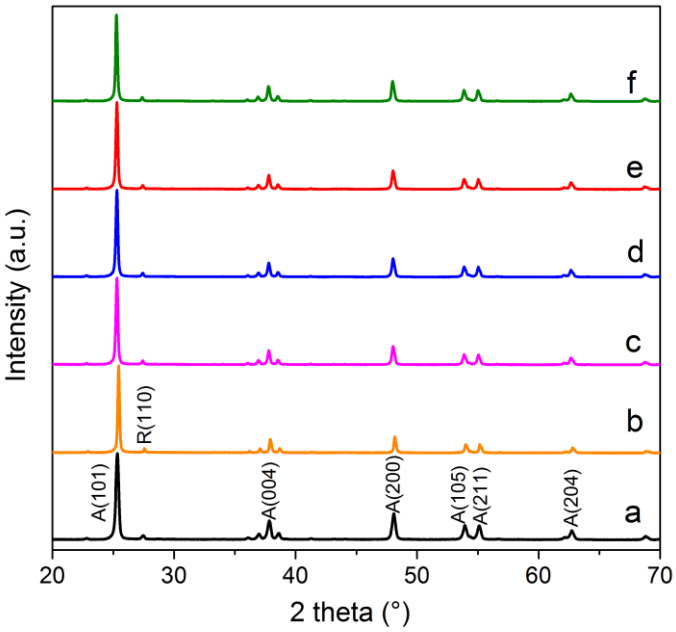


**Figure 1**. XRD pattern of the pure $TiO_2$ (a, black), 0.1 (b, orange), 0.2 (c, magenta), 0.5 (d, blue), 1.0 (e, red), and 10 wt % (f, olive) NiO-$TiO_2$ composites.

3H). The interplanar spacing of 0.18 and 0.20 nm matches with the {200} and {111} planes of the face-centered cubic (fcc) crystalline phase of NiO. STEM images before and after electron beam irradiation also indicate the selective deposition of NiO onto the {101} facet of anatase (Figure 3A and 3B).

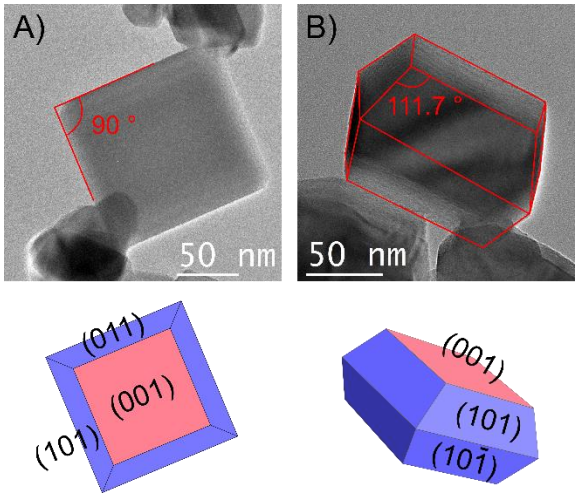


**Figure 2**. Bright field TEM images of the pure $TiO_2$ recorded along (A) the [001] zone axis and (B) the tilted along the [010] direction.

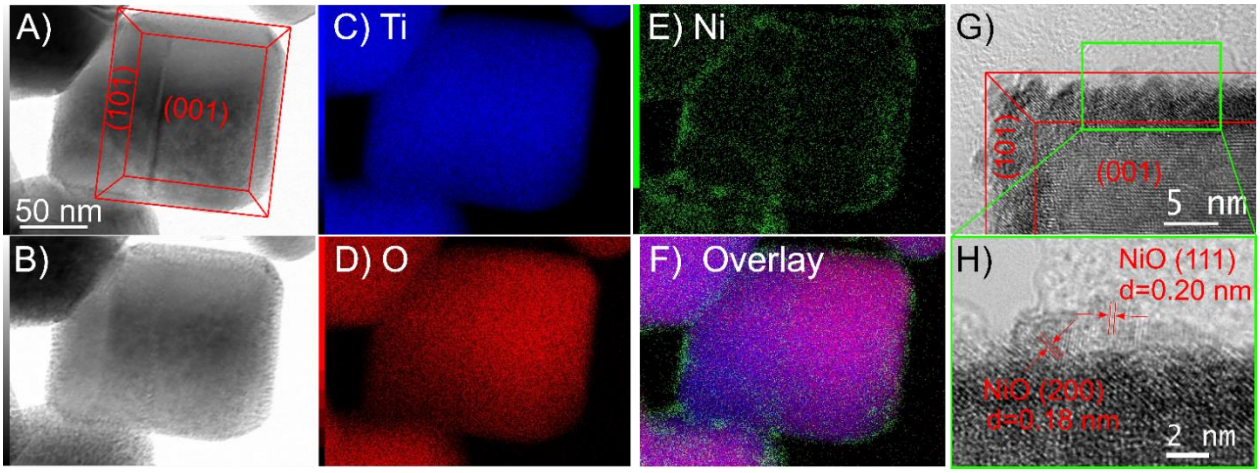


**Figure 3**. Bright field STEM image of 10 wt % NiO/$TiO_2$ (A) before and (B) after electron beam irradiation, EDX elemental mapping of (C) Ti, (D) O, (E) Ni, and (F) overlay, and HRTEM images (G and H).

$N_2$ sorption analyses were performed to determine the textural properties of the nanocomposites prepared. Regardless of the nickel oxide content, the sample showed a type-II adsorption-desorption isotherm typical of non porous or macroporous solids with BET specific areas of about 13.4-14.0 ± 0.4 $m^2.g^{-1}$ and total pore volumes of 0.036-0.044 ± 0.001 $cm^3.g^{-1}$ (Table 1 and Figure S1). These data are consistent with TEM data showing rather well dispersed nanoparticles with few aggregates. Moreover depositing up to 10 wt% NiO does not change significantly specific surface areas and total pore volumes.

**Table 1**. Textural properties ($S_{BET}$ and total pore volume) along with apparent ($K_{app}$) and normalized rate constant ($K_{norm}$) for the photodecomposition of MB using $TiO_2$ and NiO-$TiO_2$ photocatalysts.

| Sample | $S_{BET}$ ($m^2.g^{-1}$) | Total pore volume ($cm^3.g^{-1}$) | $K_{app}$ ($min^{-1}$) | $K_{norm}$ ($mg.m^{-2}.min^{-1}$) |
|---|---|---|---|---|
| Pure $TiO_2$ | 13.4 ± 0.4 | 0.036 ± 0.001 | 0.0483 | 3.60 |
| 0.1wt% NiO-$TiO_2$ | 13.5 ± 0.4 | 0.041 ± 0.001 | 0.0708 | 5.25 |
| 0.2wt% NiO-$TiO_2$ | 14.0 ± 0.4 | 0.042 ± 0.001 | 0.0177 | 1.27 |
| 0.5wt% NiO-$TiO_2$ | 14.0 ± 0.4 | 0.032 ± 0.001 | 0.0094 | 0.67 |
| 1wt% NiO-$TiO_2$ | 14.0 ± 0.4 | 0.044 ± 0.001 | 0.0099 | 0.71 |
| 10wt% NiO-$TiO_2$ | 13.7 ± 0.4 | 0.042 ± 0.001 | 0.0028 | 0.21 |

Optical properties of photocatalysts were investigated by DRS (Figure 4). Heterostructured NiO-$TiO_2$ samples exhibit visible light absorption of which edges shift toward lower energies with increasing the NiO loading even though the band gap of NiO has been reported to be 3.4-4.3 eV which corresponds to an absorption edge of 288-365 nm.[53,54] The origin of the visible light absorption exhibited by NiO-$TiO_2$ nanocomposites can be ascribed to Ti-Ni bondings at the NiO-$TiO_2$ interface or interfacial defect states.[55] DFT calculations revealed that after modification of the $TiO_2$ surface with NiO clusters, new states appear above the valence band and just below the conduction band of $TiO_2$.[31,56] Then, this might result in the narrowed band gap found for NiO-$TiO_2$ samples and thus the visible light absorption.

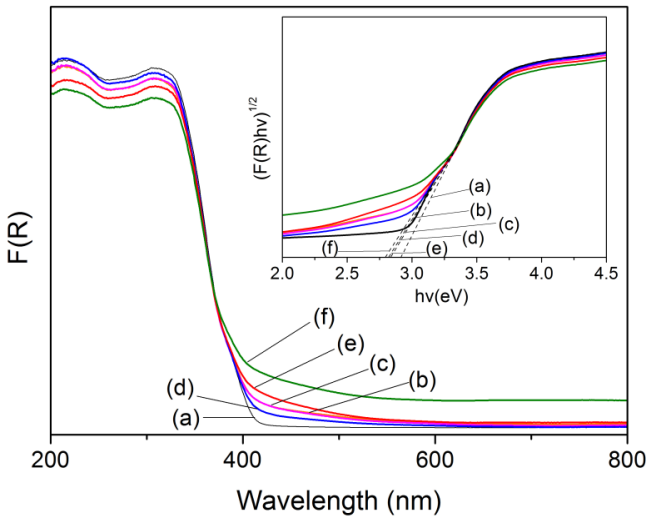


**Figure 4**. UV-Visible diffuse absorption and Tauc plot of $[F(R)h\nu]^{1/2}$ *vs hv* (inset) of the pure $TiO_2$ (a, black), NiO/$TiO_2$ containing 0.1 (b, orange), 0.2 (c, magenta), 0.5 (d, blue), 1.0 (e, red), and 10 wt % (f, olive).

Since titanium dioxide is generally considered as an indirect semiconductor,[57,58] the band gap energy ($E_g$) of the nanocomposites can be estimated from their UV-visible absorption employing the following equation: $\alpha(h\nu) = A(h\nu - E_g)^2$, where $\alpha$, $\nu$, $E_g$, and $A$ are the absorption coefficient, light frequency, band gap energy and a constant, respectively.[41] The optical band gap of the materials can be then deduced by extrapolating to zero the plot of $[\alpha(h\nu)]^{1/2}$ *vs hv* (also known as Tauc plot). The band gap decreases from 2.92 eV for pure $TiO_2$ to 2.81, 2.81, 2.82, 2.79, and 2.78 eV for 0.1, 0.2, 0.5, 1, and 10 wt % NiO/ $TiO_2$, respectively. Pure $TiO_2$ exhibited a smaller band gap energy than the one expected for pure anatase, i.e. 3.2 eV,[57] which can be related to the slight contamination of rutile and/or the presence of intrinsic bulk oxygen vacancies.

To get a deeper understanding of electronic properties of pure $TiO_2$ and heterostructured NiO-$TiO_2$, XPS measurements were carried out. In addition to carbon, nitrogen, and calcium species which is a typical contamination of ex-situ samples synthesized chemically, emissions from titanium, oxygen, nickel, and indium were detected in the survey spectra (Figure S2). High resolution scanning for Ni2p, O1s, and

Ti2p core level emissions, and valence band region emissions are shown in Figure 5. The Fermi level shifts toward a lower energy level from 3.38 eV for pure $TiO_2$ to 3.07, 3.12, 3.15, and 2.20 eV for 0.1, 0.2, 1, and 10 wt % NiO-$TiO_2$,

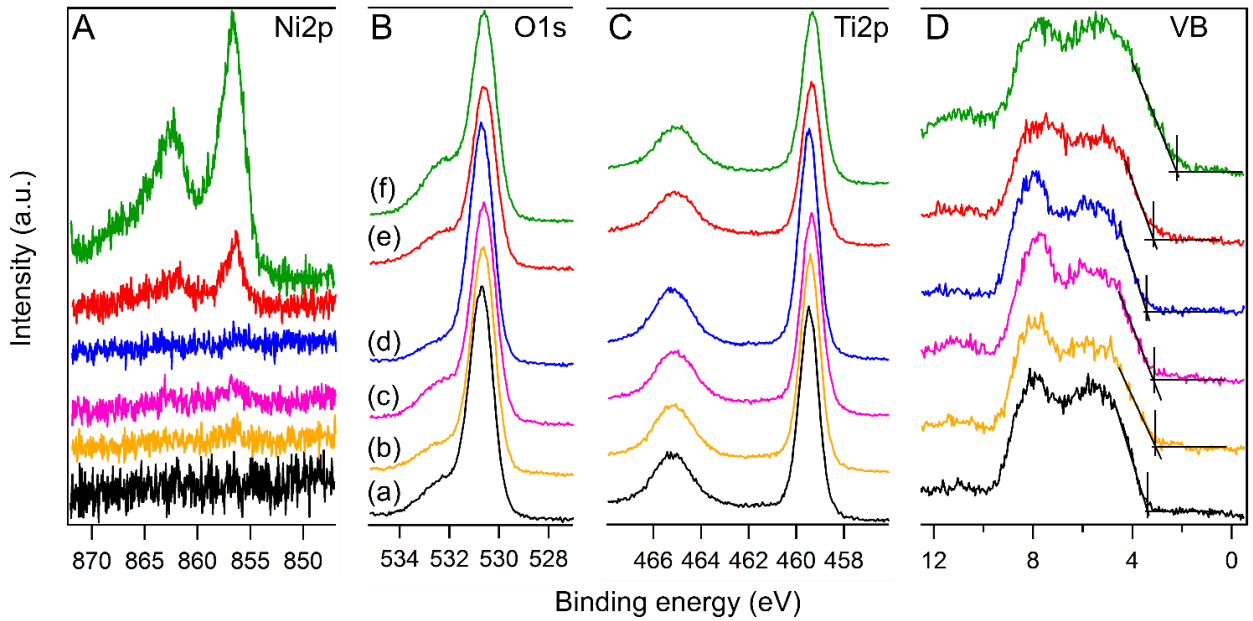


**Figure 5.** XP spectra of (A) Ni2p, (B) O1s, (C) Ti2p and (D) valence band emissions for the pure $TiO_2$ (a, black), NiO/$TiO_2$ containing 0.1 (b, orange), 0.2 (c, magenta), 0.5 (d, blue), 1.0 (e, red), and 10 wt % (f, olive).

respectively (Figure 5D). 0.5 wt % NiO-$TiO_2$ sample does not show any bending, most likely due to charging problem, leading to unexpected shifts toward higher binding energy to compensate the Fermi level shift. Core levels of prepared samples follow the shift of the Fermi level position except for 10 wt % NiO-$TiO_2$ sample, the valence band edge of which is affected not only by the Fermi level shift of the $TiO_2$, but also directly by the presence of O2p orbitals of NiO. The emission from Ti $2p_{3/2}$ doublet contains only the $Ti^{4+}$ line at 459.47 eV without $Ti^{3+}$ for the pure $TiO_2$ and the peak shifts to the lower binding energy by 140 meV with the presence of NiO (Figure 5C). O1s spectra show an intense peak assigned to Ti-O bonds accompanying a shoulder at 1.6 eV lower binding energy from the main emission line (Figure 5B). The main line of O1s emission also shows an upward bending with NiO as well as the Ti $2p_{3/2}$ peaks. The presence of Ni was evidenced by the Ni $2p_{3/2}$ emission line at 856.64 eV with a satellite line at a binding energy higher than that of the main peak by 7.7 eV for the NiO-$TiO_2$ samples (Figure 5A). Although typical NiO shows a main peak of Ni$2p_{3/2}$ accompanying a shoulder peak at 1.5 eV higher binding energy position which is known as induced by a non-screening effect,[59,60] the emission of our samples shows broadened shapes, typical also for small thicknesses, from which the main and satellite peaks cannot be distinguished. This broadening might be attributed to the ultra-thin layer of NiO on the anatase particles

as the typical intensity pattern of the satellite of NiO is pronounced when the thickness is less than a few nm resulting in the overlapping of the main and satellite peaks which cannot be clearly identified.

### 3.2. Interface analysis

To obtain further insight into the interface properties of NiO-anatase heterojunction, in-situ interface experiments were carried out by XPS and UPS measurements after each deposition steps of NiO with increasing thickness onto the stoichiometric anatase (101) and (001) substrates. Figure 6 presents the core level photoelectron spectra recorded during the stepwise deposition for the stoichiometric anatase (101) substrate (for anatase (001) see Figure S3).

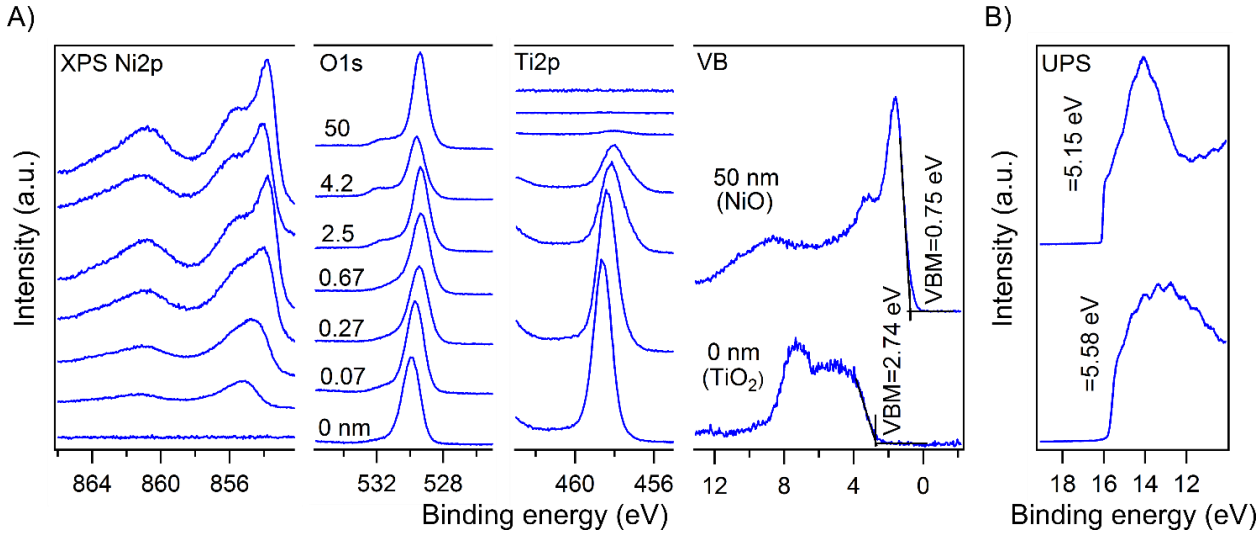


**Figure 6**. (A) XP and (B) UP spectra of the interface experiment performed by stepwise NiO deposition onto the stoichiometric anatase (101) substrate.

The emission of Ti2p shows the typical doublet peak but only the $Ti2p_{3/2}$ line is employed to follow the peak shift during the deposition. Complex main line splitting caused by multiplet contributions and satellite structures at higher binding energies cause difficulty in identifying and interpreting NiO spectra. A binding energy of 853.8 eV is assigned to $Ni2p_{3/2}$ spectra for $Ni^{2+}$ of $NiO_x$ which is clearly observed after completing NiO deposition of thicker than 2.5 nm which shows the expected two satellite peaks. The spectral feature within the main satellite at binding energy of around 861 eV indicates that mostly NiO starts to form already from the very beginning of the deposition sequence. The shoulder appearing at 1.5 eV higher binding energy compared to the main emission is assigned to a satellite emission of the $Ni^{2+}$ rather than $Ni^{3+}$ species. This satellite is a so-called nonlocal screening satellite which appears by a screening process due to oxygen atoms belonging to the octahedral $NiO_6$ coordination.[59] A broad emission at a low coverage of NiO is evident and might be associated with an imperfect octahedral structure due to surface effects.[60] With increasing the thickness of the NiO layer, the typical NiO emission

signature is detected. The contribution of both the nonlocal and surface effect prevents a determination of the exact binding energy peak position. Thus, the main satellite peak of $Ni2p_{3/2}$ at about 7 eV higher binding energy from the main line of $Ni2p_{3/2}$, which is characteristic for $Ni^{2+}$, is adopted instead of the main peak to follow the peak shift in the course of NiO deposition.

The $Ti2p_{3/2}$ peak at the beginning of the NiO deposition is rather sharp and symmetric indicating a mostly stoichiometric surface with dominant $Ti^{4+}$ oxidation state (Figure 6). However, the asymmetry of the Ti2p line to lower binding energy evidently increases, suggesting a slight increase of $Ti^{3+}$ states during NiO deposition. In the O1s region, a shoulder peak is observed at higher binding energy than the main peak by 2.3 eV which might be related to the initial formation of the O poor surface species and possible contributions of adsorbed $OH^-$.

The evolution of the Fermi level ($E_F - E_{VBM}$) of NiO and anatase substrates obtained by following the core level of Ni2p satellite and $Ti2p_{3/2}$, respectively, is shown in Figure 7.

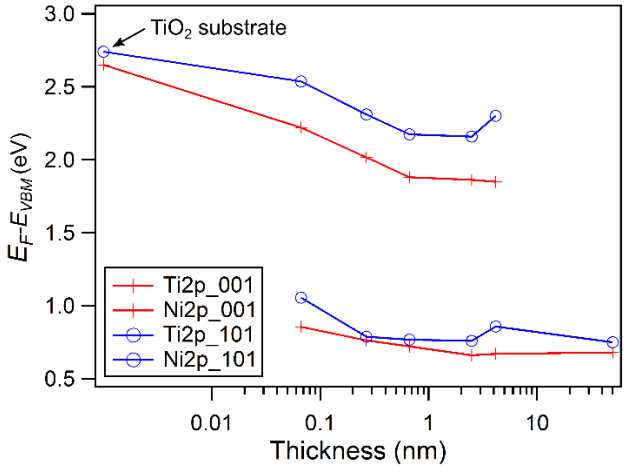


**Figure 7**. Fermi level ($E_F - E_{VBM}$) measured during stepwise deposition of NiO onto the stoichiometric anatase (101) substrate.

The values $E_F - E_{VBM}$ of pristine stoichiometric anatase substrates and the NiO top layer correspond to the values of $E_{VB}$ as determined from the valence band spectra. The Fermi level of the uncovered anatase (101) substrate is higher than that of the (001) substrate by 90 meV. This might be due to a higher density of oxygen vacancies on surface and subsurface of the (101) substrate than that of the (001). The Fermi level of both NiO and anatase shows a parallel shift to lower binding energy, indicating that the band bending occurs only in the anatase substrates and the emission line of Ni2p just follows the band bending in anatase. The Fermi level shift is attributed to the contact formation between NiO and anatase forming the p-n junction leading to band bending in contact. It is worth mentioning that the Fermi level of anatase (101) shows a smaller band bending than that of the anatase (001) by 210 meV. This is attributed to stable oxygen subsurface oxygen vacancies of the anatase (101) which would pin the Fermi level at 2.16 eV.

The work function of the uncovered anatase substrates and top layers of deposited NiO was derived from the binding energies of the secondary electron edge $E_{SE}$ according to $\Phi = h\nu - E_{SE}$. The work function of the stoichiometric anatase (101) and (001) substrates is 5.58 and 5.63 eV, respectively. The work function of NiO on the anatase (101) and (001) substrates is 5.15 and 5.17 eV, respectively. No noticeable difference in work function of NiO indicates that NiO on both orientations of anatase would possess similar stoichiometry without being influenced by different surface coordination of these orientations.

Finally, the band alignments at the interface of NiO-anatase (101) and NiO-anatase (001) as experimentally established using above data are shown in Figure 8 and in Figure S4.

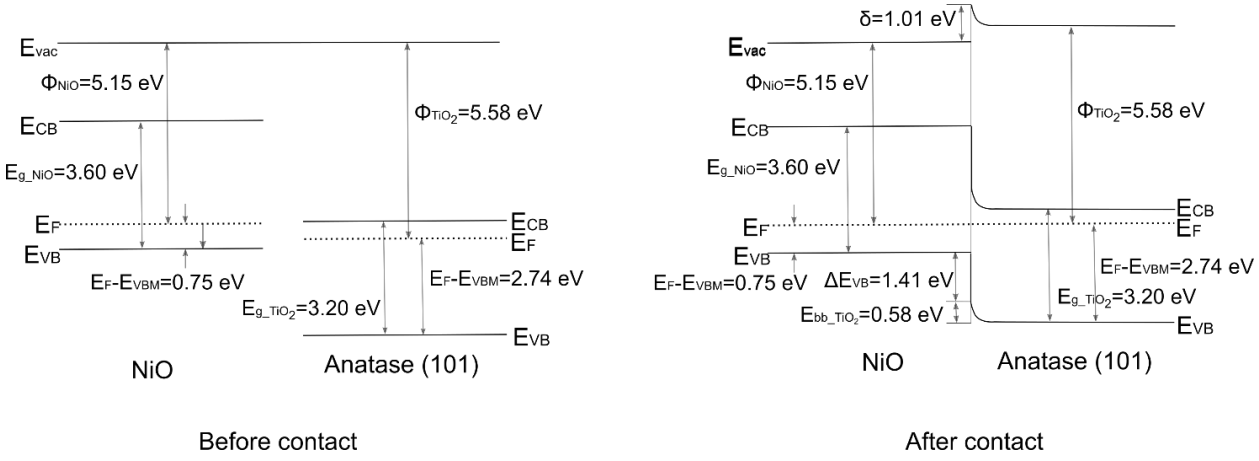


**Figure 8.** Band energy diagrams of p-NiO/n-$TiO_2$ anatase (101) before and after contact as determined from the experimental data. The important values are given in the figures.

As is evident from these diagrams, the band bending at the interface of p-doped NiO and n-doped $TiO_2$ for the anatase (001) is larger than that for the anatase (101) by 210 meV. In p-NiO the Fermi level is pinned by a high concentration of defect states ($Ni^{3+}$ related states) in the bulk of the material as there is no additional band bending observed in the NiO layers. The pinning level is found at a value of $E_F - E_{VBM}$ between 0.68 and 0.75 eV. Strong band bending within the $TiO_2$ substrates is achieved by the deposition of thin NiO layers of thicknesses larger than 1 nm, which would contribute to charge carriers separation in nanoparticle photocatalyst systems. The facts that the space charge layer observed for the NiO particles on the {101} facets of $TiO_2$ is considerably smaller can be understood based on two facets which have already been discussed in details in a previous paper. For small particles the space charge layer is inhomogeneous and only a small fraction is detected for the rare areas. Secondly, for small dimensions of the NiO overlayer onto $TiO_2$ substrates the complete space charge layer may not be found due to exhaustion of charge carriers.

### 3.3. Photocatalytic properties

To examine the photocatalytic activity of the pure $TiO_2$ and NiO-$TiO_2$ nanomaterials, the photodecomposition of MB was performed under UV illumination.

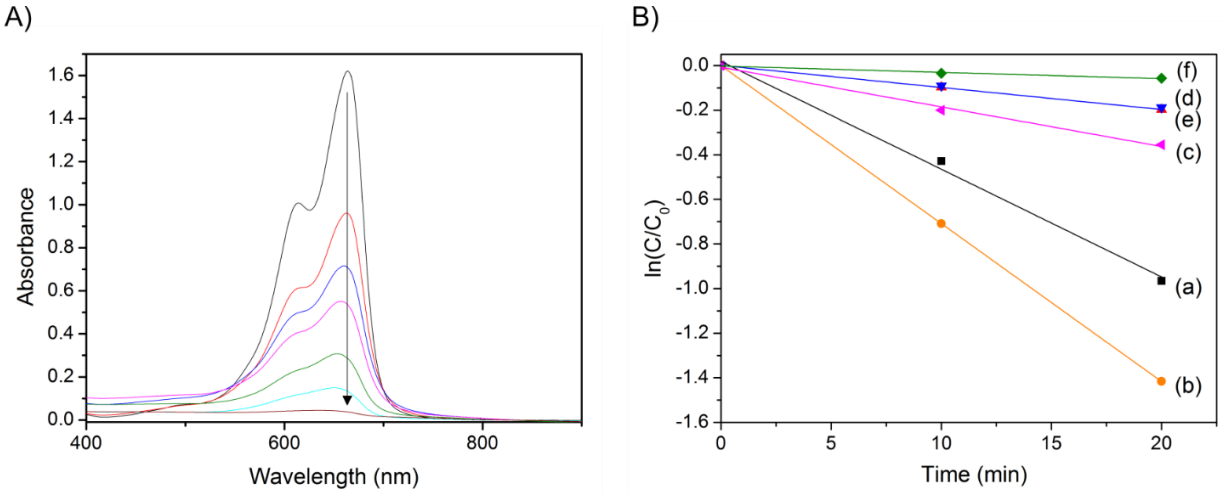


**Figure 9**. (A) Absorbance change in the visible range of methylene blue solution after various illumination time for 0.1wt% NiO-$TiO_2$: before irradiation (black), 10 min (red), 20 min (blue), 30 min (magenta), 40 min (olive), 50 min (cyan) and 60 min (purple). (B) Pseudo-first order kinetic expressed by ln($C/C_0$) *vs* irradiation time *t* of the degradation of MB for the pure $TiO_2$ (a, black), NiO/$TiO_2$ containing 0.1 (b, orange), 0.2 (c, magenta), 0.5 (d, blue), 1.0 (e, red), and 10 wt % (f, olive).

Figure 9A shows stepwise attenuation of the characteristic absorption peaks of MB during its photocatalytic decomposition in the presence of 0.1wt% NiO-$TiO_2$. In this case, MB was completely decolorized within 60 min under UV-light irradiation. The photocatalytic activities of pure $TiO_2$ and NiO-$TiO_2$ photocatalysts with various NiO contents are shown in Figure 9B. For quantitative evaluation of the reaction kinetics of the MB degradation, a pseudo-first model expressed as $ln(C/C_0) = -K_{app}t$ was applied. Here, $C_0$ and $C$ correspond to the concentration of MB in solution at time *0* and *t*, respectively, and $K_{app}$ stands for the apparent 1$^{st}$ order rate constant for MB degradation. $K_{app}$ can be obtained from the slope of the curve $ln(C/C_0)$ *vs t*. Whatever the photocatalyst the MB degradation follows the pseudo-first order reaction kinetics at the beginning of the process. Furthermore, to avoid the influence of the surface area of the photocatalysts on the rate constant, the normalized rate constant ($K_{norm}$) defined as $K_{norm} = K_{app}/S_{BET}$ was calculated as summarized in Table 2. 0.1 wt % NiO-$TiO_2$ photocatalyst shows the highest activity and its $K_{norm}$ is higher than that of the pure $TiO_2$ by 50 %. This result confirms the key role of the combination of NiO with $TiO_2$ for enhancing the photocatalytic activities which can be attributed to the enhanced charge separation due to the electric field at the interface of the p-n junction between NiO and $TiO_2$ as described below.

### 3.4. Mechanistic consideration

According to literature data, the following mechanism can be proposed.[32] After light absorption by the photocatalyst, the photoexcited electron and holes are transferred to $TiO_2$ and NiO, respectively, at the p-n junction. The electrons transferred to $TiO_2$ take part in the reduction of dissolved oxygen, forming a superoxide radical $O_2^{\bullet-}$. The $O_2^{\bullet-}$ radicals react with $H_2O$ to produce hydroxyl radicals $OH^{\bullet}$ which are strong oxidizing agents leading to dye decomposition. At the same time, the holes transferred to NiO directly react with surface adsorbed dyes leading to the dye degradation and also oxidize the surface hydroxyl groups or physisorbed $H_2O$ forming $OH^{\bullet}$. Thus, the charge carriers, the life time of which is prolonged by spatial charge separation at the p-n junction, would acquire a higher probability to encounter reactants producing radicals in the solution and then account for the high photocatalytic activities.

To get a deeper understanding of the photodecomposition mechanism in the presence of $TiO_2$ and NiO-$TiO_2$ nanomaterials, potassium iodide (KI), isopropyl alcohol (IPA) and 1,4-benzoquinone (BQ) were employed as hole ($h^+$), hydroxyl radical ($OH^{\bullet}$) and superoxide radical ($^{\bullet}O^{2-}$) scavengers, respectively, for MB degradation. The corresponding kinetic rate constants for MB decomposition normalized by that without scavengers are reported in Figure 10.

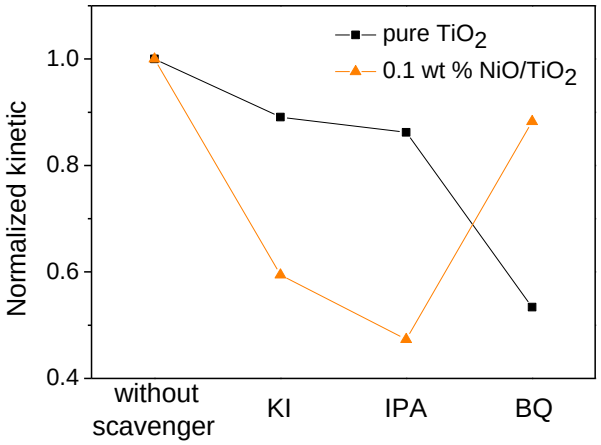


**Figure 10**. Kinetic rate constants for MB decomposition normalized by that without scavengers for pure $TiO_2$ (black) and 0.1wt% NiO/$TiO_2$ (orange) without scavengers or in the presence of potassium iodide (KI), isopropanol (IPA), and 1,4-benzoquinone (BQ).

First of all, it can be clearly seen that the species involved in the photocatalytic decomposition of MB depend on the photocatalyst used. Thus, for pure $TiO_2$ photocatalyst, the degradation efficiency of MB decreased obviously in the presence of BQ while it was almost not affected by addition of KI and IPA. This means that $^{\bullet}O^{2-}$ radicals, which are created via photo-generated electrons, are the dominant active species in the photocatalytic reaction whereas $OH^{\bullet}$ radicals play a minor role. The $TiO_2$ crystals used in this study have an averaged aspect ratio (*B*/*A*),[61] which is defined by the ratio of the short *B* and long *A*

sides of the top-truncated bipyramidal crystal, of around 0.7.[27] The value corresponds to 72 % exposure of the (101) facet and thus it is expected that electrons, which are supposed to be accumulated onto the majority (101) facet, are relevant in photocatalysis for the pure $TiO_2$. By contrast, photocatalytic activities of 0.1wt% NiO-$TiO_2$ nanomaterials were decreased by addition of KI and IPA whereas BQ has almost no effect. Although both holes and electrons would contribute to create $OH^{\bullet}$ and oxidize the MB, BQ as a scavenger of $^{\bullet}O^{2-}$ created by only electrons did not affect much the photocatalytic activities. This reveals that holes mainly dictate the photocatalytic MB decomposition on the 0.1wt% NiO-$TiO_2$ photocatalysts. Despite the $TiO_2$ crystals used mainly expose (101) facets acting as electron sinks, NiO deposited onto the (101) facets would effectively collect holes at the p-n NiO/$TiO_2$ (101) junction, but would also catalyze the reaction by lowering the activation energy and therefore holes can be competitive rather than electrons. However, simultaneous consumption of both electrons and holes are required to achieve optimal photocatalytic performances since the accumulation of electrons or holes might result in a higher recombination rate. Deposition of NiO in more than 0.2wt% of $TiO_2$ might cover the naked (101) anatase surface more than enough and lead to unreacted electrons, which will be accumulated and trigger a higher possibility of the recombination. Thus, for this NiO-$TiO_2$ (101) system, 0.1wt% NiO-$TiO_2$ photocatalyst showed the best photocatalytic activity.

## 4. Conclusion

The selective photodeposition of NiO nanoparticles onto the {101} facets of oriented $TiO_2$ anatase nanocrystals co-exposed with {001} and {101} facets was achieved for the first time to yield efficient NiO-anatase $TiO_2$ photocatalysts. The NiO-$TiO_2$ heterostructure nanoparticles showed light absorption properties shifted toward visible light region compared to those of pure $TiO_2$. Furthermore, interface model experiments of NiO deposited onto $TiO_2$ substrates were conducted and compared to NiO-$TiO_2$ facetted nanostructures to experimentally determine the energy band alignment diagrams of the NiO-oriented $TiO_2$ heterostructure. The 0.58 eV shifts of core levels toward lower binding energy were assigned to an upward band bending in $TiO_2$ anatase (101) substrates which is expected to favor electron-hole charge separation at the interface. The difference of band bending of only smaller than 0.3 eV is related to size effects. The 0.1wt% NiO-$TiO_2$ actually showed 50 % higher photocatalytic activity than the pure $TiO_2$ for MB photodegradation due to effective charge separation by the internal electric field formed at the p-n NiO-$TiO_2$ heterojunction. Finally further mechanistic studies performed by using carrier and radical scavengers revealed that holes dominantly dictate the photocatalytic reactions for NiO-$TiO_2$ nanocomposites whereas electrons mainly participate in the photocatalytic reactions rather than holes for the pure $TiO_2$. These results underline the key role of selective deposition of NiO onto anatase $TiO_2$

nanocrystals on photocatalyic processes. This work will inspire optimal designs of heterostructure systems for efficient photocatalytic process by combining an appropriate choice of co-catalysts and selective deposition onto the specific facet of supported photocatalyst crystals.

## 5. References


(1) Zhu, K.; Neale, N. R.; Miedaner, A.; Frank, A. J., Enhanced Charge-Collection Efficiencies and Light Scattering in Dye-Sensitized Solar Cells Using Oriented $TiO_2$ Nanotubes Arrays. *Nano Lett.* **2007**, *7*, 69-74.

(2) Liu, B.; Aydil, E. S., Growth of Oriented Single-Crystalline Rutile $TiO_2$ Nanorods on Transparent Conducting Substrates for Dye-Sensitized Solar Cells. *J. Am. Chem. Soc.* **2009**, *131*, 3985-3990.

(3) Yun, J.-H.; Wang, L.; Amal, R.; Ng, Y. H., One-Dimensional $TiO_2$ Nanostructured Photoanodes: From Dye-Sensitized Solar Cells to Perovskite Solar Cells. *Energies* **2016**, *9*, 1030.

(4) Wang, D.; Choi, D.; Li, J.; Yang, Z. ; Nie, Z. ; Kou, R. ; Hu, D. ; Wang, C. ; Saraf, L. V. ; Zhang, J. ; Aksay, I. A.; Liu, J., Self-Assembled $TiO_2$–Graphene Hybrid Nanostructures for Enhanced Li-Ion Insertion. *ACS Nano* **2009**, *3*, 907-914.

(5) Yang, G.; Wang, L.; Peng, S.; Wang, J.; Ji, D.; Yan, W.; Ramakrishna, S. In Situ Fabrication of Hierarchically Branched $TiO_2$ Nanostructures: Enhanced Performance in Photocatalytic $H_2$ Evolution and Li–Ion Batteries. *Small* **2017**, *13*, 1702357 (1-9).

(6) Fujishima, A.; Honda, K., Electrochemical Photolysis of Water at a Semiconductor Electrode. *Nature* **1972**, *238*, 37-38.

(7) Linsebigler, A. L.; Lu, G.; Yates, J. T., Photocatalysis on $TiO_2$ Surfaces: Principles, Mechanisms, and Selected Results. *Chem. Rev.* **1995**, *95*, 735-758.

(8) Walter, M. G.; Warren, E. L.; McKone, J. R.; Boettcher, S. W.; Mi, Q.; Santori, E. A.; Lewis, N. S., Solar Water Splitting Cells. *Chem. Rev.* **2010**, *110*, 6446-73.

(9) Dhakshinamoorthy, A.; Navalon, S.; Corma, A.; Garcia, H., Photocatalytic $CO_2$ reduction by $TiO_2$ and related titanium containing solids. *Energy Environ. Sci.* **2012**, *5*, 9217-9223.

(10) Kamat, P. V. Manipulation of Charge Transfer across Semiconductor Interface. A Criterion That Cannot Be Ignored in Photocatalyst Design. *J. Phys. Chem. Lett.* **2012**, *3*, 663-72.

(11) Takai, A.; Kamat, P. V. Capture, Store, and Discharge. Shuttling Photogenerated Electrons across $TiO_2$-Silver Interface. *ACS Nano* **2011**, *5*, 7369-76.

(12) Yang, J.; Wang, D.; Han, H.; Li, C. Roles of Cocatalysts in Photocatalysis and Photoelectrocatalysis. *Acc. Chem. Res.* **2013**, *46*, 1900-9.

(13) Trasatti, S. Work Function, Electronegativity, and Electrochemical Behaviour of Metals. *J. Electroanal. Chem. Interfac. Electrochem.* **1972**, *39*, 163-184.

(14) Maeda, K.; Domen, K. Photocatalytic Water Splitting: Recent Progress and Future Challenges. *J. Phys. Chem. Lett.* **2010**, *1*, 2655-2661.

(15) Meekins, B. H.; Kamat, P. V. Role of Water Oxidation Catalyst $IrO_2$ in Shuttling Photogenerated Holes across $TiO_2$ Interface. *J. Phys. Chem. Lett.* **2011**, *2*, 2304-2310.

(16) Liu, L.; Ji, Z.; Zou, W.; Gu, X.; Deng, Y.; Gao, F.; Tang, C.; Dong, L., In Situ Loading Transition Metal Oxide Clusters on $TiO_2$ Nanosheets As Co-catalysts for Exceptional High Photoactivity. *ACS Catal.* **2011**, *3*, 2052-2061.

(17) Ohno, T.; Sarukawa, K.; Matsumura, M. Crystal Faces of Rutile and Anatase $TiO_2$ Particles and Their Roles in Photocatalytic Reactions. *New J. Chem.* **2002**, *26*, 1167-1170.

(18) Tachikawa, T.; Yamashita, S.; Majima, T. Evidence for Crystal-Face-Dependent $TiO_2$ Photocatalysis from Single-Molecule Imaging and Kinetic Analysis. *J. Am. Chem. Soc.* **2011**, *133*, 7197-204.

(19) Liu, G.; Yu, J. C.; Lu, G. Q.; Cheng, H. M. Crystal Facet Engineering of Semiconductor Photocatalysts: Motivations, Advances and Unique Properties. *Chem. Commun.* **2011**, *47*, 6763-83.

(20) D'Arienzo, M.; Carbajo, J.; Bahamonde, A.; Crippa, M.; Polizzi, S.; Scotti, R.; Wahba, L.; Morazzoni, F. Photogenerated Defects in Shape-Controlled $TiO_2$ Anatase Nanocrystals: A Probe to Evaluate the Role of Crystal Facets in Photocatalytic Processes. *J. Am. Chem. Soc.* **2011**, *133*, 17652-17661.

(21) Zhang, P.; Tachikawa, T.; Bian, Z.; Majima, T. Selective Photoredox Activity on Specific Facet-Dominated $TiO_2$ Mesocrystal Superstructures Incubated with Directed Nanocrystals. *Appl. Catal. B: Environmental*. **2015**, *176-177*, 678-86.

(22) Sun, C.; Liu, L.-M.; Selloni, A.; Lu, G. Q.; Smith, S. C. Titania-Water Interactions: A Review of Theoretical Studies. *J. Mater. Chem.* **2010**, *20*, 10319-34.

(23) Gong, X. Q.; Selloni, A. Reactivity of Anatase TiO(2) Nanoparticles: The Role of the Minority (001) Surface. *J. Phys. Chem. B* **2005**, *109*, 19560-2.

(24) Yang, H. G.; Sun, C. H.; Qiao, S. Z.; Zou, J.; Liu, G.; Smith, S. C.; Cheng, H. M.; Lu, G. Q. Anatase $TiO_2$ Single Crystals with a Large Percentage of Reactive Facets. *Nature* **2008**, *453*, 638-41.

(25) Chen, W.; Kuang, Q.; Wang, Q.; Xie, Z. Engineering a High Energy Surface of Anatase $TiO_2$ Crystals Towards Enhanced Performance for Energy Conversion and Environmental Applications. *RSC Advances* **2015**, *5*, 20396-20409.

(26) Murakami, N.; Kurihara, Y.; Tsubota, T.; Ohno, T. Shape-Controlled Anatase Titanium(IV) Oxide Particles Prepared by Hydrothermal Treatment of Peroxo Titanic Acid in the Presence of Polyvinyl Alcohol. *J. Phys. Chem. C* **2009**, *113*, 3062-69.

(27) Amano, F.; Prieto-Mahaney, O.-O.; Terada, Y.; Yasumoto, T.; Shibayama, T.; Ohtani, B. Decahedral Single-Crystalline Particles of Anatase Titanium(IV) Oxide with High Photocatalytic Activity. *Chem. Mater.* **2009**, *21*, 2601-03.

(28) Roy, N.; Sohn, Y.; Pradhan, D. Synergy of Low-Energy {101} and High-Energy {001} TiO(2) Crystal Facets for Enhanced Photocatalysis. *ACS Nano* **2013**, *7*, 2532-40.

(29) Yu, J.; Low, J.; Xiao, W.; Zhou, P.; Jaroniec, M. Enhanced Photocatalytic Co(2)-Reduction Activity of Anatase TiO(2) by Coexposed {001} and {101} Facets. *J. Am. Chem. Soc.* **2014**, *136*, 8839-42.

(30) Ku, Y.; Lin, C.-N.; Hou, W.-M. Characterization of Coupled $NiO/TiO_2$ Photocatalyst for the Photocatalytic Reduction of Cr(VI) in Aqueous Solution. *J. Mol. Catal. A: Chemical* **2011**, *349*, 20-27.

(31) Iwaszuk, A.; Nolan, M.; Jin, Q.; Fujishima, M.; Tada, H. Origin of the Visible-Light Response of Nickel(II) Oxide Cluster Surface Modified Titanium(IV) Dioxide. *J. Phys. Chem. C* **2013**, *117*, 2709-18.

(32) Wang, M.; Hu, Y.; Han, J.; Guo, R.; Xiong, H.; Yin, Y. $TiO_2$/NiO Hybrid Shells: p-n Junction Photocatalysts with Enhanced Activity under Visible-light. *J. Mater. Chem. A* **2015**, *3*, 20727-20735.

(33) Fujita, S.-i.; Kawamori, H.; Honda, D.; Yoshida, H.; Arai, M. Photocatalytic Hydrogen Production from Aqueous Glycerol Solution Using $NiO/TiO_2$ Catalysts: Effects of Preparation and Reaction Conditions. *Appl. Catal. B: Environmental*. **2016**, *181*, 818-24.

(34) Uddin, M. T.; Nicolas, Y.; Olivier, C.; Jaegermann, W.; Rockstroh, N.; Junge, H.; Toupance, T. Band Alignment Investigations of Heterostructure $NiO/TiO_2$ Nanomaterials Used as Efficient Heterojunction Earth-Abundant Metal Oxide Photocatalysts for Hydrogen Production. *Phys. Chem. Chem. Phys.* **2017**, *19*, 19279-88.

(35) Liu, J.; Li, Y.; Ke, J.; Wang, S.; Xiao, H. Black $NiO-TiO_2$ nanorods for solar photocatalysis: Recognition of electronic structure and reaction mechanism. *Appl. Catal. B: Environmental*. **2018**, *224*, 705-14.

(36) Ensling, D.; Thißen, A.; Gassenbauer, Y.; Klein, A.; Jaegermann, W. In-Situ Preparation and Analysis of Functional Oxides. *Advanced Engineering Materials* **2005**, *7*, 945-49.

(37) Wu, Z.; Zhang, M.; Ge, S.; Zhang, Z.; Li, W.; Tao, K. Synthesis and Characterization of a Porous Amorphous Ni–B Catalyst on Titania by Silver-Catalyzed Electroless Plating. *J. Mater. Chem.* **2005**, *15*, 4928-33.

(38) Lee, S.-H.; Galstyan, V.; Ponzoni, A.; Gonzalo-Juan, I.; Riedel, R.; Dourges, M.-A.; Nicolas, Y.; Toupance, T. Finely Tuned $SnO_2$ Nanoparticles for Efficient Detection of Reducing and Oxidizing Gases: The Influence of Alkali Metal Cation on Gas-Sensing Properties. *ACS Appl. Mater. Interfaces* **2018**, *10*, 10173−84.

(39) Brunauer, S.; Emmett, P. H.; Teller, E. Adsorption of Gases in Multimolecular Layers. *J. Am. Chem. Soc.* **1938**, *60*, 309-19.

(40) Klein, A.; Green, D. J. Transparent Conducting Oxides: Electronic Structure-Property Relationship from Photoelectron Spectroscopy within Situ Sample Preparation. *J. Am. Ceram. Soc.* **2012**, *96*, 331-45.

(41) Uddin, Md. T.; Nicolas, Y.; Olivier, C.; Toupance, T.; Müller, M. M.; Kleebe, H.-J.; Rachut, K.; Ziegler, J.; Klein, A.; Jaegermann, W. Preparation of $RuO_2/TiO_2$ Mesoporous Heterostructures and Rationalization of Their Enhanced Photocatalytic Properties by band Alignmant Investigations. *J. Phys. Chem. C* **2013**, *117*, 22098-110.

(42) Ahmed, M. A.; Abdel Messih, M. F.; El-Sherbeny, E. F.; El-Hafez, S. F.; Khalifa, A. M. M. Synthesis of Metallic Silver Nanoparticles Decorated Mesoporous $SnO_2$ for Removal of Methylene Blue Dye by Coupling Adsorption and Photocatalytic Processes. *J. Photochem. Photobiol. A: Chemistry* **2017**, *346*, 77-88.

(43) Ding, J.; Ming, J.; Lu, D.; Wu, W.; Liu, M.; Zhao, X.; Li, C.; Yang, M.; Fang, P. Study of the Enhanced Visible-light-sensitive Photocatalytic Activity of $Cr_2O_3$-loaded Titanate Nanosheets for Cr(VI) Degradation and $H_2$ Generation. *Catal; Sci. Technol.* **2017**, *7*, 2283-97.

(44) Wen, X.-J.; Niu, C.-G.; Zhang, L.; Zeng, G.-M. Fabrication of $SnO_2$ Nanopaticles/BiOI n−p Heterostructure for Wider Spectrum Visible-Light Photocatalytic Degradation of Antibiotic Oxytetracycline Hydrochloride. *ACS Sustainable Chem. Eng.* **2017**, *5*, 5134-47.

(45) Ahmad, J.; Majid, K. Enhanced visible light driven photocatalytic activity of CdO–graphene oxide heterostructures for the degradation of organic pollutants. *New J. Chem.* **2018**, *42*, 3246-59.

(46) Wendt, S., Sprunger, P. T.; Lira, E.; Madsen, G. K.; Li, Z.; Hansen, J. O.; Matthiesen, J.; Blekinge-Rasmussen, A.; Laegsgaard, E.; Hammer, B.; Besenbacher, F. The Role of Interstitial Sites in the Ti3d Defect State in the Band Gap of Titania. *Science* **2008**, *320*, 1755-9.

(47) Setvín, M.; Daniel, B.; Mansfeldova, V.; Kavan, L.; Scheiber, P.; Fidler, M.; Schmid, M.; Diebold, U. Surface Preparation of $TiO_2$ Anatase (101): Pitfalls and How to Avoid Them. *Surf. Sci.* **2014**, *626*, 61-7.

(48) Thomas, A. G.; Flavell, W. R.; Mallick, A. K.; Kumarasinghe, A. R.; Tsoutsou, D.; Khan, N.; Chatwin, C.; Rayner, S.; Smith, G. C.; Stockbauer, R. L.; Warren, S.; Johal, T. K.; Patel, S.; Holland, D.; Taleb, A.; Wiame, F.

Comparison of the Electronic Structure of Anatase and Rutile $TiO_2$ Single-crystal Surfaces using Resonant Photoemission and X-ray Absorption Spectroscopy. *Phys. Rev. B* **2007**, *75*, 035105.

(49) Li, M.; Hebenstreit, W.; Diebold, U.; Henderson, M. A.; Jennison, D. R. Oxygen-Induced Restructuring of Rutile $TiO_2$(110): Formation Mechanism, Atomic Models, and Influence on Surface Chemistry. *Faraday Discussions* **1999**, *114*, 245-58.

(50) Wu, C. C.; Wu, C. I.; Sturm, J. C.; Kahn, A. Surface Modification of Indium Tin Oxide by Plasma Treatment: An Effective Method to Improve the Efficiency, Brightness, and Reliability of Organic Light Emitting Devices. *Appl. Phys. Lett.* **1997**, *70*, 1348-50.

(51) Klissurski, D.; Hadjiivanov, K.; Kantcheva, M.; Gyurova, L. Study of Peroxide-Modified Titanium Dioxide (Anatase). *J. Chem. Soc., Faraday Trans.* **1990**, *86*, 385-88.

(52) Cullity, B. D. *Answers to Problems: Elements of X-Ray Diffraction*; Addison-Wesley Publishing Company, 1978.

(53) Patil, P.; Kadam, L. Preparation and Characterization of Spray Pyrolyzed Nickel Oxide (Nio) Thin Films. *Appl. Surf. Sci.* **2002**, *199*, 211-21.

(54) Sawatzky, G.; Allen, J. Magnitude and Origin of the Band Gap in NiO. *Phys. Rev. Lett.* **1984**, *53*, 2339.

(55) Sreethawong, T.; Ngamsinlapasathian, S.; Yoshikawa, S. Surfactant-Aided Sol–Gel Synthesis of Mesoporous-Assembled $TiO_2$-NiO Mixed Oxide Nanocrystals and Their Photocatalytic Azo Dye Degradation Activity. *Chem. Eng. J.* **2012**, *192*, 292-300.

(56) Nolan, M.; Iwaszuk, A.; Lucid, A. K.; Carey, J. J.; Fronzi, M. Design of Novel Visible Light Active Photocatalyst Materials: Surface Modified $TiO_2$. *Adv Mater.* **2016**, *28*, 5425-46.

(57) Diebold, U. The Surface Science of Titanium Dioxide. *Surf. Sci. Rep.* **2003**, *48*, 53-229.

(58) Zhang, Y.-f.; Lin, W.; Li, Y.; Ding, K.-n.; Li, J.-q. A Theoretical Study on the Electronic Structures of $TiO_2$: Effect of Hartree-Fock Exchange. *J. Phys. Chem. B* **2005**, *109*, 19270-77.

(59) van Veenendaal, M. A.; Sawatzky, G. A. Nonlocal Screening Effects in 2p X-Ray Photoemission Spectroscopy Core-Level Line Shapes of Transition Metal Compounds. *Phys. Rev. Lett.* **1993**, *70*, 2459-62.

(60) Soriano, L.; Preda, I.; Gutiérrez, A.; Palacín, S.; Abbate, M.; Vollmer, A. Surface Effects in the Ni2px-Ray Photoemission Spectra of NiO. *Phys. Rev. B* **2007**, *75*, 233417.

(61) Selloni, A. Anatase Shows Its Reactive Site. *Nat. Mater*. **2008**, *7*, 613-15.

## 6. Supplementary information

*$N_2$ sorption analyses*

The $N_2$ adsorption-desorption isotherms recorded in the 0-0.99 relative pressure range of pure $TiO_2$ and NiO-$TiO_2$ nanocomposites are shown in Fig. S1. Before analysis, each sample has been degassed under vaccum at 120°C overnight.

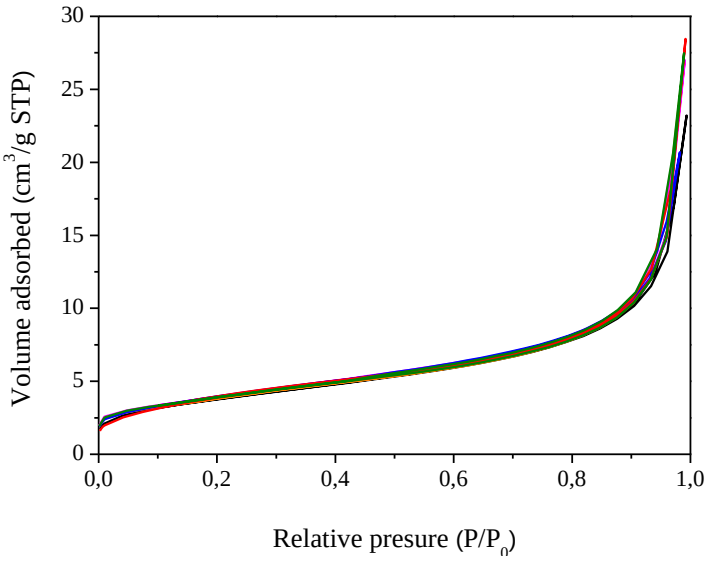


**Figure S1**: $N_2$ adsorption-desorption isotherms of $TiO_2$ (black), 0.1wt% NiO-$TiO_2$ (orange); 0.2wt% NiO-$TiO_2$ (magenta), 0.5wt% NiO-$TiO_2$ (blue), 1wt% NiO-$TiO_2$ (red) and 1wt% NiO-$TiO_2$ (olive).

Before the $N_2$ sorption study of the $TiO_2$-NiO nanomaterials, the accuracy of the Micromeritics ASAP2010 equipment was checked by recording the adsorption-desorption isotherm of a silica-alumina reference material from Micromeritics (Ref: 004-16821-02), the characteristics of which are: $S_{BET}$ = 214 ± 6 $m^2.g^{-1}$; Total pore volume = 0.63 ± 0.08 $cm^3.g^{-1}$. As a consequence, the relative uncertainty concerning $S_{BET}$ and total pore volume, determined by this method, are therefore about ± 3% and ± 13%, respectively. These relative uncertainties have been used to report the values given in Table 1.

*XPS analysis*

The XPS survey of pure $TiO_2$ and NiO-$TiO_2$ nanocomposites are shown in Fig. S2.

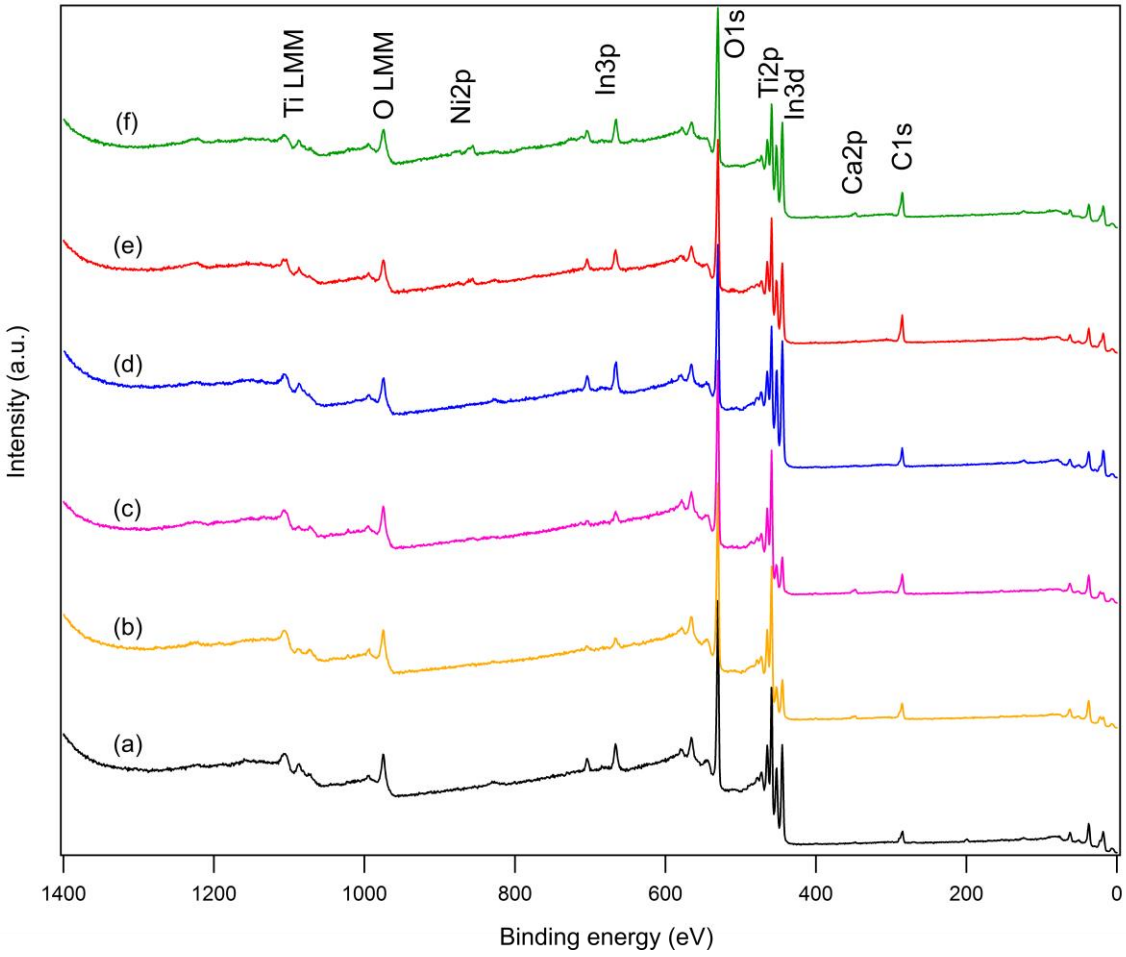


**Figure S2**: XP survey spectra of the pure $TiO_2$ (a, black), NiO/$TiO_2$ containing 0.1 (b, orange), 0.2 (c, magenta), 0.5 (d, blue), 1.0 (e, red), and 10 wt % (f, olive).

*Interface experiments for NiO-anatase (001) substrate*

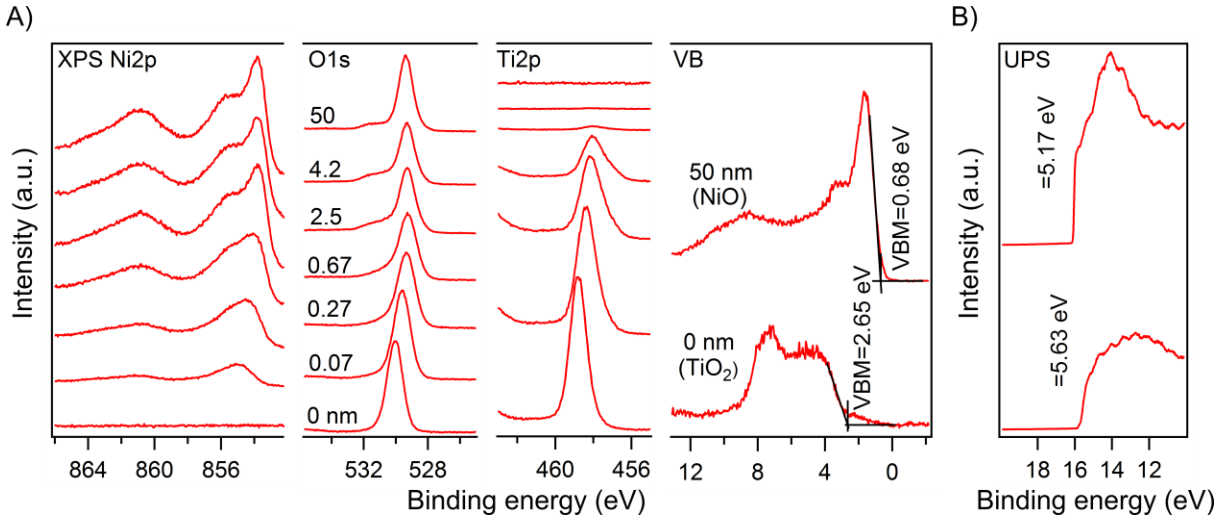


**Figure S3**. XP (A) and UP (B) spectra of the interface experiment performed by stepwise NiO deposition onto the stoichiometric anatase (001) substrate.

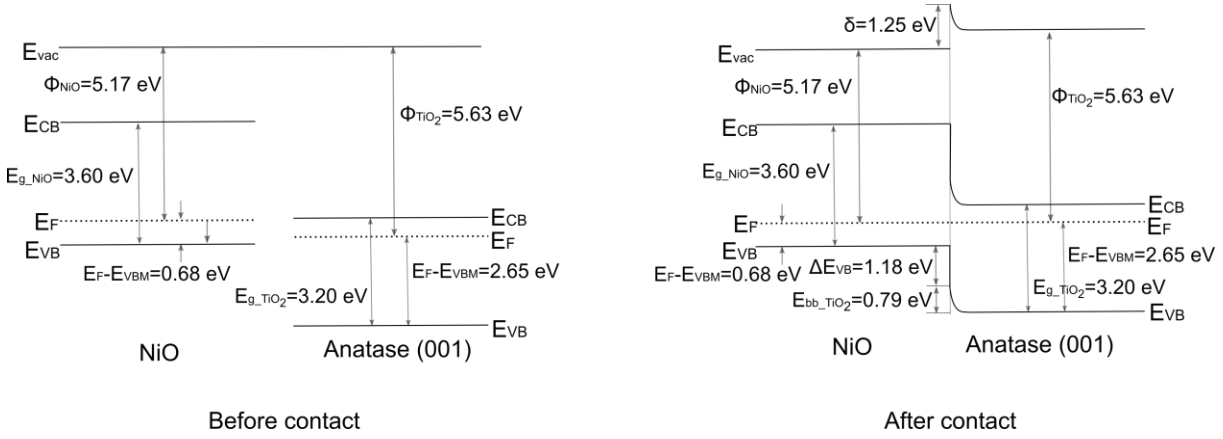


**Figure S4**. Band energy diagrams of p-NiO/n-$TiO_2$ anatase (001) as determined from the experimental data. The important values are given in the figures.

## Summary of the main results and improvement in understanding

Energy depletion along with global warming and environmental pollution gives rise to the main issues that have to be addressed in coming decades by our modern societies to provide global sustainability and human prosperity. As a consequence, there is an urgent need for the development of "green" technologies to produce alternative and environmentally friendly fuels to conventional fossil fuels or nuclear energy resources and to secure safe water and air by the efficient removal of harmful pharmaceutical or organic pollutants. In this context, photocatalytic reactions on $TiO_2$ surfaces have attracted worldwide attention due to the capability of decomposition of various air or water pollutants, $CO_2$ reduction, and water splitting. However, photocatalysis with pristine $TiO_2$ materials is far less than its practical level due to several drawbacks including charge carrier recombination and slow surface redox reactions. To draw new prospects in this field, this work aims at characterizing properly the surface properties of $TiO_2$ materials as n-type semiconductor and of the interface formed with a model p-type material, nickel oxide, and to develop new NiO-$TiO_2$ heterojunction photocatalysts for dye photodecomposition.

First of all, fundamental properties of the single crystal $TiO_2$ surfaces were investigated in detail including recent investigations concerning various distributions of oxygen vacancies on the differently oriented $TiO_2$ surfaces and their effects on water adsorption on these surfaces. Oxygen vacancies tend to reside in the subsurface or the bulk whereas they form at the site of bridging oxygen on the surface. In addition, on the anatase crystallite, the (001) facet is extremely stable against oxygen vacancies while they are easily created on the (101) facet. These differences of the stoichiometry of different polymorphs and orientations considerably affect the electronic properties and thus chemical phenomena on their surfaces such as water adsorption. However, an atomistic view of the origin of these differences is still unclear. In the second subchapter, we have introduced the basic principles of photocatalysis and specific phenomena on the $TiO_2$ surface were then outlined. Subsequently the role of co-catalysts was summarized. Co-catalysts can not only form space charge layers such as Schottky barrier and p-n junctions, which may help in charge carrier separation, but also provide effective redox reaction sites by lowering the overpotential for photoelectrochemical water splitting and reducing the activation energy for photocatalytic reactions. It is noteworthy that a balance of oxidation and reduction reactions has to be taken into consideration as their unbalance might result in accumulating electrons and/or holes, leading to higher rates of charge carrier recombination. Furthermore, the possible interface of so-called crystal facet engineering was discussed. Starting from the general concept of the influence of crystal facets on the photocatalytic properties, the different roles of anatase (001) and (101) orientation were summarized. As far as anatase is concerned, electrons migrate to the (101) surface while holes move to the (001) surface although the corresponding mechanism still remains unclear. Finally, recent development dealing with the different synthetic approaches allowing for the control of the exposed facets of anatase crystals as well as synergetic effects of facet engineering and co-catalyst deposition was reviewed. In principle, loading oxidation co-catalysts such as metal oxides onto the hole-rich facet can spatially transfer holes to the oxidation co-catalysts while depositing reduction co-catalysts such as noble metals onto the electron-rich facet can help electrons to migrate

to the reduction co-catalysts, maximizing the effect of charge carrier separation and further enhancing photocatalytic activities. However, the number of reports demonstrating this kind of synergetic effect is limited to metal oxides photocatalysts and especially for $TiO_2$. Summarizing the states of research on photocatalytic reactions using $TiO_2$ as an absorber material there have been recently a number of new approaches and mechanistic considerations in the international community. However, a detailed understanding of the discovered effects is still missing especially in interesting physical and chemical concepts.

To draw new prospects in this interdisciplinary field, the research conducted in this work consist of mixed chemical synthesis and characterization of $NiO/TiO_2$ photocatalysts, and fundamental physical analysis of well-defined oriented $TiO_2$ surfaces along with the thorough study of the interfaces formed by NiO and these $TiO_2$ surfaces. Herein, nickel oxide is employed as a p-type semiconductor as it is one of the cheapest and most abundant materials among p-type semiconductors on the earth. The series of works, which has been carried out within this thesis can be concluded as follow.

To begin with, well- defined anatase (001) and (101) substrates were prepared and studied by XPS and UPS in order to establish their fundamental electronic structures (See chapter 3.1). $TiO_2$ surfaces have been conventionally prepared by repeated-cycles of Ar ion sputtering and annealing in vacuum. But the resulting surface, which is referred as to sputtered, contains large amount of oxygen vacancies and its surface structure might be partially destroyed. Thus, to compare their electronic properties carefully, (101) and (001) surfaces are in-situ prepared inside the vacuum chamber to examine different well-defined stoichiometries: sputtered, annealed, oxidized, and stoichiometric. The orientation of the annealed (101) and (001) surfaces was confirmed by unreconstructed LEED patterns. A strong low binding energy emission of $Ti^{3+}$ in the emission of Ti2p spectra, which is a typical evidence of oxygen vacancies, was observed by XPS for only the sputtered (101) surface. Although oxygen vacancies are expected for other surface stoichiometry of the (101) and (101) surface as well, they are detectable only by surface sensitive resonant photoelectron spectroscopy. XP and UP valence band spectra show various distribution of band gap states (BGS), which consists of shallow gap states (SGS) and deep gap states (DGS) located at 0.5 and 1.6 eV below conduction band minimum, depending on the orientation and surface pretreatment. Regardless of surface conditions, DGS of the (101) surface is significantly larger than that of the (101) surface and however shows a similar intensity to that of the (101) surface for UPS. Considering a difference of surface sensitivity of XPS and UPS, this difference of DGS indicates that the defects are situated below the surface to deep subsurface or bulk for the (001) surface while they are located on the surface or only at a shallow subsurface for the (101) surface. The SGS intensity of sputtered (101) surface is larger compared to sputtered (001) surface for both XPS and UPS, implying that excess electrons of the (001) surface are largely located on defects sites while those of the (101) surface are not only localized on the defects sites but also widely delocalized on lattice Ti atoms. DGS and SGS as well as valence band surface states (VBSS) of the (001) surface for XPS gradually attenuate with decrease of the Fermi level position but still remain even after O plasma treatment. On the other hand DGS and SGS of the sputtered (101) surface for XPS have immediately disappeared after re-oxidation by O plasma and subsequent annealing in vacuum. This

indicates that defects in a deep subsurface position of the (001) surface are rather stable and tend to remain while those of the (101) surface could be refilled by O molecules or peroxo species. Along with a variation of DGS, SGS, and VBSS, the variation range in the Fermi level, which are 560 and 860 meV for the (001) and (101) surface, was achieved by controlling the surface stoichiometry. Most importantly, we consistently found a difference in the Fermi level positions between the (001) and (101) facets. The Fermi level of the (001) facet is located at a lower energy than that of the (101) facet by 150-450 meV for any surface conditions. As a result, we expect an energy junction between these facets with space charge layers where photo-generated electrons and holes are transferred to the (101) and (001) surfaces, respectively. This difference in the Fermi level for the different facets can explain why the (101) surface functions as reduction reaction sites while the (001) acts as oxidation reaction sites.

Furthermore, the surface potentials of polycrystalline anatase thin films, (001) and (101)-oriented anatase single crystals and (001) and (110)-oriented rutile single crystals with different surface stoichiometry were systematically compared by XPS and UPS (See chapter 3.2). Among electronic properties, the work function is especially relevant for photocatalysis and solar cells since it governs the band alignments of various interfaces. Differently treated surfaces of sputtered, annealed, stoichiometric, and oxidized surfaces were prepared and a large variation of work function as well as of the Fermi level was achieved by manipulating surface states. The variation of work function determined by UPS is 1.74, 1.94, and 1.39 eV for the anatase (001), anatase (101), and polycrystalline surface, respectively. The change of work function is attributed mainly to a change of the Fermi level position with respect to the valence band maximum as the ionization potential is almost constant for all surface conditions of oriented anatase single crystals with ionization potential of $7.9 \pm 0.15$ eV. Considerably higher ionization potentials of up to 9.5 eV are observed for the oxygen plasma treated surfaces due to peroxo or bridging oxygen species possibly formed on the surface. In addition, water vapor was exposed to the above differently prepared surfaces at room temperature and the resulting electronic properties were investigated by XPS and UPS. Water exposure resulted in reproducible shifts of the Ti2p and O1s core levels and the valence band edge toward higher binding energies due to a downward band bending at $TiO_2$ surfaces which leads to an accumulation of electrons at the surface. The original difference in the Fermi level difference between the anatase (001) and (101), which was present for all surface states, disappeared after water exposure. Concerning the difference of work function between anatase and rutile, for the annealed surfaces anatase was found to show a higher ionization potential than rutile by up to 0.5 eV while their Fermi level positions were similar. Aligning the vacuum energies of anatase and rutile therefore results in a valence band maximum of anatase being 0.5 eV lower in energy than that of rutile in agreement with recently established band alignment by experimental and theoretical approaches. Thus, charge separation of electrons and holes to anatase and rutile, respectively, would take place at the interfaces and this phenomenon allows for rationalizing the enhanced photocatalytic activity of mixed phases of anatase and rutile such as the commercial benchmark $TiO_2$ photocatalyst named P25.

To understand the effect of crystallographic orientation and surface states of rutile $TiO_2$ on band alignments of $NiO/TiO_2$, the energy band alignments of NiO and (001) and (110)-oriented rutile $TiO_2$ single crystal substrates was performed with reduced and oxidized surfaces by so-called interface experiment (See chapter 3.3). As a first step, electronic properties of (001) and (110)-oriented rutile $TiO_2$ single crystal substrates with reduced and oxidized surfaces were investigated by XPS and UPS. The valence band spectra of XPS show that the Fermi level position of 3.12 eV above the VBM of the reduced rutile (110) is decreased to 2.68 eV with surface oxidation. The work function of the reduced (001) derived from the secondary electron edge of UPS spectra was 4.3 eV and increased to 6.0 eV with surface oxidation. A similar shift was observed for the (001) surface. Interface experiments were carried out by XPS and UPS measurements during in-situ stepwise NiO film deposition using DC sputtering on reduced and oxidized rutile substrates for both orientations. Both identification and interpretation of the NiO spectra are rather complex due to severe main line splittings caused by multiplet contributions such as nonlocal screening and surface effects, and satellite structures at higher binding energies especially for thinner layers of NiO. However, for thicker layers, the typical NiO emission signature was obtained. There is a clear tendency of an increase of the asymmetry of the Ti2p line to lower binding energy for all heterointerfaces during, which may indicate a slight increase of $Ti^{3+}$ states during NiO deposition. In the O1s region, there are two shoulder peaks observed. The first shoulder at a higher binding energy than the main emission by 3.0 eV is assigned to peroxo species on the top of the rutile substrates, which disappears immediately after the first NiO deposition. The second one at a higher binding energy than the main peak by 2.3 eV might be attributed to the initial formation of the O poor surface species, which should show a higher binding energy. For all the four cases of NiO and different rutile heterostructures, the spectral changes of the $TiO_2$ substrates and growing NiO films are very similar to each other. However, the band bending saturates at a thinner NiO thickness for the rutile (001) compared to the rutile (110) for both annealed and oxidized substrates due to higher oxygen vacancy concentration of the rutile (001) surface than that of the rutile (110) surface. The Fermi level of rutile finally reaches the same value of about 1.6 eV independent of surface orientation and treatment. Finally, four band alignments of NiO/annealed rutile (110), NiO/annealed rutile (001), NiO/oxidized rutile (110), and NiO/oxidized rutile (001) are experimentally established using data from the interface experiments. The overall trend of the development of space charge layers in the two materials in contact of p-doped NiO and n-doped $TiO_2$ are hardly affected by the pretreatment induced differences. Evidently in p-NiO the Fermi level is pinned by a high concentration of defect states ($Ni^{3+}$ related states) in the bulk of the material as there is no additional band bending found in the NiO layers. The pinning level is found at a value of the Fermi level between 0.5 and 0.9 eV. The deposition of NiO leads to strong band bending within the $TiO_2$ substrates already for thin NiO layers, which would contribute to charge carrier separation in photocatalytic particles.

In order to demonstrate the efficiency of facet engineered photocatalysts of the p-NiO/n-$TiO_2$ heterostructures, NiO/(101)-anatase-$TiO_2$ heterostructure nanoparticles were synthesized by depositing NiO onto the (101) facet of bipyramid anatase crystals via the supercritical fluid chemical deposition (SFCD) route (See chapter 3.4).

First, bi-pyramidal anatase single crystal nanoparticles exposed to only the (101) facet was synthesized by a solvothermal method employing capping agents to control the growth of specific facets. Although the nanoparticles homogeneously agglomerate along the [001] direction before the treatment with superhydride and sulfuric acid solution, the well-ordered agglomeration has collapsed upon post-treatment with superhydride and sulphuric acid, forming partially isolated particles and mainly random agglomeration due to the small nanoparticle size. However, the well-defined structure of the bipyramidal shape of the crystallites remains unchanged after reductive, acidic, and supercritical fluid treatments. NiO was deposited on the oriented anatase particles via hydrothermal reactions employing a SFCD route with carbon dioxide and ethanol as solvents. The crystalline phase of the nanoparticles was characterized as anatase by Raman, XRD, nitrogen sorption and TEM. The crystal morphology of the heterostructures does not change for NiO amounts up to 2wt%. The uniform dispersion of NiO on the $TiO_2$ nanocrystallites was confirmed by EDX elemental maps of titanium, oxygen and nickel. The size of $TiO_2$ and NiO crystallites is 7-10 and 2-3 nm, respectively. Whatever the NiO loading, the mean mesopore size is rather constant, i.e. ranging between 4.7 and 5.2 ± 0.2 nm. The BET surface areas of $NiO/TiO_2$ nanocomposites containing less than 2wt% NiO remain close to that of pure $TiO_2$ nanoparticles, i.e. ranging between 105.1 ± 2.9 and 116.1 ± 3.2 $m^2.g^{-1}$. As a result, the supercritical fluid deposition of NiO allowed for the keeping high surface areas which was not the case for $NiO/TiO_2$ nanocomposites prepared by other methods such as sol-gel derived methods. The $NiO/TiO_2$ heteronanostructures showed visible light absorption, the edge of which shifts towards lower energies with increasing amount of NiO. The band gaps determined using Kubelka-Munk theory decrease from 3.21 eV for pure $TiO_2$ to 3.19, 3.15, 3.16, 3.13, 3.07 and 2.98 eV for 0.1, 0.25, 0.5, 1, 2, and 10 wt % $NiO/TiO_2$, respectively. XPS spectra showed the Fermi level shift toward a lower energy level ($E_F$-$E_{VB}$) from 3.34 eV for pure $TiO_2$ to 3.31, 3.29, 3.26, 3.26, 3.23, and 2.54 eV for 0.1, 0.25, 0.5, 1, 2, and 10 wt % $NiO/TiO_2$ heteroparticles, respectively. However, the observed shifts in Ti 2p and O 1s core levels remain relatively small, i.e. less than 100 meV. We attribute this contradictory effect either to the too small size of the particles to form a complete space charge layer which can saturate the band bending. But also a too homogeneously distributed NiO clusters on the $TiO_2$ for small coverage or the formation of a phase separated NiO cluster onto $TiO_2$ nanocrystallites may attribute to this effect. The 0.25wt% $NiO/TiO_2$ nanocomposite was the most efficient system for the decomposition of methylene blue (MB) as cationic dye and methyl orange (MO) dye as anionic dye, with activities 4.8 and 2.3 times higher than those of the pure $TiO_2$.

Finally, NiO/(101)-(001)-co-exposed anatase $TiO_2$ nanoparticles were successfully prepared by photo-deposition of NiO nanoparticles as a p-type co-catalyst preferentially onto the (101) facet of oriented n-$TiO_2$ anatase nanocrystals co-exposed with (001) and (101) facets (See chapter 3.5). The oriented anatase nanoparticles were prepared by gas-phase reaction of titanium(IV) chloride and oxygen. The top-truncated bi-pyramidal structures were confirmed by HRTEM images and the size of the crystallites is 50-150 nm. To prepare well-defined heterostructured NiO-$TiO_2$ particles, UV-light combined with the charge separation offered by the different redox properties of the (101) and (001) facets were exploited for the selective deposition of amorphous Ni-B on the (101) facets which led to NiO particles after further calcination in air. EDX elemental

mapping for 10 wt% $NiO/TiO_2$ shows that Ni is selectively distributed at the (101) facets, which constitute the edge of the particle. Furthermore, HRTEM images confirms that the Ni compounds selectively deposited onto the (101) facet is NiO as the interplanar spacing of 0.18 and 0.20 nm matches with the (200) and (111) planes of the face-centered cubic crystalline phase of NiO. Heterostructured $NiO/TiO_2$ samples exhibit visible light absorption of which edges shift toward lower energies with increasing the NiO due to Ti-Ni bonding at the interface or interfacial defect states. The band gaps determined using Kubelka-Munk theory decrease from 2.92 eV for pure $TiO_2$ to 2.81, 2.81, 2.82, 2.79, and 2.78 eV for 0.1, 0.2, 0.5, 1, and 10 wt % $NiO/TiO_2$, respectively. XPS spectra showed the Fermi level shift toward a lower energy level ($E_F$-$E_{VB}$) from 3.38 eV for pure $TiO_2$ to 3.07, 3.12, 3.15, and 2.20 eV for 0.1, 0.2, 1, and 10 wt % $NiO/TiO_2$, respectively. The peak of the emission from $Ti2p_{3/2}$ shifts to lower binding energy by 140 meV with the presence of NiO, which indicates band bending in the $TiO_2$ particles at the interface of the p-n junction of $NiO/TiO_2$ heterostructure nanoparticles. To obtain further insight into the interface properties of NiO-anatase heterojunctions, in-situ interface experiments were carried out by XPS and UPS measurements after each deposition steps of NiO with increasing thickness onto the stoichiometric anatase (101) and (001) substrates. The band bending at the interface of p-doped NiO and n-doped $TiO_2$ for anatase (001) is larger than that for the anatase (101) by 210 meV. In p-NiO the Fermi level is pinned by a high concentration of defect states ($Ni^{3+}$ related states) in the bulk as there is no additional band bending observed in the NiO layers. The pinning level is found at a value of $E_F$-$E_{VB}$ between 0.68 and 0.75 eV. Strong band bending within the $TiO_2$ substrates is achieved by the deposition of thin NiO layers of thicknesses larger than 1 nm, which would contribute to charge carrier separation in nanoparticle photocatalyst systems. To evaluate the photocatalytic activity of the prepared nanoparticles, the photodecomposition of MB was carried out under UV irradiation. The 0.1 wt % $NiO/TiO_2$ showed 50 % higher activities than the pure $TiO_2$. For both cases, these better performances were mainly attributed to spatial charge carrier separation due to the internal electric field at the interface of the $NiO/TiO_2$ p-n junction. To understand the main factor of the photodecomposition, potassium iodide, isopropyl, and 1,4-benzoquione were employed as hole, hydroxyl radical and superoxide radical scavengers, respectively for MB decomposition. It was found that electrons play a main role in photocatalysis for the pure $TiO_2$ as its crystallites are exposed with 72 % of the (101) facet which is considered to accumulate the photogenerated electrons. On the other hand, holes mainly dictate the photocatalytic dye decomposition on the 0.1 wt % $NiO/TiO_2$ photocatalysts. Although the (101) facet functions as electrons sink, NiO deposited onto the (101) facets would effectively collect holes at the p-n NiO/ $TiO_2$ (101) junction, but would also catalyse the reaction by lowering the activation energy and therefore hole charge transfer can be competitive compared to electron charge transfer.

This thesis has provided fundamental insights of oriented $TiO_2$ with various polymorphs and surface stoichiometry in terms of surface science, which are indispensable when considering the charge transfers of the $TiO_2$ with metals, semiconductors, or liquid. The concept of facet engineered surfaces established in this work would be operational to other metal oxide semiconductors as well. In addition, we hope that this work will inspire optimal designs of heterostructure systems for efficient photocatalytic process by combining a suitable

choice of co-catalysts and the selective deposition of the co-catalysts onto the specific facet of supported photocatalyst crystallites.

## Outlook

This work systematically investigated the electronic properties of well-defined $TiO_2$ surfaces under various surface conditions. To further understand the mechanism of photocatalytic reactions on the $TiO_2$, interactions and reactions of water and simple molecules such as oxygen on these surfaces need to be investigated by low energy electron microscopy, scanning tunnelling microscopy, scanning tunnelling spectroscopy, Low-energy ion scattering spectroscopy, and PES. This thesis suggests a potent strategy to enhance photocatalytic activities by depositing co-catalysts onto specific facets of photocatalyst crystals. To further improve the performance of heterostructure systems with $TiO_2$, further investigation of the synergetic effects of facet engineering and co-catalysts has to be carried out. In this work, NiO was deposited selectively onto only the anatase (101) facet. To compare the role of facets of the (001) and (101) facets, NiO needs to be deposited onto the (001) facet and its photocatalytic activity should be compared with the case where NiO is selectively deposited on the (101) facet. However, due to the lack of appropriate precursor for photo-deposition, so far there has been no reports which demonstrate the selective deposition of NiO onto the (001) facet. In addition, the aspect ratio of the (001) and (101) facets in anatase crystallites has to be taken into consideration since the ratio might affect the dynamics of charge carriers in the $NiO/TiO_2$ heterostructure system and thus be related with photocatalytic activities. Finally, hydrogen production by alcohol photoreforming or by water-splitting would warrant to be studied by using the $NiO/TiO_2$ heterostructures developed in this work as so far only dye decomposition was performed to evaluate the photocatalytic activity. To make the process sustainable, the use of alcohols obtained from waste or from biomass should be emphasised. The proof of such a concept could have a huge impact for industrial purposes.

## 4.3 Résumé détaillé en français

La crise énergétique mondiale combinée aux phénomènes de réchauffement climatique et de pollution environnementale a conduit à l'émergence de nombreux problèmes sociétaux qui doivent être résolus dans les prochaines décennies par les sociétés modernes pour garantir une économie prospère et durable. Par conséquent, il y a un besoin urgent de technologies « vertes » pour produire des carburants respectueux de l'environnement alternatifs aux combustibles fossiles ou nucléaire conventionnels et pour garantir une eau et un air pur via l'élimination efficace des polluants organiques et pharmaceutiques. Dans ce contexte, les réactions photocatalytiques sur les surfaces de dioxyde de titane ($TiO_2$) ont suscité une attention particulière au niveau mondial du fait de leur capacité à décomposer différents polluants de l'air ou des eaux, à réduire le dioxyde de carbone ($CO_2$) et à réaliser la photolyse de l'eau. Cependant, la photocatalyse avec des matériaux $TiO_2$ pur est loin de remplir les critères nécessaires pour une application dans les conditions réelles du fait de sérieuses limitations telles que les recombinaisons des porteurs de charge et la lenteur des réactions rédix de surface. De manière à tracer de nouvelles perspectives dans ce domaine, ce travail a eu pour objectif de caractériser soigneusement les propriétés de surface des matériaux à base de $TiO_2$ comme matériaux semiconducteurs de type n et des interfaces formées avec un matériau modèle de type p, l'oxyde de nickel, puis de développer de nouveaux catalyseurs à base d'hétérojonctions $NiO/TiO_2$ pour la photodécomposition de colorants organiques.

Dans le premier chapitre, les propriétés fondamentales de surfaces monocristallines de $TiO_2$ ont été décrites en détails au regard de la bibliographie. Cela comprend notamment des travaux récents concernant la distribution des lacunes d'oxygène sur des surfaces de $TiO_2$ orientées de manière différente et l'effet de ces lacunes sur l'adsorption d'eau sur ces surfaces. Les lacunes d'oxygène tendent à résider sous la surface ou dans le volume  tandis qu'elles apparaissent sur les sites oxygène pontant à la surface. De plus dans les cristallites de $TiO_2$ anatase, la facette (001) est particulièrement stable vis à vis de la création de lacunes d'oxygène tandis que ces dernières sont facilement créées sur les faces (101). Ces différences de stoechiométrie pour les différents polymorphes et orientations affectent considérablement les propriétés électroniques et ainsi les processus chimique sur ces surfaces tels que l'adsorption d'eau. Cependant la vision à l'échelle atomique de ces différences est encore peu claire. Les principes de la photocatalyse et les phénomènes spécifiques sur les surfaces de $TiO_2$ ont ensuite été rappelés. Puis, le rôle des co-catalyseurs a été exposé. En particulier, les co-catalyseurs peuvent non seulement former des zones de charge d'espace telles que des barrières Schottky et de jonctions p-n, qui favorisent la séparation des porteurs de charge, mais fournissent également des sites

de réaction rédox de surface en diminuant les surtensions pour la décomposition photoélectrochimique de l'eau et en réduisant les barrières d'activation pour les réactions photocatalytiques. Il mérite aussi d'être mentionné que l'équilibre entre les vitesses des réactions d'oxydation et de réduction doit être pris en compte car un déséquilibre conduirait à une accumulation d'électrons et/ou de trous, induisant un taux de recombinaison des porteurs de charge plus élevé. D'autre part, la formation d'une interface dans les nanocristaux d'oxydes métalliques semiconducteurs issue de l'ingénierie des facettes cristallines a aussi été discutée. Partant des études rapportant l'influence de la nature des facettes cristallines sur les propriétés photocatalytiques, les rôles respectifs des orientations (001) et (101) de l'anatase ont été présentés. Dans le cas de l'anatase, les électrons migrent vers la surface (101) tandis que les trous se déplacent vers la surface (001) même si le mécanisme associé demeure pour le moment inconnu. Enfin, des développements récents traitant de différentes approches synthétiques permettant le contrôle de la nature des facettes exposées par les cristaux d'anatase et des synergies issus de l'ingénierie des facettes et du dépôt de co-catalyseurs ont été analysés et résumés. En principe, le dépôt d'un co-catalyseur d'oxydation tel qu'un oxyde métallique de type p, comme l'oxyde de nickel (NiO), sur une face cristalline riche en électrons peut conduire au transfert spatial de trous vers le co-catalyseur d'oxydation tandis que le dépôt d'un co-catalyseur de réduction tel qu'un métal noble sur une face cristalline riche en électron peut favoriser la migration des électrons vers le co-catalyseur de réduction, maximisant les effets de séparation des porteurs de charge et augmentant ainsi les activités photocatalytiques. Néanmoins, le nombre de travaux démontrant ce type de synergie est limité aux photocatalyseurs de type oxyde métallique et, en particulier, à $TiO_2$. A partir de l'état des connaissances sur les réactions photocatalytiques utilisant $TiO_2$ comme matériau absorbeur, de nouvelles approches et considérations mécanistiques ont été récemment proposées par la communauté scientifique pour améliorer l'efficacité de ce système. Cependant, une compréhension détaillée des phénomènes mis en évidence par ces études demeure nécessaire notamment dans le domaine des processus de chimie et de physique des surfaces.

Dans le but d'apporter de nouvelles contributions à ce domaine pluridisciplinaire, les recherches menées au cours de ce travail ont consisté à combiner synthèse chimique et caractérisation de photocatalyseurs $NiO/TiO_2$, et des études de physique fondamentale sur des surfaces orientées de $TiO_2$ bien définies associées à des études soignées des interfaces formées par NiO avec ces surfaces de $TiO_2$. Ici, NiO a été employé comme semiconducteur de type p car c'est un des matériaux semiconducteurs de type p parmi les moins chers et constitués d'éléments abondants. Les travaux réalisés au cours de cette ont été organisés en cinq parties principales et les principaux résultats sont résumés dans ce qui suit.

Tout d'abord, des substrats d'anatase (001) et (101) bien définis ont été préparés et étudiés par spectroscopie de photoélectrons X (XPS) et Ultra-Violet (UPS) dans le but d'établir leurs structures électroniques. Les surfaces de $TiO_2$ ont été préparées de manière classique par des cycles répétés de pulvérisation ionique sous Argon suivis de recuits sous vide. Cependant la surface obtenue, nommée ensuite « pulvérisée », contenaient une grande quantité de lacunes d'oxygène et sa structure de surface pouvaient être partiellement détruite. Ainsi, pour comparer soigneusement leurs propriétés électroniques, les surfaces (101) et (001) ont été préparées *in-situ* dans la chambre sous vide pour obtenir différentes stoechiométries bien définies désignées ensuite par les termes pulvérisée, recuite, oxydée et stoechiométrique. L'orientation des surfaces recuites (101) et (001) a été confirmée à partir des figures non-reconstruites de diffraction des électrons de faible énergie (LEED). Une forte émission à faible énergie de liaison dans le spectre Ti2p caractéristique de $Ti^{3+}$, ce qui est typique de la présence de lacunes d'oxygène, n'a été observé que dans le spectre XPS des surfaces (101) pulvérisée. Bien que des lacunes d'oxygène étaient attendues pour d'autres stoechiométries de surface à la fois pour les surfaces (101) et (101), ces lacunes ne sont détectables que par spectroscopie de photoélectron sensible à la résonance de surface. Les spectres de bande de valence XPS et UPS montrent la présence de différentes distribution d'états dans la bande interdite (BGS), consistant en des états peu profonds (SGS) et profonds (DGS) dans la bande interdite situés respectivement à 0,5 et 1,6 eV sous le minimum de la bande de conduction, en fonction de l'orientation et du pré-traitement de surface. Quelles que soient les conditions de surface, les états DGS de la surface (101) sont significativement plus larges que ceux de la surface (101) mais présentent une intensité similaire à celle des surfaces (101) d'après les données UPS. En tenant compte de la sensibilité différente aux effets de surfaces des spectroscopies XPS et UPS, la différence en DGS indique que les défauts sont situés sous la surface, profondément sous la surface ou dans le volume pour la surface (001) tandis que pour la surface (101) ils sont localisés à la surface ou seulement peu profondément sous la surface. L'intensité SGS de la surface pulvérisée (101) est plus importante comparée à celle de la surface (001) pulvérisée à la fois en XPS et en UPS, ce qui implique que l'excès d'électrons de la surface (001) est localisé principalement sur les défauts tandis que celui de la surface (101) est non seulement localisé sur les défauts mais aussi largement délocalisé sur les atomes de titane du réseau. Les états DGS et SGS ainsi que les états de surface de la bande de valence (VBSS) des surfaces (001) déduits des mesures XPS s'atténuent graduellement avec une diminution de la position du niveau de Fermi mais existent encore même après traitement au plasma d'oxygène. D'autre part, les états DGS et SGS de la surface (101) pulvérisée déduits des mesures XPS disparaissent immédiatement après réoxydation sous plasma d'oxygène puis recuit sous vide. Cela indique que les défauts en position profonde sous la surface pour la surface (001) sont relativement stables et tendent à persister tandis que ceux de la surface (101) peuvent être comblés par des molécules d'oxygène ou des espèces peroxo. Parallèlement à la variation des états DGS, SGS

et VBSS, la modulation du niveau de Fermi, dont les valeurs ont été mesurées à 560 et 860 meV pour les surfaces (001) et (101), a été réalisée en contrôlant la stoechiométrie de surface. De manière remarquable, une différence de la position des niveaux de Fermi des facettes (001) et (101) du $TiO_2$ anatase a été mise en évidence. Le niveau de Fermi de la face (001) est située à une énergie inférieure à celle de la face (101), de 150 à 450 meV en fonction des conditions de surface (Figure 1). Par conséquent, une jonction est attendue entre ces deux facettes avec formation de zones de charge d'espace lorsque les électrons et les trous photogénérés sont transférés aux surfaces (101) et (001), respectivement. Cette différence des niveaux de Fermi des différentes phases cristallines constitue une explication convaincante du fait que les facettes (101) agissent comme des sites de réduction tandis que les facettes (001) jouent le rôle de sites d'oxydation.

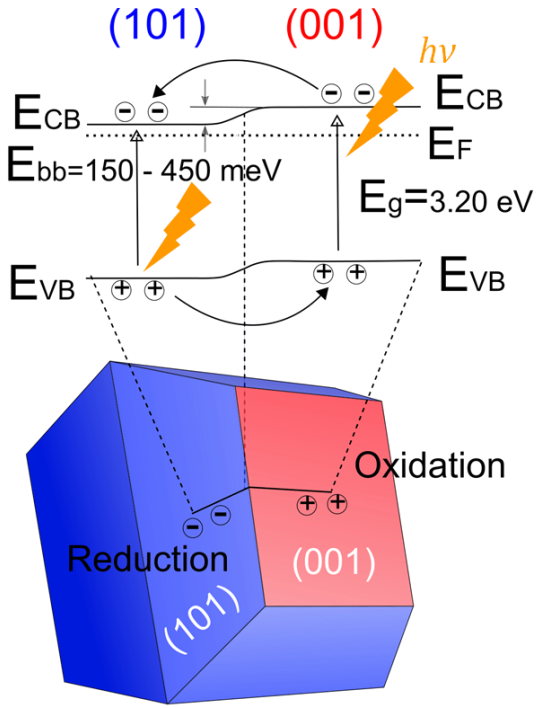


**Figure 4.1** : Processus de séparation des porteurs de charges dans des cristallites d'anatase co-exposant des facettes (001) et (101) déduit des diagrammes d'alignement des bandes d'énergie.

Dans une seconde partie, les potentiels de surface des films minces polycristallins d'anatase, de monocristaux d'anatase orientés (001) et (101), et de monocristaux de rutile orientés (001) et (110) avec différentes stoechiométries de surface ont été comparés de façon systématique par XPS et UPS. Parmi les propriétés électroniques, la détermination du travail de sortie est particulièrement pertinente pour les applications dans les domaines de la photocatalyse et des cellules solaires puisqu'il gouverne l'alignement des bandes aux différentes interfaces. Des surfaces pulvérisées, recuites, stoeichiométriques et oxydées traitées dans des conditions variées ont été préparées et d'amples variations du travail de sortie et du niveau de Fermi ont été atteintes en manipulant les états de surface.

La variation du travail de sortie déterminé par UPS est de 1,74, 1,94, et 1,39 eV pour les surfaces anatase (001), anatase (101), et polycristalline, respectivement (Figure 2). La variation du travail de sortie a été attribuée principalement à la variation du niveau de Fermi par rapport au maximum de la bande de valence puisque le potentiel d'ionisation est presque constant pour toutes les conditions de surface monocristalline d'anatase orienté avec un potentiel d'ionisation de 7.9 ± 0.15 eV. Des potentiels d'ionisation bien supérieurs, jusqu'à 9.5 eV, ont été observes pour des surfaces traitées sous plasma d'oxygène du fait de la formation probable d'espèces de surface de type peroxo ou à oxygène pontant. De plus, ces différentes surfaces ont été exposées à de la vapeur d'eau à température ambiante et les propriétés électroniques résultantes ont été étudiées par XPS et UPS. L'exposition à l'eau a conduit à des déplacements reproductibles des niveaux de cœur Ti2p et O1s et du maximum de la bande de valence vers les plus hautes énergies de liaison du fait d'une courbure de bande vers le bas au niveau de la surface de $TiO_2$ ce qui induit une accumulation d'électrons à la surface. La différence initiale de niveau de Fermi entre les surfaces anatase (001) et (101), qui existait pour tous les états de surface, a disparu après exposition à la vapeur d'eau. En ce qui concerne la différence de travail de sortie entre phases anatase et rutile, les surfaces anatase recuites ont montré une potentiel d'ionisation plus élevé que le rutile jusqu'à 0,5 eV, tandis que les positions du niveau de Fermi étaient similaires.

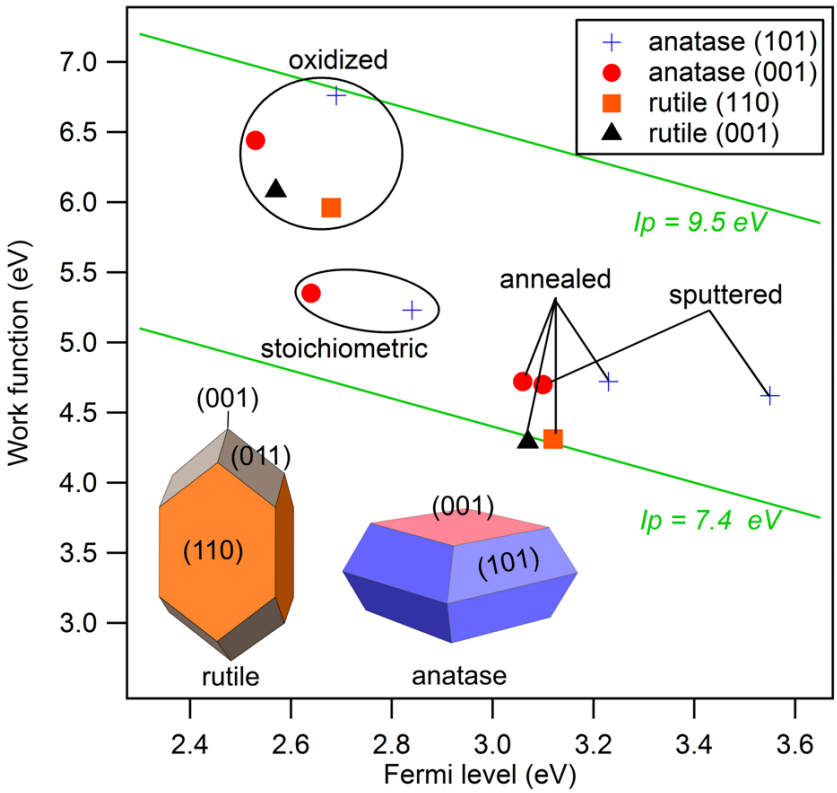


**Figure 4.2** : Travail de sortie de cristaux de TiO2 anatase et rutile d'orientations et stoechiométries variées.

L'alignement des énergies dans le vide de l'anatase et du rutile conduit le maximum de la bande de valence de l'anatase à être 0,5 eV plus bas en énergie que celui du rutile ce qui est en accord avec des études récentes sur l'alignement des bandes basées sur des données expérimentales et théoriques. Ainsi, la séparation de charge électron-trou dans des systèmes combinant anatase et rutile aurait lieu à l'interface et ce phénomène permet de comprendre l'activité photocatalytique exaltée des phases mixtes anatase-rutile comme le photocatalyeur $TiO_2$ commercial de référence connu sous le nom P25.

Pour comprendre l'effet de l'orientation cristallographique et des états de surface de la phase rutile de $TiO_2$ sur l'alignement des bandes dans le système $NiO/TiO_2$, les alignements des bandes d'énergie de NiO et de substrats de $TiO_2$ rutile monocristallin exposant des faces (001) et (110) ont été déterminées avec des surfaces réduites et oxydées en utilisant des expériences d'interface comme décrit ci-dessus. Tout d'abord, les propriétés électroniques de substrats monocristallins de $TiO_2$ rutile exposant des faces (001) et (110) ont été étudiées par XPS et UPS. La région des spectres XPS correspondant à la bande de valence indique que la position du niveau de Fermi de 3,12 eV par rapport à l'énergie du haut de la bande de valence pour la surface réduite du rutile (110) décroit à 2,68 eV pour la surface oxydée. Le travail de sortie de la surface réduite du rutile (110) déduit du seuil des électrons secondaires dans les spectres UPS a été mesurée à 4.3 eV et augmente jusqu'à 6.0 eV pour une surface oxydée. Une variation similaire a été observée pour la surface (001). Puis, les expériences d'interfaces ont été menées par des mesures spectroscopiques XPS et UPS en fonction du dépôt progressif d'un film de NiO par pulvérisation (DC) sur des substrats rutile réduits et oxydés exposant les deux orientations. L'attribution et l'interprétation des spectres XPS dans la region caractéristique de NiO s'est avérée plutôt complexe du fait du dédoublement des principale raies causé par différentes contribution telles que l'écrantage non-local et des effets de surface, et de structures satellites à des énergies de liaisons plus élevées notamment dans le cas des épaisseurs de NiO les plus fines. Cependant, pour des couches plus épaisses, la signature des émissions typiques de NiO a été obtenue. Il a été également observé une augmentation de l'asymétrie de la raie Ti2p à plus faible énergie de liaison pour toutes les hétérointerfaces ce qui pourrait indiquer une légère augmentation du nombre d'états $Ti^{3+}$ pendant le dépôt de NiO. Par ailleurs, dans la région O1s, deux épaulements ont été détectés. Le premier à énergie de liaison plus élevée de 3 eV que la raie d'émission principale a été attribué à des espèces peroxo à la surface des substrats rutile mais cet épaulement disparaît immédiatement après le premier dépôt de NiO. Le second à une plus haute énergie de 2,3 eV que celle du pic principal pourrait être attribuée à la formation initiale d'espèces de surface pauvres en oxygène dont la signature est attendue à plus haute énergie. Dans les quatre cas étudiés, les variations spectrales

des substrats de $TiO_2$ et des films de NiO en croissance sont similaires. Cependant, la courbure de bande sature à une épaisseur de NiO plus fine pour les substrats rutile (001) que pour les substrats rutile (001) à la fois pour les substrats recuits et oxydés du fait d'une plus forte concentration en lacunes d'oxygène pour la surface rutile (001) que pour la surface rutile (110). Le niveau de Fermi du rutile atteint la même valeur de 1,6 eV quels que soient l'orientation de la surface et le traitement effectué. Enfin les quatre alignements de bandes des systèmes NiO/rutile (110) recuit, NiO/ rutile (001) recuit, NiO/ rutile (110) oxydé, et NiO/rutile (001) oxydé ont été établis expérimentalement en utilisant les données issues des expériences d'interface (Figure 3).

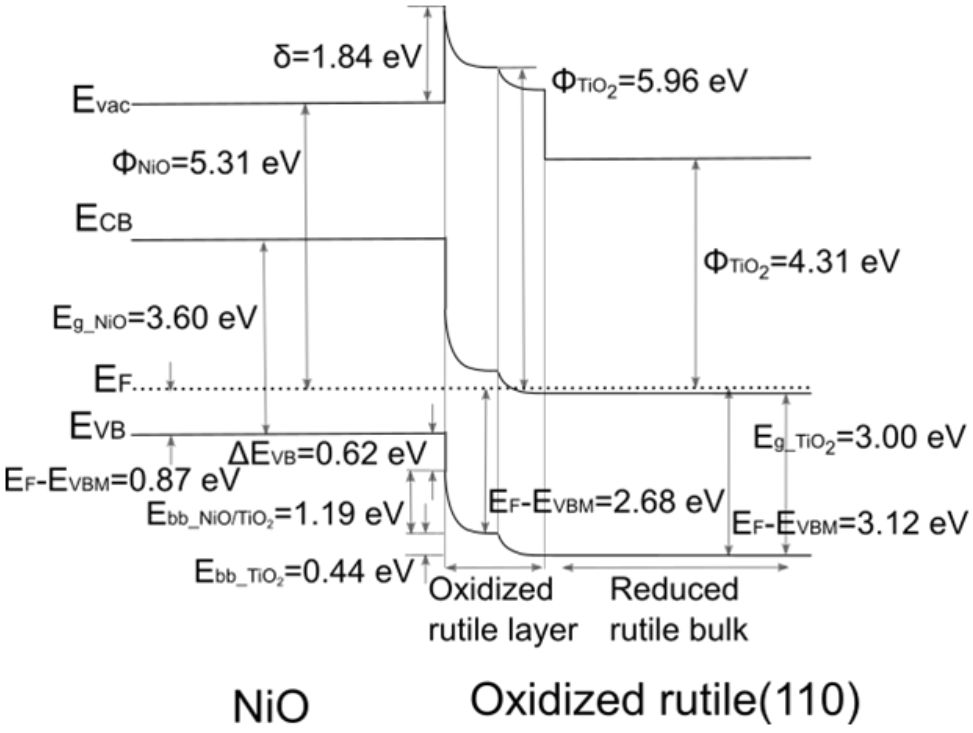


**Figure 4.3** : Alignement des bandes d'énergie pour la surface (110) du p-NiO/n-$TiO_2$ rutile oxydé déterminé à partir des expériences d'interface.

La tendance globale d'apparition de zones de charges d'espace dans les deux matériaux liée au contact entre le NiO de type p et le $TiO_2$ de type n est à peine affectée par les différences induites par les pré-traitements effectués. De façon évidente dans NiO de type p, le niveau de Fermi est bloqué par la forte concentration en défauts (états reliés à $Ni^{3+}$) dans le volume du matériau puisque qu'il n'y a pas de courbure de bande supplémentaire observée dans les couches de NiO. Ce niveau bloqué a été trouvé à une valeur du niveau de Fermi comprise entre 0,5 et 0,9 eV. Le dépôt de NiO conduit à une forte courbure de bande dans les substrats de $TiO_2$ dès les faibles épaisseurs en NiO, ce qui pourrait contribuer à la séparation des porteurs de charge dans les hétéronanostructures utilisées comme photocatalyseurs.

De manière à démontrer l'efficacité de photocatalyseurs constitués de systèmes p-NiO/n-$TiO_2$ à facettes exposées contrôlées, des hétéronanostructures NiO/(101)-anatase-$TiO_2$ ont été synthétisées en déposant NiO sur des nanocristaux de $TiO_2$ anatase exposant des faces (101) par la méthode de dépôt chimique en phase supercritique. Tout d'abord, des cristaux bipyramidaux de $TiO_2$ anatase exposant uniquement des faces (101) ont été préparés par une méthode solvothermale utilisant des agents de blocage pour contrôler la croissance des différentes facettes. Bien qu'un autoassemblage le long de la direction [001] des nanoparticules conduisant à la formation de gros agrégats ait été observé, cette agglomération ordonnée s'est écroulée lors de l'étape d'élimination des agents de blocage par traitements aux hydrures et à l'acide sulfurique conduisant à un phénomène d'agrégation résiduel aléatoire lié à la faible taille des particules. Cependant, la structure bipyramidale bien définie des cristallites de $TiO_2$ anatase reste inchangée après réaction en conditions fluide supercritique et après les traitements réducteurs et acide. Puis le NiO a été déposé avec succès sur les particules de $TiO_2$ anatase dans des conditions solvothermales en utilisant des conditions supercritiques avec le dioxyde de carbone et l'éthanol comme solvants. La nature des phases cristallines présentes dans les hétéronanostructures obtenues a été caractérisée par spectroscopie Raman, par diffraction des rayons X (DRX) et par microscopie électronique en transmission à haute résolution (MET-hr). La morphologie des particules ne change pas pour des teneurs en NiO inférieures à 2 % massique. La dispersion uniforme de NiO sur les nanocristallites de $TiO_2$ a été confirmée par analyse élémentaire par spectrographie par rayons X à dispersion d'énergie (EDX) des éléments titane, oxygène et nickel. La taille des cristallites de $TiO_2$ et de NiO ont été évalués à 7-10 nm et 2-3 nm, respectivement. Quelle que soit la teneur en NiO, la taille moyenne des mésopores est globalement constante, avec des valeurs comprises entre 4,7 and 5,2 ± 0.2 nm. Les surfaces spécifiques BET des nanocomposites NiO/$TiO_2$ contenant moins de 2% massique en NiO restent proches de celle des nanoparticules de $TiO_2$ pur, avec des valeurs comprises entre 105.1 ± 2.9 et 116.1 ± 3.2 $m^2.g^{-1}$. Par conséquent, le dépôt de NiO par la voie fluide supercritique permet de conserver des aires spécifiques élevées ce qui n'est pas le cas pour les nanocomposites NiO/$TiO_2$ préparés par d'autres méthodes telles que les voies sol-gel classiques. Les hétéronanostructures NiO/$TiO_2$ ainsi obtenues présentent une absorption dans le domaine du visible, le seuil d'absorption étant déplacé vers les faibles énergies lorsque la teneur en NiO augmente. L'énergie de la bande interdite déterminée à l'aide de la théorie de Kubelka-Munk décroît ainsi de 3,21 eV pour $TiO_2$ pur à 3,19, 3,15, 3,16, 3,13, 3,07 and 2,98 eV for 0,1, 0,25, 0,5, 1, 2, et 10% massique NiO/$TiO_2$, respectivement. Les spectres XPS révèlent un déplacement du niveau de Fermi vers les faibles énergies ($E_F$-$E_{VB}$) de 3,34 eV pour $TiO_2$ pur à 3,31, 3,29, 3.26, 3,26, 3,23, and 2,54 eV pour les héteronanostructures 0,1, 0,25, 0,5, 1, 2, et 10% massique NiO-$TiO_2$, respectivement. Cependant, les déplacements observés pour les niveaux de cœur Ti 2p et O 1s sont relativement faibles, inférieurs à

100 meV. Cet effet contradictoire peut être lié à la taille trop faible des nanoparticules qui ne permet pas la formation d'une zone de charge d'espace complète pouvant saturer la courbure de bande. En outre, la formation de clusters de NiO distribués de façon homogène à la surface des nanocristallites de $TiO_2$ pour les faibles teneurs en NiO et le phénomène de ségrégation de phase des cristallites de NiO sur les agrégats de nanoparticules de $TiO_2$ aux plus fortes teneurs de NiO peuvent aussi expliquer cet effet. Néanmoins, certaines hétérostructures possèdent des propriétés prometteuses pour la photodécomposition de colorants organiques sous illumination UV. Ainsi le nanocomposite 0,25% massique NiO/$TiO_2$ s'est avéré le système le plus efficace pour la dégradation du bleu de méthylène, comme exemple de colorant cationique, et du méthyl orange, comme exemple de colorant anionique, avec des activités photocatalytiques respectivement 4,8 et 2,3 fois supérieures à celles du $TiO_2$ pur (Figure 4).

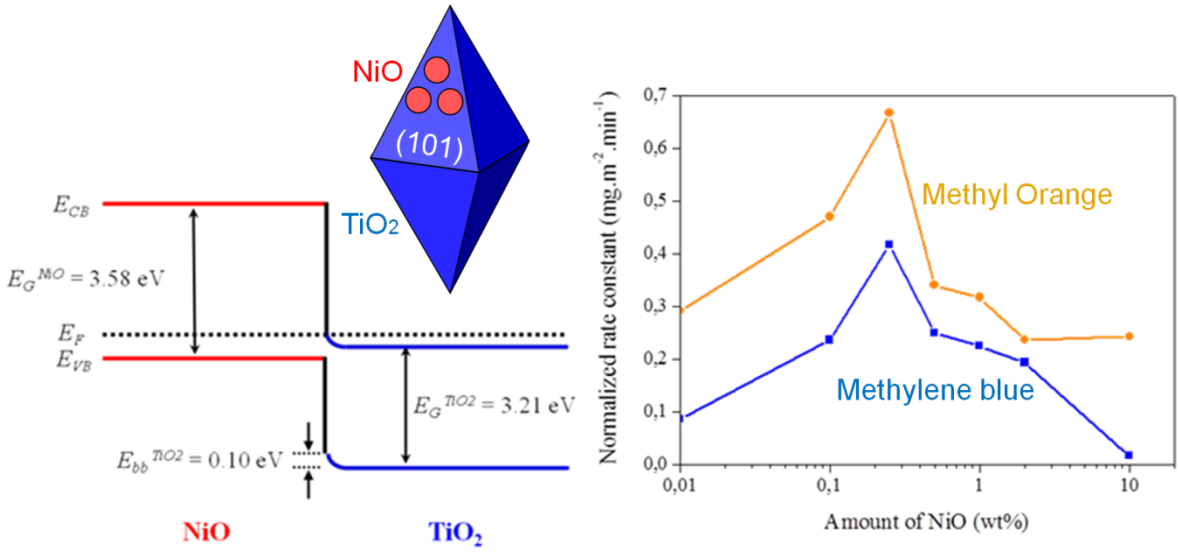


**Figure 4.4** : Alignement des bandes d'énergie et propriétés photocatalytiques des systèmes NiO/(101)-anatase-$TiO_2$ préparé$_s$ par la méthode de dépôt chimique en fluide supercritique.

Dans une dernière partie, des nanoparticules NiO/(101)-(001)-anatase $TiO_2$ ont été préparées avec succès par photodéposition préférentielle de nanoparticules de NiO, comme co-catalyseur semiconducteur de type p, sur les faces (101) de nanocristaux de $TiO_2$ anatase de type n co-exposant des facettes (001) et (101). Les nanoparticules d'anatase orientée ont été obtenues par réaction en phase gazeuse du tétrachlorure de titane et du dioxygène. La structure bipyramidale tronquée a été confirmée par MET-hr et la taille des cristallites a ainsi été estimée à 50-150 nm. Pour obtenir des hétéronanostructures bien définies, l'illumination UV associée à la séparation de charge offerte par les propriétés d'oxydo-réduction différentes des facettes (101) et (001) ont été exploitées pour déposer sélectivement du Ni-B amorphe sur les faces (101) ce qui a conduit à des particules de NiO après

calcination sous air. La cartographie EDX enregistrée pour l'échantillon 10% massique NiO/$TiO_2$ suggère que l'élément nickel est distribué sélectivement sur les faces (101) constituant les bords des particules. En outre, les images de microscopie électronique en transmission à haute résolution confirment que le nickel sur les faces (101) est du NiO puisque les distances entre plans atomiques mesurées de 0,18 et 0,20 nm correspondent aux plans (200) et (111) de la structure cristalline cubique face centrée de NiO.

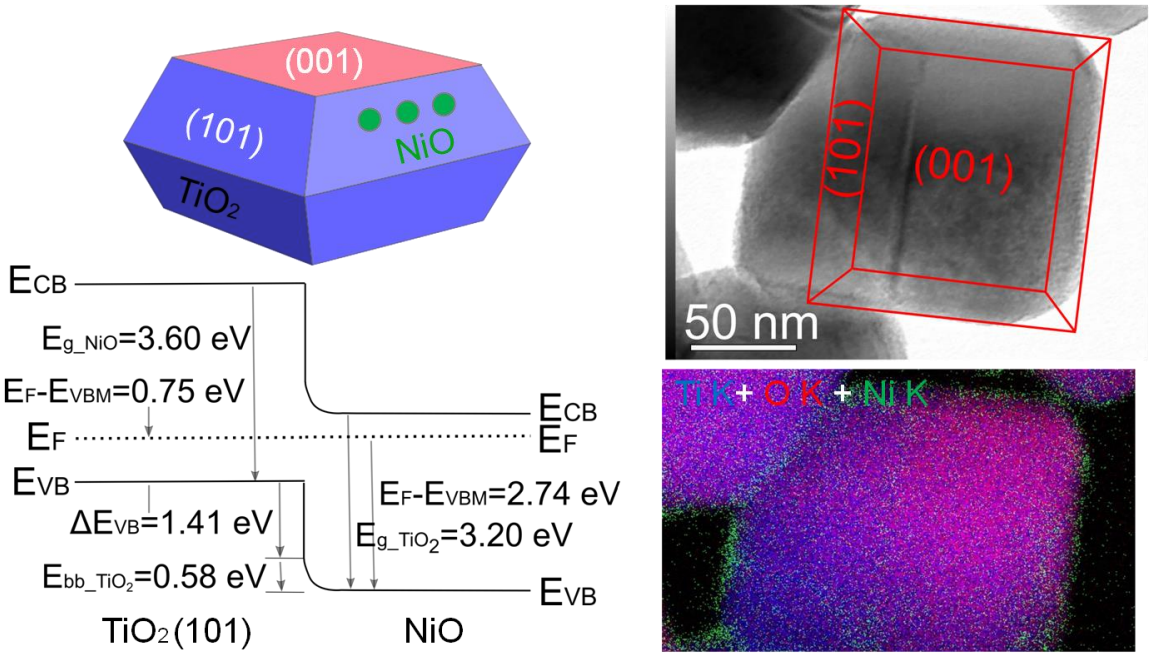


**Figure 4.5** : Dépôt sélectif photoinduit de NiO sur les facettes (101) de nanocristaux d'anatase co-exposant des faccettes (001) et (101).

Les hétérostructures NiO/$TiO_2$ présentent une légère absorption dans le visible dont le seuil se déplace vers les faibles énergies lorsque le taux en nickel augmente. Cette absorption dans le visible a été attribuée soit à des liaison Ti-Ni à l'interface des deux oxydes, soit à des défauts interfaciaux. L'énergie de la bande interdite déduite de la théorie de Kubelka-Munk diminue de 2,92 eV pour le $TiO_2$ pur à 2,81, 2,81, 2,82, 2,79, et 2,78 eV pour les échantillons 0,1, 0,2, 0,5, 1, et 10% massique NiO/$TiO_2$, respectivement. Les spectres XPS indiquent que le niveau de Fermi est déplacé vers les plus faibles énergies ($E_F$-$E_{VB}$) de 3,38 eV pour $TiO_2$ pur à 3,07, 3,12, 3,15, et 2,20 eV pour les échantillons 0,1, 0,2, 1, et 10% massique NiO/$TiO_2$, respectivement. Le pic d'émission des électrons de coeur $Ti2p_{3/2}$ se déplace vers les plus faibles énergies de liaison de 140 meV en présence de NiO, ce qui indique une courbure de bande dans les particules de $TiO_2$ à l'interface de la jonction p-n des hétéronanostructures NiO/$TiO_2$. Pour obtenir des informations plus précises sur les propriétés d'interface des hétérojonctions NiO/anatase-$TiO_2$, des expériences d'interfaces *in-situ* ont été menées

par mesures XPS et UPS après chaque étape du dépôt de NiO en augmentant l'épaisseur de NiO sur des substrats stoechiométriques de $TiO_2$ anatase (101) et (001). La courbure de bande à l'interface entre le NiO de type p et le $TiO_2$ anatase (001) de type n est plus importante de 210 meV que celle mesurée avec le $TiO_2$ anatase (101). Dans NiO le niveau de Fermi est bloqué du fait d'une forte concentration en défauts (états reliés à $Ni^{3+}$) dans le volume puisqu'il n'y a pas de courbure de bande observée dans les couches de NiO. Ce niveau de Fermi bloqué dans NiO a été trouvé à une valeur de $E_F$-$E_{VB}$ comprise entre 0,68 et 0,75 eV. La forte courbure de bande dans les substrats de $TiO_2$ a été obtenue par dépôt de fines couches de NiO dont l'épaisseur était supérieure à 1 nm, ce qui contribuerait à la séparation des porteurs de charge lors des processus photocatalytiques mettant en jeu ces matériaux. Pour évaluer l'activité photocatalytique des nanoparticules préparées, la photodégradation du bleu de méthylène sous illumination UV a été réalisée. Le système 0,1% massique NiO/$TiO_2$ a conduit à des efficacités 50% plus élevées à celles du $TiO_2$ pur. Ces meilleures performances ont été principalement attribuées à la séparation de charge spatial induite par le champ électrique interne à l'interface de la jonction p-n NiO/$TiO_2$. Pour déterminer plus précisément les facteurs principaux régissant les processus de photodécomposition, l'iodure de potassium, l'isopropanol et la 1,4-benzoquione ont été employés comme pièges à trous, à radicaux hydroxyles et à radicaux superoxydes, respectivement, lors de la photodégradation du bleu de méthylène. Il a été trouvé que les électrons jouent le rôle principal lors des processus de photodégrdation de colorants lorsque les cristallites de $TiO_2$ anatase orienté pur sont employées comme catalyseurs puisque que leurs cristallites exposent 72 % de faces (101) qui sont connues pour accumuler les électrons photogénérés. D'autre part, les trous régissent principalement las décomposition photocatalytique des colorants lorsque le photocatalyseurs 0.1% massique NiO/$TiO_2$ est utilisé. Bien que les faces (101) de l'anatase fonctionnent comme des puits à électrons, les particules de NiO deposées sur ces faces peuvent collecter efficacement les trous à la jonction p-n NiO/ $TiO_2$ (101), mais catalyser aussi la réaction en abaissant la barrière énergétique d'activation et, par conséquent, le transfert de trous peut devenir compétitif par rapport au transfert d'électrons.

Ce travail de thèse a donc permis d'obtenir des données fondamentales sur la science des surfaces de $TiO_2$ orientées de différentes phases cristallines et de stoechiométries variées, ce qui est indispensable pour l'étude des transferts de charge de $TiO_2$ vers des métaux, des semiconducteurs, ou des liquides. Le concept d'ingénierie des faces cristallines établi dans ce travail pourrait être étendu à l'avenir vers d'autres matériaux semiconducteurs. De plus, nous espérons que ce travail permette la conception d'hétérostructures optimales pour la photocatalyse en combinant un choix judicieux de co-catalyseurs et le dépôt sélectif de co-catalyseurs sur certaines facettes d'un matériau absorbeur donné.

Ce mémoire décrit une étude systématique des propriétés électroniques de surface de $TiO_2$ bien définies dans des conditions de surface variées. Pour acquérir une meilleure compréhension du mécanisme des réactions photocatalytiques sur $TiO_2$, les interactions et les réactions de l'eau ou de molécules simples telles que le dioxygène sur ces surfaces nécessitent d'être étudiées par microscopie électronique à faible énergie, par microscopie à effet tunnel, par spectroscopie de diffusion à faible énergie et par spectroscopie de photoélectrons. Cette thèse propose une stratégie générale pour améliorer les activités photocatalytiques par dépôt de co-catalyseurs sur des facettes spécifiques de cristaux de photocatalyseurs. Pour améliorer les performances de ces hétérostructures mettant en jeu $TiO_2$, des études supplémentaires sur la synergie entre l'ingénierie des facettes cristallines et le dépôt de co-catalyseurs doivent être menées. Dans ce travail, NiO a été déposé sélectivement uniquement sur la face (101) de l'anatase. Pour comparer le rôle des faces (001) et (101), le NiO nécessite aussi d'être déposé sélectivement sur la facette (001) et les propriétés photocatalytiques correspondantes devront être comparées à celles obtenues dans le cas du dépôt sélectif sur les facettes (101). Cependant, du fait du manque d'un précurseur adéquat pour un tel dépôt, il n'y a pas jusqu'à présent d'exemple de dépôt sélectif de NiO sur les facettes (001) des nanocristaux d'anatase. De plus, le rapport des dimensions des facettes (001) et (101) dans les nanocristallites d'anatase doit être pris en compte puisque ce rapport pourrait avoir une influence sur la dynamique des porteurs de charge dans les hétérostructures $NiO/TiO_2$ et donc influer sur les activités photocatalytiques. Enfin la production d'hydrogène par photoréformage d'alcools ou par photolyse de l'eau mériterait d'être étudiée en utilisant les hétérostructures $NiO/TiO_2$ développés dans ce travail puisque seuls la photodécomposition de colorants a été mise en œuvre pour évaluer leur activité photocatalytique. Pour rendre le procédé durable, l'utilisation d'alcools issus de déchets ou de la biomasse devra être privilégiée. La preuve d'un tel concept pourrait avoir un impact immense dans le domaine des applications industrielles.

**List of figures**

**List of tables**